VILNIUS UNIVERSITY

CENTER FOR PHYSICAL SCIENCES AND TECHNOLOGY

Mantas Šimėnas

ELECTRON PARAMAGNETIC RESONANCE SPECTROSCOPY OF HYBRID
METAL-FORMATE FRAMEWORKS

Doctoral dissertation
Physical sciences, physics - 02P

Vilnius, 2018

Scientific supervisor:

Prof. habil. dr. Jūras Banys (Vilnius University, physical sciences, physics - 02P)

VILNIAUS UNIVERSITETAS
FIZINIŲ IR TECHNOLOGIJOS MOKSLŲ CENTRAS

Mantas Šimėnas

HIBRIDINIŲ METALO-FORMIATO KARKASŲ TYRIMAI ELEKTRONŲ
PARAMAGNETINIO REZONANSO SPEKTROSKOPIJA

Daktaro disertacija
Fiziniai mokslai, fizika - 02P

Vilnius, 2018

Disertacija rengta 2014 - 2018 metais Vilniaus universitete.
Mokslinius tyrimus rėmė Lietuvos mokslo taryba.

Mokslinis vadovas:

Prof. habil. dr. Jūras Banys (Vilniaus universitetas, fiziniai mokslai, fizika - 02P)

Acknowledgements

Table of Contents

Abbreviations

2p	two-pulse
3p	three-pulse
Am	ammonium
Bn	1,4-butyldiammonium
CW	continuous wave
DFT	density function theory
DMA	dimethylammonium
DSC	differential scanning calorimetry
ENDOR	electron nuclear double resonance
EPR	electron paramagnetic resonance
ESEEM	electron spin echo envelope modulation
FID	free induction decay
fs	fine structure
hf	hyperfine
MA	methylammonium
MC	Monte Carlo
MHy	methylhydrazinium
MOF	metal-organic framework
NMR	nuclear magnetic resonance
XRD	X-ray diffraction
zfs	zero-field splitting

List of Samples

Sample	Formula	Doping level
DMAZn	$[(CH_3)_2NH_2][Zn(HCOO)_3]$	
DMAZn:Mn	$[(CH_3)_2NH_2][Zn(HCOO)_3]$:Mn	0.05/0.1 Mn^{2+} mol%
DMAZn-15N:Mn	$[(CH_3)_2{}^{15}NH_2][Zn(HCOO)_3]$:Mn	0.1 Mn^{2+} mol%
DMAZn:Cu	$[(CH_3)_2NH_2][Zn(HCOO)_3]$:Cu	1.0 Cu^{2+} mol%
AmZn:Mn	$[NH_4][Zn(HCOO)_3]$:Mn	0.1 Mn^{2+} mol%
MHyZn	$[CH_3NH_2NH_2][Zn(HCOO)_3]$	
MHyZn:Mn	$[CH_3NH_2NH_2][Zn(HCOO)_3]$:Mn	0.1 Mn^{2+} mol%
MHyZn:Cu	$[CH_3NH_2NH_2][Zn(HCOO)_3]$:Cu	0.3 Cu^{2+} mol%
BnZn	$[NH_3(CH_2)_4NH_3][Zn(HCOO)_3]_2$	
BnZn:Mn	$[NH_3(CH_2)_4NH_3][Zn(HCOO)_3]_2$:Mn	0.1 Mn^{2+} mol%
BnZn:Cu	$[NH_3(CH_2)_4NH_3][Zn(HCOO)_3]_2$:Cu	1.0 Cu^{2+} mol%

Introduction

The majority of solid crystals exhibit structural phase transitions that are usually accompanied by the significant changes (anomalies) of various physical properties [1]. Some of these transitions are followed by the appearance of the spontaneous electric polarization. A crystal is called ferroelectric, if the spontaneous electric polarization can be controlled by the external electric field.

Currently, many different ferroelectric materials with various chemical compositions are known. The inorganic ferroelectric compounds dominate, tough many organic crystals are also available [2]. Recently, the hybrid organic-inorganic ferroelectric and related materials emerged with comparable physical properties that stem from the combined effect of the organic and inorganic constituents [3]. A broad family of such hybrid crystals is highly porous metal-organic frameworks (MOFs) [4–6]. Usually, the synthesis of MOFs is rather simple compared with inorganic compounds, as it rarely requires high temperature and pressure.

The most popular hybrid MOFs exhibiting spontaneous electric polarization are metal-formate frameworks of chemical formula $[A][M(HCOO)_3]_n$, where A^{n+} is a molecular alkylammonium cation and M^{2+} is a metal center [7–9]. In these compounds, the A^{n+} cations are confined within the pores of the metal-formate framework. The structural phase transitions in these crystals involve the cooperative ordering of these cations and framework deformation. The properties of these transitions and nature of the phases are highly dependent on the metal center and molecular cation. Some of these compounds also exhibit magnetic properties at low temperature making them single structural phase multiferroics [8, 10, 11]. This material property is highly attractive for

1

construction of high density memory devices that can be controlled with magnetic and electric fields [12]. In such devices both magnetization and electric polarization could encode information in a single four-state multiferroic bit [13]. The applicability of multiferroics requires a deep knowledge of their magnetic and structural phase transition properties. However, despite several thorough studies of metal-formate frameworks, many questions about the phase transitions, possible ferroelectricity and role of the molecular cations in these hybrid compounds remain unanswered.

Among many characterization techniques, magnetic resonance tools such as continuous wave (CW) and pulsed electron paramagnetic resonance (EPR) as well as electron-nuclear double resonance (ENDOR) proved to be highly effective for characterization of phase transitions, structural phases as well as motional and lattice dynamics in various compounds [1, 14]. Due to the ability to probe the close vicinity of a paramagnetic center, EPR allows investigation of the local order parameter in powders, while most other methods measuring macroscopic properties such as electric polarization require electrical electrodes adding more complexity to the experiments [15]. However, many hybrid compounds do not contain intrinsic paramagnetic centers, and, thus, the usual procedure is to dope them with paramagnetic probes. The concentration of these centers shall be as low as possible to minimize the influence on the phase transition properties. Usually, transition metal ions having a similar ionic radius and the same charge as the intrinsic metal ions are used for doping.

1.1   Aim and Tasks of the Work

The aim of this work is to study the structural phase transitions, phases and dynamics of $[(CH_3)_2NH_2][Zn(HCOO)_3]$ (DMAZn), $[CH_3NH_2NH_2][Zn(HCOO)_3]$ (MHyZn), $[NH_4][Zn(HCOO)_3]$ (AmZn) and $[NH_3(CH_2)_4NH_3][Zn(HCOO)_3]_2$ (BnZn) hybrid metal-formate frameworks using EPR and ENDOR spectroscopic techniques.

The main tasks of this work are:

- to perform and analyze CW EPR experiments of Mn^{2+} and Cu^{2+} doped

DMAZn, MHyZn and BnZn frameworks;

- to perform and analyze CW EPR experiments with simultaneously applied electric field of Mn^{2+} doped DMAZn and AmZn single crystals;

- to perform and analyze pulsed EPR and ENDOR experiments of Mn^{2+} doped DMAZn, MHyZn and BnZn frameworks;

- to perform and analyze pulsed EPR and ENDOR experiments of Cu^{2+} doped DMAZn framework;

- to complement the EPR results by performing broadband dielectric spectroscopy, vibrational spectroscopy, electric polarization, pyrocurrent and NMR experiments as well as theoretical Monte Carlo simulations.

1.2   Scientific Novelty

- The EPR study of Mn^{2+} and Cu^{2+} doped DMAZn, AmZn, MHyZn and BnZn hybrid formate frameworks is presented for the first time.

- The powder CW EPR measurements are performed in the broad temperature range revealing the type and order of the structural phase transitions as well as motional effects in the high-temperature phases of Mn^{2+} and Cu^{2+} doped DMAZn, MHyZn and BnZn.

- The single crystal CW EPR experiments of Mn^{2+} doped DMAZn and AmZn are carried out with simultaneously applied electric field allowing to investigate the nature of the low-temperature phases in these frameworks.

- The pulsed EPR measurements are performed to investigate the lattice dynamics, motion in the ordered phases as well as the local environment of Mn^{2+} and Cu^{2+} ions in DMAZn, MHyZn and BnZn frameworks.

- The pulsed ENDOR experiments are performed for the first time to study the ordered structure of Mn^{2+} and Cu^{2+} doped DMAZn, MHyZn and BnZn frameworks.

- The EPR and ENDOR results are complemented by the broadband dielectric spectroscopy, vibrational spectroscopy, electric polarization, pyrocurrent and NMR experiments of MAZn, AmZn, MHyZn and BnZn frameworks as well as the Monte Carlo simulations.

1.3 Statements Presented for Defence

- CW EPR spectroscopy reveals the type and order of the structural phase transitions as well as molecular cation dynamics in Mn^{2+} and Cu^{2+} doped zinc-formate frameworks. DMAZn framework exhibits a strong first-order order-disorder phase transition, while MHyZn and BnZn compounds show weak first-order transitions close to the tricritical limit. Different phase transition behavior can be related to the number of hydrogen bonds of the central molecular cation.

- CW EPR spectroscopy with applied external electric field can be used to investigate the ferroelectric nature of Mn^{2+} doped zinc-formate frameworks. DMAZn framework exhibits domain structure in the low-temperature phase which is unaffected by the external electric field in contrast to AmZn framework. This indicates non-ferroelectric nature of DMAZn below the phase transition point.

- Pulsed EPR spectroscopy can be used to study methyl group motion in the low-temperature phase and lattice dynamics near the phase transition point of zinc-formate frameworks.

- Pulsed ENDOR spectroscopy verifies the proton positions in the structural X-ray diffraction models of zinc-formate frameworks.

1.4 Contribution by the Author

The investigated samples were synthesized by Prof. Dr. Mirosław Mączka group at Institute of Low Temperature and Structure Research of Polish Academy of

Sciences. The Author performed and analyzed the majority of the EPR experiments presented in this work. The dielectric characterization of the samples was carried out together with Sergejus Balčiūnas. The Author did all Monte Carlo simulations. The DFT calculations of EPR parameters were performed by Dr. Kęstutis Aidas.

1.5 Author Publications Included in the Thesis

1. **M. Šimėnas**, M. Ptak, A. H. Khan, L. Dagys, V. Balevičius, M. Bertmer, G. Völkel, M. Mączka, A. Pöppl, J. Banys. Spectroscopic Study of [(CH$_3$)$_2$NH$_2$] [Zn(HCOO)$_3$] Hybrid Perovskite Containing Different Nitrogen Isotopes. *J. Phys. Chem. C* **122**, 10284 (2018).

2. **M. Šimėnas**, A. Ciupa, G. Usevičius, K. Aidas, D. Klose, G. Jeschke, M. Mączka, G. Völkel, A. Pöppl, J. Banys. Electron Paramagnetic Resonance of a Copper Doped [(CH$_3$)$_2$NH$_2$][Zn(HCOO)$_3$] Hybrid Perovskite Framework. *Phys. Chem. Chem. Phys.* **20**, 12097 (2018).

3. **M. Šimėnas**, J. Banys, E. E. Tornau. Screening of Point Defects in Methylammonium Lead Halides: a Monte Carlo Study. *J. Mater. Chem. C* **6**, 1487 (2018).

4. **M. Šimėnas**, L. Macalik, K. Aidas, V. Kalendra, D. Klose, G. Jeschke, M. Mączka, G. Völkel, J. Banys, A. Pöppl. Pulse EPR and ENDOR Study of Manganese Doped [(CH$_3$)$_2$NH$_2$][Zn(HCOO)$_3$] Hybrid Perovskite Framework. *J. Phys. Chem. C* **121**, 27225 (2017).

5. **M. Šimėnas**, S. Balčiūnas, M. Mączka, J. Banys, E. E. Tornau. Exploring the Antipolar Nature of Methylammonium Lead Halides: A Monte Carlo and Pyrocurrent Study. *J. Phys. Chem. Lett.* **8**, 4906 (2017).

6. **M. Šimėnas**, A. Kultaeva, S. Balčiūnas, M. Trzebiatowska, D. Klose, G. Jeschke, M. Mączka, J. Banys, A. Pöppl. Single Crystal Electron Paramagnetic Resonance of Dimethylammonium and Ammonium Hybrid Formate Frameworks: Influence of External Electric Field. *J. Phys. Chem. C* **121**, 16533 (2017).

7. **M. Šimėnas**, S. Balčiūnas, M. Trzebiatowska, M. Ptak, M. Mączka, G. Völkel, A. Pöppl, J. Banys. Electron Paramagnetic Resonance and Electric Characterization of a [CH$_3$NH$_2$NH$_2$][Zn(HCOO)$_3$] Perovskite Metal Formate Framework. *J. Mater. Chem. C* **5**, 4526 (2017).

8. M. Mączka, M. Ptak, S. Pawlus, W. Paraguassu, A. Sieradzki, S. Balčiūnas, **M. Šimėnas**, J. Banys. Temperature- and Pressure-Dependent Studies of Niccolite-Type Formate Frameworks of [NH$_3$(CH$_2$)$_4$NH$_3$][M$_2$(HCOO)$_6$] (M = Zn, Co, Fe). *Phys. Chem. Chem. Phys.* **18**, 27613 (2016).

9. **M. Šimėnas**, A. Ciupa, M. Mączka, G. Völkel, A. Pöppl, J. Banys. EPR of Structural Phase Transition in Manganese- and Copper-Doped Formate Framework of [NH$_3$(CH$_2$)$_4$NH$_3$][Zn(HCOO)$_3$]$_2$. *J. Phys. Chem. C* **120**, 19751 (2016).

10. **M. Šimėnas**, S. Balčiūnas, M. Mączka, J. Banys, E. E. Tornau. Structural Phase Transition in Perovskite Metal-Formate Frameworks: a Potts-Type Model with Dipolar Interactions. *Phys. Chem. Chem. Phys.* **18**, 18528 (2016).

11. **M. Šimėnas**, A. Ciupa, M. Mączka, A. Pöppl, J. Banys. EPR Study of Structural Phase Transition in Manganese-Doped [(CH$_3$)$_2$NH$_2$][Zn(HCOO)$_3$] Metal-Organic Framework. *J. Phys. Chem. C* **119**, 24522 (2015).

12. M. Mendt, **M. Šimėnas**, A. Pöppl. Electron Paramagnetic Resonance in "The Chemistry of Metal-Organic Frameworks, Synthesis, Characterization, and Applications", chapter 21, pages 629-656. Wiley-Blackwell (2016).

1.6 Other Publications by the Author

1. A. Ibenskas, **M. Šimėnas**, E. E. Tornau. Multiorientation Model for Planar Ordering of Trimesic Acid Molecules. *J. Phys. Chem. C* **122**, 7344 (2018).

2. F. Gheorghiu, **M. Šimėnas**, C. E. Ciomaga, M. Airimioaei, V. Kalendra, J. Banys, M. Dobromir, S. Tascu, L. Mitoseriu. Preparation and Structural Characterization of Fe-Doped BaTiO$_3$ Diluted Magnetic Ceramics. *Ceram. Int.* **43**, 9998 (2017).

3. A. Ibenskas, **M. Šimėnas**, E. E. Tornau. A Three-dimensional Model for Planar Assembly of Triangular Molecules: Effect of Substrate-Molecule Interaction. *J. Phys. Chem. C* **121**, 3469 (2017).

4. **M. Šimėnas**, R. Matsuda, S. Kitagawa, A. Pöppl, J. Banys. Electron Paramagnetic Resonance Study of Guest Molecule-Influenced Magnetism in Kagome Metal-Organic Framework. *J. Phys. Chem. C* **120**, 27462 (2016).

5. A. Ibenskas, **M. Šimėnas**, E. E. Tornau. Numerical Engineering of Molecular Self-Assemblies in a Binary System of Trimesic and Benzenetribenzoic. *J. Phys. Chem. C* **120**, 6669 (2016).

6. **M. Šimėnas**, B. Jee, M. Hartmann, J. Banys, A. Pöppl. Adsorption and Desorption of HD on the Metal-Organic Framework $Cu_{2.97}Zn_{0.03}(btc)_2$ Studied by 3-Pulse ESEEM Spectroscopy. *J. Phys. Chem. C* **119**, 28530 (2015).

7. S. Friedlander, **M. Šimėnas**, M. Kobalz, P. Eckold, O. Ovchar, A. Belous, J. Banys, H. Krautscheid, A. Pöppl. Single Crystal Electron Paramagnetic Resonance with Dielectric Resonators of Mononuclear Cu^{2+} Ions in a Metal-Organic Framework Containing Cu_2 Paddle Wheel Units. *J. Phys. Chem. C* **119**, 19171 (2015).

8. **M. Šimėnas**, M. Kobalz, M. Mendt, P. Eckold, H. Krautscheid, J. Banys, A. Pöppl. Synthesis, Structure, and Electron Paramagnetic Resonance Study of a Mixed Valent Metal-Organic Framework Containing Cu_2 Paddle-Wheel Units. *J. Phys. Chem. C* **119**, 4898 (2015).

9. **M. Šimėnas**, A. Ibenskas, E. E. Tornau. Coronene Molecules in Hexagonal Pores of Tricarboxylic Acids: A Monte Carlo Study. *J. Phys. Chem. C* **119**, 20524 (2015).

10. Š. Svirskas, **M. Šimėnas**, J. Banys, P. Martins, S. Lanceros-Mendez. Dielectric Relaxation and Ferromagnetic Resonance in Magnetoelectric (Polyvinylidene-Fluoride)/Ferrite Composites. *J. Polym. Res.* **22**, 141 (2015).

11. **M. Šimėnas**, A. Ibenskas, E. E. Tornau. Phase transition properties of the Bell-Lavis model. *Phys. Rev. E* **90**, 042124 (2014).

12. **M. Šimėnas**, A. Ibenskas, E. E. Tornau. Effect of Lattice Coarsening and Exclusion on Phase Transition Properties of the Bell-Lavis Model. *Phase Transitions* **88**, 833 (2014).

13. A. Ibenskas, **M. Šimėnas**, E. E. Tornau. Antiferromagnetic Triangular Blume-Capel Model with Hardcore Exclusions. *Phys. Rev. E* **89**, 052144 (2014).

14. **M. Šimėnas**, E. E. Tornau. A Model of Melamine Molecules Ordering on Metal Surfaces. *J. Chem. Phys.* **141**, 054701 (2014).

15. **M. Šimėnas**, E. E. Tornau. Pin-Wheel Hexagons: A Model for Anthraquinone Ordering on Cu(111). *J. Chem. Phys.* **139**, 154711 (2013).

16. **M. Šimėnas**, A. Ibenskas, E. E. Tornau. Ordering of Triangular Molecules into the Honeycomb Phase: Estimation of Critical Temperature for Different Lattice Models of Self-Assembly. *Phase Transitions* **86**, 866877 (2013).

17. **M. Šimėnas**, R. Sobiestianskas, K. Bormanis, J. Banys, T. Ramoška. Dielectric Relaxation and Conductivity in the $PbCo_{0.5}Ta_{0.5}O_3$ Ceramics. *Solid State Ion.* **247**, 98101 (2013).

1.7 Oral Presentations by the Author at International Scientific Conferences

1. **M. Šimėnas**, M. Gusowska, M. Mączka, G. Völkel, A. Pöppl, J. Banys. Electron Paramagnetic Resonance Spectroscopy of Hybrid Metal-Formate Perovskites. *LNFK42*, 2017 October 4 - 6, Vilnius, Lithuania.

2. **M. Šimėnas**, M. Gusowska, M. Mączka, G. Völkel, A. Pöppl, J. Banys. EPR of Structural Phase Transitions in Dense Metal-Organic Frameworks. *ICPYS*, 2017 May 29 - June 2, Kharkiv, Ukraine.

3. **M. Šimėnas**, M. Gusowska, M. Mączka, G. Völkel, A. Pöppl, J. Banys. Electron Paramagnetic Resonance of Structural Phase Transitions in Metal-Formate Frameworks, *FMNT-2017*, 2017 April 24 - 27, Tartu, Estonia.

4. **M. Šimėnas**, M. Gusowska, M. Mączka, G. Völkel, A. Pöppl, J. Banys. EPR of Structural Phase Transitions in Dense Metal-Organic Frameworks. *Modern Multifunctional Materials and Ceramics*, 2017 April 19 - 20, Vilnius, Lithuania.

5. **M. Šimėnas**, M. Mączka, A. Pöppl, J. Banys. EPR Study of Structural Phase Transition in Manganese-Doped [(CH$_3$)$_2$NH$_2$][Zn(HCOO)$_3$] Metal-Organic Framework. *COST-TO-BE Spring Meeting 2016*, 2016 April 6 - 9, Warwick, UK.

6. **M. Šimėnas**, M. Kobalz, H. Krautscheid, J. Banys, A. Pöppl. Electron Paramagnetic Resonance Study of a Mixed Valent Metal-Organic Framework Containing Cu$_2$ Paddle-Wheel Units. *Open Readings 2015*, 2015 March 24 - 27, Vilnius, Lithuania.

1.8 Poster Presentations by the Author at International Scientific Conferences

1. **M. Šimėnas**, L. Macalik, K. Aidas, V. Kalendra, D. Klose, G. Jeschke, M. Mączka, G. Völkel, J. Banys, A. Pöppl. Pulse EPR and ENDOR Study of Manganese Doped [(CH$_3$)$_2$NH$_2$][Zn(HCOO)$_3$] Hybrid Perovskite. *51 RSC ESR*, 2018 April 8 - 12, London, UK.

2. **M. Šimėnas**, M. Gusowska, M. Mączka, G. Völkel, A. Pöppl, J. Banys. Electron Paramagnetic Resonance of Structural Phase Transitions in Dense Perovskite Metal-Organic Frameworks. *EUROMOF17*, 2017 October 29 - November 1, Delft, Netherlands.

3. **M. Šimėnas**, S. Balčiūnas, J. Banys, E. E. Tornau. Methylammonium Lead Iodide - a Model for a Sequence of Structural Phase Transitions. *LNFK42*, 2017 October 4 - 6, Vilnius, Lithuania.

4. **M. Šimėnas**, S. Balčiūnas, M. Gusowska, M. Mączka, Völkel, A. Pöppl, J. Banys. Phase Transitions in Dense Perovskite Formate Frameworks: EPR and Dielectric Study. *IMF17*, 2017 September 4 - 8, San Antonio, USA.

5. **M. Šimėnas**, M. Gusowska, M. Mączka, Völkel, A. Pöppl, J. Banys. Phase Transitions in Dense Perovskite Formate Frameworks: EPR and Dielectric Study. *EUROMAR17*, 2017 July 2 - 6, Warsaw, Poland.

6. **M. Šimėnas**, A. Ciupa, K. Aidas, M. Mączka, A. Pöppl, J. Banys. EPR Study of Structural Phase Transitions in Metal-Formate Frameworks. *Xth EFEPR*, 2016 September 4 - 8, Torino, Italy.

7. **M. Šimėnas**, A. Ciupa, M. Mączka, A. Pöppl, J. Banys. EPR Study of Ferroelectric Phase Transitions in Metal-Organic Frameworks Based on Perovskite Topology. *ISAF/ECAPD/PFM*, 2016 August 21 - 25, Darmstadt, Germany.

8. **M. Šimėnas**, M. Mączka, A. Pöppl, J. Banys. EPR Spectroscopy of Manganese Doped Perovskite-Type [$(CH_3)_2NH_2$][$Zn(HCOO)_3$] Metal-Organic Framework. *PACIFICHEM*, 2015 December 15 - 20, Honolulu, USA.

9. **M. Šimėnas**, A. Ibenskas, E. E. Tornau. A Monte Carlo Study on Coronene Influence on Self-Assembly of Tricarboxylic Acids. *FMNT-2015*, 2015 October 5 - 8, Vilnius, Lithuania.

10. **M. Šimėnas**, M. Mączka, A. Pöppl, J. Banys. EPR Spectroscopy of Manganese Doped [$(CH_3)_2NH_2$][$Zn(HCOO)_3$] Metal-Organic Framework: Ferroelectric Phase Transition. *7th Summer School of EFEPR*, 2015 August 24 - 31, Berlin, Germany.

11. **M. Šimėnas**, M. Mączka, A. Pöppl, J. Banys. EPR Spectroscopy of Manganese Doped Perovskite Metal Formate Framework. *EUROMAR2015*, 2015 July 5 - 10, Prague, Check Republic.

12. **M. Šimėnas**, M. Mączka, A. Pöppl, J. Banys. EPR Spectroscopy of Manganese Doped Perovskite-Type [$(CH_3)_2NH_2$][$Zn(HCOO)_3$] Metal-Organic Framework: Order-Disorder Phase Transition. *EMF 2015*, 2015 June 28 - July 3, Porto, Portugal.

13. **M. Šimėnas**, A. Pöppl, M. Kobalz, H. Krautscheid, J. Banys. EPR Spectroscopy of [$Cu(I)_2Cu(II)_2(H_2O)_2((Me-trz-mba)_2thio)_2$]$Cl_2$ Metal Organic Framework. *IXth EFEPR*, 2014 September 7 - 11, Marseille, France.

14. **M. Šimėnas**, A. Pöppl, M. Kobalz, H. Krautscheid, J. Banys. Continuous Wave EPR Spectroscopy of $[Cu(I)_2Cu(II)_2(H_2O)_2((Me-trz-mba)_2thio)_2]Cl_2$ Metal-Organic Framework. *PLU 2014*, 2014 August 31 - September 4, Wroclaw, Poland.

1.9 Other Presentations at International Scientific Conferences

1. F. Gheorghiu (presenter), C. Ciomaga, **M. Šimėnas**, M. Airimioaei, J. Banys, S. Qiao, L. Mitoseriu. Phase Modifications and Functional Properties of $Ba(Ti_{1-x}Fe_x)O_{3-x/2}$ Diluted Magnetic Ceramics (oral). *Electroceramics XVI*, 2018 July 9 - 12, Hasselt, Belgium.

2. D. De Sloovere (presenter), M. Safari, **M. Šimėnas**, J. Banys, M. K. Van Bael, A. Hardy. Solution Gel Synthesis of a Novel Sodium Titanate/Carbon Composite for Sodium Ion Battery Anodes (poster). *EMRS-Spring 2018*, 2018 June 18 - 22, Strasbourg, France.

3. **M. Šimėnas**, L. Macalik, K. Aidas, V. Kalendra, D. Klose, G. Jeschke, M. Mączka, G. Völkel, A. Pöppl, J. Banys (presenter). Pulse EPR and ENDOR Study of Manganese Doped $[(CH_3)_2NH_2][Zn(HCOO)_3]$ Hybrid Perovskite (invited, oral). *RCBJSF*, 2018 May 14 - 18, St. Petersburg, Russia.

4. **M. Šimėnas**, R. Matsuda, S. Kitagawa, A. Pöppl, J. Banys (presenter). EPR Study of Guest Molecule-Influenced Magnetism in Kagome Metal-Organic Framework (poster). *EUROMAR17*, 2017 July 2 - 6, Warsaw, Poland.

5. R. Babkin (presenter), **M. Šimėnas**, A. Pöppl, J. Banys, Y. Pashkevich, D. E. L. Vieira, A. Salak. Electron Paramagnetic Resonance Studies of Cobalt-Based Layered Double Hydroxides (oral). *ICPYS*, 2017 May 29 - June 2, Kharkiv, Ukraine.

6. **M. Šimėnas**, A. Ciupa, K. Aidas, M. Mączka, A. Pöppl, J. Banys (presenter). EPR of Structural Phase Transitions in Formate Metal-Organic Frameworks (poster). *LUP 2016*, 2016 September 5 - 9, Palanga, Lithuania.

7. **M. Šimėnas**, S. Balčiūnas, M. Mączka, J. Banys, E. E. Tornau (presenter). Structural Potts-type Phase Transition in Perovskite Metal-Formate Frameworks: Effect of Dipolar Interactions (invited, oral). *LUP 2016*, 2016 September 5 - 9, Palanga, Lithuania.

8. V. Kalendra (presenter), **M. Šimėnas**, F. Gheorghiu, C. Ciomaga, N. Horchidan, L. Mitoseriu, J. Banys. Functional Properties of $BaTiO_3$ Ceramics: the Influence of Iron Addition (poster). *LUP 2016*, 2016 September 5 - 9, Palanga, Lithuania.

9. L. P. Curecheriu (presenter), C. Ciomaga, N. Horchidan, **M. Šimėnas**, L. Mitoseriu. Effect of Fe Doped in the Ferroelectric-Relaxor Crossover in $BaZr_xTi_{1-x}O_3$ Ceramics (poster). *ISAF/ECAPD/PFM*, 2016 August 21 - 25, Darmstadt, Germany.

10. **M. Šimėnas**, A. Ciupa, K. Aidas, M. Mączka, A. Pöppl, J. Banys (presenter). EPR of Structural Phase Transitions in Formate Metal-Organic Frameworks (poster). *EUROMAR16*, 2016 July 3 - 7, Aarhus, Denmark.

11. **M. Šimėnas**, M. Mączka, Pöppl, J. Banys (presenter). EPR Spectroscopy of Manganese-Doped Perovskite-Type Metal-Organic Framework (poster). *DyProSoXXXV*, 2015 September 13 - 17, Munich, Germany.

12. **M. Šimėnas**, A. Ibenskas, E. E. Tornau (presenter). Phase Transitions in Antiferromagnetic Triangular Bell-Lavis and Blume-Capel Models (invited, oral). *PLU 2014*, 2014 August 31 - September 4, Wroclaw, Poland.

Chapter 2

Overview

In this Chapter, the structural phase transitions, hybrid metal-formate frameworks and electron paramagnetic resonance spectroscopy are introduced and discussed in a nutshell.

2.1 Structural Phase Transitions

2.1.1 Classification of Structural Phase Transitions

The majority of solid crystals can exist in several crystalline phases [2, 16]. The stability of a particular structural phase is usually influenced by the external factors such as temperature, pressure, electric as well as magnetic fields. As the stability limits of a particular phase are approached, a crystal tends to transform into another phase during a phenomenon called a structural phase transition. Such a transition is usually accompanied by the symmetry breaking, anomalies of physical properties and appearance of the so called order parameter [17]. The structural phase transition temperature T_c is called the Curie temperature.

The structural phase transitions are classified into the ferrodistortive and antidistortive as depicted in Figure 2.1 [2]. During a ferrodistortive transition, the atom positions change in such a way that the number of formula units per unit

cell remains the same [1]. Otherwise, the phase transition is said to be anti-distortive. Crystals that exhibit ferrodistortive structural transitions followed by the appearance of the spontaneous electric polarization below T_c are called pyroelectrics (e.g. LiTaO$_3$ [18]). A pyroelectric crystal is ferroelectric, if the spontaneous electric polarization can be reversed by the external electric field. One of the most famous ferroelectric compound is BaTiO$_3$ [2]. The antidistortive phase transition is called antipolar, if the spontaneous electric polarization cancels due to the oppositely directed electric dipoles in each sublattice. The polarization in some antipolar crystals may also be controlled by a sufficiently strong external electric field. In such a case, the crystal is called antiferroelectric (e.g. PbZrO$_3$ [19]).
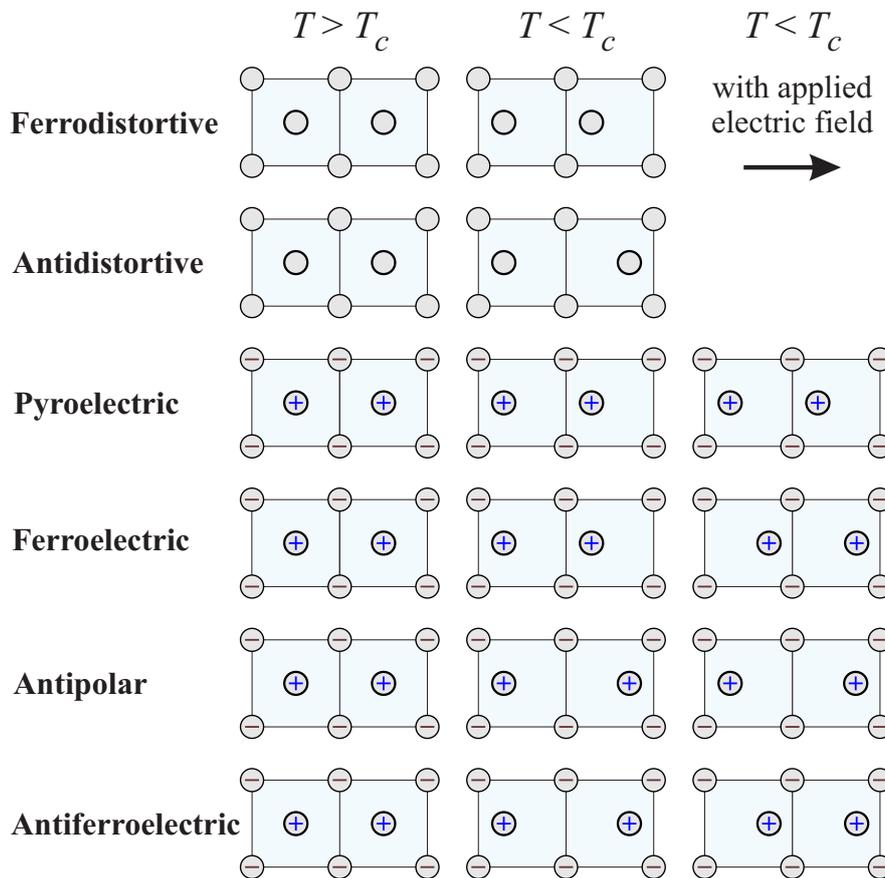
Figure 2.1: Classification of fundamental structural phase transitions. Adapted from Ref. [2].

The structural phase transitions can be further classified into an order-disorder and displacive types (see Figure 2.2) [1]. In the former class of compounds, the

phase of higher symmetry ($T > T_c$) results from the dynamic or static disorder of ions or their groups. The dynamic disorder occurs due to the thermal motion of ions in a multi-well energy landscape, while a random static occupation of potential minima results in the static disorder. Naturally, such a phase is called the disordered phase. During a structural order-disorder phase transition, the change of the energy landscape causes ions to occupy the potential wells in a correlated manner. Thus, the long-range structural order is established in the crystal (the ordered phase). The examples of the order-disorder ferroelectrics include $NaNO_2$, KH_2PO_4 and many others [1].
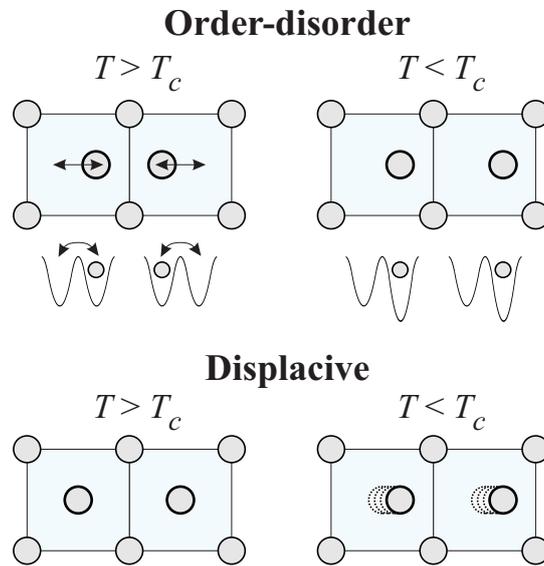
Figure 2.2: Illustrative comparison between the order-disorder and displacive structural phase transitions.

The symmetric phase ($T > T_c$) of a displacive type crystal is characterized by a single potential well occupied by the ion [1]. During a displacive structural phase transition, the energy landscape transforms to the multi-well potential, while ions cooperatively shift from position of high-symmetry as indicated in Figure 2.2.

The presented classification of the structural transitions into the order-disorder and displacive types is idealistic, since the majority of crystals fall into a middle group with shallow double-wells, highly anharmonic single wells, or tunneling wells (H-bonded ferroelectrics) [1, 2]. For such systems, this distinction is rather

obscured. For example, several recent magnetic resonance studies [20, 21] found indications of the order-disorder character of the phase transitions in BaTiO$_3$ crystal, which was considered for a long time to be an archetypal example of a displacive ferroelectric.

The structural phase transitions are usually accompanied by the anomalous change of the crystal physical properties such as volume, heat capacity, dielectric permittivity and others [16, 17]. According to the abruptness, the phase transitions can be further subdivided into the first-order and second-order transitions. A sudden (discontinuous) change of the crystal properties signifies a first-order phase transition, during which a system either absorbs or releases a fixed amount of latent heat. Such a transition is characterized by the co-existence of both structural phases meaning that only a part of a system has completed the transition. First-order phase transitions are also accompanied by the temperature hysteresis.

A second-order (continuous) phase transition exhibits a continuous change of the crystal properties over a wide range of temperature or pressure. Such a transition is characterized by the divergent susceptibilities and power-law decay of correlations [17]. The length of structural correlations at the second-order phase transition point becomes infinite meaning that the phase coexistence is not possible for this type of transition. For a weak first-order phase transition (close to the second-order), the correlation length may become relatively long causing properties similar to the second-order transition.

The structural phase transitions are also characterized by the appearance of the order parameter η in the less symmetric phase. For a first-order structural phase transition, the order parameter changes in a jump-wise manner at the transition point, while a second-order phase transition demonstrates a continuous increase described by a power law. The schematic temperature dependence of η for the strong and weak first-order as well as second order phase transitions is presented in Figure 2.3. Note the temperature hysteresis for the first-order phase transitions.

For a proper ferroelectric crystal, the order parameter is considered to be the spontaneous electric polarization. However, there exists a broad class of ferroelectrics where the spontaneous polarization arises as a secondary effect -
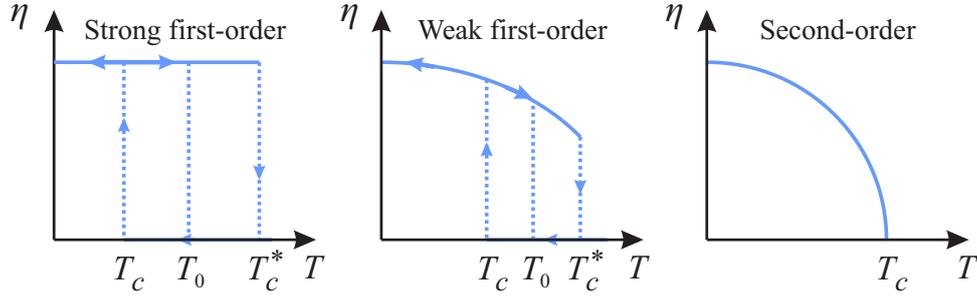
Figure 2.3: Schematic temperature dependence of the order parameter for strong and weak first-order (discontinuous) as well as for the second order (continuous) phase transitions. The first-order phase transition occurs at temperature T_0 which is between T_c and T_c^* that bound the maximal temperature hysteresis.

the so called improper ferroelectricity. In this case, the order parameter of the phase transition is not the polarization but another physical quantity with transformation properties different from those of the polarization. The anomalies of dielectric properties in the improper ferroelectrics may significantly differ from the anomalies observed in the ordinary ferroelectrics [22].

The temperature dependence of the order parameter around the phase transition point can be described using the phenomenological Landau theory which is briefly covered in the following Section.

2.1.2 Landau Theory of Phase Transitions

The cornerstone of the Landau theory is the invariance of the thermodynamic potential (e.g. free energy) of a crystal under all symmetry operations of the crystal Hamiltonian [17]. The change of the crystal symmetry at the phase transition point is sufficient for the anomalies of the physical properties to occur.

In the vicinity of the second-order phase transition, the order parameter grows continuously from zero. Thus, one can expand the thermodynamic potential Φ of a crystal in series of η [16, 17]:

$$\Phi(T, \eta) = \Phi_0 + \sum_{i=1}^{\infty} a_i \eta^i, \tag{2.1}$$

17

where Φ_0 is the equilibrium value of the potential at T_c. The temperature dependence of $\Phi(T, \eta)$ is contained in the coefficients, i.e. $a_i = a_i(T)$.

Due to the symmetry, the potential must be invariant under the change of the order parameter sign. Thus, the terms containing odd powers must vanish providing the following expression:

$$\Phi(T, \eta) = \Phi_0 + a_2\eta^2 + a_4\eta^4 + \ldots \tag{2.2}$$

One can limit the expansion to the fourth order and expand a_2 coefficient around T_c as

$$a_2(T) = a_2(T_c) + a_2'(T - T_c) + \ldots \tag{2.3}$$

The coefficient a_2 must vanish at T_c to fulfill the condition that $\eta \neq 0$ for $T < T_c$. By keeping only the second term in the last expansion, we obtain the final expression for the thermodynamic potential:

$$\Phi(T, \eta) = \Phi_0(T) + \frac{1}{2}\alpha(T - T_c)\eta^2 + \frac{1}{4}\beta\eta^4. \tag{2.4}$$

Here $\alpha = 2a_2'$ and $\beta = 4a_4'$ are positive constants.

The equilibrium value of the order parameter η_0 is found from the condition

$$\left.\frac{\partial \Phi}{\partial \eta}\right|_{\eta=\eta_0} = 0, \tag{2.5}$$

which provides

$$\begin{cases} \eta_0 = 0 & T > T_c \\ \eta_0 = \left(\frac{\alpha(T_c-T)}{\beta}\right)^{1/2} & T < T_c \end{cases}. \tag{2.6}$$

The zero value of η in the phase of higher symmetry ($T > T_c$) indeed satisfies the definition of the order parameter. In the low-symmetry phase ($T < T_c$), the order parameter follows the power-law temperature dependence with the critical exponent equal to $\frac{1}{2}$.

The dependence of the thermodynamic potential on η for the second-order phase transition is presented in Figure 2.4. For temperature higher than T_c, the potential consists of a single minimum at $\eta = 0$ which corresponds to the

symmetric phase. As the phase transition point is approached, the minimum broadens and becomes flat at T_c. In the less symmetric phase, the potential consists of two wells at the positive and negative equilibrium values of the order parameter.

Second-order
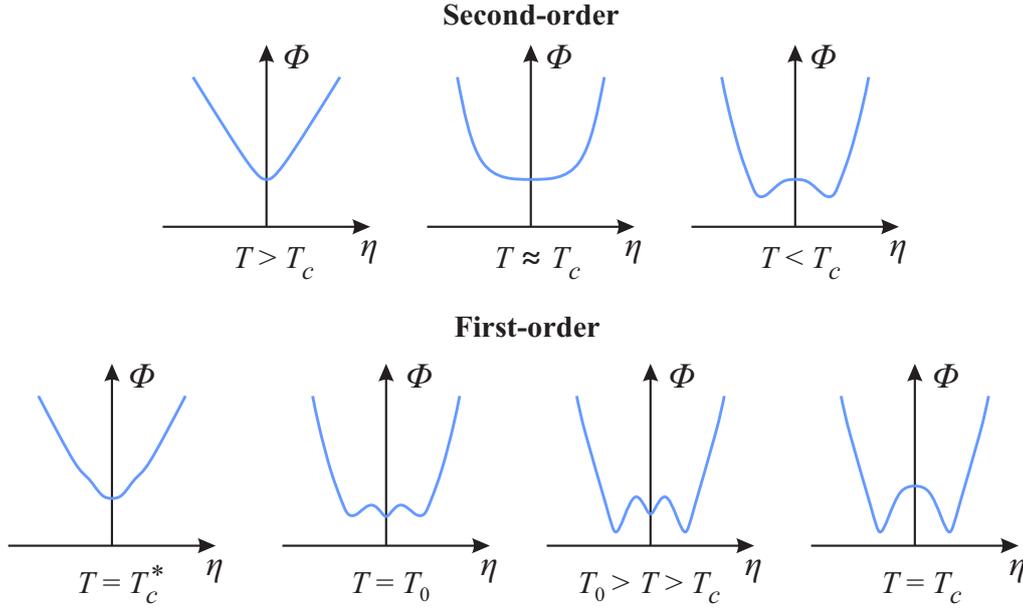
First-order

Figure 2.4: Dependence of the crystal potential on the order parameter for the second- and first-order phase transitions as obtained from the Landau theory.

The Landau theory is sufficiently universal to describe a weak first-order phase transition which exhibits a small jump of the order parameter at the transition point (see Figure 2.3) [16]. In this case, the terms up to the sixth order must be taken into account in the expansion of the potential:

$$\Phi(T,\eta) = \Phi_0(T) + \frac{1}{2}\alpha(T - T_c)\eta^2 + \frac{1}{4}\beta\eta^4 + \frac{1}{6}\gamma\eta^6, \tag{2.7}$$

where $\alpha, \gamma > 0$ and $\beta < 0$. Then the square of the order parameter of the low-symmetry phase is

$$\eta_0^2 = -\frac{\beta}{2\gamma}\left[1 \mp \left(1 - \frac{4\alpha(T - T_c)\gamma}{\beta^2}\right)^{1/2}\right]. \tag{2.8}$$

The temperature evolution of the crystal potential for a weak first-order phase transition is also presented in Figure 2.4. In the symmetric phase, the potential

exhibits a single minimum at $\eta = 0$. As temperature is decreased, points of inflection appear on the curve at T_c^*. Upon further cooling, these points transform to two additional minima that correspond to the low-temperature phase. The phase transition to this phase appears at temperature $T = T_0$ at which the depths of all three wells are equal. The minimum at $\eta = 0$ diminishes at $T = T_c$, which, in this case, defines the stability limit of the high-temperature phase. On contrary, if the crystal is heated starting from the low-temperature phase, the latter can exist up to the temperature T_c^*. The real experimental conditions may be relatively far from the thermal equilibrium, and thus the observed phase transition point may differ from T_0, tough the transition must occur between T_c and T_c^*. This temperature range corresponds to the maximum temperature hysteresis of the first-order phase transition (see Figure 2.3) and can be expressed as

$$T_c^* - T_c = \frac{\beta^2}{4\alpha\gamma}.$$ (2.9)

The strength of the first-order phase transition depends on the parameter β. For small absolute values of β, the transition corresponds to a weak first-order phase transition. As $\beta \to 0$, the temperature hysteresis of the phase transition narrows, and the discontinuous first-order character becomes continuous - the so called tricritical point is attained. However, such a continuous transition has certain features which distinguish it from the second-order phase transitions. In this case the order parameter has the following temperature dependence:

$$\eta_0 = \left(\frac{\alpha(T_c - T)}{\gamma} \right)^{1/4}.$$ (2.10)

An increase of the order parameter according to the law $(T_c - T)^{1/4}$ is much steeper compared to the $(T_c - T)^{1/2}$ dependence found for the second-order phase transition (see Eq. 2.6). The existence of the tricritical point was found experimentally in many different systems ranging from ferroelectric crystals such as KH_2PO_4 [23] or SbSI [16] to quantum magnets [24] and superconductors [25]. Note that usually the tricritical point in ferroelectrics is attained at high pressure, which involves additional experimental difficulties.

2.2 Hybrid Metal-Organic Frameworks

Lately, significant scientific attention was concentrated on the hybrid organic-inorganic compounds [26, 27]. The desirable physical and chemical functionalities of these materials stem from the versatile properties of the different organic and inorganic constituents [3]. The promising applications of the hybrid compounds include highly efficient solar cells [28], gas storage devices [29, 30], multiferroic memories [4–6] and others [31].

A very broad family of hybrid crystals is metal-organic frameworks (MOFs) or coordination polymers [26, 32]. The majority of these compounds are highly porous and have aesthetically attractive underlying framework topologies [3]. The potential applicability of these compounds stems from their structural diversity determined by the constituent units: metal ion centers (nodes) and organic linkers (see Figure 2.5) [3, 31]. Frequently, transition metal or lanthanide cations are chosen as nodes due to their high coordination number and the ability to adapt different coordination geometries [33, 34]. These metal centers and various organic linkers are responsible for peculiar optical [35], electric [36], magnetic [37] and gas-absorption related [29, 38, 39] properties of these materials. Several MOF families also exhibit structural transitions to phases with ferroelectric properties [5].
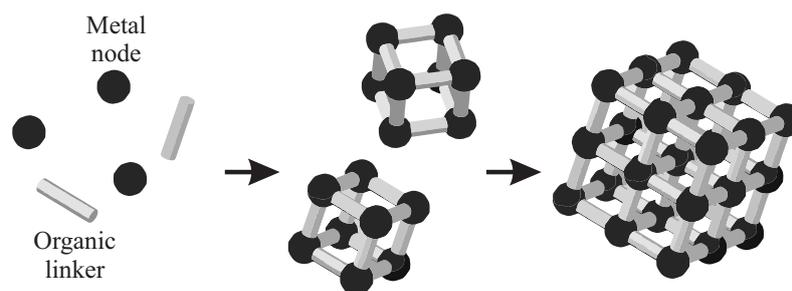
Figure 2.5: Schematic formation of a MOF from its basic constituent units: metal ion nodes (dark spheres) and organic linkers (bright cylinders).

A new highly promising subclass of such hybrid metal-organic materials is metal-formate frameworks of general chemical formula $[A][M(HCOO)_3]_n$ [5, 7, 8]. Here A^{n+} is a molecular alkylammonium cation (e.g. $(CH_3)_2NH_2^+$) and M^{2+} is a metal center (usually, a transition metal ion). In these compounds, each metal

center is surrounded by six $HCOO^-$ (formate) linkers forming MO_6 octahedra. The octahedra are linked together into metal-formate frameworks with cuboid or similar cavities (inaccessible pores). Each cavity confines a single molecular A^{n+} cation that forms hydrogen bonds with the rest of the framework. The majority of such hybrid frameworks exhibit structural phase transitions due to the cooperative ordering of these cations followed by the deformation of the framework. In some cases the transition occurs to a noncentrosymmetric phase with ferroelectric properties [4, 6]. Additionally, most of the compounds with paramagnetic transition metal ions exhibit magnetic ordering in the low-temperature region [8, 10, 11]. The simultaneous coexistence of the spontaneous electric and magnetic polarizations makes such materials single phase multi-ferroics that are highly attractive for application in four-state memory devices [12].

2.2.1   Dimethylammonium Metal-Formate Framework

The first reported and the most thoroughly studied members of the hybrid metal-formate frameworks are dimethylammonium $[(CH_3)_2NH_2][M(HCOO)_3]$ (DMAM) compounds, where M is one of the following metal cations: Mn^{2+}, Fe^{2+}, Co^{2+}, Ni^{2+}, Cu^{2+}, Zn^{2+} or Mg^{2+} [7, 8, 40]. These compounds exhibit a single structural phase transition which involves a cooperative ordering of the $(CH_3)_2NH_2^+$ (dimethylammonium, DMA^+) cations. Depending on a metal center, the phase transition temperature is $T_0 = 160 - 180$ K [7, 8], with an exception for the Mg compound ($T_0 = 270$ K) [40].

The X-ray diffraction (XRD) experiments revealed that these compounds consist of metal centers that are connected by formate anionic linkers into frameworks with pseudo cuboid cavities (see Figure 2.6) [7, 8]. Each such cavity hosts a single DMA^+ cation which forms H-bonds with the metal-formate framework. The crystalline structure of these materials has a well known AMX_3 perovskite topology, where A and X correspond to DMA^+ and $HCOO^-$ ions, respectively.

In the high-temperature phase ($T > T_0$), the DMA^+ cations are dynamically disordered, since nitrogen atoms can easily hop between three energetically favourable positions as depicted in Figure 2.6a [7, 8]. The space group of the

Figure 2.6: (a) High- and (b) low-temperature structures of DMAMn. In (a) the DMA$^+$ cation is represented as a superposition of three orientations (hydrogen atoms are omitted for clarity). Structures taken from Ref. [41].

disordered phase is trigonal R$\bar{3}$c [41]. Due to a significant degree of crystal twinning, the XRD methods encounter challenges while determining the low-temperature structure ($T < T_0$) of these perovskites. Sánchez-Andújar *et al.* managed to solve this structure for DMAMn (see Figure 2.6b) and assigned it to the monoclinic noncentrosymmetric Cc space group, which permits the ferroelectricity [41, 42]. In this phase, the DMA$^+$ cations occupy single positions in the cavities and thus the hopping motion of nitrogen is absent. The cations are arranged in the alternating check board fashion resulting in the long-range electric order of the system. Several works revealed indications of the ferroelectric behavior of the low-temperature phase in some of these hybrid perovskites, tough a proper polarization hysteresis loop was only obtained for the deuterated DMACo framework [43, 44].

The nature of phases and phase transitions in DMAM hybrid perovskites were intensively investigated using many experimental methods such as neutron diffraction [45], heat capacity [7, 8, 46], differential scanning calorimetry (DSC) [42, 47, 48], pyrocurrent [49, 50], second-harmonic generation [43] measurements, infrared, Raman [51], dielectric [7, 8, 11, 41, 52, 53], NMR [48, 53–56] and EPR [49, 57] spectroscopies. Most of these studies reported a first-order structural phase transition related to the DMA$^+$ cation ordering and metal-formate framework deformation.

Additionally, DMAM frameworks containing paramagnetic transition metal

ions were found to exhibit a magnetic order at low temperatures [8, 10, 11, 58]. The magnetoelectric coupling effect was observed in DMAMn and DMAFe frameworks [43, 49, 50, 59] making these hybrid compounds potential single phase multiferroics [12].

Despite these studies, many questions about the type and order of the structural phase transition, ferroelectric nature of the low-temperature phase, framework as well as DMA$^+$ cation dynamics in DMAM compounds remain highly controversial.

2.2.2   Methylhydrazinium Metal-Formate Framework

Another highly promising perovskite metal-formate framework contains methylhydrazinium (MHy$^+$) cations at the A-site: [CH$_3$NH$_2$NH$_2$][M(HCOO)$_3$] (MHyM), where M is Mn, Mg, Fe or Zn (see Figure 2.7). These compounds were recently investigated using XRD, DSC, Raman, IR and dielectric spectroscopies as well as measurements of the heat capacity and pyrocurrent [60]. The magnetic properties were determined by the magnetization measurements.
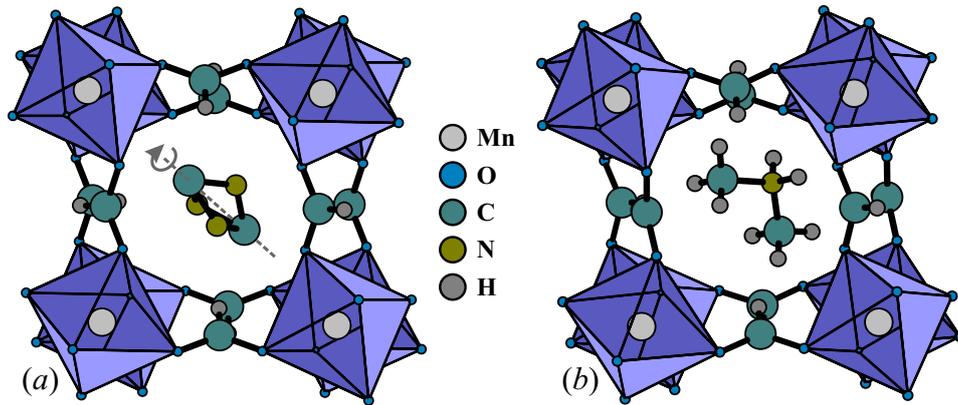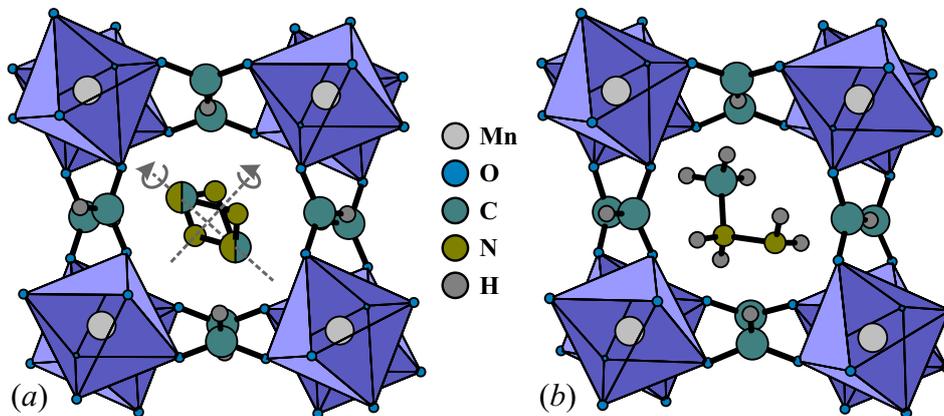

Figure 2.7: (a) High- and (b) low-temperature structures of MHyMn. In (a) the MHy$^+$ cation is represented as a superposition of six states (hydrogen atoms are omitted for clarity). Structures taken from Ref. [60].

It was found that these materials exhibit two structural phase transitions related to the ordering of MHy$^+$ cations inside the pseudo cubic cavities of metal-formate frameworks [60]. Two phase transitions are very rare in these

perovskites with another example of azetidinium zinc formate [61]. Depending on type of a metal center, the high-temperature phase transition occurs at $T_{01} = 309 - 327$ K. During this transition the space group of the crystal changes from the trigonal centrosymmetric R$\bar{3}$c to noncentrosymmetric R3c. Above T_{01} the MHy$^+$ cations can hop around the three-fold and two-fold axes resulting in six symmetrically equivalent positions (high-temperature phase) (see Figure 2.7a). The three-fold axis crosses the terminating carbon and nitrogen atoms of the MHy$^+$ cation. The molecular movement around this axis is similar to the hopping of the $(CH_3)_2NH_2^+$ cations observed in DMAM compounds [7]. The two-fold axis is roughly perpendicular to the three-fold axis and the movement around it corresponds to the flipping of the entire cation. Below T_{01} the cations partially order by strengthening the H-bonds with the formate linkers and the disorder is reduced to the three-fold (intermediate phase). A complete long-range order is established during the second phase transition at $T_{02} = 168 - 243$ K (the Mg analogue has the highest transition temperature). The corresponding change of the crystal space group is from the trigonal R3c to triclinic P1 (low-temperature phase). Note that initial measurements of the pyrocurrent for the pallet samples revealed a strong response at T_{01} and T_{02} suggesting that the intermediate and the low-temperature phases may exhibit ferroelectric behaviour. In addition, MHyMn and MHyFe analogues simultaneously demonstrated a magnetic order below 8 and 22 K, respectively [60].

The phase transitions, structural phases and MHy$^+$ cation dynamics in these hybrid perovskites were only briefly studied and thus require further attention. For example, the order and type of both transitions are obscured. The ferroelectric nature of the intermediate and low-temperature phases is also highly controversial.

2.2.3 Ammonium Metal-Formate Framework

A clear ferroelectric behavior was demonstrated in $[NH_4][Zn(HCOO)_3]$ formate framework containing ammonium (Am) cations [62]. Compounds of this family crystallize into a rare chiral hexagonal topology presented in Figure 2.8 [63]. The structure consists of octahedral metal centers connected by the anti-anti formate linkers, and the Am$^+$ cations situated in the channels.
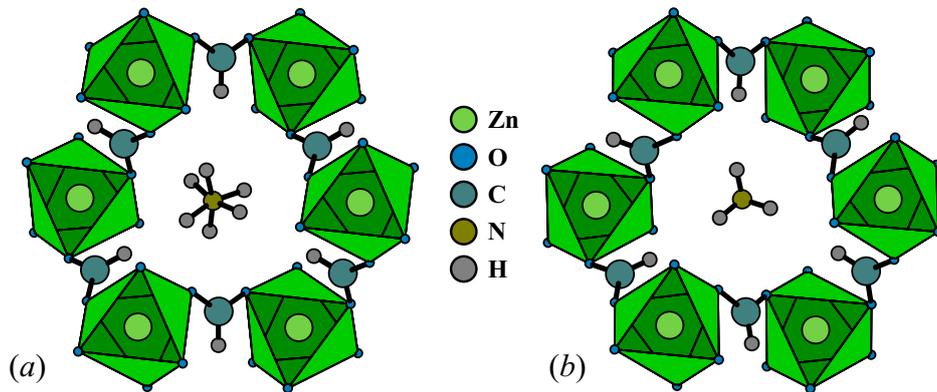
Figure 2.8: (a) High- and (b) low-temperature structures of AmZn. The Am$^+$ cation exhibits a trigonal disorder in the high-temperature phase. Structures taken from Ref. [62].

The structural phase transition in AmM (where M is Mn^{2+}, Zn^{2+} or Mg^{2+}) was studied using various experimental techniques [62, 64–67]. The most important result is the successful measurement of the electric polarization loop in AmZn below the phase transition temperature $T_c = 191$ K [62]. This demonstrates a clear ferroelectric behavior of this framework. The magnetic members of this family also exhibit ferromagnetic (AmCo and AmNi) and antiferromagnetic (AmMn) orderings at low temperatures [63, 64].

2.2.4 1,4-Butyldiammonium Metal-Formate Framework

In comparison, metal-formate frameworks containing molecular cations with double positive charge ($n = 2$) are much less studied, tough their properties match $n = 1$ analogues [68–70]. For example, $[(pnH_2^{2+})_2(H_2O)][Mg(HCOO)_3]_2$ and $[NH_3(CH_2)_4NH_3][Zn(HCOO)_3]_2$ frameworks exhibit structural phase transition during which an enormous 36-fold increase in the unit cell volume was observed [9, 71].

The structure of the $[NH_3(CH_2)_4NH_3][Zn(HCOO)_3]_2$ framework is based on the niccolite topology [9], where a $NH_3(CH_2)_4NH_3^{2+}$ (1,4-butyldiammonium, denoted as Bn^{2+}) cation is contained within a cavity formed by two one-corner-missing twinned cuboids (see Figure 2.9 for the low-temperature structure). Corners of the cuboid represent ZnO$_6$ octahedra which are interconnected via

the anionic formate linkers. NH_3^+ groups form N-H$\cdots$O H-bonds with oxygen atoms from these linkers. Above the phase transition temperature ($T_0 \approx 235$ K), the Bn^{2+} cation is trigonally distorted, and the space group of the structure is trigonal P$\bar{3}$1c. However, below this temperature the cations partly order and the structure changes to trigonal centrosymmetric R$\bar{3}$c. The disorder remains down to 100 K until all cations are frozen [9].
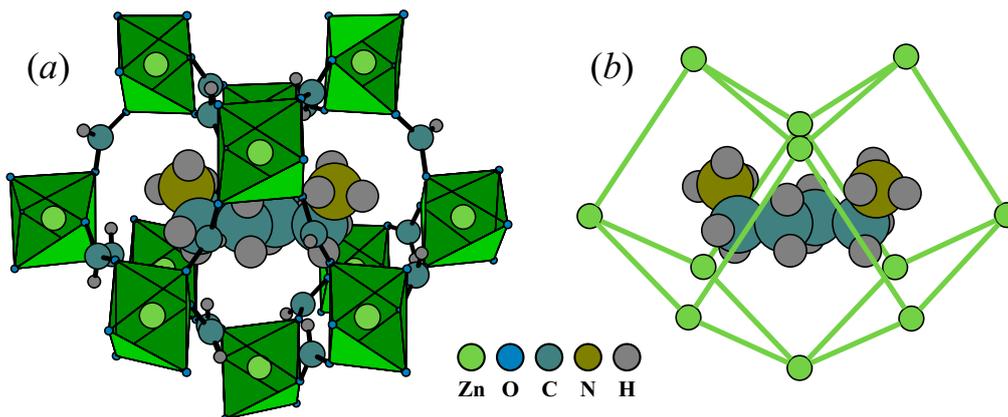
Figure 2.9: (a) Structure of BnZn framework at low temperature. (b) Topological view of the zinc-formate cavity with sticks as the HCOO⁻ linkers. Radii of atoms of the Bn^{2+} cation are enlarged for clarity. Structure taken from Ref. [9].

In addition to the XRD experiments, the BnM family was investigated using several other experimental tools. Heat capacity and DSC studies revealed structural phase transitions in Mn, Mg, Cu, Co and Zn frameworks [9, 70]. Dielectric spectroscopy indicated that the type of these transitions depends on the M^{2+} metal cation [9, 68, 69]. Dielectric spectra of Mn, Mg, Cu and Co compounds suggested paraelectric to ferroelectric phase transition, while Co and Zn members showed indications of the paraelectric to antiferroelectric transition as a jump in the dielectric permittivity at the transition point. It is claimed that the frameworks with Fe and Ni form a dipolar glass state. Pyro-current measurements supported the ferroelectric type behavior in BnMn compound [70]. In addition, at low temperature, the magnetic members of this family simultaneously exhibit magnetic long-range order making them good candidates for single phase multiferroics [12].

Despite these studies, the order and type of the observed phase transition is unknown. The proposed transition to the (anti)ferroelectric phase requires

a direct proof such as ferroelectric hysteresis measurements. The Bn^{2+} and framework dynamic effects also lack detailed descriptions.

A powerful method of choice to study the microscopic picture of the structural phase transitions, structural phases as well as molecular and lattice dynamics of the hybrid compounds is the EPR spectroscopy [1, 14, 15, 72]. Although many hybrid and related materials have no intrinsic paramagnetic centers, they can be usually doped with a small amount of paramagnetic metal ions (e.g. Mn^{2+}) which act as local probes in the structure enabling application of the EPR.

2.3 Electron Paramagnetic Resonance Spectroscopy

This Section is dedicated to the introduction of the spin Hamiltonian formalism and description of the most frequently occurring magnetic interactions. The Section ends with the short overview about the spectroscopic CW and pulsed EPR techniques.

2.3.1 Spin Hamiltonian formalism

A complete analytical solution of the Schrödinger equation of a generic paramagnetic system is rarely possible, as full Hamiltonian of such a system contains too many different interactions. However, to phenomenologically describe the experimental data obtained with EPR spectroscopy, it is sufficient and advantageous to use the so called spin Hamiltonian formalism [73–75]. The spin Hamiltonian contains only the spin coordinates and thus it takes into account only the interactions that involve electron or nuclear spins. In this formalism, the spatial degrees of freedom of a wavefunction are contained in the magnetic parameters expressed as the phenomenological second-rank tensors. The relative orientation and size of principal components of these tensors contain information about the paramagnetic center under study.

In the most general form, the spin Hamiltonian can be expressed as [75]

$$\mathcal{H} = \mathcal{H}_{EZ} + \mathcal{H}_{FS} + \mathcal{H}_{HF} + \mathcal{H}_{NZ} + \mathcal{H}_{NQ} + \mathcal{H}_{EX}. \tag{2.11}$$

The terms in this equation describe the following interactions: $\mathcal{H}_{\mathrm{EZ}}$ - the electron Zeeman interaction, $\mathcal{H}_{\mathrm{FS}}$ - the fine structure interaction (zero-field splitting), $\mathcal{H}_{\mathrm{HF}}$ - the hyperfine interaction between the electron spin and surrounding nuclear spins, $\mathcal{H}_{\mathrm{NZ}}$ - the nuclear Zeeman interaction, $\mathcal{H}_{\mathrm{NQ}}$ - the nuclear quadrupole interaction for nuclei with nuclear spin quantum numbers higher than $\frac{1}{2}$ and $\mathcal{H}_{\mathrm{EX}}$ - the magnetic exchange interaction between the electron spins.

The number of energy levels of a spin system is given by the dimension of the Hilbert space, which is spanned by the eigenfunctions of the spin Hamiltonian. For n interacting electron or nuclear spins this dimension is

$$n = \prod_{i=1}^{n} (2J_i + 1). \tag{2.12}$$

Here J represents the spin quantum number of electron or nucleus.

In the following sections all terms of Eq. 2.11 will be discussed in more detail.

2.3.2 Electron Zeeman interaction

Both classical electrodynamics and quantum mechanics predict that the electron possesses a non-zero magnetic moment $\boldsymbol{\mu}$, which is proportional to the total angular momentum $\boldsymbol{J}$ [76]:

$$\boldsymbol{\mu} = \gamma \boldsymbol{J} = \gamma(\boldsymbol{L} + \boldsymbol{S}), \tag{2.13}$$

where $\boldsymbol{L}$ and $\boldsymbol{S}$ are the orbital and spin angular momenta of the electron, respectively. Proportionality constant γ is called the gyromagnetic ratio and is expressed as

$$\gamma = -\frac{e}{2m_e} g_J, \tag{2.14}$$

where e and m_e are charge and mass of an electron. The quantity g_J is called the Lande g-factor and is given by

$$g_J = \frac{3J(J+1) + S(S+1) - L(L+1)}{2J(J+1)}. \tag{2.15}$$

The J, L and S are the total, orbital and spin angular momentum quantum numbers, respectively. A free electron has $S = \frac{1}{2}$, while the orbital angular momentum is zero. Thus, according to Eq. 2.15, its g-factor should be equal to 2. However, due to the higher-order quantum electrodynamic corrections, this value is slightly higher than 2. As for now, the free electron g-factor is one of the most precisely measured physical quantities: $g_e = 2.0023193043617(15)$ [77].

Due to a non-zero magnetic moment, the energy of a free electron is affected by an external magnetic field $\boldsymbol{B}$. The Hamiltonian of this interaction is given by the classical equation [78]

$$\mathcal{H} = -\boldsymbol{\mu} \cdot \boldsymbol{B}. \tag{2.16}$$

By taking into account Eq. 2.13 and Eq. 2.14, one can express this Hamiltonian as

$$\mathcal{H}_{EZ} = \beta_e g_e \boldsymbol{B} \boldsymbol{S}, \tag{2.17}$$

where $\beta_e = e\hbar/2m_e$ is called the Bohr magneton. This equation describes the electron Zeeman interaction, which usually dominates the spin Hamiltonian. For the external magnetic field directed along the z-axis (i.e. $\boldsymbol{B} = (0, 0, B)$), one obtains

$$\mathcal{H}_{EZ} = \beta_e g_e B \boldsymbol{S}_z, \tag{2.18}$$

where $\boldsymbol{S}_z$ is the z-component of the spin angular momentum operator. The eigenvalues of Eq. 2.18 can be easily calculated to be $\beta_e g_e B m_S$, where $m_S = \pm\frac{1}{2}$ is the magnetic electron spin quantum number. Note that the difference between these values is proportional to the external magnetic field, while at zero magnetic field, the energy levels are degenerate (see Figure 2.10). Thus, the quantization of the angular momentum leads to the quantized energy levels of a free electron in the external magnetic field. The essence of the EPR spectroscopy lies on the ability to induce the transitions between these levels using the electromagnetic radiation.

The free electron picture is idealistic, since in most cases electrons interact with the environment, which can significantly affect the energy splitting between two Zeeman levels. In most solid state paramagnetic systems, the electron ground state is non-degenerate and therefore the orbital angular momentum is quenched, leading to $L = 0$ [75]. In such a case one would also expect the g-factor to be equal to g_e (see Eq. 2.15), but significant deviations from this value
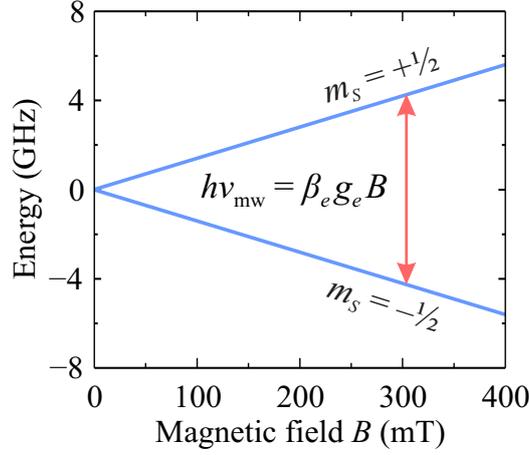
Figure 2.10: Magnetic field dependent energy levels of a free electron. Red arrow indicates EPR transition.

are observed experimentally, especially for the transition metal ions [79]. In addition, the electron Zeeman interaction is frequently orientation dependent, meaning that the Zeeman splitting depends on the relative orientation between the paramagnetic system and the external magnetic field. These phenomena arise from the spin-orbit coupling which mixes the ground state with the excited states that posses a nonzero orbital angular momentum. The coupling is described by the following Hamilton operator [75]

$$\mathcal{H} = \beta_e \boldsymbol{B} \left(\boldsymbol{L} + g_e \boldsymbol{S}\right) + \lambda \boldsymbol{L} \boldsymbol{S}, \tag{2.19}$$

where the second term is the spin-orbit interaction characterized by the spin-orbit coupling constant λ. Using the second-order perturbation theory, one can transform this Hamiltonian to the electron Zeeman interaction Hamiltonian with scalar g_e substituted by the second-rank $\boldsymbol{g}$-tensor [80]:

$$\boldsymbol{g} = g_e \boldsymbol{1} + 2\lambda \boldsymbol{\Lambda}, \tag{2.20}$$

where $\boldsymbol{\Lambda}$ is a symmetric second-rank tensor with the following components [75]

$$\Lambda_{ij} = \sum_{n \neq 0} \frac{\langle \psi_0 | L_i | \psi_n \rangle \langle \psi_n | L_j | \psi_0 \rangle}{\varepsilon_0 - \varepsilon_n}. \tag{2.21}$$

Here ψ_0 and ψ_n denote the ground state, which is occupied by the electron, and

the n-th excited state, respectively. The energies of these states are ϵ_0 and ϵ_n. Note that the closer the excited state is to the ground state, the higher deviation from the g_e value is expected. For example, the separation between the energy levels for organic free radicals is large, and thus the principal values g_{xx}, g_{yy} and g_{zz} of the **g**-tensor are close to g_e. In contrast, for transition metal ion complexes, the deviations from g_e can be significant, since their energy levels lie close to each other due to the directly coordinated ligands. Larger deviations also benefit from the fact that spin-orbit coupling, as a relativistic effect, is proportional to the mass of the atom [80]. These observations indicate that the knowledge of the **g**-tensor can provide important information about the coordination, symmetry and origin of an unpaired electron.

The effect of a local symmetry on the **g**-tensor can be classified into three categories [74]:
(i) Cubic. This symmetry corresponds to three coordination environments: cubical, ideal octahedral and tetrahedral. The EPR spectrum of a paramagnetic center possessing cubic symmetry shows no anisotropy, i.e. all principal values of the **g**-tensor are equal: $g_{xx} = g_{yy} = g_{zz}$.
(ii) Axial. All systems having at least three-fold rotational symmetry axis belong to this symmetry type. In this case, the **g**-tensor is anisotropic and has two equal principal values: $g_{xx} = g_{yy} \neq g_{zz}$. The usual notation is $g_{xx} = g_{yy} \equiv g_\perp$ and $g_{zz} \equiv g_\parallel$, where parallel component is directed along the symmetry axis.
(iii) Rhombic. This is the general low-symmetry case with all principal values being different: $g_{xx} \neq g_{yy} \neq g_{zz}$.

2.3.3 Nuclear Zeeman interaction

The nuclear Zeeman interaction describes the coupling of a magnetic nucleus with the external magnetic field. This interaction is very similar to the electron Zeeman interaction, while the main difference is that it is about three orders of magnitude weaker. The Hamiltonian expressing this interaction is [75]

$$\mathcal{H}_{\mathrm{NZ}} = -\beta_n g_n \boldsymbol{B} \boldsymbol{I}, \tag{2.22}$$

where the nuclear spin operator $\boldsymbol{I}$ and the nuclear g_n factor depend on a specific nucleus. The quantity $\beta_n = e\hbar/2m_p$ is called the nuclear magneton, where m_p is the proton mass. The nuclear Zeeman interaction usually has no influence on the continuous-wave EPR spectrum, since it shifts the energy levels of all spin manifolds by the same amount. However, this interaction plays a significant role in the nuclear frequency spectra obtained by the pulsed EPR techniques.

2.3.4   Hyperfine interaction

One of the most important sources of information in EPR spectroscopy is the hyperfine (hf) interaction, which is a magnetic interaction between an unpaired electron and magnetic nucleus. Its contribution to the spin Hamiltonian can be expressed as [75]

$$\mathcal{H}_{\mathrm{HF}} = \boldsymbol{S}\boldsymbol{A}\boldsymbol{I}, \tag{2.23}$$

where $\boldsymbol{A}$ is the hf tensor. This Hamiltonian can be further decomposed into the isotropic Fermi contact $\mathcal{H}_{\mathrm{F}}$ and the electron-nuclear dipole-dipole coupling $\mathcal{H}_{\mathrm{dd}}$ terms. The origin of the Fermi contact interaction is the non-zero probability of finding the s-state electron at the nucleus. The expression of this term is

$$\mathcal{H}_{\mathrm{F}} = A_{\mathrm{iso}}\boldsymbol{S}\boldsymbol{I}, \tag{2.24}$$

where

$$A_{\mathrm{iso}} = \frac{2}{3}\mu_0 g_e g_n \beta_e \beta_n |\psi(0)|^2. \tag{2.25}$$

$\mu_0 = 4\pi \cdot 10^{-7}\,\mathrm{NA}^2$ is the permeability of vacuum and $|\psi(0)|^2$ denotes the electron spin density at the nucleus site. Note that due to the configuration interactions and spin polarization mechanisms, the electrons from the p, d and f orbitals may also contribute to this term [80, 81]. The determined value of A_{iso} provides information about the bonding and shape of the electron orbitals.

The electron-nuclear dipole-dipole coupling $\mathcal{H}_{\mathrm{dd}}$ originates from the dipolar interaction between the electron and nuclear magnetic moments. The nuclear magnetic moment $\boldsymbol{\mu}_n$ (situated at the origin) creates the following vector

potential at a point $\boldsymbol{r}$ [78]:

$$\boldsymbol{A}(\boldsymbol{r}) = \frac{\mu_0}{4\pi} \frac{\boldsymbol{\mu}_n \times \boldsymbol{r}}{r^3}. \tag{2.26}$$

A local magnetic field at this point is

$$\boldsymbol{B}(\boldsymbol{r}) = \nabla \times \boldsymbol{A}(\boldsymbol{r}) = \frac{\mu_0}{4\pi} \left\{ \frac{3(\boldsymbol{\mu}_n \boldsymbol{r}) \boldsymbol{r}}{r^5} - \frac{\boldsymbol{\mu}_n}{r^3} \right\}. \tag{2.27}$$

Then the energy of an electron at point $\boldsymbol{r}$ is

$$E_{\mathrm{dd}} = -\boldsymbol{\mu} \boldsymbol{B}(\boldsymbol{r}) = -\frac{\mu_0}{4\pi} \left\{ \frac{3(\boldsymbol{\mu}_n \boldsymbol{r})(\boldsymbol{\mu} \boldsymbol{r})}{r^5} - \frac{\boldsymbol{\mu} \boldsymbol{\mu}_n}{r^3} \right\}. \tag{2.28}$$

The Hamiltonian of this interaction is obtained by replacing classical variables by quantum mechanical operators:

$$\mathcal{H}_{\mathrm{dd}} = \frac{\mu_0}{4\pi} g_e g_n \beta_e \beta_n \left\{ \frac{3(\boldsymbol{Ir})(\boldsymbol{Sr})}{r^5} - \frac{\boldsymbol{IS}}{r^3} \right\}. \tag{2.29}$$

The spatial dependence is removed by integrating over the spatial components of the electron wave-function. The result is the anisotropic dipole-dipole coupling described by the spin Hamiltonian [75]

$$\mathcal{H}_{\mathrm{dd}} = \boldsymbol{STI}, \tag{2.30}$$

where $\boldsymbol{T}$ is a traceless and symmetric dipolar coupling tensor with the components [74]

$$T_{ij} = \frac{\mu_0}{4\pi} g_e g_n \beta_e \beta_n \left\langle \frac{3r_i r_j - \delta_{ij} r^2}{r^5} \right\rangle. \tag{2.31}$$

In the principal axis system, this tensor has the following form

$$\boldsymbol{T} = \frac{\mu_0}{4\pi} \frac{g_e g_n \beta_e \beta_n}{r^3} \begin{pmatrix} -1 & 0 & 0 \\ 0 & -1 & 0 \\ 0 & 0 & 2 \end{pmatrix} = \begin{pmatrix} -T & 0 & 0 \\ 0 & -T & 0 \\ 0 & 0 & 2T \end{pmatrix}. \tag{2.32}$$

Note that this expression neglects the $\boldsymbol{g}$-tensor anisotropy effects, but it is still a good approximation in cases where these effects are small.

The dipolar coupling $\boldsymbol{T}$ has high significance in the EPR spectroscopy, as it can

be used to estimate the distance r between the interacting electron and nucleus. Using the point-dipole approximation, the dipolar parameter T can be expressed as [82]:

$$T = \frac{\mu_0}{4\pi}\frac{g_e g_n \beta_e \beta_n}{h r^3}.$$
(2.33)

Note the cubic r dependence.

2.3.5 Zero-field splitting

Paramagnetic centers having total electron spin $S > \frac{1}{2}$ (e.g. Mn^{2+} ion with $S = \frac{5}{2}$) and the non-cubic symmetry exhibit the splitting of energy levels already at zero magnetic field - the so called zero-field splitting (zfs). This results in the unequal separations of the $2S + 1$ spin states at a given value of the applied magnetic field [80], which provides a fine structure (fs) of the EPR spectrum.

The origin of this interaction is the electron-electron dipole-dipole and spin-orbit couplings [72]. The fs Hamiltonian can be written as

$$\mathcal{H}_{\text{FS}} = \boldsymbol{S}\boldsymbol{D}\boldsymbol{S},$$
(2.34)

where $\boldsymbol{D}$ is the symmetric and traceless zfs tensor. In the principal axis system of $\boldsymbol{D}$, the Hamiltonian becomes

$$\mathcal{H}_{\text{FS}} = D_{xx}\boldsymbol{S}_x^2 + D_{yy}\boldsymbol{S}_y^2 + D_{zz}\boldsymbol{S}_z^2.$$
(2.35)

It is convenient to define new zfs parameters: $D = 3D_{zz}/2$ and $E = (D_{xx} - D_{yy})/2$. For cubic symmetry $D = E = 0$ (no zfs), while axial symmetry results in $D \neq 0$ and $E = 0$. Lower symmetries yield $D \neq 0$ and $E \neq 0$. With these parameters, the Hamiltonian is transformed into the form

$$\mathcal{H}_{\text{FS}} = D\left[\boldsymbol{S}_z^2 - \frac{1}{3}S(S+1)\right] + E(\boldsymbol{S}_x^2 - \boldsymbol{S}_y^2).$$
(2.36)

As an example, let us calculate the eigenvalues of this Hamiltonian for an arbitrary $S = 1$ system. The best way to proceed is to use the spin shift operators $\boldsymbol{S}_+ = \boldsymbol{S}_x + i\boldsymbol{S}_y$ and $\boldsymbol{S}_- = \boldsymbol{S}_x - i\boldsymbol{S}_y$ [76] and express the Hamiltonian in the

$|S, m_S\rangle$ basis. This leads to the following matrix representation

$$\mathcal{H}_{\text{FS}} = \begin{pmatrix} D/3 & 0 & E \\ 0 & -2D/3 & 0 \\ E & 0 & D/3 \end{pmatrix} \tag{2.37}$$

with the eigenvalues

$$E_{xx} = \frac{D}{3} - E \tag{2.38}$$

$$E_{yy} = \frac{D}{3} + E \tag{2.39}$$

$$E_{zz} = -\frac{2D}{3}. \tag{2.40}$$

For an axial symmetry, $E_{xx} = E_{yy}$, and the degeneracy is not completely lifted at zero magnetic field. For lower symmetry, all eigenvalues are different (nondegenerate). Note that for half-integer spin systems, at least a two-fold degeneracy remains at zero magnetic field. This is a result of the Kramer's theorem, which states that no electrostatic interactions can completely lift the degeneracy of a system containing an odd number of electrons [79].

The energy level diagrams for an $S = 1$ spin system in the external magnetic field are presented in Figure 2.11 [72]. For a system without a zfs, all three m_S levels are degenerate at $B = 0$, while separation between the levels is the same for any value of B. For the axially symmetric zfs tensor, the degeneracy is partly lifted causing unequal separation of energy levels for $B > 0$.

For some transition metal ions with group spin $S > \frac{1}{2}$, higher order zfs terms must be taken into account to properly describe the fs [79]. In this case, the fs Hamiltonian is expressed in terms of the extended Stevens operators $\hat{O}_k^q(\boldsymbol{S})$ ($k = 2, 4, 6$ and $q = +k, ..., -k$) as [83]

$$\mathcal{H}_{\text{FS}} = \sum_k \sum_q B_k^q \hat{O}_k^q(\boldsymbol{S}). \tag{2.41}$$

Here B_k^q are real associated coefficients describing the magnitude of the corresponding zfs. The traditional second-order zfs parameters D (axial) and E (orthorhombic) are related to these coefficients: $D = 3B_2^0$ and $E = B_2^2$. In
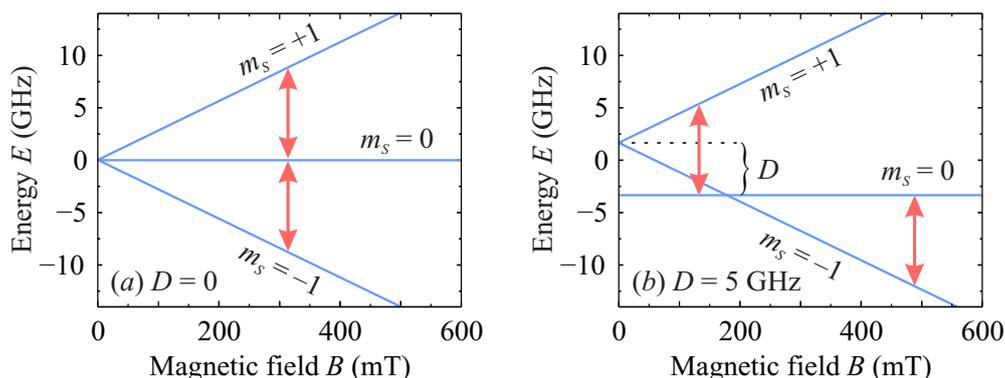
Figure 2.11: (a) Energy level diagram for an $S = 1$ spin system ($g = g_e$) without a zfs. (b) Energy level diagram for the same system with a substantial zfs ($D = 5\,\text{GHz}$, $E = 0$). Here the z-axis of the $\boldsymbol{D}$ tensor is parallel to $\boldsymbol{B}$. Red arrows indicate EPR transitions.

addition, the fourth-order parameters a (cubic) and F (axial) are expressed as $a = 24B_4^4$ and $F = 180B_4^0 - 36B_4^4$. Here a and F are defined in a molecular reference frame which coincides with a 4-fold symmetry axis of the cubic system. Note that a and F parameters are frequently used for the description of the Mn^{2+} and Fe^{3+} EPR spectra [79]. The corresponding expressions for $\hat{\boldsymbol{O}}_k^q(\boldsymbol{S})$ operators can be found in Ref. [83].

2.3.6 Nuclear quadrupole interaction

Nuclei with $I > \frac{1}{2}$ have a nonzero nuclear quadrupole moment which can interact with the electric field gradient at the nucleus site. In the EPR spectrum, the nuclear quadrupole interaction can cause line shifts and the appearance of the forbidden transitions, tough these effects are of second order and rarely observable [72]. However, the influence of this interaction may be significant in the NMR spectra detected by pulsed EPR techniques [75].

2.3.7 Magnetic exchange interaction

The magnetic exchange interaction describes the effects whenever the orbitals of two unpaired electrons overlap significantly. The exchange interaction originates

from the Pauli exclusion principle and the Coulomb interaction. This interaction is the cornerstone for explaining the ferromagnetic and related phenomena, since the dipole-dipole interaction is too weak to overcome the thermal fluctuations [84]. This interaction may have a dominant influence on the EPR spectrum, tough in many cases its manifestation is rather difficult to interpret [85].

In 1934, H. A. Kramers proposed and later P. W. Anderson developed another electron exchange mechanism called superexchange [85]. In contrast to the ordinary exchange interaction, it does not involve a direct overlap of the magnetic orbitals, since the exchange is mediated via the orbitals of diamagnetic units that are present between the interacting magnetic centers.

2.3.8   CW EPR spectroscopy

The CW EPR spectroscopy is usually implemented by sweeping the external magnetic field and continuously irradiating the sample with constant frequency ν_{mw} microwaves [74]. The microwaves induce EPR transitions between the electron spin levels at a certain value of the external magnetic field which is called the resonance field. The increased microwave absorption is detected via the change of the quality factor of a resonator. Due to the external field modulation and phase sensitive detection, a first-derivative signal is usually recorded (see Figure 2.12)[86]. The most common EPR spectrometers operate at the S- ($\nu_{\mathrm{mw}} \sim 3$), X- (~ 9.5), Q- (~ 34) or W-band (~ 95 GHz) frequency, tough more exotic quasi-optical machines are also available [87].

For EPR transitions to occur, three conditions must be satisfied. First of all, the separation between the energy levels must be equal to ν_{mw}. Secondly, the populations of energy levels must be unequal. In the equilibrium, the population difference is established due to the Boltzmann distribution, which states that the population ratio of energy levels in the $S = \frac{1}{2}$ system is equal to $\exp\left(-\beta_e g B/k_B T\right)$. This indicates that at low temperatures (or higher magnetic fields) the ratio is lower, leading to the stronger EPR signal intensity. However, at low temperatures, the relaxation from the upper energy level to the lower state can be much slower than the characteristic time of the microwave irradiation causing equal populations of energy levels. Such a situation is called
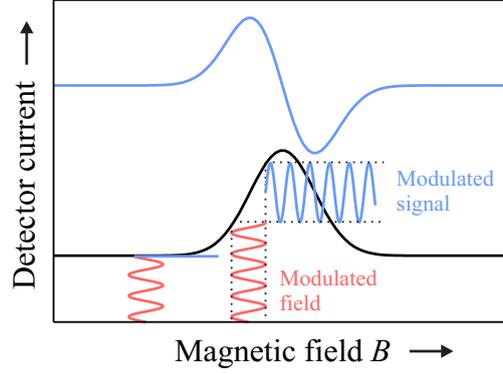
Figure 2.12: Illustration of the magnetic field modulation on the absorption EPR spectrum. The demodulated CW EPR signal (top) appears as a first-derivative of this spectrum. Typical frequency of the modulating field is 100 kHz.

saturation and it may lead to severe distortions of the EPR spectrum [86]. The third condition involves the quantum selection rules that for the perpendicular transitions ($\boldsymbol{B}_1 \perp \boldsymbol{B}$) are $\Delta m_S = \pm 1$ and $\Delta m_I = 0$ (here $\boldsymbol{B}_1$ denotes the magnetic component of the microwave field).

To obtain these selection rules, let us consider the time-dependent Zeeman Hamiltonian [75]

$$\boldsymbol{\mathcal{H}}_1 (t) = \beta_e \boldsymbol{B}_1 (t) \, \boldsymbol{g} \boldsymbol{S}, \qquad (2.42)$$

which describes the coupling between the electron spin and the oscillating microwave field $\boldsymbol{B}_1(t)$. The famous Fermi's golden rule states that the transition probability between two eigenstates $|\phi_k\rangle$ and $|\phi_l\rangle$ of the static spin Hamiltonian $\mathcal{H}$ is [76]

$$P_{k \rightarrow l} \propto |\langle \phi_k | \mathcal{H}_1 (t) | \phi_l \rangle|^2, \qquad (2.43)$$

For the perpendicular transitions ($\boldsymbol{B}_1 \perp \boldsymbol{B}$) one obtains

$$P_{k \rightarrow l} \propto B_1^2 \, |\langle \phi_k | \boldsymbol{S}_x | \phi_l \rangle|^2 = B_1^2 |\langle \varphi_{n,k} | \varphi_{n,l} \rangle|^2 \, |\langle \varphi_{e,k} | \boldsymbol{S}_x | \varphi_{e,l} \rangle|^2$$
$$\propto B_1^2 |\langle \varphi_{n,k} | \varphi_{n,l} \rangle|^2 \, |\langle \varphi_{e,k} | \boldsymbol{S}_+ + \boldsymbol{S}_- | \varphi_{e,l} \rangle|^2. \quad (2.44)$$

Here $\boldsymbol{S}_+$ and $\boldsymbol{S}_-$ are the electron spin ladder operators and $|\phi_{k(l)}\rangle$ are written as the tensor product of the electron $|\varphi_{e,k(l)}\rangle$ and nuclear $|\varphi_{n,k(l)}\rangle$ wavefunctions. It is clear that the transition probability is non-zero if and only if $|\phi_k\rangle$ and $|\phi_l\rangle$ differ by $\Delta m_S = \pm 1$ and $\Delta m_I = 0$. In some cases, due to the state mixing, the

m_S and m_I are no longer good quantum numbers and therefore the forbidden $|\Delta m_S| > 1$ and $|\Delta m_I| > 0$ transitions may be observed. Different selection rules may also be obtained using other EPR setups where $\boldsymbol{B}_1$ is not perpendicular to $\boldsymbol{B}$ (e.g. the so called parallel setup where $\boldsymbol{B}_1 \parallel \boldsymbol{B}$) [86].

The EPR spectroscopy is frequently used to study anisotropic systems that have different degree of crystallinity (crystals, powders, amorphous solids or glasses). First, let us analyze a CW EPR spectrum of a single crystal with $S = \frac{1}{2}$ electron spins and axially symmetric $\boldsymbol{g}$-tensor (components $g_\parallel$ and $g_\perp$). When the external magnetic field is parallel to the symmetry axis (principal direction of the $g_\parallel$ component), the resonance condition becomes $B_\parallel = h\nu_{\mathrm{mw}}/\beta_e g_\parallel$. On the other hand, if $\boldsymbol{B}$ is perpendicular to the symmetry axis, the resonance field is $B_\perp = h\nu_{\mathrm{mw}}/\beta_e g_\perp$. For the orientations in-between $B_\parallel$ and $B_\perp$, the resonance occurs at

$$B\left(\theta\right) = \frac{h\nu_{\mathrm{mw}}}{\beta_e g\left(\theta\right)}, \tag{2.45}$$

where the effective g-factor $g(\theta)$ is [74]

$$g\left(\theta\right) = \sqrt{g^2 \sin^2\theta + g^2 \cos^2\theta} \ . \tag{2.46}$$

Here angle θ is the angle between the external magnetic field and symmetry axis of the paramagnetic center. Thus, the EPR spectrum of a single crystal with anisotropic $\boldsymbol{g}$-tensor consists of a single line at each measured orientation as depicted in Figure 2.13a.

In contrast, the EPR spectrum of the same powder system would range from $B_\parallel$ to $B_\perp$, since the crystallites would form random angular distribution with respect to the external magnetic field. To obtain the spectrum of powder, contributions from different values of the angle θ must be summed over. The general expression for the probability of a spin system to experience a resonance field between B and $B + dB$ is given by [74]

$$p\left(B\right) dB \propto \frac{\sin\theta}{dB/d\theta} dB, \tag{2.47}$$

where $p(B)$ is the probability density function. The numerator of this equation indicates that the probability (spectral line intensity) is largest for $\theta = \frac{\pi}{2}$. This condition reflects the fact that there are many crystallites with symmetry
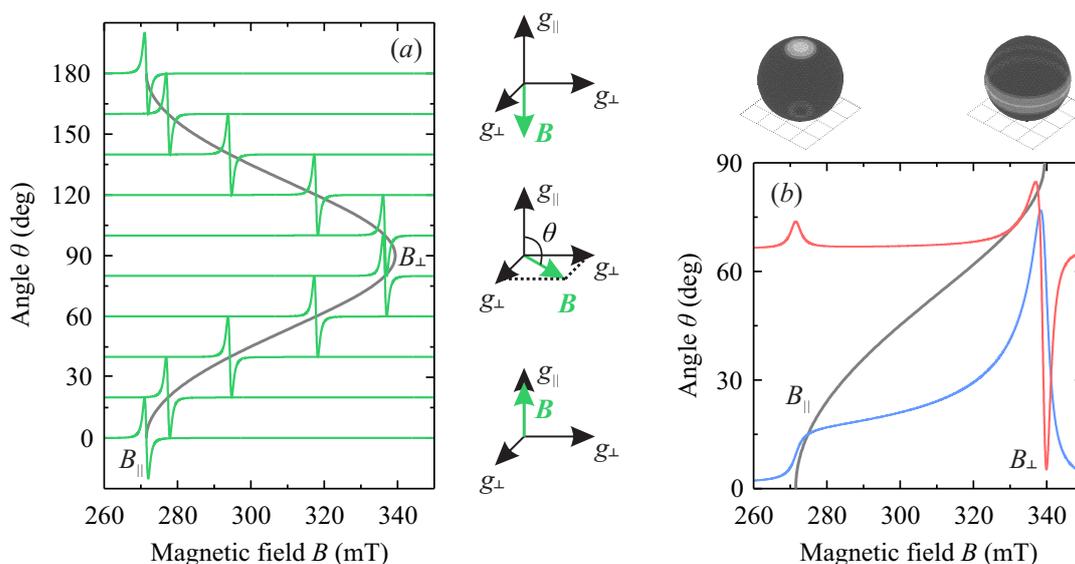
Figure 2.13: (a) Angular dependent CW EPR spectra of an $S = \frac{1}{2}$ spin system with $g_\parallel = 2.5$ and $g_\perp = 2$. (b) The corresponding powder CW EPR spectrum. The blue and red curves in (b) indicate absorption and modulated spectra, respectively. The gray curves indicate angular dependence of the resonance field for a single crystallite. The orientations contributing to the $g_\parallel = 2.5$ and $g_\perp = 2$ spectral regions are indicated on the unit spheres.

axis perpendicular to $\boldsymbol{B}$. In contrast, there are almost none crystallites having symmetry axes parallel to the field ($\theta = 0$). Thus, the EPR signal intensity at the $B_\parallel$ position is significantly lower. The denominator shows that the highest line intensity is expected near the extrema of B vs. θ curve, i.e. at $B_\parallel$ and $B_\perp$ positions (see Fig. 2.13b).

In many solid state systems, the anisotropic $\boldsymbol{g}$-tensor is complemented by the anisotropy of other interactions. For instance, the anisotropy of the hf $\boldsymbol{A}$ tensor leads to the orientation dependent hf splitting. As an example, let us consider a randomly oriented axially symmetric system of coupled $S = \frac{1}{2}$ and $I = \frac{3}{2}$ spins. Such a spin system is a good representative of a paramagnetic Cu^{2+} ion. The energy level diagram for this case is presented in Fig. 2.14a, while the corresponding CW EPR spectrum is shown in Fig. 2.14b. Note a different hf splitting at $g_\perp$ and $g_\parallel$ spectral positions.

The anisotropy effects are also observed for systems having electron spin $S > \frac{1}{2}$ and nonzero zfs. As an example, let us consider interacting $S = \frac{5}{2}$ and $I = \frac{5}{2}$ spin
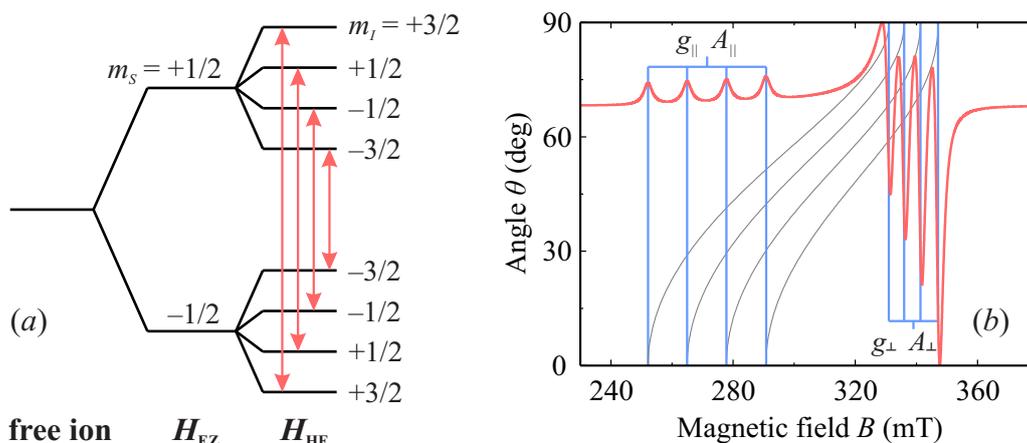
Figure 2.14: (a) Schematic energy level diagram and (b) X-band CW EPR spectrum for a randomly oriented system of coupled $S = \frac{1}{2}$ and $I = \frac{3}{2}$ spins (typical for Cu^{2+} centers). Both the **g**- and **A** tensors are axially symmetric ($g_\parallel = 2.5$, $g_\perp = 2.0$, $A_\parallel = 450$ MHz and $A_\perp = 150$ MHz). The angular dependence of the resonance field for different m_I values is indicated in (b). For clarity, the hf splittings in the energy level diagram are exaggerated.

system with isotropic **g**-tensor (typical for Mn^{2+} ion in the high-spin state [14]). The energy level diagram for this system at some value of the external magnetic field is presented in Figure 2.15a. It consist of six m_S levels that result in five $\Delta m_S = \pm 1$ EPR transitions. Due to a substantial zfs, the levels are not equally spaced. Hence, the resonance fields for the EPR transitions are different resulting in the fs of the EPR spectrum (see 2.15b). The powder spectrum is dominated by the signal of the so called central fs transition ($m_S = -\frac{1}{2} \leftrightarrow \frac{1}{2}$). The lines of the outer transitions ($m_S = \pm\frac{3}{2} \leftrightarrow \pm\frac{1}{2}$ and $\pm\frac{5}{2} \leftrightarrow \pm\frac{3}{2}$) have much smaller intensity due to a pronounced angular dependence (spread of the spectral density). The hf interaction between the electron and nuclear spins results in a further splitting of each energy level into six m_I sublevels providing 30 allowed $\Delta m_S = \pm 1$ and $\Delta m_I = 0$ transitions. The corresponding Q-band CW EPR spectrum is presented in Figure 2.15c, where each fs transition consists of six hf lines.

Despite a good applicability of the CW EPR spectroscopy to characterize the core nucleus of a paramagnetic center, this technique frequently fails to detect weak hf interactions of the ligand nuclei [72]. The main reason for this limitation is that a typical inhomogeneous CW EPR linewidth is of the order of 10 MHz-100 MHz, whereas a ligand hf interaction is only few MHz [75]. Thus, such
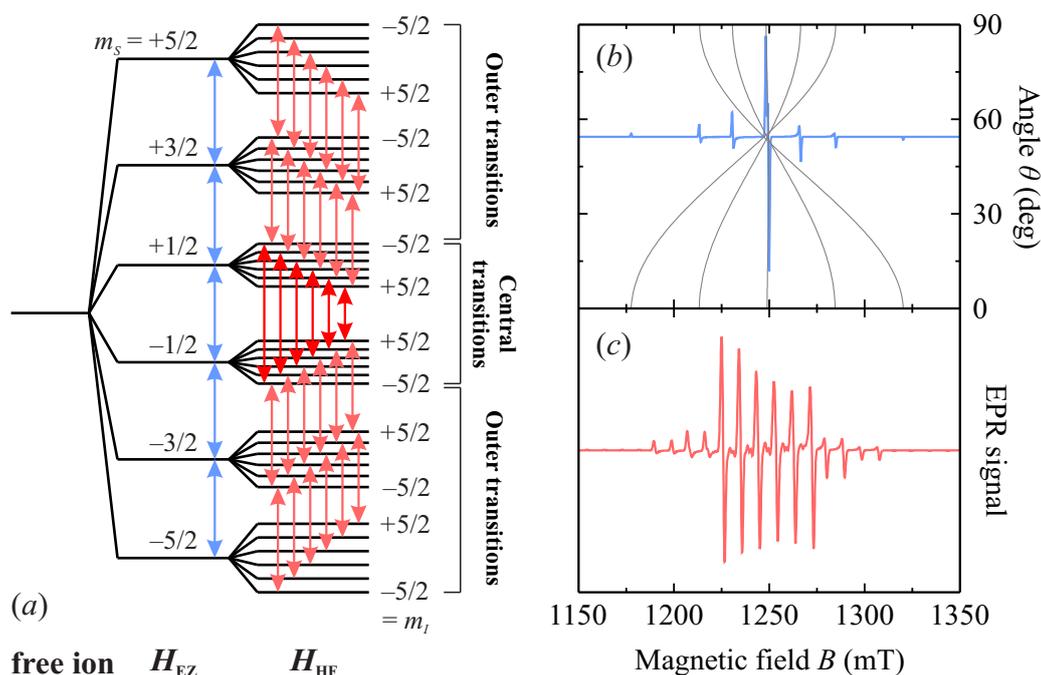
Figure 2.15: (a) Schematic energy level diagram and EPR transitions for a randomly oriented system of coupled $S = \frac{5}{2}$ and $I = \frac{5}{2}$ spins. (b) A corresponding Q-band CW EPR spectrum for $A_{\text{iso}} = 0$ (no hf interaction). (c) The same spectrum for $A_{\text{iso}} = 260$ MHz (typical for Mn^{2+} ions in the high-spin state). Other parameters: $g = g_e$, $D = 500$ MHz, $E = 0$. The angular dependence of the resonance field for different EPR transitions is also indicated in (b).

small splittings are often hidden in the spectral lines of the core nucleus. These limitations are usually overcome using the pulsed EPR techniques.

2.3.9 Pulsed EPR spectroscopy

In the past few decades, enormous contribution was made to the field of the pulsed EPR spectroscopy, making it one of the most important methods to study the structure and dynamics of diluted paramagnetic materials [88]. During such experiments, the spin system is manipulated using short microwave pulses (typical length is several ns) [75]. The two most popular pulsed techniques used to investigate weak interactions between the unpaired electrons and ligand nuclei are the electron spin echo envelope modulation (ESEEM) [89–91] and the electron nuclear double resonance (ENDOR) [92, 93] spectroscopies. Both

methods measure the nuclear transition frequencies allowing to determine the hf and nuclear quadrupole interactions, that usually are not resolved in a CW EPR spectrum. Before going into more details of these technique, it is worth to analyze a spin Hamiltonian of a general $S = \frac{1}{2}$ and $I = \frac{1}{2}$ spin system.

2.3.10   The $S = \frac{1}{2}$ and $I = \frac{1}{2}$ spin system

Many pulsed EPR experiments can be described by considering coupled $S = \frac{1}{2}$ electron and $I = \frac{1}{2}$ nuclear spins. The corresponding spin Hamiltonian of this system has a Hilbert space dimension of 4 and is given by [75]

$$\mathcal{H} = \omega_S \boldsymbol{S}_z - \omega_I \boldsymbol{I}_z + \boldsymbol{S}\boldsymbol{A}\boldsymbol{I}, \tag{2.48}$$

where ω_S and ω_I are the electron resonance and the nuclear Larmor angular frequencies, respectively. By assuming the axial symmetry and high-field approximation, the terms involving $\boldsymbol{S}_x$ and $\boldsymbol{S}_y$ operators can be discarded providing

$$\mathcal{H} = \omega_S \boldsymbol{S}_z - \omega_I \boldsymbol{I}_z + A \boldsymbol{S}_z \boldsymbol{I}_z + B \boldsymbol{S}_z \boldsymbol{I}_x. \tag{2.49}$$

In the point-dipole approximation, A and B parameters are [82, 90]

$$A = 2\pi T \left[\frac{3}{g^2} (g_\parallel^2 \cos\theta \cos\theta_I + g_\perp^2 \sin\theta \sin\theta_I \cos\phi_I) \times \right.$$

$$\left. (\cos\theta \cos\theta_I + \sin\theta \sin\theta_I \cos\phi_I) + 2\pi A_{\text{iso}} \right], \tag{2.50}$$

$$B^2 = b^2 + c^2, \tag{2.51}$$

where

$$b = 2\pi T \left[\frac{3}{g^2} (g_\parallel^2 \cos\theta \cos\theta_I + g_\perp^2 \sin\theta \sin\theta_I \cos\phi_I)(\cos\theta \cos\theta_I \cos\phi_I - \sin\theta \cos\theta_I) \right.$$

$$\left. + \left(\frac{A_{\text{iso}}}{T} - 1 \right) \left(\frac{g_\perp^2 - g_\parallel^2}{g^2} \right) \sin\theta \sin\phi_I \right] \tag{2.52}$$

and

$$c = 2\pi T \left[\frac{3}{g^2} (g_\parallel^2 \cos\theta \cos\theta_I + g_\perp^2 \sin\theta \sin\theta_I \cos\phi_I)(\sin\theta_I \sin\phi_I) \right] \qquad (2.53)$$

with

$$g^2 = g_\parallel^2 \cos^2\theta + g_\perp^2 \sin^2\theta. \qquad (2.54)$$

Here $g_\parallel$ and $g_\perp$ are the principal components of the axially symmetric $\boldsymbol{g}$-tensor. A_iso and T denote the isotropic and dipolar hf components of the hf tensor $\boldsymbol{A}$:

$$\boldsymbol{A} = \boldsymbol{T} + \boldsymbol{A}_\text{iso} = \begin{pmatrix} -T & 0 & 0 \\ 0 & -T & 0 \\ 0 & 0 & 2T \end{pmatrix} + A_\text{iso}\boldsymbol{1}, \qquad (2.55)$$

where $\boldsymbol{1}$ is the 3×3 identity matrix. The angles θ, θ_I and ϕ_I are defined in Fig. 2.16 [82]. The orientation of the $\boldsymbol{g}$-tensor is chosen in such a way that the vector $\boldsymbol{r}$ joining electron and ligand nucleus lies in the xz-plane with the angle θ_I to the z-axis. θ is the angle between the external magnetic field $\boldsymbol{B}$ and the $g_\parallel$-axis. ϕ_I marks the azimuthal angle between the x-axis and the projection of $\boldsymbol{B}$ onto the xy-plane. The unpaired electron is assumed to lie at the origin.
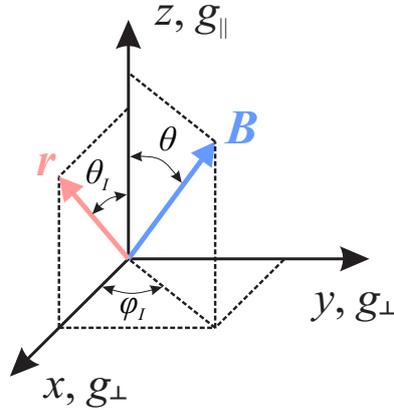
Figure 2.16: Reference frame of a coupled $S = \frac{1}{2}$ and $I = \frac{1}{2}$ spin system in the axially symmetric environment. The xyz-frame corresponds to the principal axis system of the electron $\boldsymbol{g}$-tensor. Vector $\boldsymbol{r}$ joins the unpaired electron at the origin and the ligand nucleus.

The main information about the ligand is contained in the hf tensor $\boldsymbol{A}$ and its relative orientation to the molecular frame. The isotropic hf interaction A_iso measures the unpaired electron density at the nucleus site (overlap of orbitals),

45

while the dipolar hf parameter may be used to determine the electron-nucleus distance r (see Eq. 2.33) [72].

For the isotropic $\boldsymbol{g}$-tensor, the A and B parameters given by Eq. 2.50 and 2.51 simplify to

$$A = 2\pi T \left(3\cos^2\theta -1\right) + 2\pi A_{\text{iso}} \tag{2.56}$$

and

$$B = 6\pi T \cos\theta \sin\theta \; . \tag{2.57}$$

The parameter B has the highest value for $\theta = \frac{\pi}{4}$, while it vanishes for $\theta = \frac{\pi}{2}$ and 0.

The schematic energy level diagram and its stick spectrum for the $S = \frac{1}{2}$ and $I = \frac{1}{2}$ system is presented in Fig. 2.17, where the so called weak-coupling case ($|A| < |2\omega_I|$) is assumed. The corresponding EPR spectrum consists of two allowed (solid lines) and two forbidden (dashed lines) electron spin transitions (see Fig. 2.17b). Here m_S and m_I are good quantum numbers only for the isotropic ($B = 0$) case, since then the spin Hamiltonian given by Eq. 2.49 is diagonal in the $|m_s, m_I\rangle$ basis. The two nuclear transition frequencies ω_α and ω_β are of the main interest in the pulsed EPR spectroscopy (see Fig. 2.17c for nuclear resonance spectrum). They correspond to $m_S = \frac{1}{2}$ and $m_S = -\frac{1}{2}$ electron spin manifolds and can be expressed as [90]

$$\omega_\alpha = \sqrt{\left(\omega_I - \frac{A}{2}\right)^2 + \left(\frac{B}{2}\right)^2} \tag{2.58}$$

and

$$\omega_\beta = \sqrt{\left(\omega_I + \frac{A}{2}\right)^2 + \left(\frac{B}{2}\right)^2}. \tag{2.59}$$

Thus, by measuring ω_α and ω_β transitions, one obtains A and B parameters that contain information about the hf coupling tensor $\boldsymbol{A}$ of the ligand nucleus.

So far the temporal evolution of the spin system was neglected and only the static Hamiltonian was considered. It is clear that this treatment is not sufficient to describe the pulsed EPR experiments, as the spin ensemble experiences a time-dependent perturbation during the applied microwave pulse. A proper analysis of such experiments is given by the so called product operator formalism which
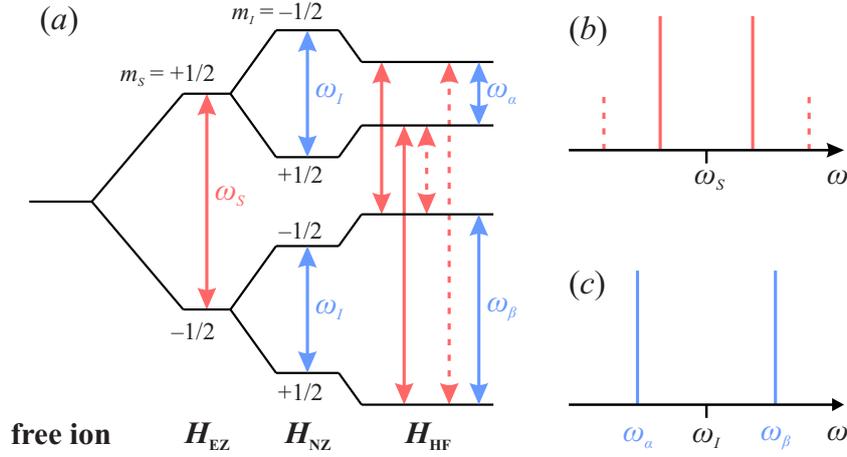
Figure 2.17: (a) Energy level diagram and stick spectra of (b) electron and (c) nuclear transitions of a coupled $S = \frac{1}{2}$ and $I = \frac{1}{2}$ spin system.

is briefly discussed in the following.

2.3.11 Product operator formalism

The time evolution of a spin system can be described by the Liouville-von Neumann equation [75, 76]

$$\frac{d\boldsymbol{\sigma}\left(t\right)}{dt} = -\mathrm{i}\left[\boldsymbol{\mathcal{H}}\left(t\right), \boldsymbol{\sigma}\left(t\right)\right], \tag{2.60}$$

where $\boldsymbol{\mathcal{H}}(t)$ is a time-dependent Hamiltonian and $\boldsymbol{\sigma}(t)$ is a density operator given by

$$\boldsymbol{\sigma}\left(t\right) = \sum_{k} p_k \left|\psi_k\left(t\right)\right\rangle\!\left\langle\psi_k\left(t\right)\right|. \tag{2.61}$$

Here p_k is the time-independent probability for a system to be in the time-dependent $|\psi_k(t)\rangle$ state.

For an $S = \frac{1}{2}$ spin system, it is convenient to decompose $\boldsymbol{\sigma}(t)$ into a linear combination of orthogonal basis operators having clear physical meaning, e.g. Cartesian basis: $(\boldsymbol{S}_x, \boldsymbol{S}_y, \boldsymbol{S}_z, \mathbf{1})$ [75]. A space spanned by the orthogonal basis operators is called the Liouville space. For a coupled $S = \frac{1}{2}$ and $I = \frac{1}{2}$ spin ensemble, the expansion of $\boldsymbol{\sigma}(t)$ is performed in the Liouville space formed by

47

taking the tensor product of two Cartesian bases:

$$\{\boldsymbol{A}_1, \boldsymbol{A}_2, \ldots, \boldsymbol{A}_{16}\} = 2 \cdot \left\{ \boldsymbol{S}_x, \boldsymbol{S}_y, \boldsymbol{S}_z, \frac{1}{2}\mathbb{1}_S \right\} \otimes \left\{ \boldsymbol{I}_x, \boldsymbol{I}_y, \boldsymbol{I}_z, \frac{1}{2}\mathbb{1}_I \right\} =$$

$$= \left\{ \frac{1}{2}\mathbb{1}, \boldsymbol{S}_x, \boldsymbol{S}_y, \boldsymbol{S}_z, \boldsymbol{I}_x, \boldsymbol{I}_y, \boldsymbol{I}_z, 2\boldsymbol{S}_x\boldsymbol{I}_x, 2\boldsymbol{S}_x\boldsymbol{I}_y, 2\boldsymbol{S}_x\boldsymbol{I}_z, 2\boldsymbol{S}_y\boldsymbol{I}_x, 2\boldsymbol{S}_y\boldsymbol{I}_y, 2\boldsymbol{S}_y\boldsymbol{I}_z, 2\boldsymbol{S}_z\boldsymbol{I}_x, \right.$$

$$\left. 2\boldsymbol{S}_z\boldsymbol{I}_y, 2\boldsymbol{S}_z\boldsymbol{I}_z \right\}. \quad (2.62)$$

Here a certain normalization is applied.

The main point of the product operator formalism is that any spin Hamiltonian can be also expressed in terms of the product operators as

$$\mathcal{H} = \sum_k \omega_k \boldsymbol{B}_k, \quad (2.63)$$

where ω_k and $\boldsymbol{B}_k$ are the expansion coefficients and product operators, respectively.

In the Heisenberg picture, the evolution of a product operator $\boldsymbol{A}$ to an operator $\boldsymbol{C}$ under another product operator $\boldsymbol{B}$ can be expressed as [76]

$$\boldsymbol{C} = e^{-i\varphi B} \boldsymbol{A} e^{i\varphi B} \equiv \boldsymbol{A} \xrightarrow{\varphi B} \boldsymbol{C}. \quad (2.64)$$

It is sufficient to calculate the commutator between $\boldsymbol{A}$ and $\boldsymbol{B}$ to obtain $\boldsymbol{C}$ [75]:

$$\boldsymbol{A} \xrightarrow{\varphi B} \boldsymbol{C} = \begin{cases} \boldsymbol{A}\cos\varphi - i\,[\boldsymbol{B}, \boldsymbol{A}]\sin\varphi & , \boldsymbol{A} \neq \boldsymbol{B} \\ \boldsymbol{A} & , \boldsymbol{A} = \boldsymbol{B} \end{cases}. \quad (2.65)$$

As an example of this formalism, let us consider an ensemble of $S = \frac{1}{2}$ electron spins in the external magnetic field. Then the spin Hamiltonian consists only of the electron Zeeman interaction:

$$\mathcal{H} = \omega_S \boldsymbol{S}_z. \quad (2.66)$$

In this case the initial density matrix of the ensemble in the thermal equilibrium

and in the strong-field limit is proportional to $\boldsymbol{S}_z$:

$$\boldsymbol{\sigma}(t=0) = \frac{e^{-\boldsymbol{\mathcal{H}}\hbar/k_BT}}{\mathrm{Tr}e^{-\boldsymbol{\mathcal{H}}\hbar/k_BT}} \propto -\boldsymbol{S}_z. \qquad (2.67)$$

Now suppose that the system is driven out of the equilibrium by applying a non-selective microwave pulse of length t_p. The non-selectivity of the pulse means that it has high excitation bandwidth, i.e. it contains enough non-zero Fourier expansion modes to cover all intrinsic resonance frequencies of the spin system. Since the excitation bandwidth is proportional to $1/t_p$, the non-selective pulse has to be short and strong. In contrast, a pulse is called selective, if it excites only one (or few) transitions. During the time t_p, the magnetization of the spin system is rotated by the so called flip angle $\beta_1 = \omega_1 t_p$, where $\omega_1 = \gamma_e B_1$ and γ_e denotes the gyromagnetic ratio of the free electron. In the product operator formalism, the application of a pulse from x-direction is considered as an interaction with the product operator $\beta_1 \boldsymbol{S}_x$. The interaction given by the static Hamiltonian can be neglected during the microwave pulse [75].

For example, consider an application of a non-selective $\boldsymbol{S}_x$ pulse with $\beta_1 = \frac{\pi}{2}$ on the initial density matrix given by Eq. 2.67. Using Eq. 2.65 with $\boldsymbol{A} = -\boldsymbol{S}_z$, $\varphi = \frac{\pi}{2}$ and $B = \boldsymbol{S}_x$ one obtains

$$\boldsymbol{\sigma}(t=0) = -\boldsymbol{S}_z \xrightarrow{\frac{\pi}{2}\boldsymbol{S}_x} \boldsymbol{S}_y. \qquad (2.68)$$

In a simple vector model this means that the application of the $\frac{\pi}{2}$ pulse along the x-axis rotates the spin magnetization by $90°$ around the same axis. From the quantum mechanical point of view, the electron spin polarization $\boldsymbol{S}_z$ is transferred to the electron coherence $\boldsymbol{S}_y$ [75].

After the application of a $\frac{\pi}{2}$-pulse, the evolution of the electron coherence (non-diagonal density matrix elements) is governed by the static spin Hamiltonian (Eq. 2.66), i.e.

$$\boldsymbol{S}_y \xrightarrow{\Omega_S t \boldsymbol{S}_z} \cos\left(\Omega_S t\right)\boldsymbol{S}_y - \sin\left(\Omega_S t\right)\boldsymbol{S}_x, \qquad (2.69)$$

where $\Omega_S = \omega_S - \omega_{\mathrm{mw}}$ is the angular frequency in the rotating reference frame. The electron coherence oscillates with frequency Ω_S and, due to the internally fluctuating fields, decays exponentially with the so called phase memory relaxation time T_m. This decay is detected in the resonator and is called the

free induction decay (FID). Simultaneously, the magnetization returns to the equilibrium value at a rate determined by the spin-lattice relaxation time T_1.

In order to obtain more information about a spin system, the FID is Fourier transformed to yield a spectrum in the frequency-domain [75, 94]. However, such Fourier EPR experiment has two main drawbacks that complicate its applicability. First, the excitation window of an ordinary microwave pulse is approximately 1 mT, while the spectrum could easily cover a range of 60 mT [82]. Second limitation is the dead-time of the spectrometer, which prevents the detection of the initial part of the FID, resulting in a distorted spectrum. The best way to avoid these limitations is to use the so called Hahn echo pulse sequence: $\pi/2 - \tau - \pi - \tau - \mathrm{echo}$ (see Fig. 2.18) [95]. In this experiment, the first $\frac{\pi}{2}$-pulse deflects the magnetization vectors of different spin-packets (corresponding to different Ω_S) to the xy-plane, where they start to spread out (electron coherence is disappearing). After time τ, the π-pulse is applied along the same direction causing the inversion of the magnetization. After another τ period, magnetization refocuses giving rise to an echo. This echo contains information about the investigated spin system. For example, by directly integrating the Hahn echo at different magnetic field values, one performs the so called echo-detected field sweep experiment which yields the field-dependent EPR absorption spectrum.
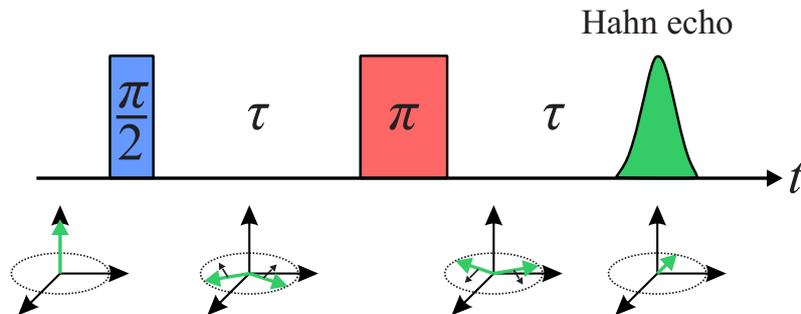

Figure 2.18: Hahn echo pulse sequence and its effect on the spin magnetization. Note how the transverse magnetization is reversed after the application of the π-pulse.

2.3.12   Two-pulse ESEEM

In 1965 Rowan *et al.* [90] discovered that the Hahn echo intensity is modulated by the nuclear transition frequencies and their combinations, as the time interval τ between the pulses is incremented. This phenomenon was named electron spin echo envelope modulation (ESEEM). The two-pulse (2p) ESEEM sequence is presented in Figure 2.19. The ESEEM technique is highly advantageous, since it does not require any radio frequency irradiation to detect nuclear transitions. It is well suited for structural studies of various systems including frozen solutions and powders [88].
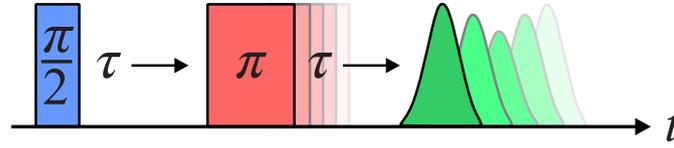

Figure 2.19: Pulse sequence for 2p ESEEM experiment. The echo is modulated by the nuclear transition frequencies and their combinations as the interpulse delay τ is incremented.

A quantitative analysis of a 2p ESEEM experiment can be carried out using the discussed product operator formalism. For the coupled $S = \frac{1}{2}$ and $I = \frac{1}{2}$ spin system (Eq. 2.49), the echo intensity is [75, 91]

$$V_{2p}(\tau) = 1 - \frac{k}{4}\left[2 - 2\cos\omega_\alpha\tau - 2\cos\omega_\beta\tau + \cos\omega_-\tau + \cos\omega_+\tau\right], \qquad (2.70)$$

where ω_α and ω_β are the basic nuclear angular frequencies given by Eq. 2.58 and 2.59. The combination frequencies are $\omega_{+(-)} = \omega_\alpha \pm \omega_\beta$. The modulation depth parameter k is

$$k = \left(\frac{B\omega_I}{\omega_\alpha\omega_\beta}\right)^2. \qquad (2.71)$$

This expression indicates that the ESEEM effect vanishes, if the anisotropic hf interaction component B is zero. The modulation also disappears when the magnetic field vector $\boldsymbol{B}$ approaches the principal axes of the dipolar hyperfine tensor T (see Eq. 2.57) [75].

As an example of the 2p ESEEM effect, let us consider a system with a single $S = \frac{1}{2}$ electron spin coupled with proton ($I = \frac{1}{2}$) which has axially symmetric hf

tensor $\boldsymbol{A} = [A_{xx}, A_{yy}, A_{zz}] = [3, 3, -6]$ MHz. The simulated ESEEM time pattern and the corresponding frequency spectrum for a powder system is presented in Fig. 2.20. It can be seen that the frequency spectrum consists of the nuclear frequencies $\nu_{\alpha(\beta)} = \omega_{\alpha(\beta)}/2\pi$ and their combinations.
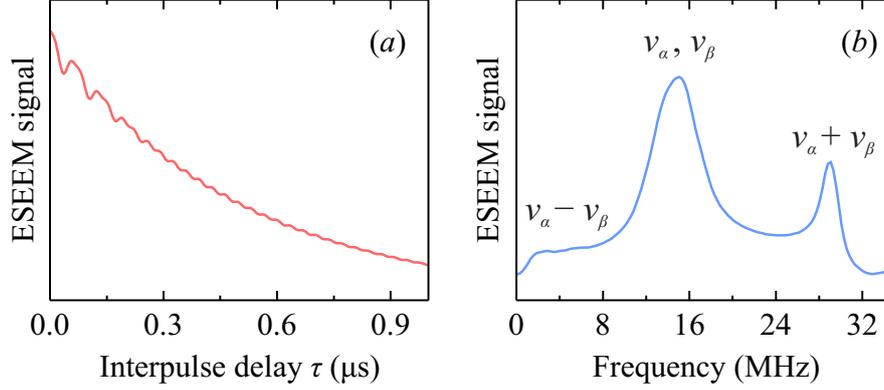

Figure 2.20: Simulated 2p ESEEM (a) time-domain pattern and (b) frequency spectrum for a coupled electron-proton system. The following parameters were used for the simulation: $g = g_e$, $\boldsymbol{A} = [3, 3, -6]$ MHz, $T_1 = 2$ μs, $T_m = 1$ μs, $B = 340$ mT. Simulation performed with EasySpin [96].

The applicability of the 2p ESEEM technique has two main drawbacks. First, the obtained spectrum contains sum and difference of the nuclear frequencies complicating the analysis. Secondly, it is hard to achieve high τ values due to the electron spin coherence decay with the phase memory time T_m which is short compared to the T_1 relaxation time. In addition, the T_m governed decay of the signal results in broader spectral lines in comparison with the nuclear resonance linewidths that are determined by the nuclear phase memory time. These limitations are absent in the three-pulse (3p) ESEEM experiments.

2.3.13   Three-pulse ESEEM, stimulated echo

A 3p ESEEM pulse sequence ($\frac{\pi}{2} - \tau - \frac{\pi}{2} - \tau' - \frac{\pi}{2} - \tau - \text{echo}$) is depicted in Fig. 2.21. The first $\frac{\pi}{2}$-pulse generates the electron coherence. After time τ, the second $\frac{\pi}{2}$-pulse transfers this coherence to the nuclear coherence which further evolves with frequencies ω_α and ω_β during time period τ'. Finally, the last $\frac{\pi}{2}$-pulse transfers the nuclear coherence back to the electron coherence that is refocused after another time period τ. This results in a so called stimulated echo [75, 91].
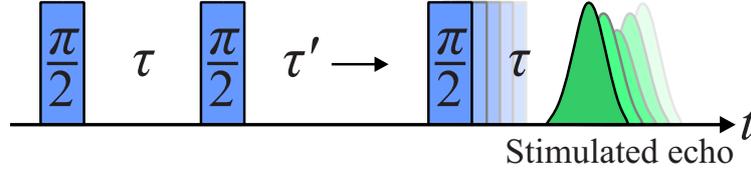
Figure 2.21: Pulse sequence for 3p ESEEM experiment. The echo is modulated by the nuclear transition frequencies as the interpulse delay τ' is incremented.

If the time interval τ' is varied, the stimulated echo envelope is solely modulated with the basic nuclear frequencies ω_α and ω_β. This leads to a much simpler spectrum compared with the 2p ESEEM case. Another advantage of 3p ESEEM experiment is that the decay of coherence is governed by the transverse nuclear relaxation time or the electron spin-lattice relaxation time T_1 that can be much longer than T_m [88].

The 3p ESEEM modulation for a coupled $S = \frac{1}{2}$ and $I = \frac{1}{2}$ spin system can be expressed as [75]

$$V_{3p}(\tau, T) = 1 - \frac{k}{4}\Big[(1 - \cos{(\omega_\beta \tau)})(1 - \cos{(\omega_\alpha(T + \tau))}) + (1 - \cos{(\omega_\alpha \tau)}) \times$$
$$(1 - \cos{(\omega_\beta(T + \tau))})\Big], \quad (2.72)$$

where the modulation depth k is given by Eq. 2.71. Note that the amplitude of the modulation is τ-dependent due to the $1 - \cos{(\omega_\alpha \tau)}$ and $1 - \cos{(\omega_\beta \tau)}$ prefactors. For $\tau = 2\pi n/\omega_{\alpha(\beta)}$ ($n = 1, 2, ...$), the modulation $V_{3p}(\tau, T)$ vanishes and the so called "blind spots" are observed in a frequency spectrum [97]. This is a strong drawback of all pulse sequences based on the stimulated echo, as blind spots could result in severe spectrum distortions. This limitation can be partly overcome by performing several experiments at different τ values or using the so called remote echo detection sequence [98].

2.3.14 Relaxation measurements

The transverse (spin-spin) and longitudinal (spin-lattice) relaxation of a paramagnetic center can provide information about the molecular and lattice (phonon) dynamics [75, 79].

Let us consider a spin system after application of a π-pulse which inverts its population (magnetization). The system tends to reach the thermal equilibrium during the longitudinal relaxation characterized by time T_1. This process involves the energy transfer from the excited spin system to the lattice phonons. The origin of this relaxation is the phonon vibrations that produce locally fluctuating electric and magnetic fields which cause the electron spin transitions [79]. Different relaxation pathways dominate at different temperatures, since the phonon energy density is strongly temperature dependent.

The T_1 relaxation mechanisms are divided into the direct and Raman processes (see Figure 2.22). The direct process involves the flipping of the excited spin and emission (absorption) of a single phonon. During the Raman process, a phonon of any frequency may flip a spin and scatter with a different frequency (two-phonon process). The direct process is a first-order process and thus it has much higher probability. However, for the direct process to occur, the energy of the spin transition ω_S must match the phonon energy. This limitation is absent for the Raman (second-order) process. At high temperature, the maximum of the phonon energy density is at $\omega \gg \omega_S$, and thus the Raman process dominates the relaxation. As the temperature is decreased, the maximum shifts to the lower frequency and the direct mechanism starts to dominante [79].
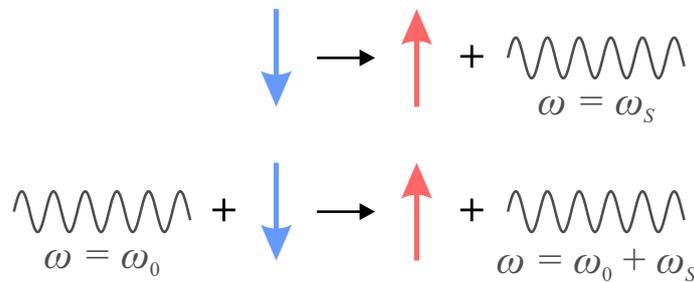

Figure 2.22: Schematic illustration of the (top) direct and (bottom) Raman mechanisms of the spin-lattice relaxation.

During the transverse relaxation, the spin system looses the spin coherence due to the fluctuating internal fields [79]. This process does not require the exchange of energy with the environment. The effective mechanism of the coherence decay is the energy-conserving flip-flop transition of two spins [75]. During such a spin-spin interaction, one of the spins changes its state providing energy for a transition of the second spin. The characteristic empirical time of the

transverse relaxation is the phase-memory time T_m.

The T_m and T_1 relaxation times are usually measured using pulse sequences. For the T_m measurements, the 2p ESEEM pulse sequence is used (see Figure 2.19). As the interpulse delay τ is incremented, the echo amplitude decays exponentially with the phase memory time T_m. Several pulse sequences exists for the measurements of T_1 relaxation time, while the saturation and the inversion recovery sequences are the most popular [88]. The inversion recovery sequence ($\pi - \tau' - \pi/2 - \tau - \pi - \tau - \text{echo}$) is presented in Figure 2.23. The first π-pulse inverts the magnetization which starts to relax with time T_1. As the interpulse delay τ' is incremented, the magnetization recovery is obtained by echo integration.
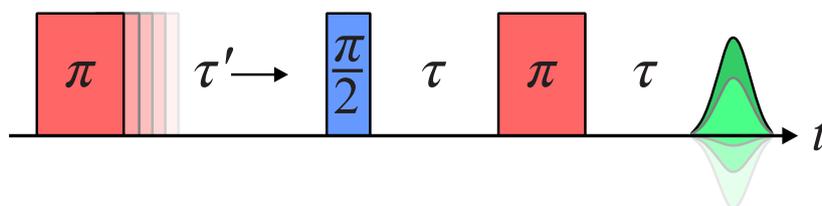

Figure 2.23: Inversion recovery pulse sequence for measurement of the longitudinal relaxation time T_1.

2.3.15 Pulsed ENDOR spectroscopy

Pulsed ENDOR spectroscopy is another powerful tool used to probe the local magnetic environment of paramagnetic centers by measuring the nuclear transition frequencies of nuclear spins [72]. As in the ESEEM technique, the main target of the ENDOR spectroscopy is the determination of the hf coupling between the unpaired electron and the nearby nuclei. This tool is more technologically demanding, as, in addition to the ordinary microwave irradiation, ENDOR spectroscopy also uses pulses of radio-frequency.

The two most common ENDOR pulse sequences have been introduced by Davies [93] and Mims [92] (see Figure 2.24). Both experiments are based on a spin polarization transfer during the sweep of the radio-frequency pulse frequency [88]. The polarization transfer during the Davies ENDOR experiment is depicted

in Figure 2.24c for a coupled $S = \frac{1}{2}$ and $I = \frac{1}{2}$ spin system. The initial selective microwave π-pulse excites a single EPR transition and inverts the population of the involved energy levels. Then the applied selective radio-frequency π-pulse transfers the polarization between the nuclear sublevels causing the population difference of the initial levels to disappear. Consequently, the echo intensity becomes lower.
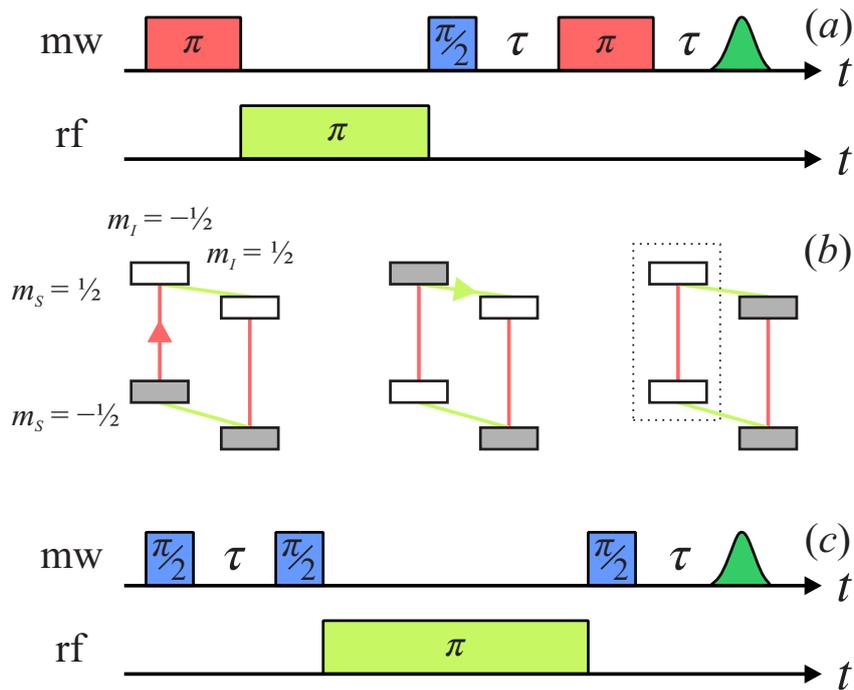

Figure 2.24: (a) Davies and (c) Mims ENDOR pulse sequences. (b) Spin polarization transfer in a coupled $S = \frac{1}{2}$ and $I = \frac{1}{2}$ system during the Davies ENDOR experiment.

The transfer of polarization during the Mims ENDOR experiment does not require selective microwave pulses [88]. However, as the pulse sequence is based on the stimulated echo, one expects blind spots in the Mims ENDOR spectrum for $\tau = 2\pi n / A_{\text{iso}}$ ($n = 1, 2, ...$) [75].

"But what if we could see them?"

Werner Heisenberg

Chapter 3

Results and Discussion

This Chapter is devoted to the presentation and discussion of the EPR results of DMAZn, AmZn, MHyZn and BnZn frameworks doped with paramagnetic transition metal ions.

3.1   EPR Spectroscopy of DMAZn

In this Section, the CW and pulsed EPR spectroscopy results of Mn^{2+} and Cu^{2+} doped DMAZn frameworks (samples **DMAZn:Mn**, **DMAZn-15N:Mn** and **DMAZn:Cu**) are presented [99–103]. A pure DMAZn framework exhibits a structural phase transition at 163 K (refer to Section 2.2.1 for more details). The EPR results are supported by the pyrocurrent, dielectric permittivity and electric polarization measurements of pure DMAZn single crystal (sample **DMAZn**) as well as Monte Carlo simulations [104]. Some CW EPR results are compared with the measurements of Mn^{2+} doped AmZn framework (**AmZn:Mn**). A detailed description of the sample synthesis is presented in Appendix A. The experimental EPR details are given in Appendix B.

3.1.1 CW EPR of manganese doped DMAZn

3.1.1.1 CW EPR of manganese doped DMAZn powder

The X- and Q-band CW EPR spectra of **DMAZn:Mn** recorded during cooling from the room temperature to 40 K are presented in Figure 3.1. The observed spectra resemble typical powder patterns of the Mn^{2+} ions in the $3d^5$ electron configuration and $^6S_{5/2}$ electron ground state. The total electron spin $S = \frac{5}{2}$ of Mn^{2+} gives rise to a zfs which causes five fs transitions. Each such transition is further split into six hf lines due to the interaction with ^{55}Mn nucleus (see Figure 2.15 for more details) [14, 79, 105].
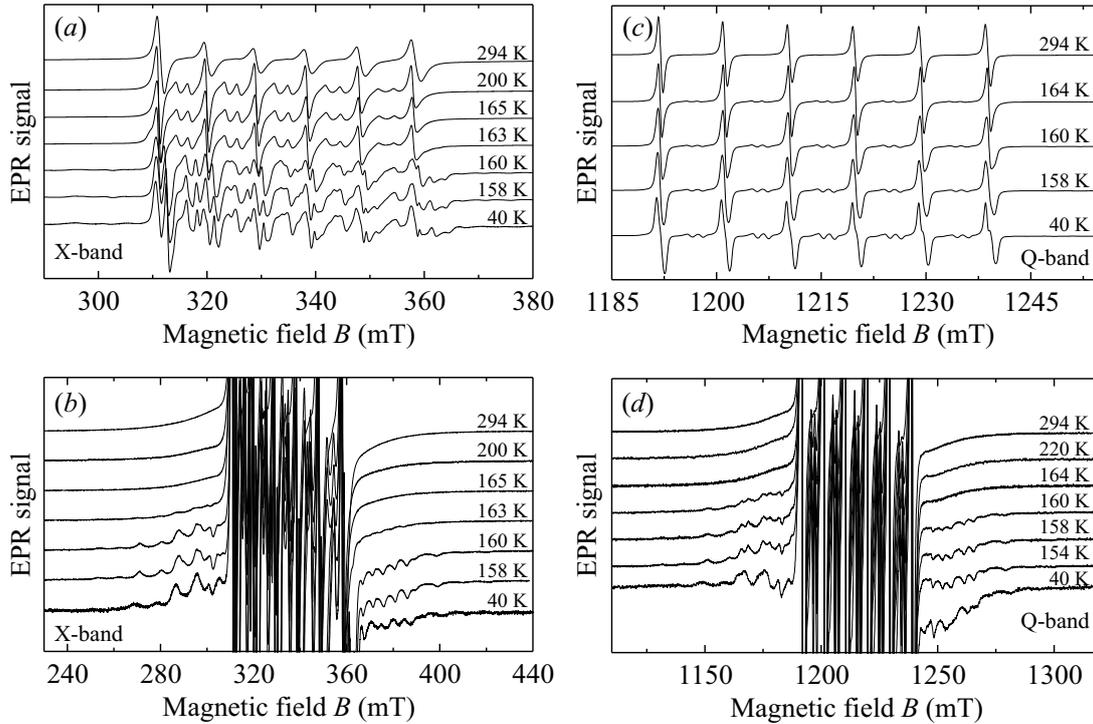

Figure 3.1: Normalized (a), (b) X- and (c), (d) Q-band CW EPR spectra of **DMAZn:Mn** powder recorded at different temperatures. Emphasis on (a), (c) central and (b), (d) outer fs transitions. Note the abrupt change in the spectra at about 163 K.

The observed room temperature spectra are dominated by the six hf lines of the central fs transition ($m_s = -\frac{1}{2} \leftrightarrow \frac{1}{2}$). The outer fs transitions ($m_s = \pm\frac{3}{2} \leftrightarrow \pm\frac{1}{2}$ and $m_s = \pm\frac{5}{2} \leftrightarrow \pm\frac{3}{2}$) are not resolved implying a small zfs and/or some internal

strain effects causing a distribution of the zfs parameters. On cooling, a sudden drastic change in the spectra measured at both frequencies is observed at about 163 K. Below this temperature, the outer fs transitions are clearly resolved indicating a higher value of the zfs and negligible strains. The temperature at which the change in the spectra occurs corresponds to the phase transition temperature of the pure DMAZn framework, as revealed by the pyrocurrent measurements of **DMAZn** single crystal sample (see Figure D.1, Appendix D). The same phase transition temperature was also observed by different experimental methods in other studies [7, 51, 54, 55]. Thus, the abrupt change of the CW EPR spectra is assigned to the phase transition in **DMAZn:Mn**. This demonstrates that the incorporation of the Mn^{2+} ions into the framework was successful and that these probes are indeed sensitive to the structural changes occurring during the transition.

The CW EPR spectra of **DMAZn:Mn** were further analyzed using the spectral simulations. The following spin Hamiltonian was used to describe the Mn^{2+} spectra [79]:

$$\mathcal{H} = \beta_e \boldsymbol{B g S} + \boldsymbol{S A I} + \mathcal{H}_{\mathrm{FS}}. \tag{3.1}$$

Here the first term describes the electron Zeeman interaction characterized by the $\boldsymbol{g}$-tensor of the Mn^{2+} center. The hf interaction is taken into account by the second term, where $\boldsymbol{A}$ is the hf tensor. The fs of the spectrum is described by the last term which is expressed using the extended Stevens operators $\hat{\boldsymbol{O}}_k^q(\boldsymbol{S})$ as:

$$\mathcal{H}_{\mathrm{FS}} = \sum_k \sum_q B_k^q \hat{\boldsymbol{O}}_k^q(\boldsymbol{S}). \tag{3.2}$$

The real coefficients B_k^q characterize the magnitude of the corresponding zfs (see Ref. [83] and Section 2.3.5 for more details).

The simulation of the X- and Q-band EPR spectra recorded at 180 K (high-temperature phase) are presented in Figure 3.2. It is sufficient to use the isotropic $\boldsymbol{g}$- and $\boldsymbol{A}$ tensors to obtain a perfect agreement with the experimental spectra. The spin Hamiltonian parameters used for simulation are $g = 2.00053(5)$, $A_{\mathrm{iso}} = -264(1)$ MHz, $D = 200(20)$ MHz and $E \approx 0$. As mentioned above, in the experimental spectra at $T > 163$ K, the outer fs transitions are not resolved indicating a broad distribution of the axial zfs parameter D. A Gaussian distri-

bution of D with the FWHM of $\Delta D \approx 150$ MHz was used for the simulation. Such a broad distribution also results in a high determination error of D. Note that other zfs coefficients (including a and F) had a tiny effect on the simulated spectra and thus were excluded from the simulation. The same set of spin Hamiltonian parameters was used for simulation at both frequencies.
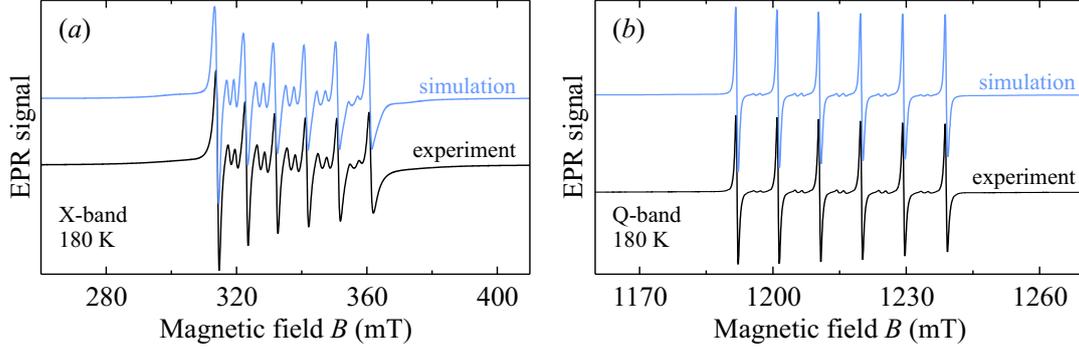

Figure 3.2: Measured (black) and simulated (blue) (a) X-band and (b) Q-band CW EPR spectra of **DMAZn:Mn** powder recorded at 180 K (high-temperature phase).

The determined magnitude of A_{iso} is typical for a Mn$-$O coordination bond [14, 106]. This indicates that Mn^{2+} probe ions successfully substituted the Zn^{2+} ions in the lattice of DMAZn. A nonzero value of D demonstrates that the local symmetry of the Mn^{2+} ions is noncubic. This is indeed supported by the room temperature XRD analysis [7, 41] which indicates that the ZnO$_6$ and MnO$_6$ octahedra in DMAZn and DMAMn frameworks slightly deviate from the ideal cubic symmetry. A very broad distribution of D parameter originates from the differently distorted MnO$_6$ octahedra due to the hopping motion of the DMA$^+$ cations within the metal-formate cages.

The simulated multifrequency (X-, Q- and W-band) CW EPR spectra of the low-temperature phase of **DMAZn:Mn** are presented in Figures 3.3. A perfect agreement between the experimental (80 K) and simulated spectra was achieved by including B_2^{-2}, B_4^0, B_4^2 and B_4^4 zfs coefficients. The spin Hamiltonian parameters are: $g = 2.00053(5)$, $A_{\text{iso}} = -264(1)$ MHz, $D = 422(1)$ MHz, $E = 58(2)$ MHz, $B_2^{-2} = 25(1)$ MHz, $B_4^2 = 0.30(3)$ MHz, $B_4^0 = 0.27(3)$ MHz and $B_4^4 = 0.83(4)$ MHz. Accordingly, the cubic a and axial F fourth order fs parameters are 20(1) MHz and 18(1) MHz. Note that similar values of a and F parameters were observed in other systems with paramagnetic Mn^{2+} centers [14]. The low temperature

spectra have well resolved outer fs transitions, indicating that the distribution of D is much narrower compared with the high temperature-phase spectra. $\Delta D \approx 30$ MHz was used for the simulation at 80 K. Note that the W-band EPR measurements allowed to more accurately determine the g-factor of the Mn^{2+} ions.
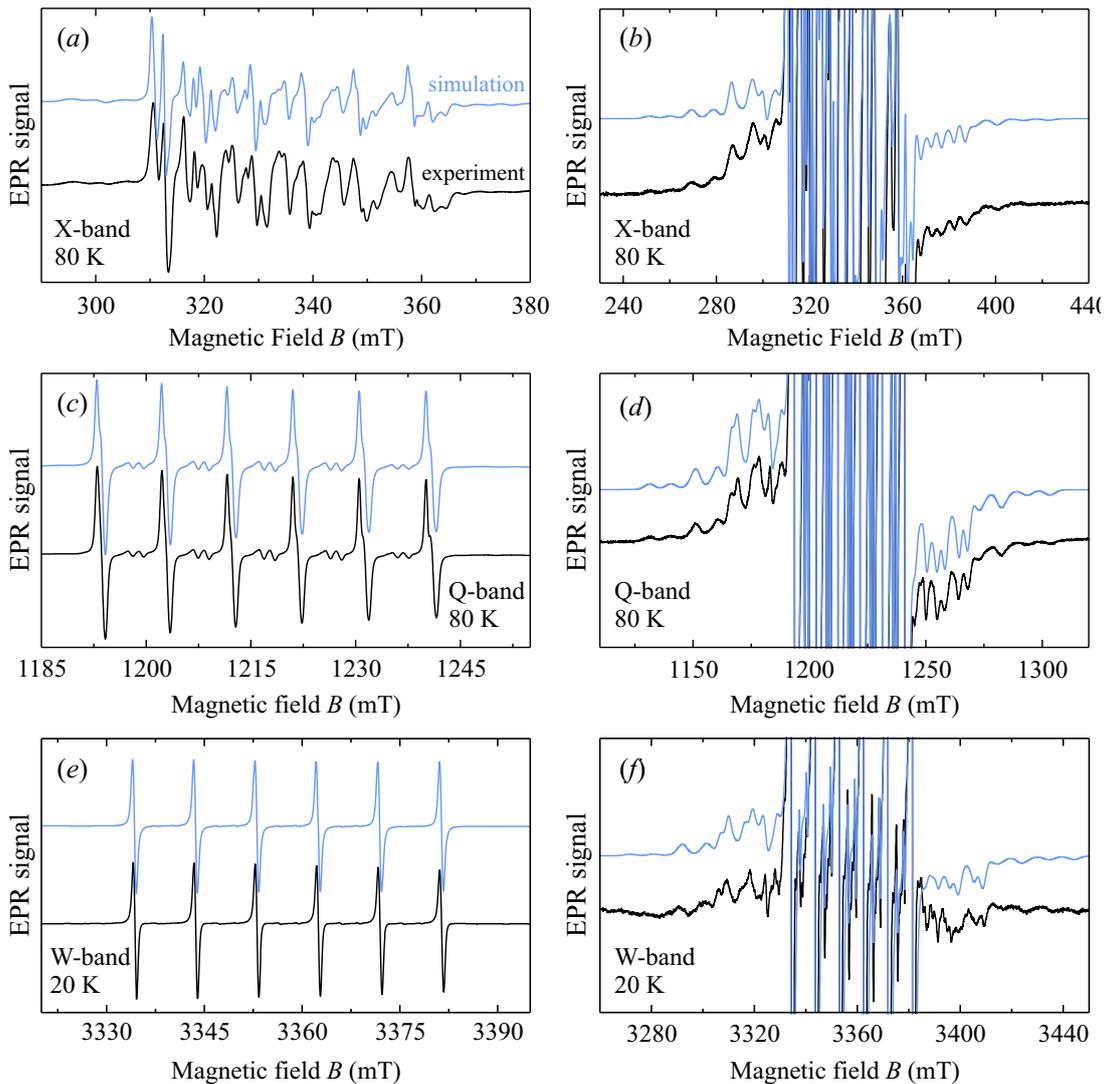

Figure 3.3: Measured (black) and simulated (blue) (a), (b) X-band, (b), (c) Q-band and (e), (f) W-band CW EPR spectra of **DMAZn:Mn** powder in the low-temperature phase. The X- and Q-band spectra were measured at 80 K. The W-band experiment was performed at 20 K.

The observed much higher value of D parameter as well as a non-negligible E demonstrate that in the low temperature phase the symmetry of the MnO_6

octahedron deviates significantly from cubic. Note that using XRD a highly non-cubic environment of octahedron (six different Mn−O distances) was detected in pure DMAMn framework [41]. In addition, a much smaller distribution width ΔD in the low-temperature phase is likely related to a significantly reduced DMA$^+$ cation motion due to the established long-range order in the system. The observed well-defined zfs parameters indicate uniformly deformed MnO$_6$ octahedra.

The temperature dependence of the spin Hamiltonian parameters was determined from the X- and Q-band CW EPR spectra. No significant changes of the g-factor and A_{iso} parameters were observed. The obtained temperature dependence of the axial zfs parameter D clearly indicates a discontinuous phase transition at $T_0 = 163$ K (see Figure 3.4) which is in agreement with the pyrocurrent measurements (Figure D.1) and majority of other studies [11, 42, 44]. The dependence is also reproduced on heating (not shown here) with a temperature hysteresis of $\Delta T \approx 3$ K. The overall increase of D with decreasing temperature in the low-temperature phase reveals a further gradual deformation of the framework.
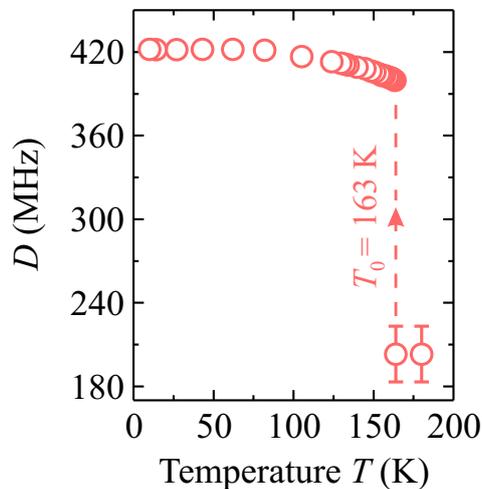

Figure 3.4: Temperature dependence of the axial zfs parameter D of the Mn^{2+} ions in **DMAZn:Mn**.

The observed temperature dependence of D resembles a behavior typical for a phase transition order parameter η_0 (see Figure 2.3) [16]. There is no observable splitting into two fs branches due to the positive and negative values of the

order parameter and thus it may be assumed that the axial zfs parameter is proportional to the square of the order parameter: $D = D_0 + C\eta_0^2$. Here D_0 denotes the value of D just above T_0.

The determined temperature dependence of D was analyzed using Eq. 2.8 which describes the order parameter behavior for a weak first-order phase transition. The best approximation provided the maximum temperature hysteresis of $\beta^2/4\alpha\gamma = 200(20)$ K. This value is higher than the phase transition temperature itself meaning that the Landau model is not suitable to describe the ordering in DMAZn. Note that Eq. 2.8 characterizes the first-order phase transition close to the second-order [16]. Thus, the failure of this equation to describe the behavior of η indicates that the transition in DMAZn is of the strong first-order character. In addition, there is experimental evidence that the disorder of the DMA$^+$ cations persists below T_0 suggesting a more complex ordering mechanism which is not accounted in this model [8, 54]. Finally, Eq. 2.8 provides two solutions of the order parameter that are equal in magnitude, but opposite in direction, while the order parameter in DMAZn system is expected to have a three-fold symmetry.

The first-order nature of the phase transition in DMAM framework was also obtained by the Monte Carlo (MC) simulations using a statistical three-state lattice model (see Appendix E for model and simulation details). In the proposed model, the H-bonding between the DMA$^+$ cations and the metal-formate cages is considered to be the driving mechanism of the ordering. This bonding is effectively mimicked by the Potts-type interaction. In addition, the cations also interact via the dipolar interactions. Simulations revealed that in the absence of the dipolar interactions, the well-known three-state Potts model can be used to describe the ordering. This model exhibits a first-order phase transition. However, the inclusion of sufficiently strong dipolar interactions provides a stronger first-order character of the transition in agreement with the experimental results.

The temperature dependence of the Mn^{2+} peak-to-peak CW EPR linewidth Γ of the $m_I = -\frac{5}{2}$ hf line of the central fs transition is presented in Figure 3.5a. The linewidth significantly narrows as the temperature is decreased in the high-temperature phase, while a sharp anomaly of Γ is observed at the phase transitions point.
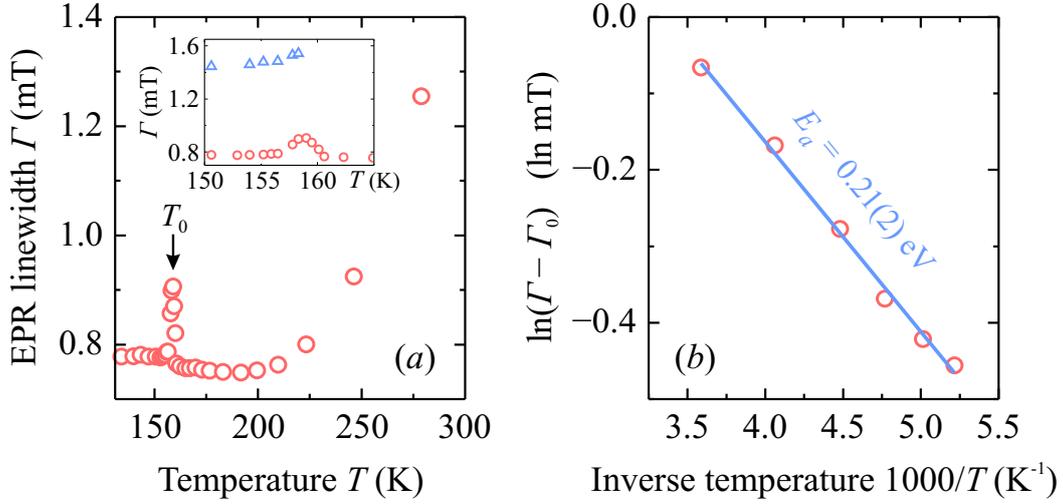
63

Figure 3.5: (a) Temperature dependence of the peak-to-peak CW EPR linewidth of Mn^{2+} centers in **DMAZn:Mn**. (b) Arrhenius analysis of the temperature dependent Γ in the disordered phase. Inset in (a) presents Γ about the phase transition point. The blue triangles mark the EPR linewidth of the hf line of the outer fs transition.

There could be two possible reasons for the observed maximum of Γ at T_0. First, it could be related to the sudden change of the axial zfs parameter at the phase transition point which causes the broadening of the lines of the central fs transition. On the other hand, such an anomaly is frequently observed in many other ferroelectric and related materials, e.g. triglycine sulfate [107], trissarcosine calcium chloride [108, 109], $SrTiO_3$ [110] and others [15]. It is attributed to the critical fluctuations of the order parameter. To check which scenario is more feasible, the linewidth of the outer fs transitions was determined, as it should be much less affected by the change of the zfs parameters. However, the outer fs transitions are not resolved in the disordered phase, and thus the linewidth was accurately obtained only below T_0 (see inset in Figure 3.5a). A sudden decrease of Γ is also observed for the outer fs transitions suggesting that the anomaly is related to the order parameter fluctuations at T_0.

The decrease of Γ with lowering of temperature in the disordered phase may originate from the gradual slowing down of the DMA^+ cation motion. As indicated in Figure 3.5b, it can be well described by the Arrhenius law: $\Gamma - \Gamma_0 = \Gamma_\infty e^{-E_a/k_B T}$. Here E_a is the activation energy of motion, Γ_∞ is the CW EPR linewidth in the high temperature limit, Γ_0 is the residue linewidth unre-

lated to the motion and k_B is the Boltzmann constant. The best fit provides $E_a = 0.21(2)$ eV. The determined activation energy is close to the value obtained by NMR (0.24 eV) for DMAZn [55] and DMAMg [48] frameworks. The dielectric spectroscopy of DMACo provided value of 0.28 eV [52]. In these studies, the observed motional effect was assigned to the hopping of the DMA$^+$ cations. To support the CW EPR results, temperature dependent dielectric permittivity measurements of **DMAZn** single crystal were performed in a broadband frequency range (see Figures D.2 and D.3a in Appendix D). The Arrhenius analysis of the electric dipole relaxation provided activation energy of 0.27(1) eV (Figure D.3b) in a good agreement with the EPR result. Thus, the observed temperature dependence of Γ in the disordered phase can be assigned to the deformation of the MnO_6 octahedra due to the hopping motion of the DMA$^+$ cations.

The Mn^{2+} doped DMAZn framework containing ^{15}N isotope (**DMAZn-15N:Mn**) was also investigated using CW EPR spectroscopy. The obtained temperature dependent X-band CW EPR spectra of **DMAZn-15N:Mn** (Figure C.1 in Appendix C) are essentially the same as for **DMAZn:Mn**, which contains natural composition of nitrogen isotopes. The axial zfs parameter D and CW EPR linewidth of the Mn^{2+} centers in **DMAZn-15N:Mn** also exhibit anomalous behavior at the same phase transition temperature as observed in **DMAZn:Mn**. The linewidth analysis in the disordered phase revealed the same activation energy of 0.21(2) eV for the DMA$^+$ cation motion.

The isotope effect may provide important information about the properties of the structural phase transitions. For example, a substantial increase of the phase transition temperature upon deuteration is frequently observed in classical H-bonded ferroelectrics such as KH_2PO_4 [1]. In contrast, the transitions occur at lower temperature as heavier isotopes are introduced in many displacive dielectric crystals like ferroelectric $BaTiO_3$ [111] or antiferroelectric $PbZrO_3$ [112]. In order-disorder type compounds such as $NaNO_2$, $(NH_4)_2SO_4$ or NH_4LiSO_4 the isotope effect is usually negligible as ^{14}N is replaced by ^{15}N [112, 113]. Thus, the absence of this effect in **DMAZn-15N:Mn** reveals the order-disorder nature of the structural phase transition in DMAZn framework.

The ^{15}N (nuclear spin $I = \frac{1}{2}$) NMR measurements of **DMAZn-15N:Mn** sample were also performed to directly probe the nitrogen motion. The obtained NMR

spectrum and temperature dependent spin-lattice relaxation time T_1 are presented in Figure D.4 (Appendix D). The spectrum consists of a single line, while the temperature dependence of T_1 exhibits a maximum at 184 K and a minimum at 300 K. A minimum of the spin-lattice relaxation time is usually related to a motional process [114]. Asaji *et. al.* detected two minima in the ^{1}H proton relaxation time of DMAZn framework which were assigned to the hopping motion of the whole DMA$^+$ cation and methyl group rotation [48, 55]. The analysis of the T_1 relaxation time revealed activation energy of $E_a = 0.20(1)$ eV (see Appendix D for more details). The obtained value is in a perfect agreement with the EPR result indicating that both spectroscopies detect the same motional process which is the hopping of the DMA$^+$ cations. However, in the EPR case, this process manifests itself indirectly via the deformation of the MnO$_6$ octahedra that are H-bonded with the molecular cations.

Summary

The multifrequency CW EPR measurements of Mn^{2+} doped DMAZn powders revealed that the Mn^{2+} centers successfully replaced Zn^{2+} ions in the structure of DMAZn and formed MnO$_6$ octahedra. These ions are susceptible to the structural phase transition in DMAZn, as the CW EPR spectrum experiences drastic changes at the phase transition temperature $T_0 = 163$ K.

The simulations of the high-temperature phase spectra indicate a broad distribution of the axial zfs parameter D. The origin of this broadening was assigned to the deformation of the MnO$_6$ octahedra due to the hopping motion of the DMA$^+$ cations. In the low-temperature phase, the long-range order is established causing uniform deformation of the octahedra and well resolved fs. The axial zfs parameter D exhibits a sudden jump at T_0 which is typical for a first-order (discontinuous) phase transition. This result is supported by the MC simulations.

The CW EPR linewidth of the Mn^{2+} probe ions also exhibits anomalous behavior at T_0 which is assigned to the order parameter fluctuations. The temperature dependent linewidth in the high-temperature phase indicates a motional process which follows the Arrhenius law. The obtained activation energy of this process

is 0.21(2) eV, which is characteristic for the DMA$^+$ cation hopping in these frameworks. This proves a tight relation between the deformation of the MnO$_6$ octahedra and the DMA$^+$ cation motion.

The CW EPR measurements of sample containing ^{15}N isotope revealed a negligible isotope effect indicating order-disorder nature of the structural phase transition in DMAZn framework. The ^{15}N NMR measurements provided the same activation energy as obtained from the CW EPR linewidth analysis indicating that both methods detect the hopping motion of the DMA$^+$ cations.

3.1.1.2   CW EPR of manganese doped DMAZn single crystal

The phase transition and the low-temperature phase of DMAZn is further investigated by performing single crystal CW EPR measurements of **DMAZn:Mn**. The crystal used for the measurements is depicted in Figure A.2a (Appendix A).

The temperature dependence of the X-band CW EPR spectrum of **DMAZn:Mn** single crystal is presented in Figure 3.6 revealing that the phase transition drastically influences the Mn^{2+} spectrum. The high-temperature phase spectrum shows unresolved outer fs transitions implying a distribution of the zfs parameters. Below the phase transition point T_0, the DMA$^+$ cation motion significantly slows down, and the long-range order is established, providing well resolved outer fs transitions. As the temperature is further decreased, the spectrum becomes wider indicating higher value of the axial zfs parameter D due to the increasing distortion of the MnO$_6$ octahedra. All these observations are in agreement with the powder CW EPR measurements.

It was observed that a rapid cooling of the sample (fast insertion to the cryostat operating at 70 K) results in a CW EPR spectrum with unresolved outer fs transitions which is similar to the spectrum obtained for the high-temperature phase (see Figure C.2 in Appendix C). The spectrum did not transform to the pattern characteristic to the low-temperature phase even after keeping the sample at 70 K for several hours. This may indicate that the dynamic disorder of the DMA$^+$ cations becomes quenched at a fast cooling rate resulting in many different environments of the Mn^{2+} probe ions and hence the distribution of the zfs parameters. Note that in an NMR study of DMAZn framework Besara et.
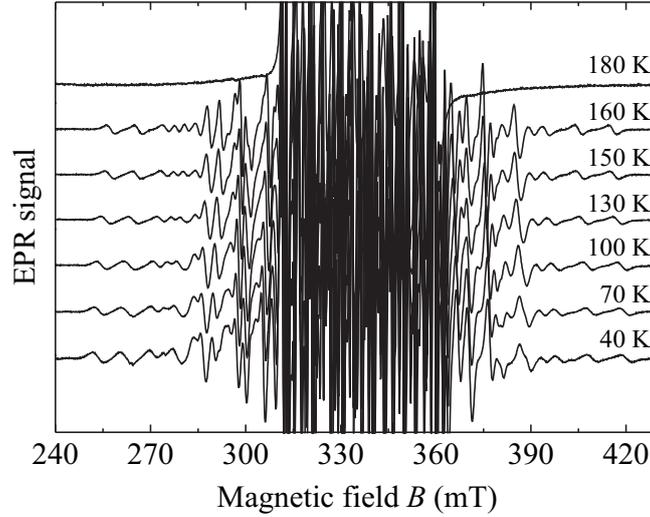
Figure 3.6: Temperature dependent X-band CW EPR spectra of **DMAZn:Mn** single crystal obtained at a fixed arbitrary orientation.

al. [54] observed that the temperature dependence of the proton spin-lattice relaxation rate follows different paths on cooling and warming if the sample is cooled below 40 K. However, in the current experiment the cooling memory effect is observed independently on the lowest reached temperature.

The Mn^{2+} probe centers were further investigated by recording the angular dependence of the low-temperature CW EPR spectra of **DMAZn:Mn** single crystal. The sample was rotated around three approximately perpendicular directions in such a way that the magnetic field vector was in the $(1\bar{1}2)$, $(\bar{1}02)$ or (012) plane. The obtained spectra are presented in Figure 3.7 and Figures C.3 and C.4 (Appendix C) revealing several magnetically inequivalent Mn^{2+} sites. The central part of the spectra is very complicated, since the $m_S = -\frac{1}{2} \leftrightarrow \frac{1}{2}$ fs transitions have the least expressed angular dependence resulting in a high density of the EPR lines. In addition, there is a significant overlap between the allowed and forbidden hf transitions in this spectral region. The rotation patterns of the outer transitions are better resolved, especially of the $m_S = \pm\frac{5}{2} \leftrightarrow \pm\frac{3}{2}$ transitions that exhibit apparent angular dependences at all three orientations of the single crystal. Note that the observed maximum spans of the angular patterns are close to the widths of the powder spectra.

The initial XRD study of the low-temperature structure of DMAMn perovskite revealed two MnO_6 octahedra that are tilted with respect to each other (Fig-
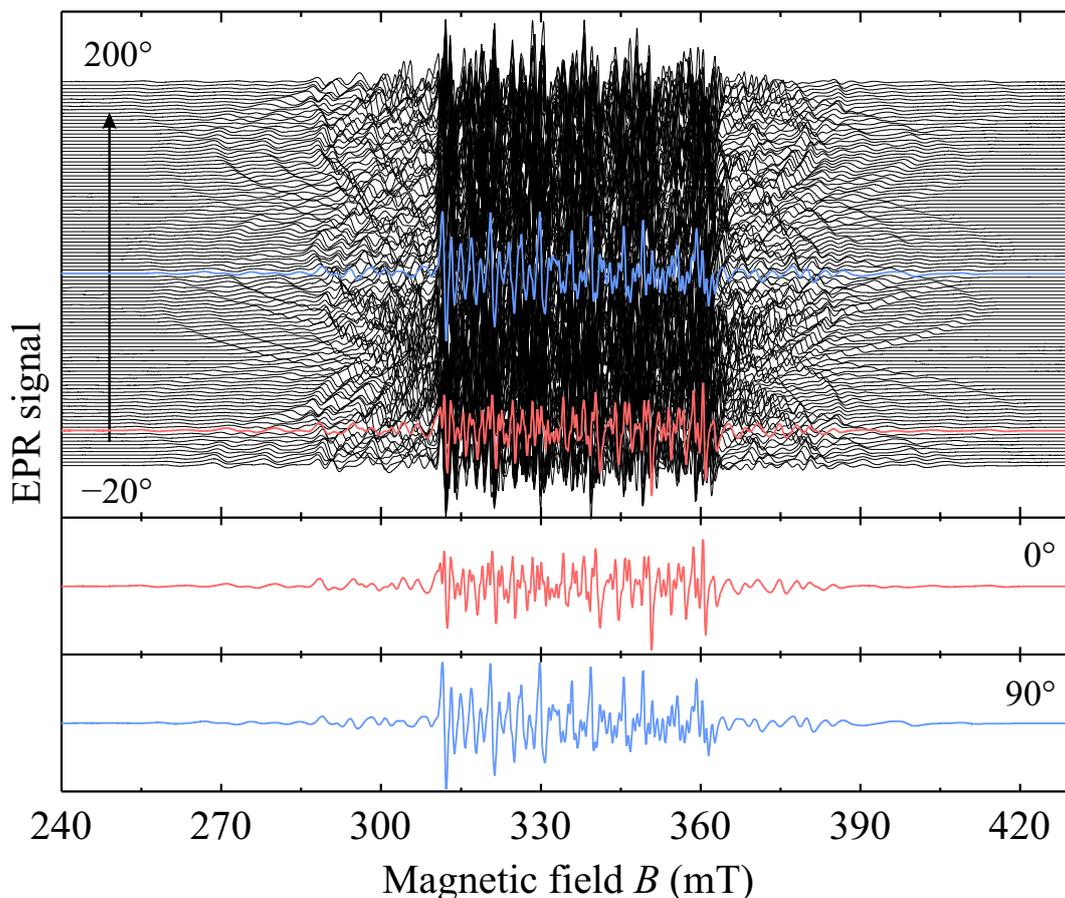
68

Figure 3.7: Angular dependent CW EPR spectra of **DMAZn:Mn** single crystal obtained at 70 K by rotating the magnetic field vector in the $(1\bar{1}2)$ plane. Spectra recorded at $0°$ and $90°$ are explicitly presented. The zero angle corresponds to the magnetic field vector in the (012) plane. Measurements performed by Anastasia Kultaeva at Leipzig University.

ure 2.6) [41]. However, the experimental angular dependent EPR spectra of **DMAZn:Mn** clearly show more than two Mn^{2+} sites indicating crystal twinning or ferroelectric domain phenomena. Spectral simulations of the obtained angular dependences were performed to determine how many differently oriented MnO_6 octahedra are in the system.

The angular dependent resonance fields of the EPR lines are presented in Figure 3.8 for all three orientations of the single crystal. The simulations were performed only for the outermost hf lines ($m_I = \pm\frac{5}{2}$) of the $m_S = \pm\frac{5}{2} \leftrightarrow \pm\frac{3}{2}$ fs transitions that show well pronounced angular dependence. The spin Hamilto-

nian parameters determined from the powder EPR experiments were used for the simulation. To simplify the simulation procedure, only the second-order parameters D and E, which have the main influence on the angular patterns, were taken into account. Note that the $g-$ and A tensors of the Mn^{2+} ions in **DMAZn:Mn** are isotropic and therefore provide no additional angular dependence.
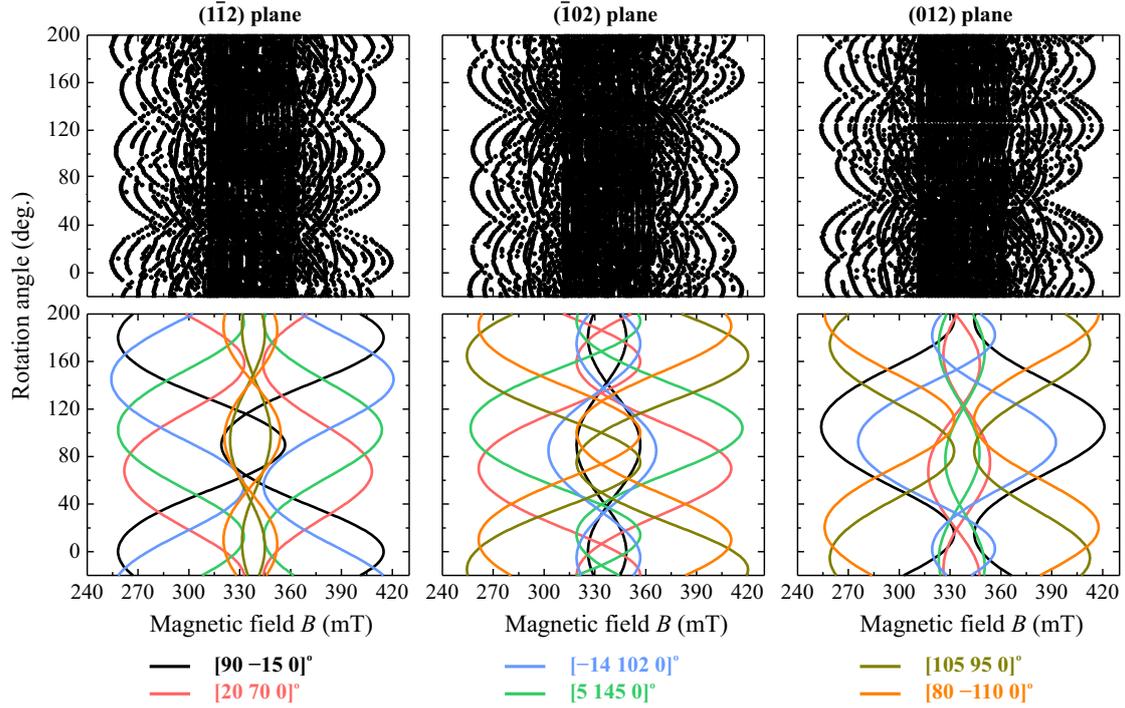

Figure 3.8: Experimental (above) and simulated (below) angular dependent CW EPR signal of **DMAZn:Mn** single crystal obtained by rotating the magnetic field vector in the $(1\bar{1}2)$, $(\bar{1}02)$ and (012) planes.

Six magnetically inequivalent Mn^{2+} sites were required to simulate the determined angular dependences (see Figure 3.8). The simulation agrees rather well with the experimental data taking into account a nonideal crystal shape and alignment as well as simplified spin Hamiltonian. The corresponding Euler angles of the six D tensors of the Mn^{2+} ions are also indicated in Figure 3.8. The Euler angles are defined in a reference frame depicted in Figure A.2b. Note that the third angle was impossible to determine accurately, since each Mn^{2+} center exhibits clear rotation patterns only in two out of three planes (in one plane these patterns overlap with the central part of the spectra).

The obtained six Mn^{2+} sites are in agreement with the later XRD study that indeed revealed the same number of MnO_6 octahedra in the low-temperature phase of DMAMn framework [42]. The six MnO_6 octahedra arise from the three crystalline twins each containing two centers. The crystal twinning is observed only in the low-temperature phase, and thus each twin contains the ordered arrangement of the DMA^+ cations. The crystalline twins can be mapped to each other by a rotation around the crystallographic pseudo-C_3 axis by $120°$ which is related to the initial three-fold disorder of the DMA^+ cations [42].

The X-band CW EPR measurements of **DMAZn:Mn** single crystal with the applied electric field were performed to investigate whether the detected crystalline twins correspond to the ferroelectric domains. If the domains are ferroelectric, the electric field should change their volumes causing the redistribution of the Mn^{2+} line intensities in the EPR spectrum. The obtained low-temperature single crystal spectrum of **DMAZn:Mn** with the simultaneously applied external electric field of 12 kV/cm is presented in Figure 3.9. The spectrum recorded at the same orientation, but without the electric field, is presented for comparison. No clear and reliable differences between both spectra are observed. Such measurements were done for several other crystal orientations and two other poling directions, but the outcome was the same. This suggests that the low-temperature phase of DMAZn is either not a proper ferroelectric or the applied electric field is too small to significantly influence the domain structure. The electric field dependence of the electric polarization of a **DMAZn** single crystal sample was also measured. The obtained results are presented in Figure 3.9c revealing no hysteresis loop [115], despite the much stronger electric field used in this experiment. It was not possible to use stronger fields due to the electrical breakdown of the samples.

To support the experiments on **DMAZn:Mn**, the same type of measurements with the applied electric field were performed for a single crystal sample of manganese doped AmZn framework (**AmZn:Mn**, see Appendix A for sample preparation details) which is known to be ferroelectric [62]. Figure 3.10 shows the CW EPR spectra of **AmZn:Mn** recorded at 150 K (low-temperature phase) with and without the external electric field. A clear redistribution of the EPR line intensities can be seen when the electric field is present indicating that it influences the volumes of the domains as expected for a proper ferroelectric ma-
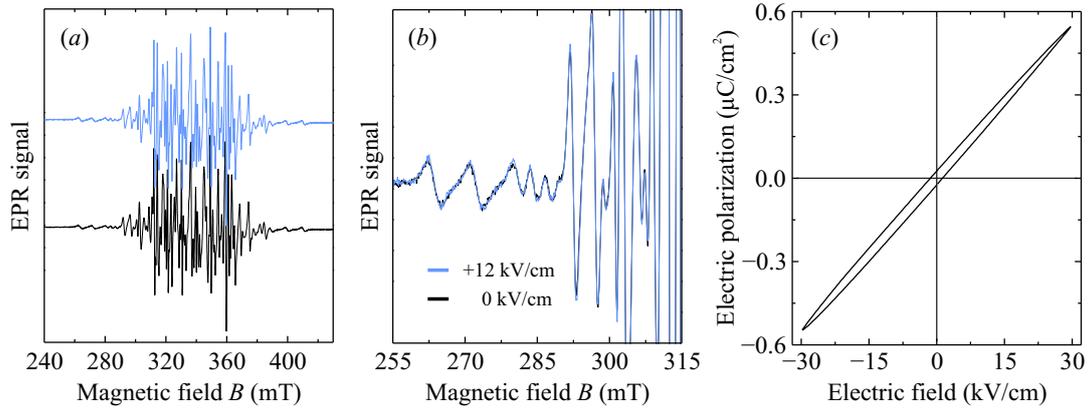
Figure 3.9: (a)-(b) Single crystal X-band CW EPR spectra of **DMAZn:Mn** measured at arbitrary orientation after cooling to 130 K with and without the applied external electric field. (c) Electric field dependence of the electric polarization of **DMAZn** at 145 K. The sample was poled along the [012] direction.

terial [2]. The measurements were verified several times at different orientations of the single crystal. Note that no reliable effect of the electric field on the EPR spectrum of **AmZn:Mn** was observed in the disordered (paraelectric) phase.
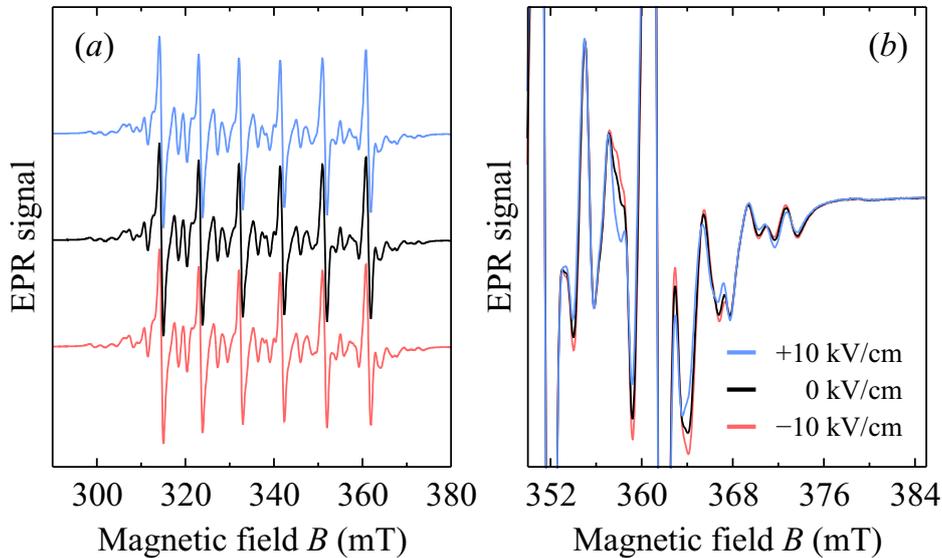

Figure 3.10: (a) X-band CW EPR spectra of **AmZn:Mn** single crystal measured at arbitrary orientation after cooling to 150 K with and without the applied external electric field. The right-wing of the spectrum is magnifiend in (b). The sample was poled along the c-axis.

The redistribution of the ferroelectric domains upon the application of the elec-

tric field should polarize the single crystal sample. The electric polarization is proportional to the change of the domain volumes that also determine the intensities of the EPR signals of the corresponding Mn^{2+} centers. It was recorded how the EPR signal of **AmZn:Mn** changes as the electric field is swept from -10 to $10\,kV/cm$. The obtained dependence of the relative EPR signal is presented in Figure 3.11a revealing a typical ferroelectric hysteresis loop. The EPR results of **AmZn:Mn** are also supported by the electric measurements of the electric polarization presented in Figure 3.11b. Note that similar electric field-induced changes of the EPR spectrum (including the ferroelectric hysteresis loops) were previously thoroughly studied in the well-known KD_2PO_4 and related ferroelectrics [116–121].
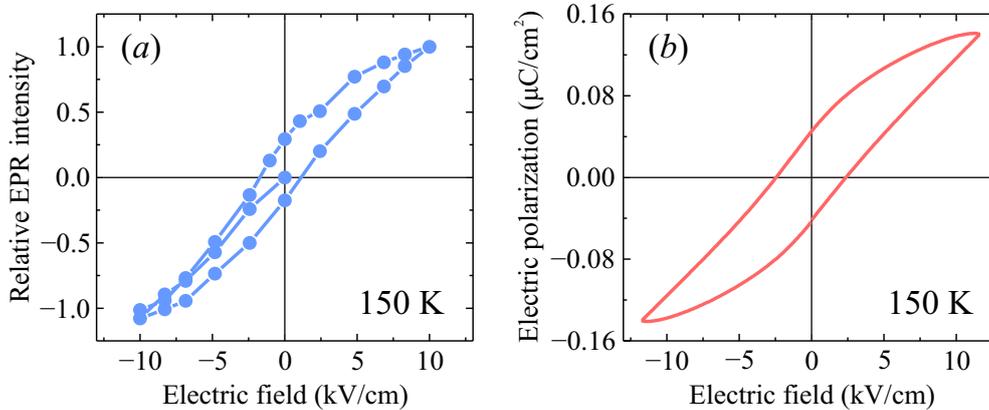

Figure 3.11: (a) Electric field dependence of the CW EPR signal intensity of **AmZn:Mn** at 338.2 mT. (b) Electric polarization hysteresis loop of **AmZn:Mn**. The sample was poled along the c-axis, and the measurements performed at 150 K. The error bars in (a) are smaller than data points.

Summary

The temperature dependence of the X-band CW EPR spectrum of **DMAZn:Mn** single crystal revealed that the Mn^{2+} probes are susceptible to the local structural changes occurring at T_0. The observed unresolved fs of the high-temperature spectrum originates from the hopping motion of the DMA^+ cations. This motion significantly slows down at T_0 providing well-defined fs parameters. The effect of the phase transition on the single crystal EPR spectrum of **DMAZn:Mn** corresponds well with CW EPR results on the powder sample.

A rapid cooling of the sample through the phase transition point provided a spectrum similar to the high-temperature phase. This may indicate a new state of the dimethylammonium formate frameworks characterized by the quenched dynamic disorder of the DMA$^+$ cations.

The angular dependent CW EPR experiments were performed by rotating the single crystal sample of **DMAZn:Mn** around three distinct directions. The simulation of the angular patterns revealed six magnetically inequivalent Mn^{2+} sites in **DMAZn:Mn** independently confirming the crystal twinning model proposed by the XRD study [42].

The origin of the crystalline twins was further investigated by performing single crystal EPR experiments with the simultaneously applied electric field. No reliable spectral differences between the measurements with and without this external stimulus were observed raising serious doubts about the proper ferroelectric origin of DMAZn framework. This result was supported by the electric field dependent electric polarization measurements.

The same type of experiments on Mn^{2+} doped ferroelectric AmZn single crystal provided a clear ferroelectric hysteresis loop of the relative EPR line intensity in agreement with the electric polarization measurements. This result is an independent evidence of the ferroelectric behavior of the ammonium formate framework. It also demonstrates that the single crystal EPR spectroscopy can be used to investigate the polar nature of the low-temperature phases in various hybrid materials. Such microscopic experiments are highly attractive, since the usual measurements of the electric polarization involve difficulties related to the size and conductivity of the sample.

3.1.2   Pulsed EPR of manganese doped DMAZn

The CW EPR methods usually probe only the first coordination sphere of the paramagnetic center, and thus the much weaker hf interactions of the distant nuclei are not resolved in the spectrum. Such interactions can be detected by the more powerful pulsed EPR and pulsed ENDOR spectroscopies [75, 88] (see Section 2.3.9). This allows investigating a much broader spatial region around the paramagnetic Mn^{2+} probe in **DMAZn:Mn**.

The X-band echo-detected field sweep EPR spectra of **DMAZn:Mn** recorded at 170 K and 6 K are presented in Figure 3.12. As expected, they correspond to the powder patterns of the Mn^{2+} ions with the $3d^5$ electron configuration and the high-spin $^6S_{5/2}$ ground state. The 6 K spectrum was simulated using the electron Zeeman, hf and fs parameters of the Mn^{2+} center determined by the CW EPR spectroscopy (see Figure 3.3).
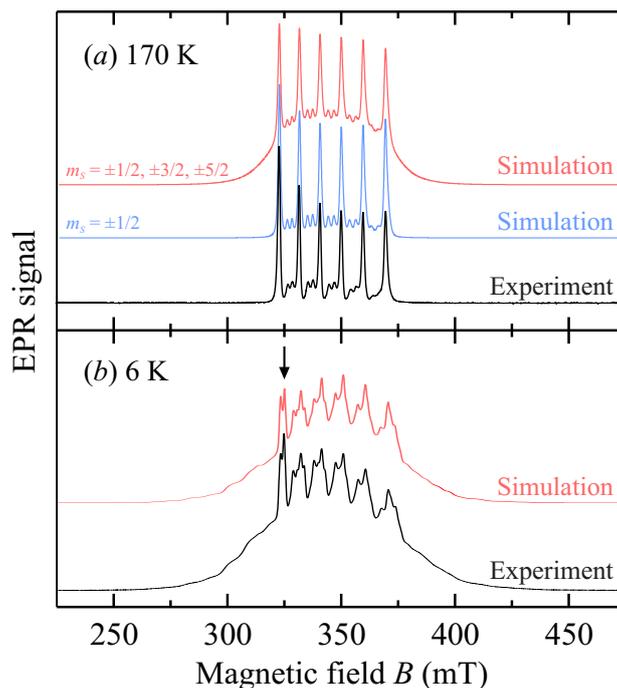

Figure 3.12: X-band 2p echo-detected field sweep spectra of **DMAZn:Mn** recorded at (a) 170 K and (b) 6 K. Simulations indicated in red were obtained by taking into account all fs transitions, while blue simulation corresponds to the central fs transition. The arrow indicates the field position at which most of the pulsed EPR and ENDOR experiments were performed.

An attempt was made to simulate the high-temperature spectrum measured at 170 K using the parameters obtained from the CW EPR experiment. A clear mismatch between the spectra can be seen in Figure 3.12a, since the experimental pattern does not contain broad spectral wings outside the central EPR transition ($m_s = -\frac{1}{2} \leftrightarrow \frac{1}{2}$). As discussed for the CW EPR case, these wings correspond to the fs ($m_s = \pm\frac{3}{2} \leftrightarrow \pm\frac{1}{2}$ and $\pm\frac{5}{2} \leftrightarrow \pm\frac{3}{2}$) which can be described using highly distributed axial zfs parameter. The outer fs transitions are absent in the experimental echo-detected spectrum, while it simultaneously shows the forbidden hf lines indicating a substantial zfs of the Mn^{2+} centers. At first glance, these two

observations contradict each other. A plausible explanation of this discrepancy is that the phase memory time is substantially shorter for the outer fs transitions. Therefore, these transitions cannot be detected in the echo-detected field sweep experiment. This assumption is supported by simulation of only the central fs transition using the same set of the Mn^{2+} ion parameters. The spectrum obtained in such a way is in a perfect agreement with the experiment (Figure 3.12a).

The EPR transition dependent relaxation time was also recently observed in frozen solutions containing Gd^{3+} [122]. This behavior was assigned to the fluctuating (transient) zfs. The energy levels of the outer fs transitions are much more susceptible to these fluctuations resulting in much shorter relaxation compared with the central transition. For the case of **DMAZn:Mn**, such fluctuations occur due to the DMA^+ cation hopping which affects the MnO_6 octahedra.

The hf interactions between the Mn^{2+} ions and distant nuclei are too weak to be resolved in the field sweep EPR spectra. Thus, the ENDOR and ESEEM experiments, which can detect these small interactions, were performed allowing to further study the low-temperature phase of **DMAZn:Mn**. The Mims ENDOR spectroscopy was used to investigate the local environment of the Mn^{2+} probes. Figure 3.13d presents the ^1H ENDOR spectrum of **DMAZn:Mn** recorded at 325 mT, $\tau = 144$ ns and 6 K. It consists of well resolved hf splittings at the perpendicular edge singularities of the powder pattern indicating several proton species in the close vicinity of the Mn^{2+} ions. The splittings corresponding to the parallel components of the ^1H hf coupling tensors are poorly resolved and thus are not explicitly presented.

The obtained ENDOR pattern was simulated using the ^1H hf coupling tensors obtained by the DFT calculations (see Appendix E for more details). The calculated tensors are listed in Table E.1. In the simulations, the spin Hamiltonian parameters of the Mn^{2+} centers determined in the CW EPR experiments were used. First, the simulation was performed by using only the protons from the formate $HCOO^-$ linkers. The corresponding ENDOR pattern is presented in Figure 3.13a indicating that the strongest experimentally observed hf coupling originates from these linkers. The simulation was further improved by including protons from the DMA^+ cations surrounding the Mn^{2+} probe. The simulated pattern is presented in Figure 3.13b revealing a satisfactory agreement with the
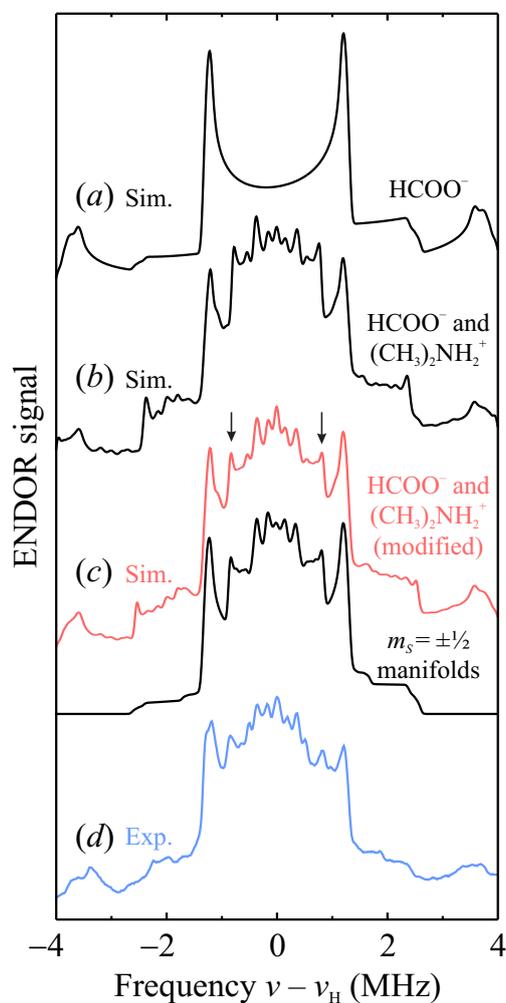
Figure 3.13: (a-c) Simulated and (d) measured (6 K) X-band ^{1}H Mims ENDOR pattern of **DMAZn:Mn** at 325 mT and $\tau = 144$ ns. The simulation in (a) was performed by taking into account only protons from the HCOO$^-$ linkers, while in (b) protons from the DMA$^+$ cations were also included. The ^{1}H hf couplings used in (a) and (b) simulations were obtained from the DFT calculations. The simulation in (c) was performed using slightly adjusted ^{1}H hf couplings of the methyl groups (lines indicated by the arrows). The bottom spectrum in (c) was obtained taking into account only the $m_s = -\frac{1}{2} \leftrightarrow \frac{1}{2}$ transition and neglecting the zfs.

experiment. An even better match was obtained after a slight adjustment of the calculated hf couplings of protons from the methyl groups of the DMA$^+$ cations (see Figure 3.13c). This modification corresponds to a decrease of the Mn-H distance by about 0.08 Å. The small adjustment of the ^{1}H hf couplings could be justified, since the crystal structure of DMAMn [41] framework was determined at 100 K while the ENDOR pattern was recorded at 6 K. Another possible origin of this discrepancy is that the DFT calculations are based on the low-temperature structure of DMAMn compound, while the experiments are performed for the manganese doped DMAZn framework.

The ENDOR spectrum using a spin system with an effective $S = \frac{1}{2}$ electron spin was also simulated to account for only the $m_s = -\frac{1}{2} \leftrightarrow \frac{1}{2}$ transition. The obtained results are presented in Figure 3.13c revealing an absence of the lines at $|\nu - \nu_{\mathrm{H}}| \gtrsim 3\,\mathrm{MHz}$ (here ν_{H} is the Larmor frequency of protons). This indicates that the origin of these lines is not the strongly coupled ^{1}H species, but the nuclear transitions in the $|m_S| > \frac{1}{2}$ spin manifolds. Slight changes of the central part of the spectrum are also observed although the agreement with the experimental pattern remains acceptable.

The comparison between the pulsed ENDOR experiment and the DFT-based simulations confirms the successful incorporation of the Mn^{2+} probes at the Zn^{2+} lattice sites in DMAZn framework. More importantly, the ENDOR data verifies the proton positions determined by the XRD. This confirms the refinement of the low-temperature space group of these frameworks as the monoclinic noncentrosymmetric Cc [41].

The local environment of the Mn^{2+} ions in **DMAZn:Mn** was further probed using 2p and 3p ESEEM spectroscopy. The 2p ESEEM time- and frequency-domain signals recorded at 325 mT and 10 K are presented in Figure 3.14a and c. The time-domain pattern shows superimposed short and long period oscillations. The corresponding frequency spectrum reveals three peaks at about 2.1, 13.8 and 27 MHz. The line at 13.8 MHz corresponds to protons, while the high-frequency bump at roughly $2\nu_{\mathrm{H}}$ is the proton combination peak (refer to Section 2.3.12 for more details) [88].

The 2p ESEEM time-domain signal decays with a relatively short phase memory time resulting in broad and poorly resolved lines in the frequency spectrum. In
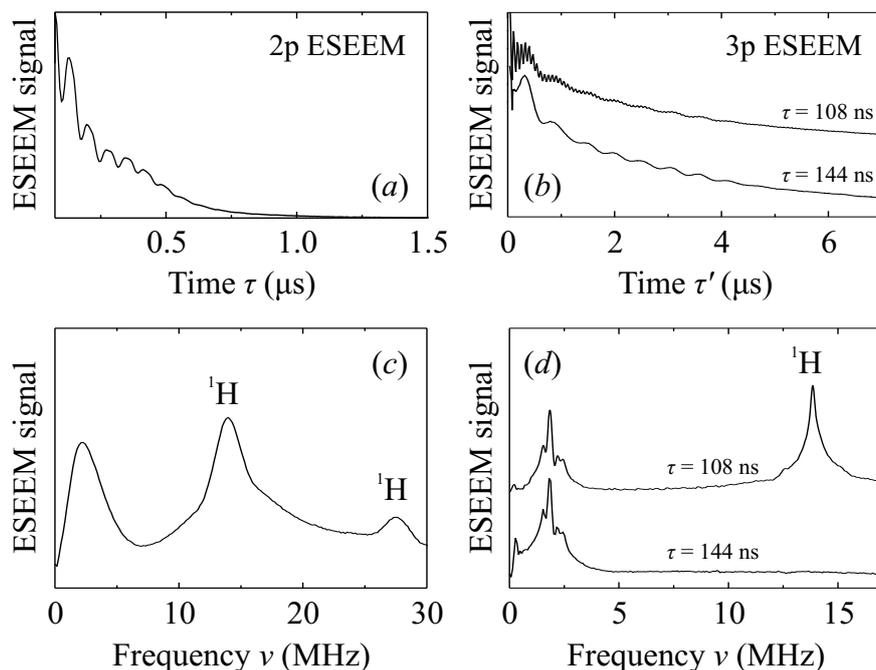
Figure 3.14: X-band 2p and 3p ESEEM (a)-(b) time-domain and (c)-(d) frequency-domain signals of **DMAZn:Mn** recorded at 325 mT and 10 K. The 3p ESEEM experiments were performed at $\tau = 108$ ns and 144 ns. The proton lines are indicated in the frequency spectra.

contrast, the time-domain signal in a 3p ESEEM experiment is limited by the much longer transverse nuclear or longitudinal electron relaxations providing narrower lines (Section 2.3.13) [88]. The 3p ESEEM time-domain traces and frequency spectra obtained at 325 mT and 10 K are presented in Figure 3.14b and d. Measurements were performed using the interpulse delays $\tau = 108$ ns and 144 ns. The obtained ESEEM decay for $\tau = 108$ ns also exhibits superimposed modulations of short and long period oscillations. The corresponding frequency spectrum consists of much narrower lines, although the internal structure of the proton line is still hardly resolved. The width of the proton peak is about 3 MHz which is in agreement with the ^{1}H hf couplings determined by the ENDOR spectroscopy. The low-frequency signal consists of several lines below 3 MHz with the most intense peak at 1.85 MHz. The decay recorded for $\tau = 144$ ns reveals only the long period modulation, since the proton signal is absent due to the suppression effect (blind spot) at the ^{1}H Larmor frequency [88]. The resulting spectrum consists of the same low-frequency signal as obtained for the $\tau = 108$ ns case.

A possible origin of the low-frequency signal could be nitrogen ^{14}N nuclei ($I = 1$) of the DMA$^+$ cations. To investigate this, the 3p ESEEM measurements at X-, Q- and W-band microwave frequencies were performed. The obtained spectra are presented in Figure 3.15. They reveal that the observed signal is independent on the external magnetic field. This surprising result indicates that it cannot originate from nitrogen nuclei, since one would expect a significant nuclear Zeeman effect for a system with nuclear spin $I > 0$. In addition, the identical signal was obtained for **DMAZn:Mn-15N** sample containing ^{15}N isotope ($I = \frac{1}{2}$) (Figure C.5 in Appendix C) completely ruling out the possibility that the origin of this signal is nitrogen.
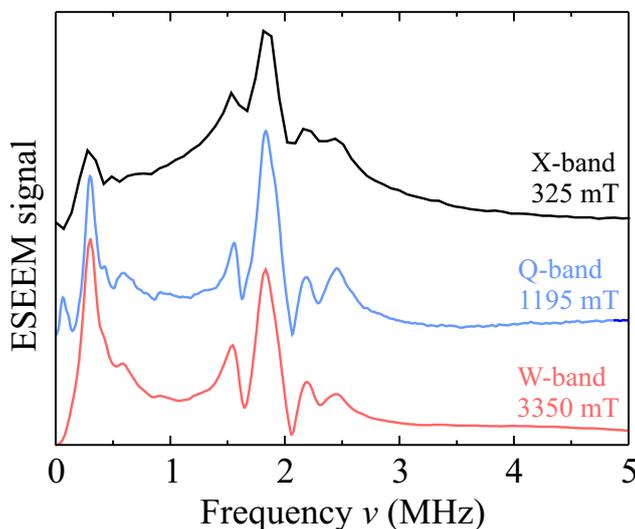

Figure 3.15: Low-frequency 3p ESEEM signal of **DMAZn:Mn** recorded at 325 (X-band), 1195 (Q-band), 3350 mT (W-band) and 10 K.

Several NMR studies revealed that the motion of the DMA$^+$ cations persists in the ordered phase of DMAZn [48, 54, 55]. Thus, the ESEEM experiments at different temperatures were performed to check whether one can observe the influence of these motional effects on the echo modulation. The temperature dependent 2p and 3p ESEEM spectra are presented in Figure 3.16 (see Figure C.6 for the time-domain traces) indicating that the low-frequency signal starts to diminish above 40 K and completely disappears at about 70 K. Figure 3.17 reveals the temperature dependence of the modulation depth parameter k of this signal, which was determined from the 3p ESEEM time-domain traces at 400 ns (see inset for the definition of k). A sudden decrease of the modulation

depth is observed above 40 K, while $k = 0$ above 70 K. Note that Besara *et al.* [54] observed a glassy behavior in DMAZn below 40 K, while Asaji *et al.* [55] reported a small anomaly in the spin-lattice relaxation time of ^{1}H at 79 K.
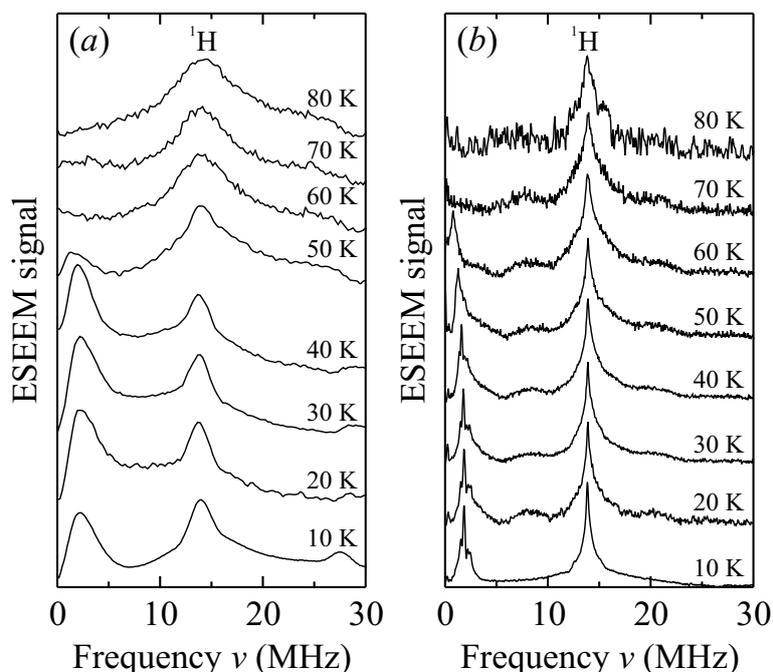

Figure 3.16: Temperature dependent X-band (a) 2p and (b) 3p ESEEM frequency spectra of **DMAZn:Mn** recorded at 325 mT. 3p ESEEM experiments performed at $\tau = 108$ ns. Spectra are normalized to the proton line.

The hopping motion of the DMA$^+$ cation should be frozen on the ESEEM time scale below T_0 as demonstrated by the dielectric (Appendix D) [52] and NMR [48, 55] spectroscopies. However, the reorientation of the methyl groups around the C$_3$ symmetry axes is still expected in the ordered phase [55]. As determined by the NMR, the characteristic time of this motion is about 10^{-7} s at 70 K [54, 55]. The highest peak of the low-frequency ESEEM signal is roughly at 2 MHz which is in a good agreement with the time scale of the methyl group rotation. Thus, it can be speculated that the decrease of the modulation depth of the low-frequency signal is related to the averaging of some anisotropic magnetic interactions due to the onset of the methyl group dynamics.

The measurements of the phase memory time T_m and the longitudinal relaxation time T_1 of the Mn^{2+} centers were also performed to further investigate the low-temperature phase of **DMAZn:Mn**. Figure 3.18a reveals a monotonous decrease
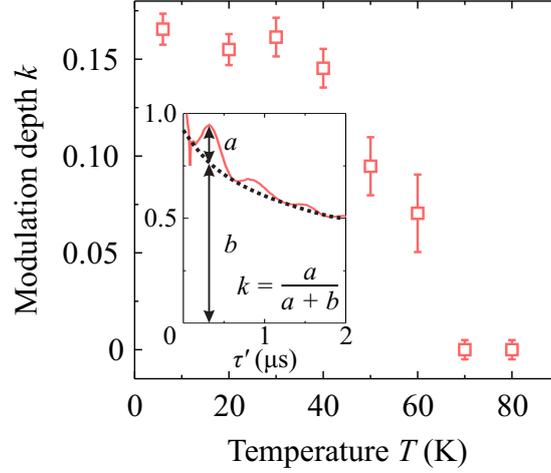
Figure 3.17: Temperature dependence of the modulation depth k of the low-frequency X-band 3p ESEEM signal of **DMAZn:Mn**. The definition of the parameter k is given in the inset.

of T_m with increasing temperature. The relaxation time starts to diminish at about the same temperature as the modulation depth of the low-frequency ESEEM signal. Thus, the decrease of T_m can be related to the methyl group rotations that cause fluctuations of the Mn^{2+} ion magnetic environment. The phase memory time at the phase transition point exhibits anomalous behavior which is related to the critical dynamics of the order parameter fluctuations or enhanced motion of the DMA^+ cations above T_0 (see Figure C.7). The anomaly of T_m was previously observed in trissarcosine calcium chloride [108], $KH_3(SeO_3)_2$ [123] and similar materials. This anomaly is related to the anomalous behavior of the CW EPR linewidth of **DMAZn:Mn** (see Figure 3.5). Note that a reliable measurement of T_m above 180 K was not possible due to too fast relaxation.

The phase memory relaxation rate exhibits the Arrhenius behavior and can be described using the following equation:

$$T_m^{-1} = T_{m,\infty}^{-1} e^{-E_a/k_B T},\tag{3.3}$$

where E_a denotes the activation energy of the motional process and $T_{m,\infty}^{-1}$ is the phase memory relaxation rate at infinite temperature. In the low-temperature phase, two processes were identified with activation energies $E_a = 17(1)$ and $E_a = 5.8(4)$ meV. The inset in Figure 3.18a presents the corresponding fits. A
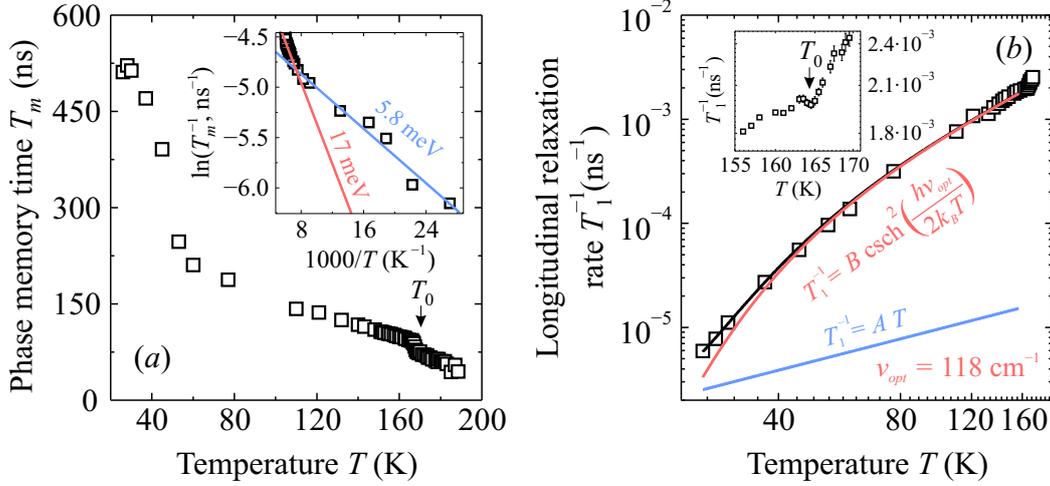
Figure 3.18: Temperature dependence of the phase memory time and the longitudinal relaxation rate of the Mn^{2+} centers in **DMAZn:Mn**. The inset in (a) shows the Arrhenius behavior of T_m^{-1} below T_0. The curves in (b) are the total (black) and separate (blue and red) contributions to the longitudinal relaxation rate. The inset in (b) emphasizes the behavior of the longitudinal relaxation rate about T_0. If not indicated, the error bars are smaller than data points. Measurements performed at 325 mT and X-band frequency.

third process was also observed in the high-temperature phase with an activation energy of about 78 meV (see Figure C.7). The obtained activation energy in this phase is similar to the values obtained by NMR for the methyl group rotations in DMAZn framework [48, 54, 55]. However, the energies of the low-temperature phase are significantly smaller. Such activation energies are frequently observed for quantum tunnelling motion of the protons from the methyl groups [124]. This may indicate a substantial contribution of such process to the observed low-temperature phase memory relaxation in **DMAZn:Mn**.

The longitudinal relaxation time T_1 was determined by the inversion recovery pulse sequence [88]. The measured magnetization kinetics were fit using a recovery function for the continuously distributed relaxation times (see Ref. [125] for more details). The obtained temperature dependence of the most probable longitudinal relaxation rate T_1^{-1} is presented in Figure 3.18b. The experimental data was approximated using the following equation [123]:

$$T_1^{-1} = AT + B\mathrm{csch}^2(h\nu_{opt}/2k_BT), \tag{3.4}$$

where the first term describes a direct (one-phonon) relaxation process with the acoustic lattice phonons. The second term takes into account a Raman (two-phonon) process which involves the optical phonon branch of frequency ν_{opt}. A and B are constants. The best fit provided $\nu_{opt} = 3.5(3) \times 10^{12}$ Hz which corresponds to $118(10)$ cm^{-1}. Note that IR and Raman study reports a similar frequency of the lattice phonons that involve metal-oxygen octahedra in DMAZn and DMAFe frameworks [51]. A combined *ab initio* lattice dynamics and molecular dynamics study also revealed strong metal-formate phonon bands below 500 cm^{-1} for the related formate frameworks [126].

The behavior of the longitudinal relaxation rate around the phase transition point is presented in the inset of Figure 3.18b. A small dip of T_1^{-1} is observed at T_0, which was verified by several measurements. Such a minimum of the longitudinal relaxation rate at the phase transition was detected for many other ferroelectric or related compounds such as rochelle salt [125], $KH_3(SeO_3)_2$ [123], betaine phosphite [127], trissarcosine calcium chloride [128], triglycine sulfate [129] and lead titanate [130]. A minimum of T_1^{-1} occurs due to the enhanced damping of the optical phonon mode ν_{opt} which governs the longitudinal relaxation. The observed increase of the mode damping may originate from the coupling with the relaxational mode responsible for the phase transition [125] or due to the structural changes occurring at T_0.

Summary

The echo-detected field sweep EPR spectra of Mn^{2+} centers were recorded for the both structural phases of **DMAZn:Mn** framework. The low-temperature spectrum was simulated using the spin Hamiltonian parameters taken from the CW EPR analysis. The high-temperature phase spectrum revealed much faster phase memory relaxation of the outer fs transitions. This behavior was assigned to the fluctuating zfs of the Mn^{2+} ions in the high-temperature phase of the framework. These fluctuations are caused by the hopping motion of the DMA^+ cations confirming a tight interaction between the two subsystems of the material.

The X-band ^{1}H Mims ENDOR spectrum displayed several proton species in the

vicinity of the Mn^{2+} probes. The experimental spectrum was simulated using the proton hf coupling tensors obtained by the DFT calculations. A good agreement between the experimental and simulated ENDOR patterns verifies the structural framework model and the proton positions that are often difficult to determine accurately by the XRD methods.

The ESEEM spectroscopy revealed a signal of weakly coupled protons in agreement with the ENDOR results. A remarkable low-frequency ESEEM signal which is unaffected by the external magnetic field was also observed. The modulation depth of this signal starts to decrease above 40 K and reaches zero at 70 K. This temperature range and the frequency of the signal suggest that the modulation disappears due to the rotations of the methyl groups of the DMA^+ cations.

The relaxation time measurements of the Mn^{2+} ions revealed further information about the motion of the DMA^+ cations and the dynamics of the metal-formate lattice. A monotonous decrease with increasing temperature of the phase memory time was observed in the ordered phase of the framework. This behavior was assigned to the methyl group motion which causes fluctuations of the local Mn^{2+} ion environment. Two motional mechanisms were identified in the low-temperature phase with the activation energies of 17(1) meV and 5.8(4) meV. Such activation energies are frequently observed for quantum tunnelling motion of the protons from the methyl groups. A third process with higher activation energy was observed in the high-temperature phase.

The longitudinal relaxation of the Mn^{2+} ions is dominated by the direct process with the acoustic lattice phonons and the two-phonon Raman process with the optical lattice mode of 118(10) cm^{-1} frequency. A small anomalous dip of the longitudinal relaxation rate at T_0 was observed and assigned to the increased damping of the hard optical mode governing the relaxation.

3.1.3 CW EPR of copper doped DMAZn

The CW EPR spectroscopy was further used to study the structural phase transition and dynamic effects of DMAZn framework doped with paramagnetic copper ions. The X-, Q- and W-band CW EPR spectra of DMAZn doped with 1

Cu^{2+} mol% (**DMAZn:Cu**) recorded at 140 K (low-temperature phase) are presented in Figure 3.19. The spectra are typical anisotropic EPR powder patterns of the Cu^{2+} ions in an axially symmetric environment (refer to Figure 2.14 for more details). Each Cu^{2+} ion has a $3d^9$ electron configuration and thus possesses a single unpaired electron with spin $S = \frac{1}{2}$. The spectra display four resolved hf lines at lower magnetic field values that originate from the interaction between the unpaired electron and copper nucleus (both abundant ^{63}Cu and ^{65}Cu isotopes have nuclear spin $I = \frac{3}{2}$).
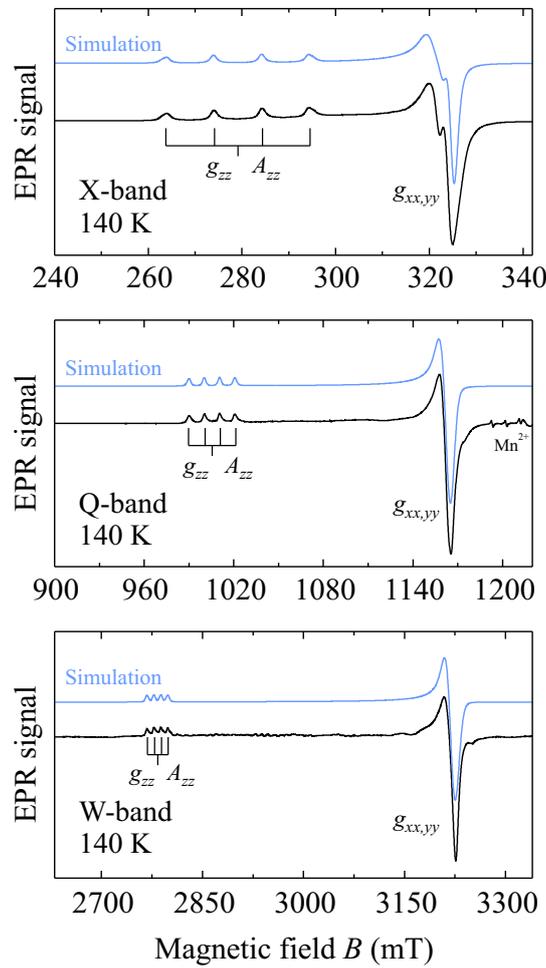
Figure 3.19: X-, Q- and W-band CW EPR spectra of the Cu^{2+} ions in **DMAZn:Cu** recorded at 140 K (low-temperature phase). The corresponding spectral simulations are indicated in blue.

The experimental spectra were simulated using the following spin Hamiltonian

[79]:

$$\mathcal{H} = \beta_e \boldsymbol{B}\boldsymbol{g}\boldsymbol{S} + \boldsymbol{S}\boldsymbol{A}\boldsymbol{I}, \tag{3.5}$$

where the first term describes the electron Zeeman interaction characterized by the $\boldsymbol{g}$-tensor of the Cu^{2+} center. The second term takes into account the hf interaction between the unpaired electron spin and the nuclear spin of the copper ^{63}Cu or ^{65}Cu nucleus. This interaction is described by the hf tensor $\boldsymbol{A}$. $\boldsymbol{B}$ and β_e denote the external magnetic field and Bohr magneton, respectively.

The spectra of the low-temperature phase can be well simulated using axially symmetric and collinear $\boldsymbol{g}$- and $\boldsymbol{A}$ tensors with the following components: $g_{xx,yy} = 2.086(3)$, $g_{zz} = 2.410(1)$, $A_{xx,yy} = 36(10)$ MHz and $A_{zz} = 341(1)$ MHz. Here the principal values of the hf interaction tensor refer to those of the ^{63}Cu isotope. The uncertainty of $A_{xx,yy}$ components is rather high due to the unresolved hf lines in the $g_{xx,yy}$ spectral region. The same set of the spin Hamiltonian parameters was used for the multifrequency simulation of the EPR spectra. Such values of g_{zz} and A_{zz} parameters are frequently observed for the Cu^{2+} ions in an axially elongated symmetry [131, 132] indicating that copper centers successfully replaced zinc in the lattice and formed CuO_6 octahedra [133]. Note that traces of the incorporated Mn^{2+} impurities were also detected in **DMAZn:Cu** (lines at about 1200 mT in the Q-band spectrum).

The multifrequency CW EPR spectra of **DMAZn:Cu** obtained at 270 K (high-temperature phase) are presented in Figure 3.20. The shape of the powder patterns at this temperature may imply an orthorhombic Cu^{2+} $\boldsymbol{g}$-tensor ($g_{xx} \neq g_{yy}$). However, such distortion of the CuO_6 octahedra is improbable as the high-temperature phase is expected to be more symmetric compared to the low-temperature phase where the axial symmetry of the $\boldsymbol{g}$-tensor is observed. Thus, it is more likely that the measured spectra consist of the superimposed axially symmetric and additional broad background patterns.

The temperature evolution of the X- and Q-band CW EPR spectra of **DMAZn:Cu** is presented in Figure 3.21 and 3.22, respectively (see Figure C.8 in Appendix C for the W-band spectra). The broad background line diminishes with decreasing temperature, while the spectra gradually transform to the axially symmetric powder patterns below T_0. As the temperature is lowered, the intensity of the resolved hf lines increases much faster than expected for the Curie law behavior.
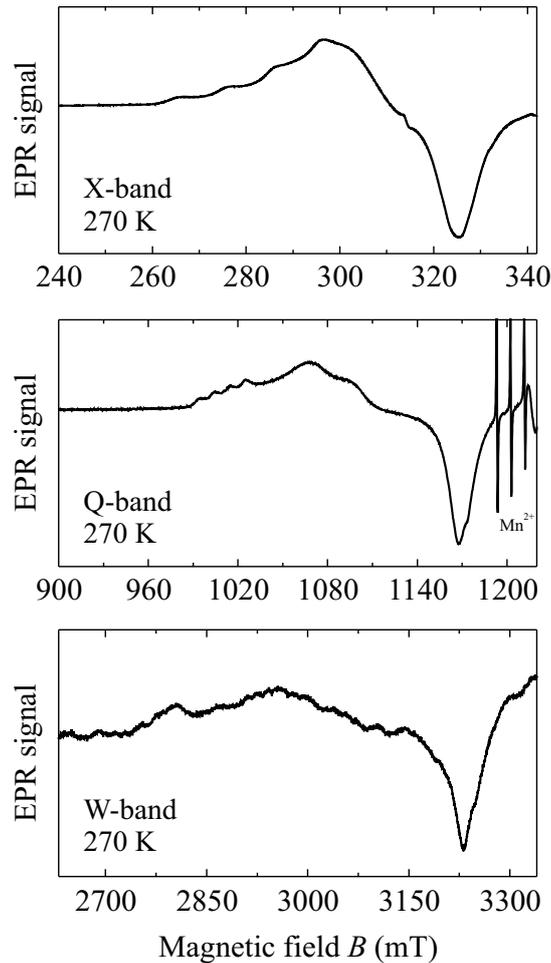
Figure 3.20: X-, Q- and W-band CW EPR spectra of the Cu^{2+} ions in **DMAZn:Cu** measured at 270 K (high-temperature phase). The sharp EPR lines at about 1200 mT in the Q-band spectrum originate from the incorporated Mn^{2+} ions.

This indicates that the spectral intensity of the broad line is transferred to the resolved axially symmetric pattern.

A similar shape of the powder pattern could also originate from substantial dynamic effects that average the *g*-tensor anisotropy producing a broad line situated in between the g_{zz} and $g_{xx,yy}$ spectral regions. However, such effects should first average out the much weaker hf interaction, while in this case the spectra still display the well resolved hf lines in the g_{zz} spectral region. A possible explanation of this behavior could be that the observed high-temperature spectra originate from the Cu^{2+} ions experiencing broad distribution of the character-

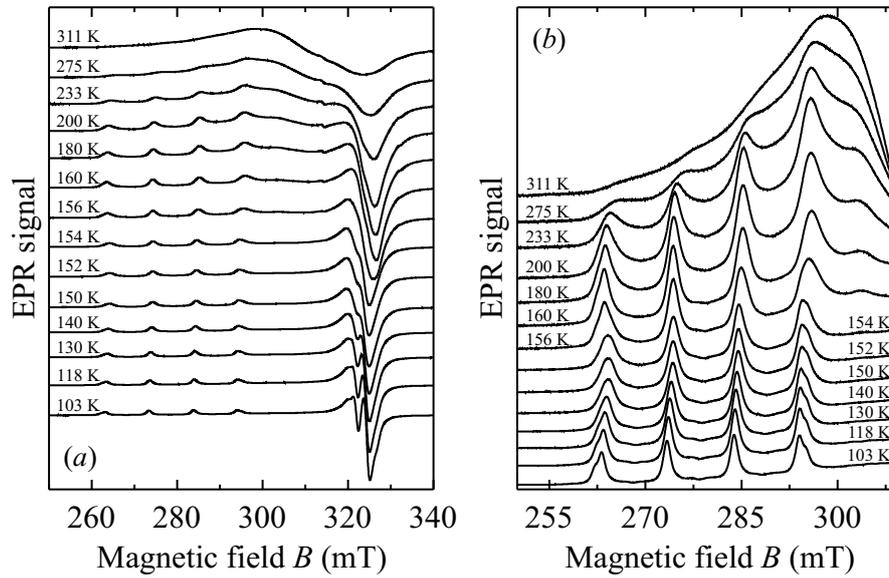Figure 3.21: (a) Normalized temperature dependent X-band CW EPR spectra of the Cu^{2+} ions in **DMAZn:Cu**. The g_{zz}-part of the spectra is illustrated in (b).
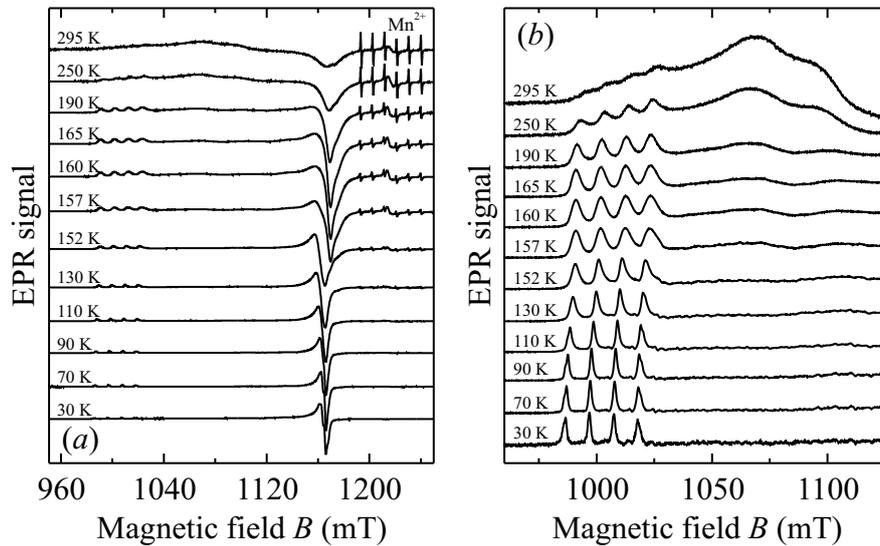

Figure 3.22: (a) Normalized temperature dependent Q-band CW EPR spectra of the Cu^{2+} ions in **DMAZn:Cu**. The g_{zz}-part of the spectra is illustrated in (b).

89

istic motional times. The ions experiencing slow dynamics provide resolved axially symmetric powder pattern, while ions in the intermediate motion regime contribute to the broad background line. Note that the broad spectral line seems to occur at slightly lower temperatures at X-band frequency compared to the Q-band case. This is in agreement with a thermally excited motional process, as a faster motion (higher temperature) is needed to average the Q-band spectrum.

Such distribution of the dynamics may be expected in **DMAZn:Cu**. In the lattice regions with higher copper concentration, the dynamics of the DMA$^+$ cations would be suppressed due to the Jahn-Teller distortion of the CuO_6 octahedra. Note that the DMA$^+$ cations are ordered and do not exhibit hopping in DMACu framework [133, 134]. A slower cation motion would result in a longer characteristic deformation time of the CuO_6 octahedra providing an axially symmetric powder spectrum. In contrast, regions containing lower copper concentration would provide faster dynamics, since the hopping motion of the neighboring DMA$^+$ cations would be less affected. As the temperature is decreased, the dynamics slows down and the spectrum gradually transforms to the slow-motional regime. In the low-temperature phase, all CuO_6 octahedra are equally axially distorted due to the uniformly ordered DMA$^+$ cations.

It should be noted that the averaging of the spectral anisotropy into a broad line in the high-temperature phase is likely caused by the interplay between the DMA$^+$ hopping and the dynamic Jahn-Teller distortion. The rotating DMA$^+$ cation constantly reestablishes H-bonds with the oxygen atoms of the CuO_6 octahedra (see Figure 3.23). This results in a constantly changing energy landscape (warped Mexican-hat potential [135]) of the dynamic Jahn-Teller effect. As temperature is lowered, the hopping frequency decreases together with the Jahn-Teller dynamics, causing transfer of the spectral intensity to the axially symmetric Cu^{2+} species.

The X-band CW EPR measurements for DMAZn doped with 0.1, 2, 5 and 10 mol% of Cu^{2+} were also performed. The obtained temperature dependent spectra are presented in Figures 3.24 and 3.25. The powder patterns of the 0.1, 1 (**DMAZn:Cu**) and 2 mol% samples are very similar at room temperature despite a dipolar broadening of the resolved Cu^{2+} hf lines for higher copper concentration. The hf lines are barely visible in the 5 mol% powder, while
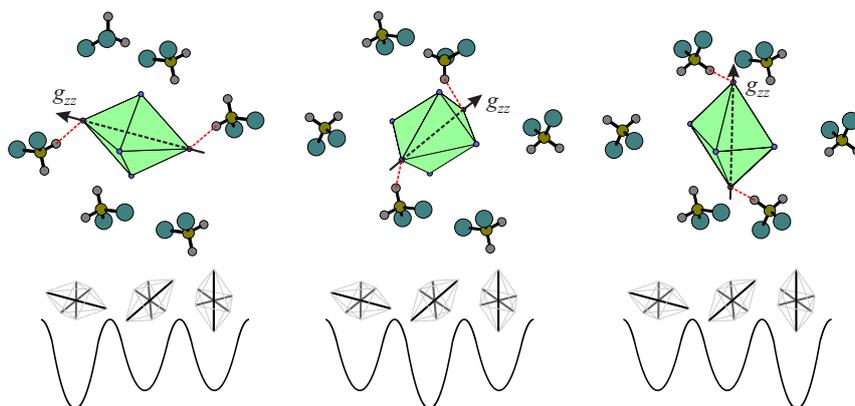
Figure 3.23: Examples of the DMA$^+$ cation arrangement around the Cu^{2+} center in **DMAZn:Cu**. The corresponding schematic energy landscapes of the dynamic Jahn-Teller distortion are presented below. In the high-temperature phase, the hopping of the DMA$^+$ cations is constantly changing the asymmetry of the potential wells. Without the crystal field, the potential wells would be symmetric. The H-bonds are indicated in red. Some hydrogen atoms of the cations are omitted for clarity.

they are completely absent for the 10 mol% case. The spectra of 0.1 and 1 (**DMAZn:Cu**) mol% recorded at 120 K (low-temperature phase) are almost the same. However, for higher doping, an additional broad line is observed even in the low-temperature phase. For the 10 mol% case, the spectrum consists only of this line, and the resolved axially symmetric pattern is completely absent. A close inspection of this line reveals the characteristic shape of a signal of an $S = \frac{1}{2}$ center with orthorhombic *g*-tensor and unresolved hf interactions. Figure 3.25 shows simulation of the line using the *g*-tensor for the exchange coupled Cu^{2+} ions in DMACu (corresponding to 100 mol% doping) as determined by Wang *et. al.* by high-frequency CW EPR study [136]. A perfect agreement between the experiment and simulation demonstrates that for higher level of doping regions of very high Cu^{2+} ion concentration are formed. This indicates that the Cu^{2+} probes in DMAZn tend to disperse inhomogeneously. This observation supports the idea that the characteristic time of the Cu^{2+} center dynamics has a broad distribution which is related to the regions of different ion concentration.

One cannot rule out that the origin of the broad spectral line detected in the high-temperature phase of **DMAZn:Cu** could be also related to the Cu$-$Cu exchange interaction which was detected in the low-temperature phase of sample
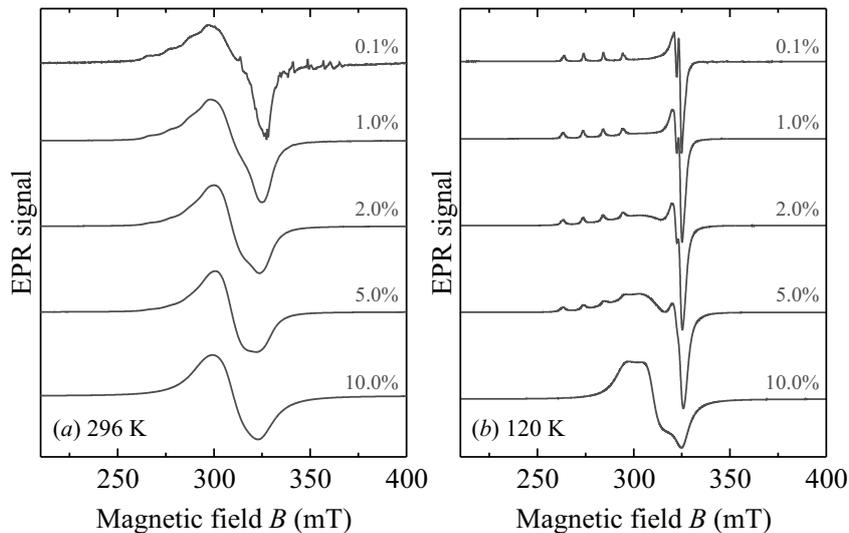
Figure 3.24: Normalized X-band CW EPR spectra of DMAZn framework doped with different amount of Cu^{2+} ions. Spectra recorded at (a) 296 and (b) 120 K.
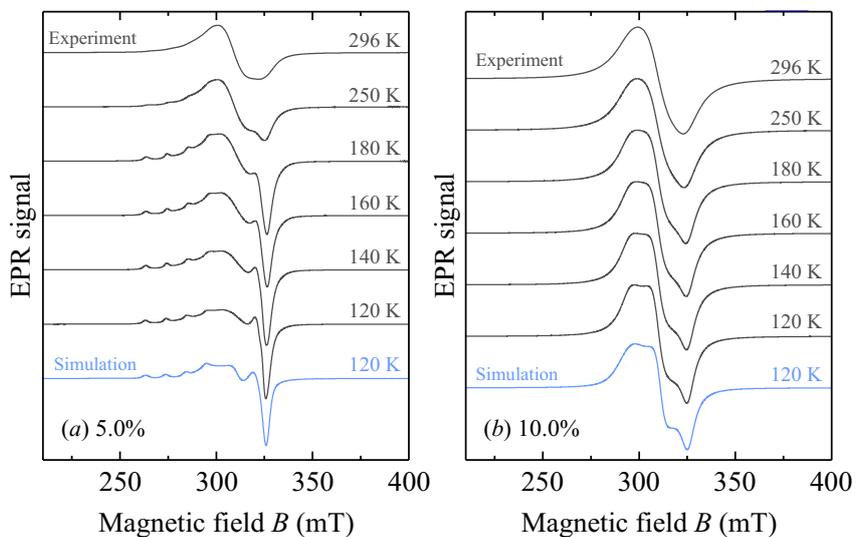

Figure 3.25: Normalized temperature dependent X-band CW EPR spectra of DMAZn doped with (a) 5 mol% and (b) 10 mol% of Cu^{2+}. Simulated 120 K spectra are indicated in blue. The simulation in (a) was performed using two species representing isolated and exchange coupled Cu^{2+} ions with the following spin Hamiltonian parameters: $\boldsymbol{g} = [2.085, 2.085, 2.413]$, $\boldsymbol{A} = [36, 36, 345]$ MHz and $\boldsymbol{g}_{ex} = [2.078, 2.175, 2.290]$ [136]. The simulation in (b) was performed using only the $\boldsymbol{g}_{ex}$-tensor of the exchange coupled Cu^{2+} ions.

doped with 10 mol%. For low doping levels, this interaction would have to be temperature dependent in the high-temperature phase and absent in the low-temperature phase making this scenario less likely. In addition, a strong dipolar coupling between the Cu^{2+} ions would be expected in the low-temperature phase, while the spectra do not indicate any dipolar splittings or strong dipolar broadening.

It was also investigated how the CW EPR peak-to-peak linewidth Γ of the resolved axially symmetric Cu^{2+} species is affected by the temperature and phase transition. The linewidth decreases with the decreasing temperature in both the high-temperature and low-temperature phases, while an anomalous increase at $T_0 = 154$ K is observed (see Figure 3.26). The linewidth in the high-temperature phase follows the Arrhenius law: $\Gamma - \Gamma_0 = \Gamma_\infty e^{-E_a/k_B T}$. Here E_a is the activation energy of a dynamic process, Γ_0 and Γ_∞ denote the linewidth in the low and high temperature limits, respectively. The analysis provides $E_a = 0.16(1)$ eV (see inset in Figure 3.26) which is rather close to the value of 0.21 eV determined by the CW EPR for the hopping of the DMA^+ cations in **DMAZn:Mn**. Thus, the broadening of the well resolved Cu^{2+} signal with increasing temperature may be related to the enhanced DMA^+ cation motion, as it is directly coupled with the CuO_6 octahedra via the H-bonds. The smaller E_a value obtained here may originate from the combined effect of the DMA^+ motion and the dynamic Jahn-Teller distortion.

The observed linewidth anomaly at T_0 demonstrates that the Cu^{2+} ions are also sensitive to the structural phase transition in **DMAZn:Cu**. A similar anomaly was observed for **DMAZn:Mn** as indicated in Figure 3.5. It is also likely caused by the critical dynamics of the order parameter fluctuations. This behavior is encountered while studying structural phase transitions in ferroelectric and related materials such as triglycine sulfate [107], trissarcosine calcium chloride [109] and $SrTiO_3$ [110].

The EPR spectrum of the Cu^{2+} ions in **DMAZn:Cu** exhibits a sudden change at T_0 which is visible in both g_{zz} and $g_{xx,yy}$ spectral regions (see Figures 3.21 and 3.22). This indicates that not only the linewidth, but also the spin Hamiltonian parameters of the Cu^{2+} ions are affected by the phase transition. The temperature dependent $g_{xx,yy}$, g_{zz} and A_{zz} tensor components are presented in Figure 3.27. A
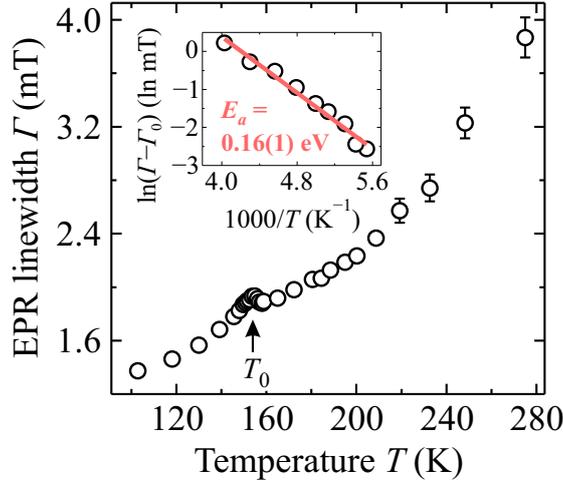
93

Figure 3.26: Temperature dependence of the X-band CW EPR linewidth of the Cu^{2+} centers in **DMAZn:Cu**. The linewidth was determined from the hf transitions in the g_{zz} field region. The Arrhenius analysis of the linewidth in the high-temperature phase is presented in the inset.

clear sharp jumps of these parameters are observed at T_0. This finding indicates that the Cu^{2+} ion probes in **DMAZn:Cu** also detect a strong first-order structural phase transition in agreement with the Mn^{2+} CW EPR study of **DMAZn:Mn**. The observed increase of g_{zz} and decrease of A_{zz} at T_0 reveals that the CuO_6 octahedra become less axially distorted during the phase transition on cooling [132]. The overall temperature dependence of all three parameters outside the T_0 region is typical for the dynamic Jahn-Teller effect [137].

Summary

The temperature dependent Cu^{2+} ion environment in **DMAZn:Cu** was probed using a multifrequency CW EPR approach. The high-temperature phase X-, Q- and W-band CW EPR spectra revealed a well resolved axially symmetric powder pattern superimposed with a broad spectral line. The origin of such a spectrum may be assigned to a distribution of the characteristic times of the Cu^{2+} ion dynamics. The corresponding spectra of the low-temperature phase indicated that the Cu^{2+} ions are exclusively present in an axially symmetric coordination environment. The *g*- and hf tensor components revealed an elongated octahedral coordination confirming the successful incorporation of the Cu^{2+} ions at the zinc
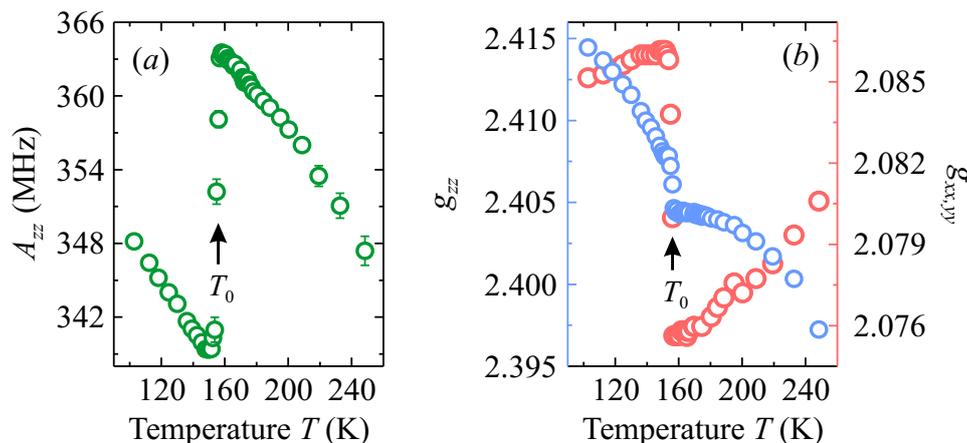
Figure 3.27: Temperature dependence of (a) A_{zz} and (b) g_{zz} (blue), $g_{xx,yy}$ (red) parameters of the Cu^{2+} ions in **DMAZn:Cu**. The error bars are smaller than data points, if not explicitly indicated.

lattice sites. Magnetic interactions among these ions seem to be negligible and they consequently appear to be well dispersed over the zinc lattice sites because of their well resolved EPR powder pattern.

The distributed dynamics of the Cu^{2+} ions may originate from crystal regions with different copper concentration. The measurements of DMAZn doped with higher amounts of Cu^{2+} revealed a substantial magnetic exchange interactions among the paramagnetic ions. For 10 mol% doping level, the axially symmetric powder pattern with a resolved Cu^{2+} hf interaction was not visible anymore but an exchange narrowed orthorhombic spectrum without the hf splitting developed. This indicates that the majority of the Cu^{2+} centers participate in the exchange process. These observations confirmed an inhomogeneous distribution of the copper centers in DMAZn.

The CW EPR linewidth of the Cu^{2+} spectrum with resolved hf interaction decreases with decreasing temperature. The temperature dependent linewidth in the high-temperature phase exhibits the Arrhenius behavior with the activation energy of 0.16 eV. The obtained value was assigned to the combined effect of the DMA^+ cation motion and dynamic Jahn-Teller distortion. The linewidth exhibits anomalous behavior at T_0 which is attributed to the critical dynamics of the order parameter fluctuations.

The temperature dependence of the Cu^{2+} **g**- and hf tensors revealed sudden

jumps at the phase transition temperature indicating a strong character of the first-order phase transition. The overall temperature dependence of tensor components outside the phase transition region was assigned to the dynamic Jahn-Teller effect.

3.1.4 Pulsed EPR of copper doped DMAZn

The pulsed EPR and ENDOR techniques were used to investigate the local environment of the Cu^{2+} ions in the low-temperature phase of **DMAZn:Cu**. The echo-detected field sweep X-band EPR spectrum of **DMAZn:Cu** recorded at 40 K is presented in Figure 3.28. The calculated derivative of the spectrum is in a good agreement with the CW EPR results.
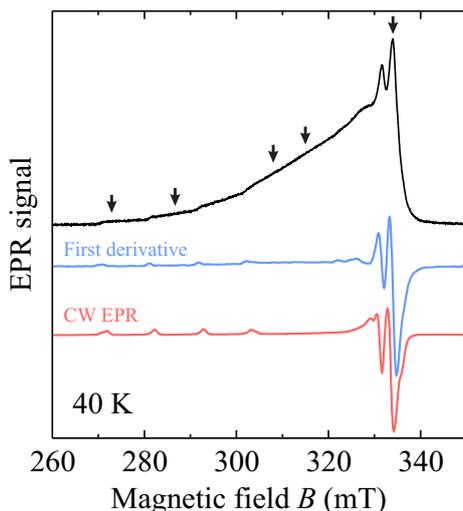

Figure 3.28: 2p echo-detected field sweep EPR spectrum of Cu^{2+} centers in **DMAZn:Cu** obtained at 40 K. The arrows indicate magnetic field values of ENDOR experiments.

The hf interactions between the unpaired electrons and distant protons are too weak to be resolved in the field sweep EPR spectrum. However, these interactions can be usually observed using the ESEEM and ENDOR spectroscopies. The [1]H Mims ENDOR spectra of **DMAZn:Cu** recorded at 10 K are presented in Figure 3.29. Measurements were performed at different magnetic field values (indicated in Figure 3.28) to account for the orientation selectivity [75]. The obtained spectra indicate well resolved hf splittings at the perpendicular edge

singularities of the ^{1}H ENDOR powder patterns. Several ^{1}H species in the vicinity of the Cu^{2+} ion can be identified with the largest splitting of about 2.3 MHz. The spectrum recorded at 287.6 mT also shows rather well resolved parallel edge singularities with the splitting of about 4.6 MHz. A small signal with a splitting of about 6 MHz can also be observed. The DFT calculations revealed that the strongest hf coupling of 4.2 MHz occurs for a proton from the formate linker with the $Cu-{}^{1}H$ distance of 3.35 Å (see Table E.2 in Appendix E for more details). Note that the DFT structural optimization was performed for a rather small cluster due to many atoms in the unit cell of DMAZn. This may be the reason for a discrepancy between the calculated and measured hf couplings.
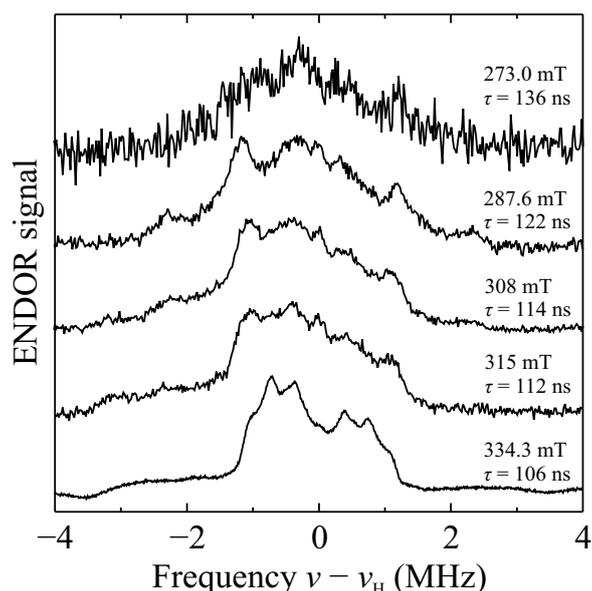

Figure 3.29: [1]H Mims ENDOR spectra of **DMAZn:Cu** recorded at 10 K and different magnetic fields. The values of the interpulse delay τ were selected to avoid suppression of the signals at the proton Larmor frequency ν_H.

The 3p ESEEM spectroscopy was also employed to probe the Cu^{2+} ion environment. A single structureless peak was observed in the spectrum at the proton Larmor frequency indicating weakly coupled protons in the vicinity of the copper centers. The width of the peak is about 4 MHz in agreement with the [1]H Mims ENDOR results.

97

Summary

The X-band Mims ENDOR spectroscopy revealed several proton species in the vicinity of the Cu^{2+} ions in the low-temperature phase of **DMAZn:Cu**. The determined range of the ${}^1H$ hf couplings was found to be in a reasonable agreement with the DFT calculations based on the XRD model of DMAZn. This confirmed the successful incorporation of the Cu^{2+} ions at zinc lattice sites in DMAZn framework. The ESEEM spectrum demonstrated a single line of weakly coupled protons in agreement with the ENDOR spectroscopy.

3.2 EPR Spectroscopy of MHyZn

In this Section, the CW and pulsed EPR spectroscopy results of the Mn^{2+} and Cu^{2+} doped MHyZn frameworks (samples **MHyZn:Mn** and **MHyZn:Cu**) are presented [138]. A pure MHyZn framework exhibits two structural phase transition (see Section 2.2.2 for more details). Some EPR results are supported by the pyrocurrent, dielectric permittivity and electric polarization measurements of a pure MHyZn single crystal (sample **MHyZn**). A detailed description of the samples synthesis is presented in Appendix A. The experimental EPR details are given in Appendix B.

3.2.1 CW EPR of manganese doped MHyZn

The X- and Q-band CW EPR spectra of **MHyZn:Mn** powder sample recorded at 140 K are presented in Figure 3.30a and b. The observed spectra are typical powder patterns of the Mn^{2+} ions in the $3d^5$ electron configuration (${}^6S_{5/2}$ electron ground state) [79]. The observed spectra are dominated by the six hf lines of the central fs transition, while the outer transitions have much lower intensity (see Figure 2.15 for more details).

The spectra is described using the spin Hamiltonian [79]:

$$\mathcal{H} = \beta_e \boldsymbol{BgS} + \boldsymbol{SAI} + \boldsymbol{SDS}. \tag{3.6}$$
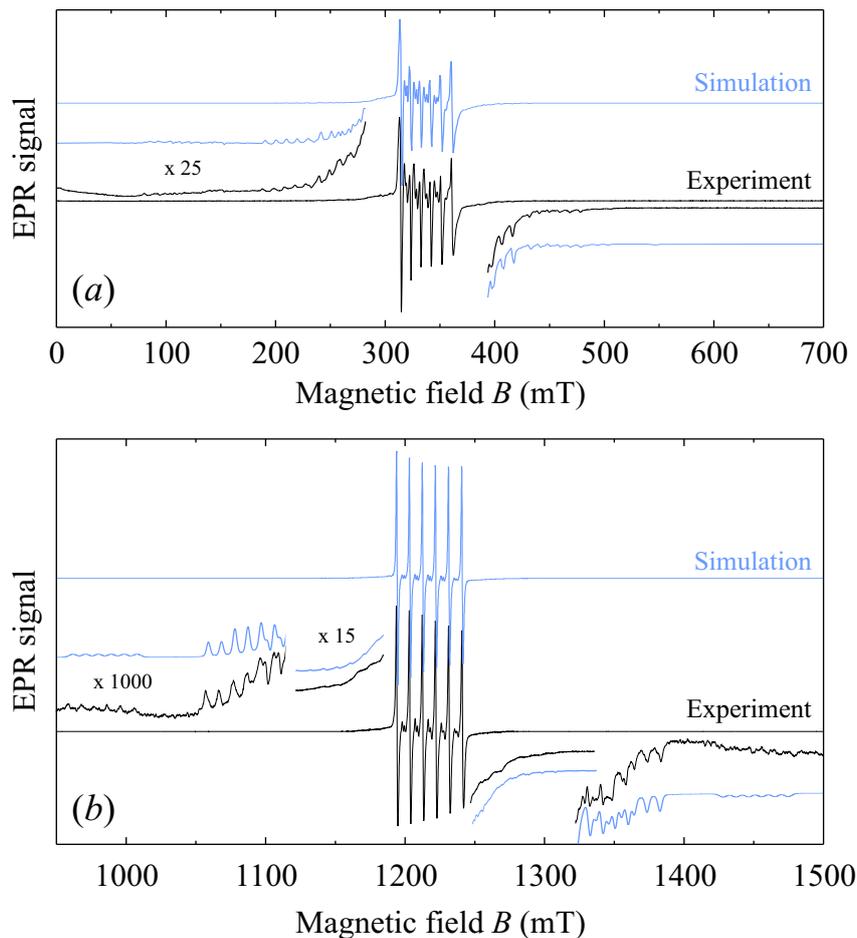
Figure 3.30: Experimental and simulated Mn^{2+} (a) X-band and (b) Q-band CW EPR spectra of **MHyZn:Mn** obtained at 140 K. The outer transitions are magnified for clarity.

Here g denotes the g-tensor of the Mn^{2+} center. The hf interaction is described by the second term, where A is the hf tensor of manganese nucleus. The last term takes into account the fs of the Mn^{2+} spectrum. The fs tensor D can be parametrized by the axial D and the orthorhombic E zfs parameters.

Spectral analysis reveals resolved outer transitions ($\pm\frac{5}{2} \leftrightarrow \pm\frac{3}{2}$) at about 970 and 1450 mT in the Q-band spectrum (see Figure 3.30b) indicating that the absolute value of the axial zfs parameter D is about 1.8 GHz at 140 K. Simulations indicate that for such a value of D, the central fs transition exhibits a pronounced angular dependence and therefore it is significantly shifted with respect to the recorded central transition. In addition, there is a clear mismatch between the

intensities of the outer and central fs transitions. This implies that the spectra of **MHyZn:Mn** consist of two Mn^{2+} species with different spin Hamiltonian parameters. The first species have very low intensity but well resolved fs and high value of D parameter. The spectrum of the second species is described with much smaller D and poorly resolved fs. The intensity of the first signal is much lower, and thus the central transition is superimposed by the intense central transition of the second Mn^{2+} species and hence cannot be observed. The second (major) species is assigned to the Mn^{2+} ions incorporated into the lattice of MHyZn, while the origin of the first signal with $D = 1.8$ GHz remains unclear. The intensity of this signal increased after keeping the sample for several days in a humid environment. Thus, it might be attributed to some Mn^{2+} impurity phase on the surface of crystallites formed after interaction with water molecules. Note that the surface water causes the recrystallization of a similar $[NH_2NH_3][M(HCOO)_3]$ framework from the thermodynamically unstable chiral polymorph to the stable perovskite structure [139]. It is also possible that some of the cavities do not contain MHy^+ cations (the excess charge might be compensated by protons) and therefore the neighboring MnO_6 octahedra have a different distortion.

The simulations of the X- and Q-band spectra are also presented in Figure 3.30. The incorporated Mn^{2+} species revealed an isotropic $\boldsymbol{g}$- and hf $\boldsymbol{A}$ tensors characterized by the scalar g-factor and isotropic hf coupling constant A_{iso}. The best simulation was obtained with the following parameters for these species: $g = 2.0002(2)$, $A_{iso} = -262(1)$ MHz. Note that the same set of spin Hamiltonian parameters was used to simulate both spectra. The determined values are typical for the Mn^{2+} ions, while A_{iso} also indicates Mn-O coordination which confirms the formation of the MnO_6 octahedra [14, 106]. The fs of these species seems to be poorly resolved due to the distributions ΔD and ΔE of D and E parameters [140]. The simulations were performed using $D = 350$ MHz, $\Delta D = 350$ MHz, $E = 50$ MHz and $\Delta E = 150$ MHz. The contribution of the Mn^{2+} impurity phase to the overall spectrum can be well simulated using $D = 1.8$ GHz and $E = 100$ MHz. The ratio of the spectral intensities of both species provided that the relative contribution of the impurity phase is roughly 3%.

Such a broad distribution of D was also observed in high-temperature phase of **DMAZn:Mn**. It was assigned to the fluctuations caused by the hopping motion

of the DMA$^+$ cations. This motion significantly slows down in the ordered phase and thus ΔD approaches zero below T_0. The fs of **DMAZn:Mn** was described using $D = 422$ MHz and $E = 58$ MHz (see Figure 3.3). It almost coincides with the fs observed in **MHyZn:Mn** indicating very similar distortion of the MnO$_6$ octahedra at low temperature in both systems. However, the outer transitions of the incorporated manganese species remain unresolved in the intermediate and the low-temperature phases of **MHYZn:Mn**. This suggests several different Mn^{2+} ion environments or persisting motion of the MHy$^+$ cations on the EPR time scale.

The temperature dependent spectra of **MHyZn:Mn** are presented in Figure 3.31 revealing small changes of the linewidth and the shape of the forbidden hf transitions in the central part of the spectra. These observations indicate that the zfs parameters depend on temperature, but remain broadly distributed. The spectrum recorded at 324 K was simulated using $D = 200$ MHz, $\Delta D = 250$ MHz (see Figure 3.31). Note that the XRD study revealed that the metal-formate framework is almost unaffected by the transition at T_{01} [60] and thus no significant spectral changes are expected at this point. As the temperature is decreased below T_{01}, the spectrum remains almost the same down to about 240 K where the intensity of the forbidden hf transitions starts to increase. The simulation of the spectrum obtained at 180 K provides $D = 290$ MHz and $\Delta D = 320$ MHz. The increase of D and ΔD with the decreasing temperature indicates that the MnO$_6$ octahedra become more distorted due to the ordering of the MHy$^+$ cations. The spectra above 240 K resemble the pattern obtained for **DMAZn:Mn** at $T > T_0$ (see Figure 3.1).

The temperature dependence of the CW EPR peak-to-peak linewidth Γ of the $m_I = \frac{1}{2}$ central transition line is presented in Figure 3.32. The linewidth exhibits clear minima at 174 and 308 K. The temperatures of the anomalies are in a good agreement with the transition points observed in **MHyZn** by the pyrocurrent and dielectric permittivity measurements (see Figures D.5a and D.6 in Appendix D). This demonstrates that the Mn^{2+} probes are indeed sensitive to both phase transitions. A small difference in the phase transition temperatures could be explained by slightly higher T_{01} and smaller T_{02} of MHyMn framework [60] compared with the pure zinc compound. Note that the measurements of the electric field dependent polarization do not indicate the ferroelectric behavior of
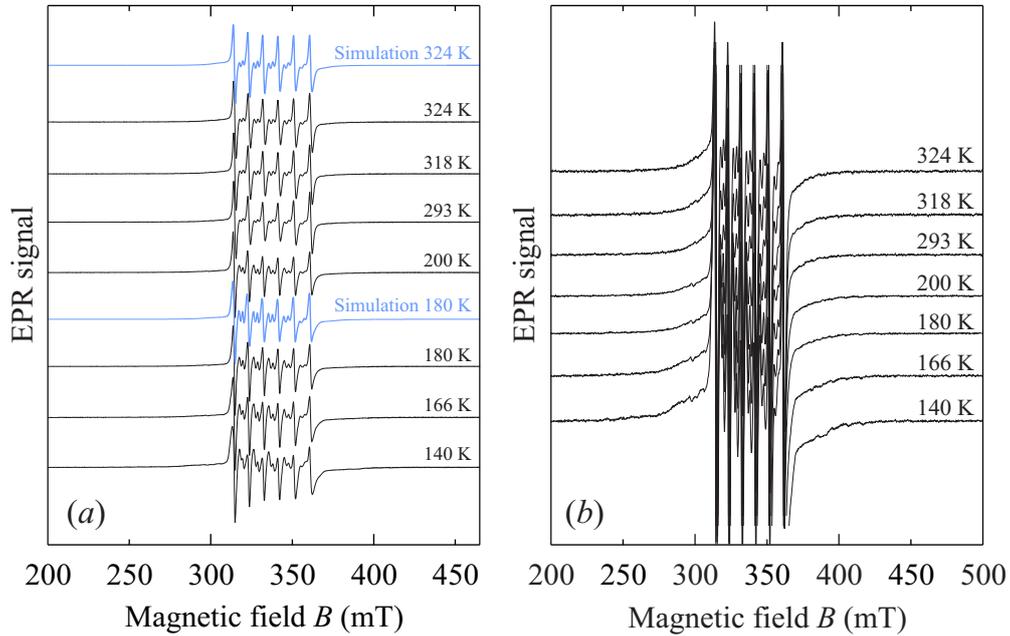
Figure 3.31: Normalized temperature dependent X-band CW EPR spectra of **MHyZn:Mn**. Emphasis on (a) central and (b) outer transitions. Simulation of the 324 K spectrum is also presented in (a).
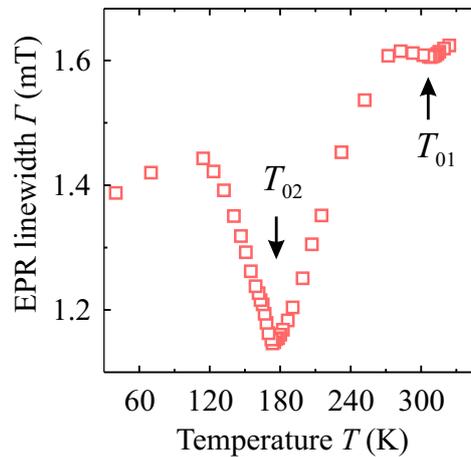
MHyZn (Figure D.5b).

Figure 3.32: Temperature dependence of the X-band CW EPR peak-to-peak linewidth of the Mn^{2+} ions in **MHyZn:Mn**.

The observed minima of Γ are puzzling, since an opposite behavior was observed for **DMAZn:Mn** and **DMAZn:Cu** (Figures 3.5 and 3.26) as well as for other ferroelectric and related materials [107, 110]. There are also few examples

in the literature reporting minimum of the EPR linewidth at the phase transition point in γ-irradiated KH_2PO_4 [141] and $Pb(Fe_{0.5}Nb_{0.5})O_3$ [142]. The provided explanation for the minimum is that the EPR linewidth is determined by the longitudinal spin-lattice relaxation time T_1 which is influenced by the damping or softening of the phonon modes [141, 142]. However, for **MHyZn:Mn** this explanation is unlikely, since T_1 is about an order of magnitude longer than the phase memory time T_m near T_{02} (see below). Therefore, the observed behavior of Γ is assigned to the increase in the distribution widths of the spin Hamiltonian parameters leading to the inhomogeneous line broadening. Since the distributions are related to the ordering of MHy^+ cations and framework deformation, the observed anomalies coincide with the phase transition points.

Summary

The X- and Q-band CW EPR spectra of **MHyZn:Mn** revealed a successful incorporation of the Mn^{2+} probes into the structure at the zinc lattice sites and formation of the MnO_6 octahedra. The temperature dependent Mn^{2+} spectra show poorly resolved outer fs transitions and experience only small changes in the intermediate phase. Spectral simulations revealed the increase of the zfs parameter D with decreasing temperature which is related to the gradual ordering of the system. The zfs parameters of the Mn^{2+} ions below T_{02} are comparable to those of **DMAZn:Mn** indicating that the MnO_6 octahedra in both frameworks are experiencing similar structural distortions upon the transition into the low-temperature phase. However, the local ordering of the cations in **MHyZn:Mn** appears to be more complex which is reflected in the substantially larger distribution widths of the zfs parameters. The temperature dependence of the EPR linewidth shows minima at both phase transition points that may be related to the changes of the distribution widths of the spin Hamiltonian parameters.

3.2.2   Pulsed EPR of manganese doped MHyZn

The pulsed EPR techniques were used to further probe the local environment of the Mn^{2+} ions in the low-temperature phase of **MHyZn:Mn** powder sample.

The 2p echo-detected field sweep pulsed EPR spectrum of **MHyZn:Mn** recorded at 25 K is presented in Figure 3.33. It is in a good agreement with the CW EPR pattern. This indicates the uniform distribution of the Mn^{2+} centers, since the regions with high ion concentration would exhibit much faster spin relaxation, causing differences between the CW and pulsed EPR spectra.
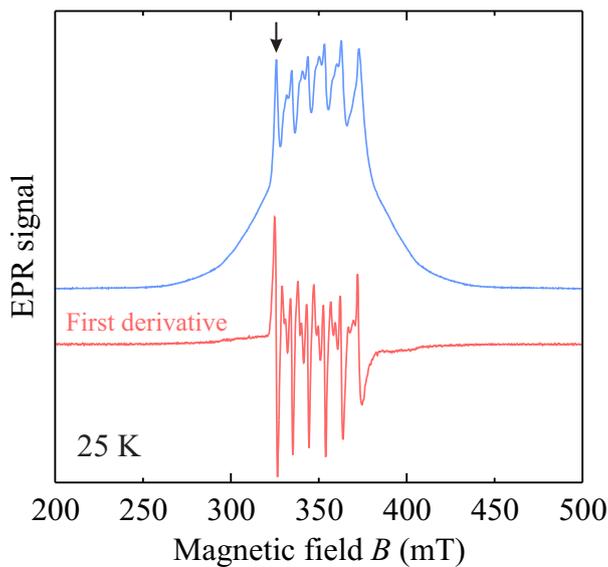

Figure 3.33: 2p echo-detected field sweep pulsed EPR spectrum of **MHyZn:Mn** powder recorded at 25 K. The corresponding first derivative spectrum is presented below. The arrow marks a position at which the ESEEM, ENDOR and relaxation time measurements were performed.

The Mims ENDOR experiments were performed to resolve small hf interactions between the Mn^{2+} centers and protons in **MHyZn:Mn**. A typical [1]H Mims ENDOR pattern recorded at 7 K and 325 mT is presented in Figure 3.34. At least three well resolved hf splittings can be observed indicating three protons in the vicinity of Mn^{2+} probe ion. These splittings correspond to $90°$ edge singularities in the powder pattern and are $A_{\perp}^{H} = 2.43$, 1.5 and 0.73 MHz. The $0°$ edge singularities were not resolved due to the low signal-to-noise ratio. Essentially the same spectrum was observed at other field positions indicating no orientation selectivity. Because there is no direct chemical bonding between the Mn^{2+} ions and the protons, the isotropic contribution to the observed hf splittings is negligible (especially for the weaker couplings) and thus the point-

dipole approximation should be valid (also see Eq. 2.33): [75]:

$$A_\perp^{\mathrm{H}} = \frac{\mu_0}{4\pi} \frac{g g_{\mathrm{H}} \beta_e \beta_n}{d_{\mathrm{Mn\text{-}H}}^3}. \tag{3.7}$$

Here $d_{\mathrm{Mn\text{-}H}}$ is the Mn-H distance. g and g_{H} are the g-factors of the Mn^{2+} center and proton.
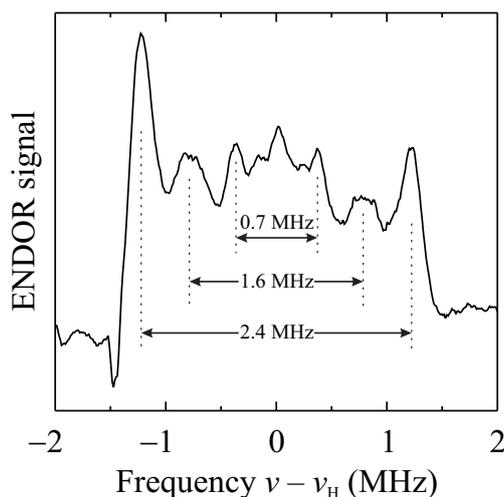

Figure 3.34: [1]H Mims ENDOR spectrum of the Mn^{2+} ions in **MHyZn:Mn** measured at 7 K and 325 mT. The best resolved ^{1}H hf splittings are indicated by the arrows.

The determined distances are 3.18, 3.7 and 4.76 Å. The shortest distance is assigned to protons from the formate anions joining metal-oxygen octahedra (XRD determined distance varies from 3.02 to 3.14 Å [60]). Note that almost the same hf splitting of the formate protons was also observed for **DMAZn:Mn** (Figure 3.13). The distance of 3.7 Å corresponds to protons bonded to central nitrogen atom of the MHy^+ cation (XRD distance varies from 3.73 to 3.76 Å [60]). The third proton species were also assigned to these cations. A good agreement between the XRD and ENDOR confirms the incorporation of the Mn^{2+} probes at the zinc lattice sites and verifies the proton positions in the XRD-based structural model.

The hf couplings of distant nuclei were also studied by performing 2p and 3p ESEEM experiments of **MHyZn:Mn**. The obtained frequency-domain spectra of both pulse sequences revealed a single line at the [1]H Larmor frequency

indicating weak ^{1}H hf couplings. This corresponds well with the ENDOR results. Note that the peculiar low-frequency signal observed for **DMAZn:Mn** was not detected.

Measurements of the longitudinal relaxation time T_1 and the phase memory time T_m of the Mn^{2+} electron spins in **MHyZn:Mn** were performed to further investigate the low-temperature phase and the phase transition at T_{02}. The temperature dependence of the phase memory time is presented in Figure 3.35a revealing a monotonous decrease of T_m with increasing temperature. Unfortunately, T_m was possible to measure only below T_{02} due to too fast relaxation. As indicated in the inset of Figure 3.35a, the phase memory relaxation rate T_m^{-1} exhibits the Arrhenius behavior: $T_m^{-1} = T_{m,\infty}^{-1} e^{-E_a/k_B T}$, where E_a and $T_{m,\infty}^{-1}$ are the activation energy and relaxation rate at infinite temperature, respectively. The following fit parameters were determined: $E_a = 15(1)$ meV and $T_{m,\infty}^{-1} = 4.8(3) \times 10^7$ s^{-1}.
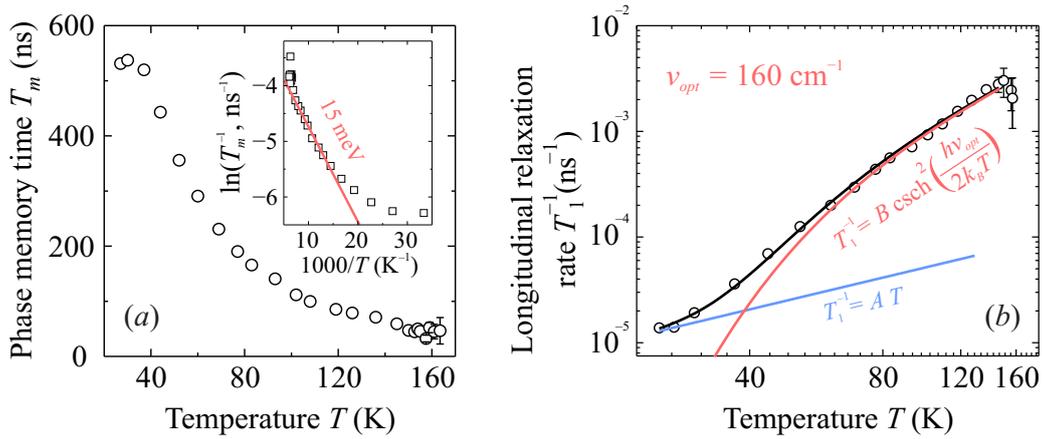

Figure 3.35: Temperature dependence of (a) the phase memory time T_m and (b) the most probable spin-lattice relaxation rate of the Mn^{2+} ions in **MHyZn:Mn** measured at 325 mT. Inset in (a) shows the Arrhenius behavior of the relaxation rate T_m^{-1} below T_{02}. The curves in (b) mark the total and separate contributions to the relaxation rate. The measurement error is smaller than data point, if not explicitly indicated.

The decrease of T_m with rising temperature may be attributed to the motion of the MHy$^+$ cations below T_{02} causing fluctuations of the local fields that enhance the phase memory relaxation. The obtained activation energy is more than an order of magnitude smaller than determined for the MHy$^+$ cation hopping motion using the dielectric spectroscopy (0.33 eV, see Figure D.7 in Appendix D).

Thus, the cause of the T_m relaxation might be related to the quantum tunnelling motion of the methyl group protons of the MHy$^+$ cations [124]. Note that likely the same process with activation energy of 17(1) meV was also observed for **DMAZn:Mn** (Figure 3.18).

The longitudinal relaxation time T_1 was measured using the inversion recovery pulse sequence [88]. The obtained magnetization kinetics were fit using a recovery function for the continuously distributed relaxation times [125]. The fits were reliable in the whole investigated temperature range. The temperature dependence of the most probable longitudinal relaxation rate T_1^{-1} is presented in Figure 3.35b. A monotonous increase of T_1^{-1} can be observed up to about 150 K and it is described using the following equation:

$$T_1^{-1} = AT + B\mathrm{csch}^2(h\nu_{opt}/2k_BT). \tag{3.8}$$

Here the first term takes into account a direct (one-phonon) process with the acoustic lattice phonons, while the second term is a Raman (two-phonon) process with the optical phonon branch of frequency ν_{opt}. The best fit provided $\nu_{opt} = 4.8(3) \times 10^{12}$ Hz or 160(10) cm^{-1}, which is close to 118(10) cm^{-1} obtained for **DMAZn:Mn**. The IR and Raman spectroscopy of **MHyZn:Mn** indeed revealed strong phonon modes below 400 cm^{-1} that involve vibrations of the Zn/Mn-oxygen octahedra [51, 56, 65] (see Raman data in Figure D.8).

It seems that the longitudinal relaxation rate starts to decrease above 150 K. The fit error in this temperature range is rather big due to very small echo intensity. This behavior is in agreement with a minimum observed for **DMAZn:Mn** compound (Figure 3.18) and other ferroelectric or related materials [125, 127–130]. It is attributed to the damping of the mode governing the Mn^{2+} spin relaxation due to a coupling with the relaxational mode that drives the phase transition. The temperature dependent Raman measurements indicate a severe broadening of the phonon modes as T_{02} is approached (see Figure D.8). In addition, some modes near ν_{opt} frequency experience a slight softening that may indicate increased damping. Note that due to too fast T_m relaxation, it was not possible to measure T_1 at higher temperatures and thus only the low-temperature wing of the minimum is observed.

Summary

The 2p echo-detected field sweep EPR spectrum of the Mn^{2+} ions was recorded for the low-temperature structural phase of **MHyZn:Mn**. The obtained pattern is in agreement with the CW EPR results indicating homogeneous distribution of the manganese centers.

The pulsed ENDOR spectroscopy was used to determine the hf interaction between the Mn^{2+} probes and the neighboring protons. The recorded spectrum revealed at least three ^1H species that are not resolved in the ESEEM experiments due to too weak hf couplings. The point dipole approximation was used to evaluate the Mn-H distances. The obtained results verify the XRD data and prove the incorporation of the Mn^{2+} ions in the framework structure.

The pulsed EPR techniques were also used to measure the longitudinal and phase memory relaxation times in the low-temperature phase of **MHyZn:Mn**. The obtained data provided information about the dynamics of the MHy^+ cations and the crystal lattice. The observed gradual decrease of T_m with rising temperature indicates a motional effect that was described by the Arrhenius law with the activation energy of 15(1) meV. It is about an order of magnitude smaller than obtained from the dielectric spectra for the hopping motion of the entire MHy^+ cations. Since the hopping should be hindered below T_{02}, the origin of this motion might be related to the methyl group motion.

The dependence of the longitudinal relaxation rate of **MHyZn:Mn** below 30 K is governed by a direct process with the acoustic lattice phonons. At higher temperatures, two-phonon Raman process of an optical lattice mode at 160(10) cm^{-1} dominates the relaxation behaviour. The IR and Raman spectra revealed strong lattice modes close to this wave number that involve vibrations of the metal-oxygen octahedra. In addition, there are indications that the longitudinal relaxation rate begins to decrease as T_{02} is approached from below. This behavior is caused by the damping of the hard optical mode responsible for the longitudinal relaxation. The damping occurs due to its coupling with the relaxational mode that governs the phase transition.

3.2.3 CW EPR of copper doped MHyZn

The CW and pulsed EPR of **MHyZn:Mn** revealed important information about the dynamics of the low-temperature phase transition, movement of the MHy$^+$ cations and structure of the framework. However, the poorly resolved fs of the Mn^{2+} spectra stimulates doping of MHyZn compound with paramagnetic Cu^{2+} centers.

The obtained temperature dependent X-band CW EPR spectra of **MHyZn:Cu** are presented in Figure 3.36 revealing typical anisotropic powder patterns of Cu^{2+} ions (see Figure 2.14 for more details). Four resolved hf lines can be observed on a broad background line at lower magnetic fields in the spectrum recorded at 330 K (Figure 3.36b). As the temperature is decreased, the background component diminishes, while the second set of resolved hf lines appears and becomes dominant upon further cooling. The observed temperature behavior is similar to the one detected for **DMAZn:Cu** framework (Figure 3.21).
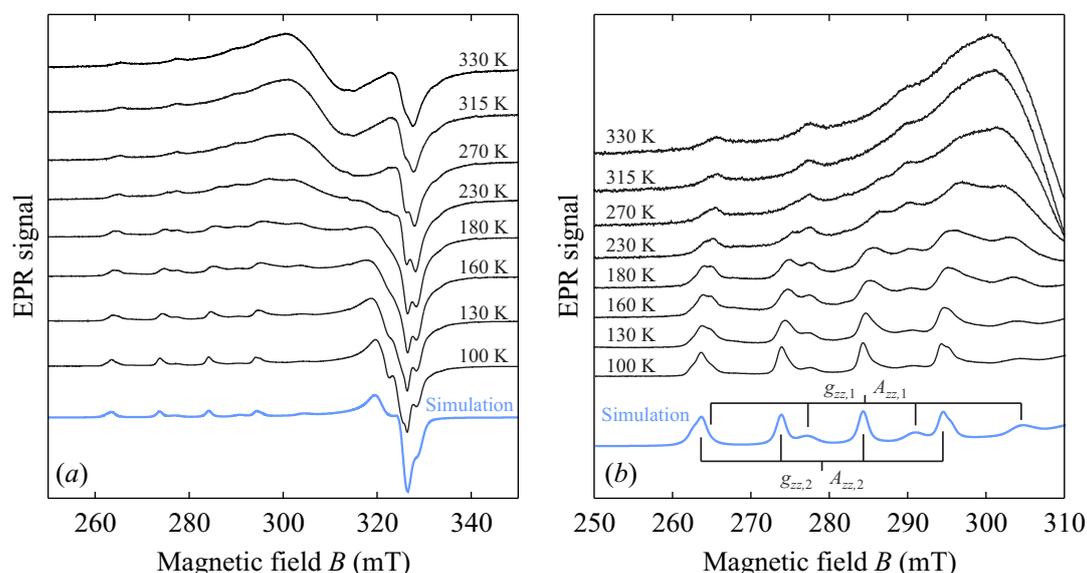

Figure 3.36: (a) Normalized temperature dependent X-band CW EPR spectra of the Cu^{2+} ions in **MHyZn:Cu**. The g_{zz}-part of the spectra is illustrated in (b). The simulation of the spectrum recorded at 100 K is presented in blue.

The spectrum of each resolved Cu^{2+} ion species can be described using the spin Hamiltonian which includes the electron Zeeman and hyperfine interactions

[79]:

$$\mathcal{H}_i = \beta_e \boldsymbol{B} \boldsymbol{g}_i \boldsymbol{S} + \boldsymbol{S} \boldsymbol{A}_i \boldsymbol{I}. \tag{3.9}$$

Here $i = 1, 2$ denotes two Cu^{2+} species. The copper centers are characterized by the $\boldsymbol{g}_i$- and hf $\boldsymbol{A}_i$ tensors. The spectrum recorded at 100 K was simulated using axially symmetric and collinear tensors with the following components: $g_{xx,yy,1} = 2.075(4)$, $g_{zz,1} = 2.380(2)$, $A_{zz,1} = 448(4)$ MHz and $g_{xx,yy,2} = 2.089(2)$, $g_{zz,2} = 2.422(1)$, $A_{zz,2} = 347(1)$ MHz. The hf tensor components $A_{xx,yy}$ of both species were not resolved. Similar values of g_{zz} and A_{zz} parameters are often observed for Cu^{2+} ions in an octahedral environment [131, 132] suggesting that copper successfully replaced zinc and formed CuO_6 octahedra in the structure of MHyZn.

The temperature dependences of g_{zz} and A_{zz} parameters were measured to check whether the Cu^{2+} probes are susceptible to the phase transitions in **MHyZn:Cu**. No reliable anomalous behavior of $g_{zz,1}$ and $A_{zz,1}$ parameters was observed. Thus, the origin of these species remains unclear. It might be an impurity phase, as observed for **MHyZn:Mn**, or the incorporated ions that are unaffected (within the accuracy of the measurements) by the phase transitions.

In contrast, the hf splitting of the second species suddenly decreases from about 360 MHz at 178 K (corresponds to T_{02}) to 342 MHz at 140 K (Figure 3.37a). This indicates that these ions are susceptible to the low-temperature phase transition and thus are incorporated within the framework structure. The $\boldsymbol{g}$- and hf tensor components of these species are very similar to that obtained for the related **DMAZn:Cu** ($g_{xx,yy} = 2.086(3)$, $g_{zz} = 2.410(1)$ and $A_{zz} = 341(1)$ MHz at 140 K, Figure 3.19). This indicates that the distortion of the CuO_6 octahedra is similar in both compounds. Above 200 K, the determination of $A_{zz,2}$ becomes complicated due to the significant line broadening which likely originates from the intensified dynamic Jahn-Teller effect and hopping motion of the MHy^+ cations above T_{02} in agreement with the **DMAZn:Cu** results. Note that no significant anomalies of the EPR intensity and $g_{zz,2}$ parameter were detected. Outside the phase transition region, the temperature dependence of $g_{zz,2}$ and $A_{zz,2}$ is typical for the dynamic Jahn-Teller effect [137].

The anomalous component $\Delta A_{zz,2}$ of $A_{zz,2}$ parameter was determined by subtracting the hf splitting at $T > T_{02}$ from the temperature dependence and taking
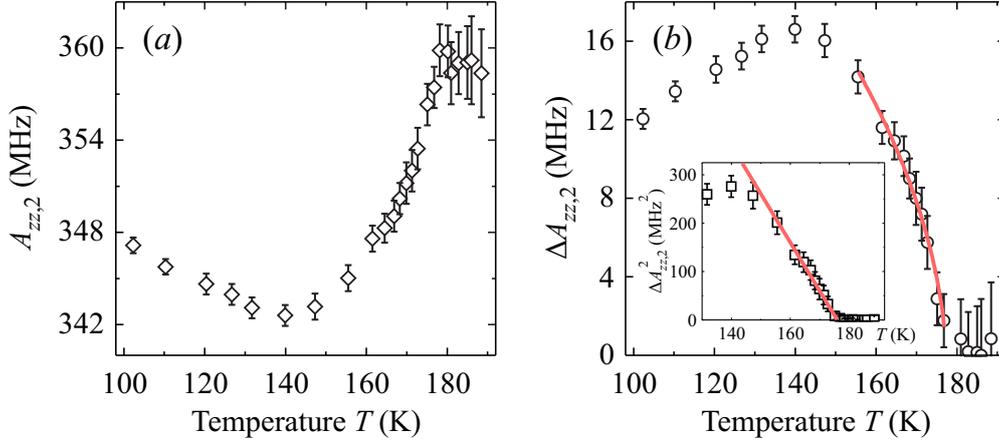
Figure 3.37: Temperature dependence of (a) the Cu^{2+} hf parameter $A_{zz,2}$ and (b) the anomalous part $\Delta A_{zz,2}$ of **MHyZn:Cu**. The inset in (b) shows the square of $\Delta A_{zz,2}$.

the absolute value. The obtained $\Delta A_{zz,2}$ is presented in Figure 3.37b revealing a behavior typical for an order parameter η_0. One can assume that $\Delta A_{zz,2}$ is proportional to the square of the order parameter ($A_{zz,2} \sim \eta_0^2$), since no splitting into two hf branches (positive and negative values of η_0) is observed.

The temperature dependence of $\Delta A_{zz,2}$ (or η_0^2) resembles a weak first-order phase transition (refer to Figure 2.3) [16]. In this case, the expression of η_0 is given by Eq. 2.8. The experimental data was described using this equation with $T_{02} = 177.4$ K (solid curve in Figure 3.37b). The obtained ratio $\beta^2/4\alpha\gamma = 0.3$ K indicates a very narrow temperature hysteresis. In addition, the fit shows a weakly expressed jump at T_{02} which demonstrates a behavior close to the tricritical point ($\beta \to 0$). For $\beta = 0$, one obtains $\Delta A_{zz,2} \sim \eta_0^2 \sim (T_{02} - T)^{1/2}$ (see Eq. 2.10). Thus, the square of $\Delta A_{zz,2}$ should be proportional to temperature. Indeed, such a linear dependence is observed in **MHyZn:Cu** as presented in the inset of Figure 3.37b.

Usually, a tricritical region in other crystals is attained using high pressure [16, 23]. Thus, the observed indications of this behavior in MHyZn at the ambient conditions makes this framework rather unique. It may be used to study this phenomenon much easier, though prior to such studies, investigation with applied pressure should be performed to verify the tricritical behavior.

Summary

The room temperature X-band CW EPR spectrum of **MHyZn:Cu** revealed well resolved Cu^{2+} hf lines superimposed on a broad background line in the g_{zz} spectral region. As temperature decreases in the intermediate structural phase, the broadening gradually transforms to the second set of well resolved Cu^{2+} hf lines. This effect can be related to the ordering of the MHy^+ cations that influences the CuO_6 octahedra.

The hf coupling A_{zz} of the second Cu^{2+} ion species in **MHyZn:Cu** exhibits an anomalous decrease at T_{02} that was assigned to the framework distortions. The anomalous part of A_{zz} was related to the square of an order parameter that exhibits the typical behaviour for a weak first-order phase transition close to the tricritical limit.

3.3 EPR Spectroscopy of BnZn

In this Section, the CW and pulsed EPR spectroscopy results of the Mn^{2+} and Cu^{2+} doped BnZn frameworks (samples **BnZn:Mn** and **BnZn:Cu**) are presented [143]. A pure BnZn framework exhibits a structural phase transition at about 235 K (see Section 2.2.4). Some EPR results are supported by the pyrocurrent and electric polarization measurements of pure BnZn single crystal (sample **BnZn**) [144]. A detailed description of the samples synthesis is presented in Appendix A. The experimental EPR details are given in Appendix B.

3.3.1 CW EPR of manganese doped BnZn

The X- and Q-band CW EPR spectra of **BnZn:Mn** powder measured above and below the phase transition temperature $T_0 = 235$ K are presented in Figure 3.38. The detected patterns are typical for the Mn^{2+} ions in the $3d^5$ electron configuration ($^6S_{5/2}$ electron ground state) [79]. The spectra consist of the well resolved hf lines of the central fs transition, while the outer fs transitions are unresolved and appear as broad spectral wings (Figure 3.38b,d). This indicates

broadly distributed values of parameters describing the zfs [105]. The fs is slightly better resolved in the spectrum recorded at 160 K, however, the lines are still too broad to precisely determine the zfs parameters. Note that the spectrum merely changed as the sample was cooled to 15 K.
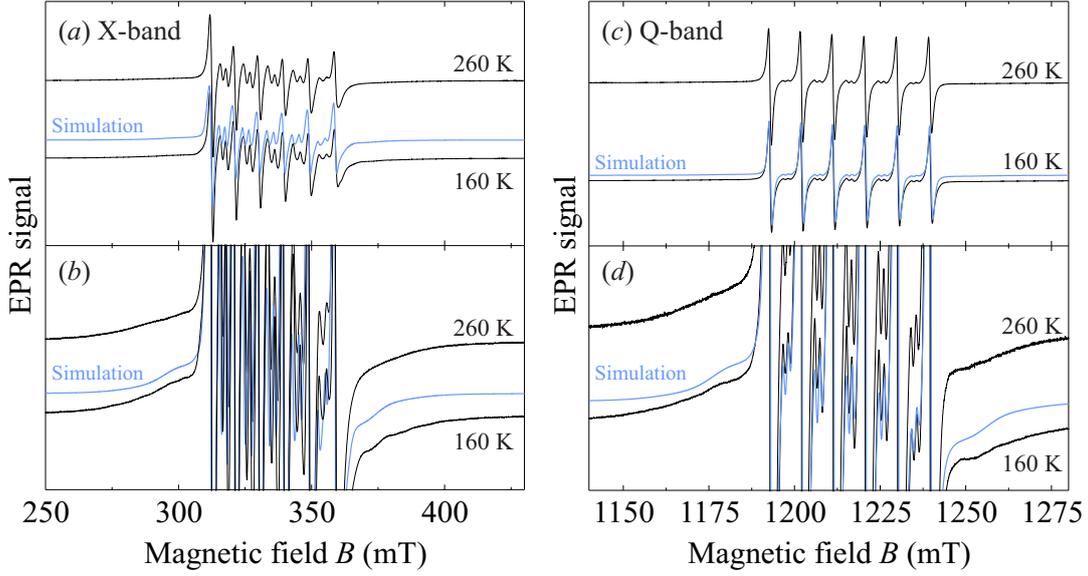

Figure 3.38: Normalized X- and Q-band CW EPR spectra of **BnZn:Mn** measured at 260 K and 160 K. Simulated 160 K spectrum is presented in blue. Emphasis on (a), (c) central and (b), (d) outer fs transitions.

The spectra recorded at 160 K were simulated to roughly estimate the parameters of the unresolved fs. The spin Hamiltonian used for simulation is [79]

$$\mathcal{H} = \beta_e \boldsymbol{BgS} + \boldsymbol{SAI} + \boldsymbol{SDS}, \tag{3.10}$$

where the first term describes the electron Zeeman interaction characterized by the electron $\boldsymbol{g}$-tensor. The second term takes into account the hf interaction, while the last term describes the fs. $\boldsymbol{A}$ and $\boldsymbol{D}$ are the hf and fs tensors, respectively. The simulated spectra (see Figure 3.38) agree sufficiently well with the experiment. For simulations, the isotropic $\boldsymbol{g}$- and $\boldsymbol{A}$ tensors were used with the corresponding components $g = 2.0016(1)$ and $A_{\mathrm{iso}} = -262(1)$ MHz. The determined value of A_{iso} indicates Mn$-$O coordination [106] suggesting that the Mn^{2+} ions successfully replaced Zn^{2+} and formed MnO$_6$ octahedra. The axial zfs parameter and its distribution used for the simulation are $D = 300(50)$ MHz and $\Delta D = 250(70)$ MHz, respectively. The orthorhombic zfs parameter E was

113

set to zero.

Note that a similar value and distribution of D was obtained for **DMAZn:Mn** and **MHyZn:Mn** frameworks (Sections 3.1.1.1 and 3.2.1). In the former compound, the broadening disappeared below the phase transition point and thus it was assigned to the fluctuations caused by the DMA$^+$ cations. The motion of these cations slows down significantly below the phase transition point resulting in the uniformly deformed MnO_6 octahedra. For **MHyZn:Mn** compound, the fs remained unresolved in all three structural phases.

The XRD data [9] for undoped BnZn framework indicates seven differently distorted ZnO_6 octahedra in the low temperature phase. In the high temperature phase two different ZnO_6 octahedra are found. Thus, a broad distribution of D in **BnZn:Mn** could result from a combined effect of the Bn^{2+} cation motion and several different geometries of the MnO_6 octahedra. The expected change in the spectrum due to the ordering of the Bn^{2+} cations could be masked by a distribution of D originating from different Mn^{2+} environments. Note that a Bn^{2+} cation is much bigger than DMA$^+$ and MHy$^+$ cations and its characteristic motional time is expected to be much slower. One cannot eliminate a possibility that even in the high temperature phase this time is much slower than the time scale of our experiment and thus the motion of the cation barely affects the distribution of D.

The X-band spectra recorded at different temperatures were used to determine the peak-to-peak CW EPR linewidth Γ of the low-field hf line ($m_I = -\frac{5}{2}$) of the central fs transition. The obtained temperature dependence of Γ is presented in Figure 3.39. An anomalous increase of Γ is observed at the phase transition point $T_0 = 235$ K in agreement with the pyrocurrent measurements of **BnZn** single crystal (Figure D.9a, Appendix D). The linewidth of an unsaturated purely homogeneous EPR line is inversely proportional to the transverse relaxation time T_2 of the paramagnetic species ($\Gamma \sim 1/T_2$) [79]. The determined value of T_m (see below) is too long to account for the width of about 1.2 mT indicating that inhomogeneous CW EPR lines are observed for **BnZn:Mn**. Nevertheless, the anomaly implies a decrease of T_2 at the phase transition temperature, since broadening of the homogeneous lines of the individual spin packets would also increase the observed inhomogeneous EPR linewidth.
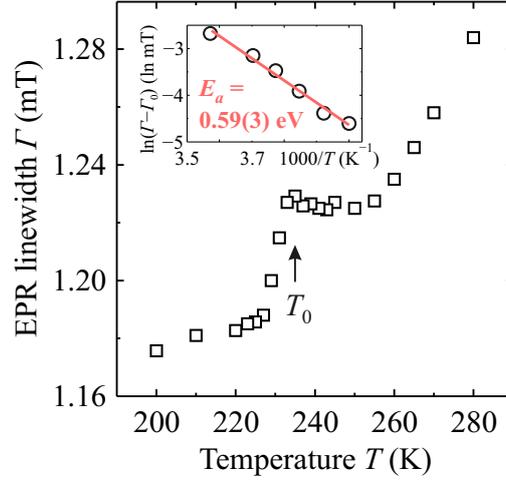
Figure 3.39: Temperature dependence of the peak-to-peak CW EPR linewidth of **BnZn:Mn**. Error bars are smaller than the data points. The Arrhenius analysis of the linewidth in the high-temperature phase is presented in the inset.

Such an anomalous behavior of Γ is caused by a critical order parameter fluctuations [108] and it is usually encountered in many other ferroelectric and related materials such as triglycine sulfate [107], trissarcosine calcium chloride [108, 109], SrTiO$_3$ [110]. A sudden anomalous increase of the linewidth was also observed for **DMAZn:Mn** and **DMAZn:Cu** frameworks (Figures 3.5 and 3.26). In addition, as indicated in Figure 3.18, a sudden decrease of T_m was also detected at the phase transition point of **DMAZn:Mn**. Note that the linewidth anomaly of **BnZn:Mn** seems to be much broader.

The observed overall decrease of the linewidth with decreasing temperature may indicate a motional effect which is not related to the phase transition. The linewidth in the high-temperature phase was analyzed using the Arrhenius law: $\Gamma - \Gamma_0 = \Gamma_\infty e^{-E_a/k_B T}$ (see inset in Figure 3.39). The obtained activation energy $E_a = 0.59(3)$ eV is in a good agreement with the value of 0.50 eV determined from the dielectric spectroscopy [9, 144]. The observed temperature behavior of the CW EPR linewidth is likely caused by the Bn^{2+} cation motion. The determined activation energy is roughly twice as obtained for DMAZn and MHyZn compounds. This difference may be related to much bigger mass and size of Bn^{2+} compared to DMA$^+$ and MHy$^+$ cations. The higher activation energy could also be a consequence of the significantly higher phase transition temperature of BnZn framework.

115

Summary

Simulation of the X- and Q-band CW EPR spectra revealed that Mn^{2+} centers replaced Zn^{2+} ions and formed MnO_6 octahedra in **BnZn:Mn**. A broad distribution of the zfs parameters was observed indicating different crystal field environments around the Mn^{2+} ions.

The CW EPR linewidth of the Mn^{2+} centers in **BnZn:Mn** exhibits anomalous increase at the phase transition point. The anomaly was assigned to the decrease of the transverse relaxation time T_2 of Mn^{2+} centers due to the order parameter fluctuations at T_0.

The overall decrease of the linewidth with decreasing temperature indicates a motional effect. The analysis of the linewidth in the high-temperature phase of **BnZn:Mn** revealed Arrhenius process with the activation energy of 0.59 eV. It was assigned to the motion of the Bn^{2+} cations.

3.3.2   Pulsed EPR of manganese doped BnZn

The pulsed EPR techniques were further used to investigate the local Mn^{2+} ion environment in the low-temperature phase of **BnZn:Mn** powder. The 2p echo-detected field sweep pulsed EPR spectrum of **BnZn:Mn** recorded at 15 K is presented in Figure 3.40. The obtained pattern is in a perfect agreement with the CW EPR measurements indicating that Mn^{2+} probes are well distributed within the crystal lattice. Otherwise, the regions with a high local Mn^{2+} concentration would not contribute to the echo-detected spectra due to much faster relaxation. This would likely cause difference between the echo-detected pulsed and CW EPR spectra.

Surprisingly, the Hahn echo in **BnZn:Mn** was observable up to about 230 K indicating very well isolated Mn^{2+} centers. No echo was detected in the high-temperature phase, presumably, due to the enhanced Bn^{2+} cation motion. This result is in agreement with the CW EPR linewidth analysis which indicates anomalous decrease of the transverse relaxation time at T_0. The determined longitudinal relaxation time T_1 and the phase memory time T_m at 200 K are 260 ns and 37 ns, respectively.
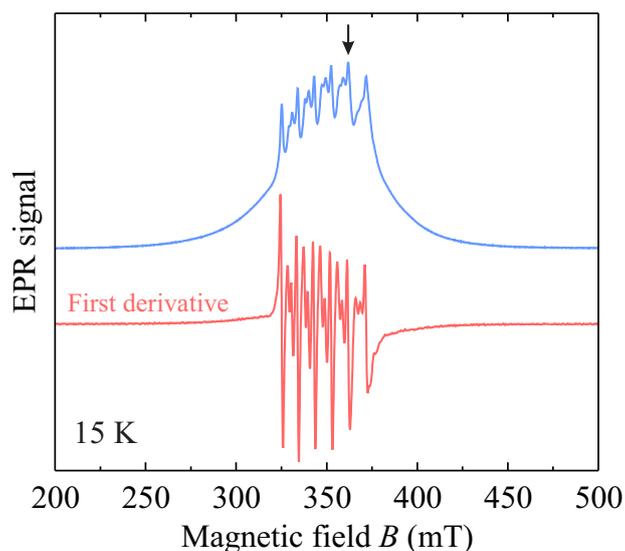
Figure 3.40: 2p echo-detected field sweep pulsed EPR spectrum of **BnZn:Mn** powder recorded at 15 K. The corresponding first derivative spectrum is presented below. The arrow marks a position at which the ENDOR experiment was performed.

The spectral resolution of the echo-detected field sweep EPR spectrum is insufficient to resolve the hf interactions between the paramagnetic Mn^{2+} centers and ligand nuclei such as ^1H. Thus, Mims ENDOR experiments were performed to investigate the local environment of the Mn^{2+} ions in the low-temperature phase of **BnZn:Mn**. The ^1H ENDOR pattern of **BnZn:Mn** (Figure 3.41) recorded at 361.8 mT, $\tau = 104$ ns and 15 K shows at least four different proton species. The corresponding hf splittings at $90°$ edge singularities in the powder pattern are $A_\perp^H = 0.7$, 1.1, 1.9 and 2.3 MHz. Note that due to the low signal to noise ratio, the splittings at the $0°$ edge singularities were not resolved. Essentially the same ENDOR pattern was obtained for $\tau = 130$ ns (not presented). No orientation selectivity was assumed in the analysis, since measurements at several field positions yielded the same pattern.

It can be assumed that the isotropic part of the proton hf coupling tensors is negligible, since the first coordination shell of the Mn^{2+} ion is occupied by oxygen. In such a case, the point dipole approximation is valid and thus one can use Eq. 3.7 to obtain the Mn-H distances d_{Mn-H}. The observed splittings correspond to distances of 4.8, 4.2, 3.5 and 3.2 Å. Careful analysis of BnZn structure obtained by XRD [9] suggests that the most strongly coupled protons
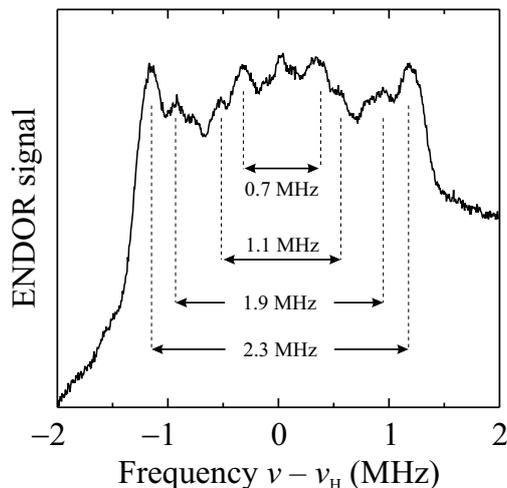
117

Figure 3.41: ^{1}H Mims ENDOR spectrum of the Mn^{2+} ions in **BnZn:Mn** measured at 15 K and 325 mT. The best resolved ^{1}H hf splittings are indicated by the arrows.

originate from the formate linkers. For these protons, the Zn-H distance obtained from the XRD analysis varies from 3.0 to 3.1 Å. Weaker couplings correspond to protons from the Bn^{2+} molecular cation. XRD revealed $d_{Zn-H} = 3.6$ Å for protons bonded to nitrogen which is in a perfect agreement with $d_{Mn-H} = 3.5$ Å obtained from ENDOR spectroscopy. Protons at distances of 4.2 and 4.8 Å can be assigned to methylene groups. A good correspondence between the ENDOR and XRD studies confirms that the Mn^{2+} ions are incorporated at the Zn^{2+} lattice sites in **BnZn:Mn**. Additionally, ENDOR analysis verifies the proton positions in the structure obtained by the XRD [9], which are often difficult to determine precisely by the X-ray based methods.

Note that the same splitting of the strongest ^{1}H hf interaction was also observed for **DMAZn:Mn** (Figure 3.13) and **MHyZn:Mn** (Figure 3.34) frameworks that also contain MnO$_6$ octahedra connected via the formate anions. This demonstrates that the hf coupling of about 2.3 MHz could be used as a fingerprint to identify whether the Mn^{2+} centers successfully replaced the diamagnetic ions in various formate frameworks.

Summary

The echo-detected field sweep pulsed EPR spectrum of **BnZn:Mn** is in a good correspondence with the CW EPR results demonstrating that the Mn^{2+} ions are well distributed within the crystal lattice.

The X-band ^1H Mims ENDOR spectrum of **BnZn:Mn** shows at least four different proton species in the local environment of the Mn^{2+} probes. The obtained ^1H hf couplings were compared with the available XRD data. The most strongly coupled proton was assigned to formate linkers, while the other three protons were found to originate from the ammonium and methylene groups of the Bn^{2+} cation confirming successful incorporation of the Mn^{2+} ions at the Zn^{2+} lattice sites. The ENDOR results also verify the proton positions in the framework structure obtained by the XRD methods.

3.3.3   CW EPR of copper doped BnZn

The EPR investigation of the Mn^{2+} ions in **BnZn:Mn** revealed details about the motional effects and low-temperature structure, but did not provide insights about the nature of the structural phase transition. Thus, alternative paramagnetic Cu^{2+} probe ions were introduced into the lattice.

The X-band CW EPR spectra of **BnZn:Cu** powder recorded at different temperature are presented in Figure 3.42. The spectra are typical anisotropic powder patterns of the Cu^{2+} ions with $3d^5$ electron configuration (refer to Figure 2.14 for more details). Four resolved hf lines can be observed on a broad background line at lower magnetic fields. As the temperature is decreased, the intensity of the background component becomes lower. In addition, each resolved hf line is split into two below 180 K indicating two Cu^{2+} ion species with slightly different hf couplings. This result is in agreement with the XRD data [9] which indicates several differently distorted ZnO_6 octahedra in the low temperature phase of BnZn.

A similar temperature evolution of the broad background line was observed for **DMAZn:Cu** (Figure 3.21) and **MHyZn:Cu** (Figure 3.36) frameworks. It was
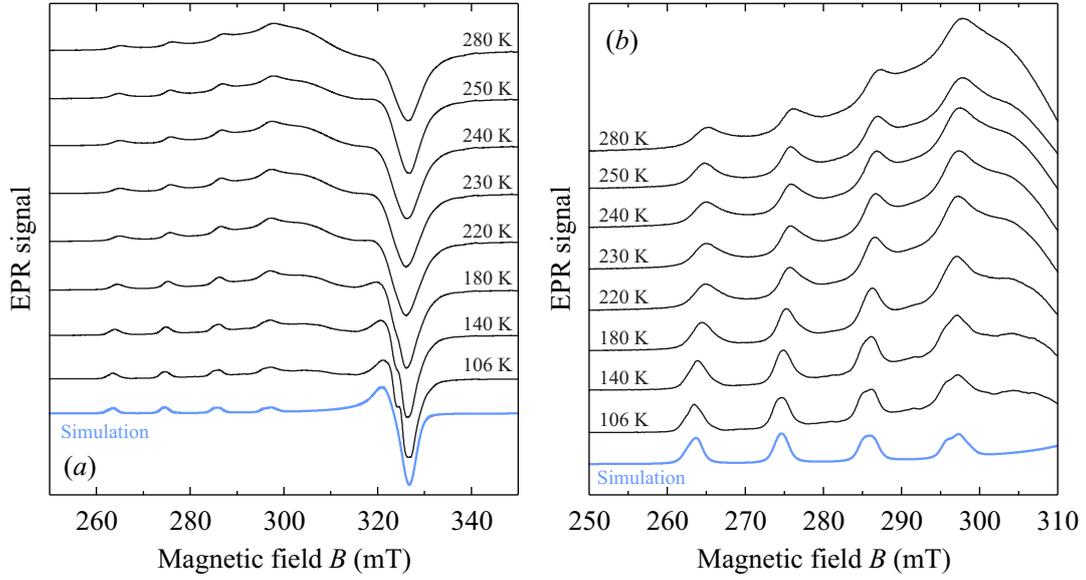
Figure 3.42: (a) Normalized temperature dependent X-band CW EPR spectra of the Cu^{2+} ions in **BnZn:Cu**. The g_{zz}-part of the spectra is illustrated in (b). Simulation of the spectrum recorded at 106 K is presented in blue.

assigned to the combined effect of the molecular cation motion and Jahn-Teller dynamics. The broad background line was absent in the ordered phases of these compounds, while for **BnZn:Cu** it is still notable even at 106 K. This may indicate substantial dynamics even in the low-temperature phase of **BnZn:Cu**. Note that the pyrocurrent measurements of **BnZn** (see Figure D.9a) revealed further ordering (freezing) of the dipole system below T_0 [9]. The second explanation for the remaining broad line in the CW EPR spectra of the low-temperature phase is the magnetic exchange interaction between the Cu^{2+} centers. A similar broad line was observed for a slightly higher Cu^{2+} ion doping level ($\gtrsim 2$ mol%) of DMAZn framework, as presented in Figure 3.24b.

The spectrum recorded at 106 K was simulated using the following spin Hamiltonian with included electron Zeeman and hf interactions [79]:

$$\mathcal{H}_i = \beta_e \boldsymbol{B} \boldsymbol{g}_i \boldsymbol{S} + \boldsymbol{S} \boldsymbol{A}_i \boldsymbol{I}. \tag{3.11}$$

Here $i = 1, 2$ denotes two Cu^{2+} species. Simulation was performed using axially symmetric and collinear Cu^{2+} $\boldsymbol{g}_i$- and $\boldsymbol{A}_i$ tensors with the following components: $g_{xx,yy,1} = 2.086(3)$, $g_{zz,1} = 2.409(3)$, $A_{zz,1} = 376(1)$ MHz and $g_{xx,yy,2} = 2.086(3)$,

120

$g_{zz,2} = 2.418(3)$, $A_{zz,2} = 362(1)$ MHz. The hf tensor components $A_{xx,yy}$ of both species were not resolved. The obtained values of g_{zz} and A_{zz} components are typical for the Cu^{2+} ions in an octahedral environment [131, 132] indicating that copper successfully replaced zinc and formed CuO_6 octahedra in BnZn framework.

The temperature dependence of the Cu^{2+} hf component $A_{zz,1}$ is presented in Figure 3.43. Above 237 K, $A_{zz,1}$ increased with increasing temperature, whereas the value of this parameter gradually decreased from 371(1) MHz at 237 K to 362(1) MHz at 220 K. As the temperature was further lowered, $A_{zz,1}$ steadily increased again to 380(1) MHz at 87 K. The value of $g_{zz,1}$ parameter was constantly rising from 2.401(1) at 267 K to 2.412(1) at 87 K without any significant anomaly within the accuracy of the measurements. Note that the same behavior was also obtained for **DMAZn:Cu** (Figure 3.27) and **MHyZn:Cu** (Figure 3.37) frameworks.

The observed temperature dependence of $A_{zz,1}$ and $g_{zz,1}$ outside the phase transition region is typical for the dynamic Jahn-Teller effect [137]. The decrease of $A_{zz,1}$ on cooling in the temperature interval between 237 K and 220 K indicates that the Cu^{2+} ion probes are susceptible to the phase transition in **BnZn:Cu**. All these findings demonstrate that these ions were successfully incorporated at the Zn^{2+} lattice sites in BnZn framework.

According to Shang et al. [9], BnZn framework exhibits an antiferroelectric order below $T_0 = 235$ K. This is in agreement with very small pyrocurrent anomaly observed for **BnZn** single crystal at T_0 (Figure D.9a). However, the electric field dependent electric polarization measurements did not reveal the double hysteresis loop which is characteristic to the antiferroelectric phase (Figure D.9b). Thus, the origin of the low-temperature structure of BnZn remains obscured.

The phase transition in **BnZn:Cu** was further investigated by analyzing the temperature dependence of $A_{zz,1}$. The anomalous component $\Delta A_{zz,1}$ of the hf coupling was obtained by subtracting a line from the $A_{zz,1}$ data points (see Figure 3.43). The obtained temperature dependence of $\Delta A_{zz,1}$ resembles the order parameter for a weak first-order phase transition (refer to Figure 2.3). For the case of the antiferroelectric ordering, $\Delta A_{zz,1}$ measures the two spontaneous sublattice polarizations, which have different signs but same magnitude.
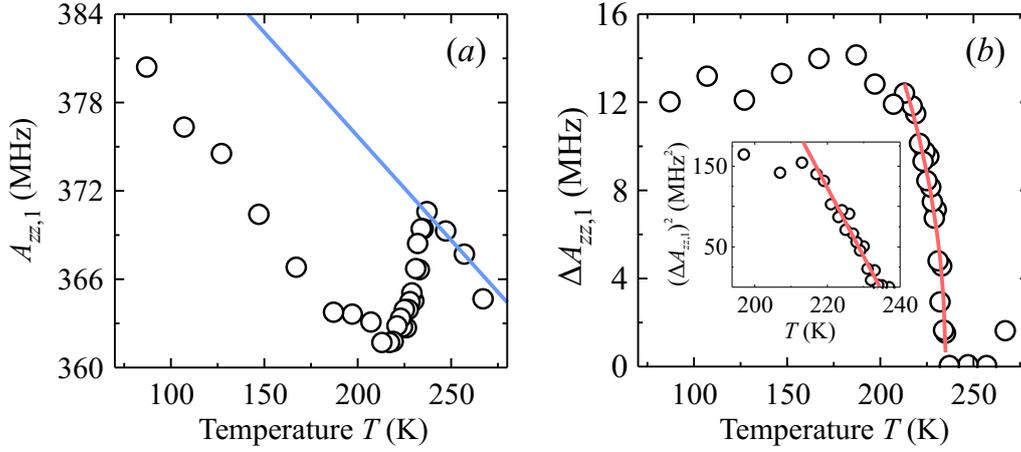
Figure 3.43: Temperature dependence of (a) Cu^{2+} hf parameter $A_{zz,1}$ and (b) $\Delta A_{zz,1}$ of **BnZn:Cu**. The square of $\Delta A_{zz,1}$ is indicated in the inset. The error of $A_{zz,1}$ is less than 2 MHz. The blue line was subtracted from $A_{zz,1}$ to obtain $\Delta A_{zz,1}$.

The EPR parameter can show either a linear ($\Delta A_{zz,1} \sim \eta_0$) or a quadratic dependence ($\Delta A_{zz,1} \sim \eta_0^2$) on the order parameter depending on the local symmetry of the paramagnetic probe ion. In the former case, a splitting into two hf branches would be observed whereas the latter case leads just to a shift of the resonance lines measured by $\Delta A_{zz,1}$ as observed here for **BnZn:Cu**. Thus, the anomalous hf component $\Delta A_{zz,1}$ must be proportional to the square of the order parameter η_0 (sublattice polarizations in case of the antiferroelectric ordering).

The solid curve in Figure 3.43b represents a satisfying fit of the experimental data using Eq. 2.8 with $\beta^2/4\alpha\gamma < 0.1$ K indicating a negligible temperature hysteresis. The analysis shows that $\Delta A_{zz,1}$ follows the temperature dependence as expected for a weak first-order phase transition, where the jump in the anomalous component at T_0 is only weakly expressed. This indicates that the absolute value of the parameter β must be small and the phase transition appears to be close to a tricritical point where $\beta \to 0$ [1, 2]. For $\beta = 0$, $\Delta A_{zz,1} \sim \eta_0^2 \sim (T_c - T)^{1/2}$ holds (see Eq. 2.10). Thus, the square of $\Delta A_{zz,1}$ should be proportional to temperature, as indeed is observed for **BnZn:Cu** (see inset in Figure 3.43b).

Note that the same peculiar behavior was detected for **MHyZn:Cu** framework (Figure 3.37). In contrast, **DMAZn:Cu** framework exhibits an ordinary strong first-order phase transition (compare with Figure 3.27). The perovskite tolerance

factors of DMAZn and MHyZn compounds are very similar [60] and thus the perovskite distortion is an unlikely reason for the observed differences. A possible reason for this behavior is the number of H-bonds the central molecule forms with the metal-formate framework. Four $N-H \cdots O$ bonds are formed in MHyZn [60] and BnZn [70] compounds, while DMAZn exhibits only two such bondings [7].

Summary

The X-band CW EPR spectra of **BnZn:Cu** powder revealed well resolved Cu^{2+} hf lines superimposed with a broad background line. The simulation of the resolved signal allowed to determine the spin Hamiltonian parameters of the Cu^{2+} centers in **BnZn:Cu**. The obtained parameters are typical for ions in the octahedral environment indicating successful incorporation of Cu^{2+} into the structure of BnZn. The intensity of the broad line becomes lower with decreasing temperature indicating motional and dynamic Jahn-Teller effects. The broad line is also observable in the low-temperature phase suggesting substantial magnetic exchange interactions between the Cu^{2+} ions.

Temperature dependence of A_{zz} parameter shows a complex behavior which originates from distortion of the octahedra caused by ordering of the Bn^{2+} cations and framework deformation at the phase transition temperature $T_0 = 235$ K. The anomalous part of the Cu^{2+} hf coupling below T_0 follows a temperature dependence typical for the order parameter of a weak first-order phase transition. A more detailed analysis revealed a behavior close to the tricritical limit.

"The present is the only things that has no end."

Erwin Schrödinger

Conclusions

- The multifrequency CW EPR revealed that the Mn^{2+} and Cu^{2+} ions replaced zinc in the structures of DMAZn, MHyZn and BnZn and formed MnO_6 and CuO_6 octahedra. A significant broadening of the CW EPR spectra of these compounds was observed due to the dynamic effects of the molecular cations. The temperature dependent linewidth in the disordered phases of Mn^{2+} and Cu^{2+} doped DMAZn as well as Mn^{2+} doped BnZn frameworks revealed the Arrhenius processes that were assigned to the molecular cation motion. The determined activation energies were found to be in a good agreement with the NMR and dielectric spectroscopy studies indicating that all these techniques observed the same motional effect. In the EPR case, this process was detected indirectly via the deformation of the octahedra that are H-bonded with the molecular cations. The CW EPR linewidth of these compounds also displayed an anomalous increase at the phase transition point which was assigned to the order parameter fluctuations.

- The temperature dependent spin Hamiltonian parameters of the Mn^{2+} and Cu^{2+} centers in DMAZn, MHyZn and BnZn revealed the order and behavior of the transitions to the ordered phases. DMAZn framework exhibits a strong first-order phase transition, while the transitions in MHyZn and BnZn are of a weak first-order character close to the tricritical limit. This difference may be related to the number of H-bonds the central molecule forms with the metal-formate framework. The CW EPR measurements of Mn^{2+} doped DMAZn framework containing ^{15}N isotope revealed a negligible isotope effect on the transition temperature indicating order-disorder nature of the transition.

- The CW EPR of Mn^{2+} doped DMAZn single crystal displayed six MnO_6 octahedra in agreement with the crystal twinning structural model. To check for a possible ferroelectric response, EPR measurements were performed with a simultaneously applied external electric field. No spectral differences between the experiments with and without the field were observed raising serious doubts about the proper ferroelectric origin of DMAZn. This result was supported by the electric polarization measurements. The same type of experiments on Mn^{2+} doped AmZn framework indicated a clear ferroelectric behavior.

- The pulsed ENDOR spectroscopy of Mn^{2+} and Cu^{2+} doped DMAZn as well as Mn^{2+} doped MHyZn and BnZn revealed several protons in the vicinity of the paramagnetic probes. The determined proton hf couplings were found to be in a good agreement with the couplings expected from the XRD models. This confirmed successful incorporation of the paramagnetic centers into the frameworks and, more importantly, verified structural models and proton positions that are difficult to determine with the XRD.

- The pulsed echo-detected field sweep EPR spectra of the ordered phases of Mn^{2+} and Cu^{2+} doped DMAZn as well as Mn^{2+} doped MHyZn and BnZn frameworks were found to be in agreement with the CW EPR results. The high-temperature phase spectrum of Mn^{2+} doped DMAZn revealed much faster phase memory relaxation of the outer fs transitions. This peculiar behavior was assigned to the fluctuating (transient) zfs caused by the hopping motion of the DMA^+ cations confirming a tight relation between the organic and inorganic subsystems.

- The ESEEM spectroscopy of the ordered phases of Mn^{2+} and Cu^{2+} doped DMAZn as well as Mn^{2+} doped MHyZn displayed a signal of weakly coupled protons in agreement with the ENDOR results. For DMAZn containing Mn^{2+} centers, a remarkable low-frequency ESEEM signal, which is unaffected by the external magnetic field, was also observed. The origin of this modulation may be related to the methyl group dynamics.

- The phase memory time measurements of the Mn^{2+} ions in the ordered phases of DMAZn and MHyZn revealed methyl group motion which causes fluctuations of the local ion environment. The determined activation energies are

typical for quantum tunnelling dynamics of the methyl group protons. The longitudinal relaxation of the Mn^{2+} ions in these compounds is dominated by the interaction with the acoustic and optical lattice phonons. A small anomalous dip of the longitudinal relaxation rate at the transition point was observed and assigned to the increased damping of the hard optical mode governing the relaxation. The damping likely occurs due to the coupling of this mode with the relaxational mode of the transition.

Appendix A

Sample Synthesis Details

The samples for EPR and other characterization techniques were prepared by Prof. Dr. Mirosław Mączka group at Institute of Low Temperature and Structure Research of Polish Academy of Sciences. The concentrations of the paramagnetic transition metal ions in samples for the EPR experiments was chosen as small as possible, while keeping a reasonable signal-to-noise ratio of the EPR signal.

The following chemicals used for sample synthesis were commercially available: $ZnCl_2$ (99%, Fluka), $MnCl_2$ (99%,Sigma-Aldrich), $CuCl_2$ (99.995%, Sigma-Aldrich), methanol (99.8%, Sigma-Aldrich) formic acid (98%, Fluka), $(CH_3)_2NH$ in methanol (Sigma-Aldrich), dimethylamine-15N hydrochloride (Sigma-Aldrich), HCOONa (99%, Sigma-Aldrich), $[NH_4][HCOO]$ (99%, Fluka), methylhydrazine (98%, Sigma-Aldrich), 1,4-diaminobutane (99%, Sigma-Aldrich).

DMAZn:Mn powder

DMAZn:0.05 Mn^{2+} mol% powder sample was obtained by a slow diffusion method. In a typical experiment, 16 mL methanol solution containing 12.8 mmol of $(CH_3)_2NH$ and 12.8 mmol of formic acid was placed at the bottom of a glass tube. Sixteen milliliters methanol solution containing 1.5992 mmol of $ZnCl_2$ and 0.0008 mmol of $MnCl_2$ was gently added on this solution. The tube was sealed, and after 5 days colorless crystals were harvested.

To check the structure of the sample, powder XRD pattern was measured at room temperature. The obtained pattern corresponds to DMAZn (see Figure A.1). No additional impurity phases were detected.
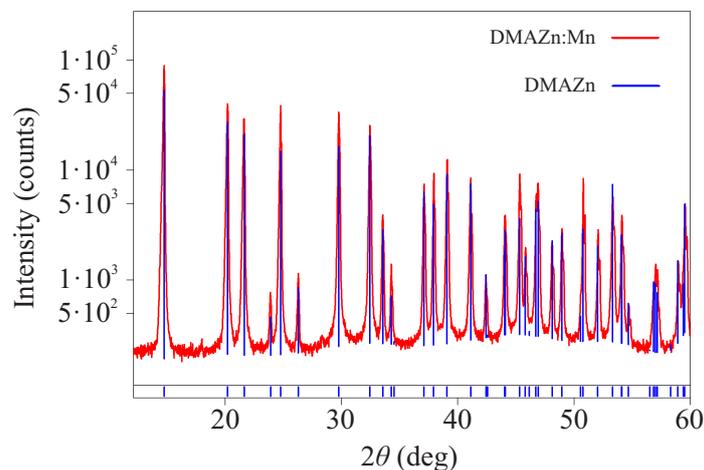

Figure A.1: Powder XRD pattern of **DMAZn:Mn**. For comparison a pattern of pure DMAZn framework is presented in blue [41]. Measured by Prof. Dr. Remigijus Juškėnas at Vilnius University.

DMAZn-15N:Mn powder

To obtain $[(CH_3)_2{}^{15}NH_2][Zn(HCOO)_3]$:0.1 Mn^{2+} mol% powder sample, 2 mmol of dimethylamine-15N hydrochloride was dissolved in 5 mL of methanol and this solution was added to a methanol solution containing 2 mmol of HCOONa. The mixture was stirred for about 20 min., and afterwards a white precipitate was filtered. To the obtained clear and transparent solution, 0.2 mL of formic acid and 10 mL of methanol solution containing 0.999 mmol of $ZnCl_2$ and 0.001 mmol of $MnCl_2$ were added, mixed together and left at room temperature in a glass beaker. The precipitated white crystallites were harvested after 3 days, washed three times with methanol and dried at room temperature.

DMAZn single crystal

DMAZn single crystal sample was synthesized by a slow diffusion method. In a typical experiment, 2.5 mL of 2.0 M solution of $(CH_3)_2NH$ in methanol and

1 mL of formic acid were added to 10 mL of methanol. This solution was placed at the bottom of a glass tube. To this solution was layered 2 mL of methanol, followed by 20 mL of methanol solution containing 1.0 mmol of $ZnCl_2$. The tube was sealed and kept undisturbed. The colorless crystals were harvested after 1 week, washed three times with methanol, and dried at room temperature. XRD was used to determine the crystal axes of the single crystal sample.

DMAZn:Mn single crystal

DMAZn:0.1 Mn^{2+} mol% single crystal sample was synthesized by a slow diffusion method. In a typical experiment, 2.5 mL of 2.0 M solution of $(CH_3)_2NH$ in methanol and 1 mL of formic acid were added to 10 mL of methanol. This solution was placed at the bottom of a glass tube. To this solution was layered 2 mL of methanol, followed by 20 mL of methanol solution containing 0.999 mmol of $ZnCl_2$ and 0.001 mmol of $MnCl_2$. The tube was sealed and kept undisturbed. The colorless crystals were harvested after 1 week, washed three times with methanol, and dried at room temperature. XRD was used to determine the crystal axes of the single crystal sample.

A single crystal sample used for EPR experiments is presented in Figure A.2. A cuboid shape of the crystal was assumed, and the axes of the Cartesian reference frame were chosen to coincide with the edges of the crystal.
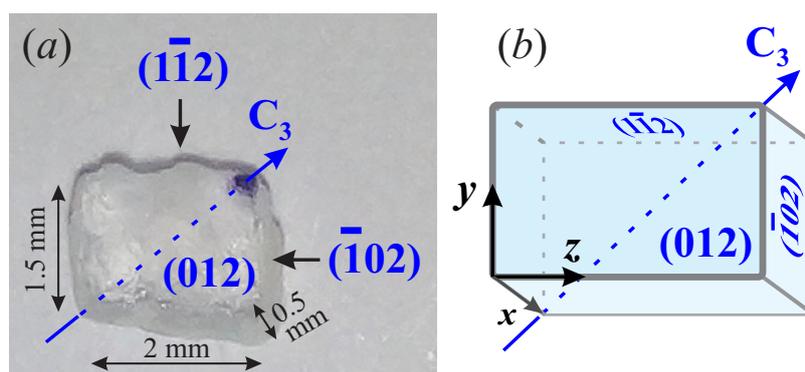

Figure A.2: (a) Photographed and (b) portrayed crystal of **DMAZn:Mn** used for the CW EPR measurements.

AmZn:Mn single crystal

AmZn:0.1 Mn^{2+} mol% single crystal was also obtained by a slow diffusion method. In a typical experiment 20 mL methanol solution containing 20 mmol of $[NH_4][HCOO]$ and 20 mmol of formic acid was placed at the bottom of a glass tube. To this solution was gently added 30 mL of methanol solution containing 1.998 mmol of $ZnCl_2$ and 0.002 mmol of $MnCl_2$. The tube was sealed and kept undisturbed. The colorless crystals were harvested after 1 week, washed three times with methanol, and dried at room temperature. XRD was used to determine the crystal axes of the single crystal sample.

DMAZn:Cu powder

Solution containing 10 mL of methanol, 5 mL of 2.0 M solution of dimethylamine in methanol and 4 mL of HCOOH was placed at the bottom of a glass tube. On this solution, 15 mL methanol solution containing corresponding mixtures of metal salts was gently added to obtain single crystals of DMAZn doped with 0.1, 1, 2, 5 and 10 Cu^{2+} mol%. The tubes were sealed and kept undisturbed. Crystals were harvested after 2 days. The mostly studied sample corresponds to a 1 Cu^{2+} mol% doping (**DMAZn:Cu**).

MHyZn:Mn powder

The manganese doped MHyZn:0.1 Mn^{2+} mol% was synthesized by a slow diffusion method. In this method, 10 mL of methanol solution containing 0.5 mL of methylhydrazine and 2 mL of HCOOH was placed at the bottom of a glass tube. To this solution, 15 mL of methanol solution containing 2 mmol of metal salts was gently added. The tube was sealed and kept undisturbed. Colorless crystals were harvested after 5 days, washed with methanol and dried at room temperature.

MHyZn:Cu powder

To obtain MHyZn:0.3 Cu^{2+} mol%, 0.3 mL of methylhydrazine and 1 mL of formic acid were added to 10 mL of methanol. To this mixture, 15 mL of methanol solution containing 0.997 mmol of $Zn(ClO_4) \cdot 6\,H_2O$ and 0.003 mmol of $CuCl_2$ was added and stirred for 5 minutes. This solution was left undisturbed at room temperature and tiny crystals that grew within a few hours were separated from the liquid, washed 3 times with methanol and dried at room temperature.

MHyZn single crystal

MHyZn single crystal was also synthesized by a slow diffusion method. During the synthesis, 10 mL of methanol solution containing 0.5 mL of methylhydrazine and 2 mL of HCOOH was placed at the bottom of a glass tube. To this solution, 15 mL of methanol solution containing 2 mmol of metal salts was gently added. The tube was sealed and kept undisturbed. Colorless crystals were harvested after 5 days, washed with methanol and dried at room temperature. XRD was used to determine the crystal axes of the single crystal sample.

BnZn:Mn powder

BnZn:0.1 Mn^{2+} mol% was also obtained by a slow diffusion method. In a typical experiment, 15 mL of methanol solution containing 10 mmol of 1,4-diaminobutane and 80 mmol of formic acid was placed at the bottom of a glass tube. On this solution 25 mL of methanol solution containing 1.998 mmol of $ZnCl_2$ and 0.002 mmol of $MnCl_2$ was gently added. The tube was sealed and kept undisturbed. Colorless crystals were harvested after 5 days, washed three times with methanol, and dried at room temperature.

BnZn:Cu powder

To obtain BnZn:1 Cu^{2+} mol%, 15 mL of methanol solution containing 10 mmol of 1,4-diaminobutane and 80 mmol of formic acid was placed at the bottom of

a glass tube. On this solution was gently added 25 mL of methanol solution containing 1.98 mmol of $ZnCl_2$ and 0.02 mmol of $CuCl_2$. The tube was sealed and kept undisturbed. Colorless crystals were harvested after 5 days, washed three times with methanol, and dried at room temperature.

BnZn single crystal

Single crystal of BnZn was obtained using a slow diffusion method. In a typical experiment, 15 mL of methanol solution containing 10 mmol of 1,4-diaminobutane and 80 mmol of formic acid was placed at the bottom of a glass tube. On this solution, 25 mL of methanol solution containing 2 mmol of metal salt was gently layered. The tube was sealed and kept undisturbed. Colorless BnZn crystals were harvested after 5 days, washed 3 times with methanol and dried at room temperature.

Appendix B

EPR and ENDOR Experimental Details

CW EPR spectroscopy

A Bruker E580 spectrometer was used to perform the X-band (~ 9.5 GHz) CW EPR experiments. The Q-band (~ 34 GHz) CW EPR spectra were recorded with a Bruker EMX 10-40 spectrometer. A Bruker E680 spectrometer was employed for the W-band (~ 95 GHz) CW EPR experiments. Most of the CW EPR experiments were performed using a modulation field of 0.4 mT and 100 kHz. The sample temperature at X-band was determined using a T-type thermocouple placed next to the sample in the EPR tube. During the measurements, the temperature stability was ± 0.1 K.

CW EPR spectroscopy with applied external electric field

The X-band CW EPR experiments with simultaneously applied external electric field were performed using a Bruker E580 spectrometer. For the measurements, two parallel silver paste electrodes were applied on single crystal samples that were glued to the plastic rod using nail polish. The electrodes were connected to a DC voltage supply by two thin copper wires that were introduced into the ER 4102ST rectangular cavity. No parasitic EPR signals were detected for the empty

setup. Electric field up to 12 kV/cm was used for poling of the samples. Most of the measurements were performed after cooling the samples in the applied electric field while keeping the crystal at the same position. The quality of the electric contact was checked after and before the EPR measurements by a Fluke PM6304 RCL meter.

Pulsed EPR and ENDOR spectroscopy

A Bruker E580 EPR spectrometer was used for pulsed EPR and ENDOR measurements at X-band microwave frequency. Pulsed EPR experiments at Q- and W-band frequencies were performed with Bruker E600 and E680 spectrometers. The 2p echo-detected field sweep, 2p and 3p ESEEM experiments were recorded using nonselective microwave pulses. The typical $\pi/2$ microwave pulse length was $t_{\pi/2} = 16$ ns. The baselines of the obtained ESEEM time-domain patterns were corrected by subtracting exponential decays. The remaining signals were Fourier transformed to the frequency-domain spectra. The longitudinal relaxation time T_1 was determined using the inversion recovery pulse sequence. The temperature dependent relaxation time measurements were performed on heating. For most of the ENDOR experiments, the Mims pulse sequence was used with the microwave and radiofrequency pulse lengths of $t_{\pi/2} = 16$ ns and $t_{RF} = 10$ μs, respectively. To avoid the suppression effects (blind spots), the 3p ESEEM and Mims ENDOR experiments were performed using different values of the interpulse delay τ. Spectral simulations were performed using EasySpin 5.1.5 simulation software [96].
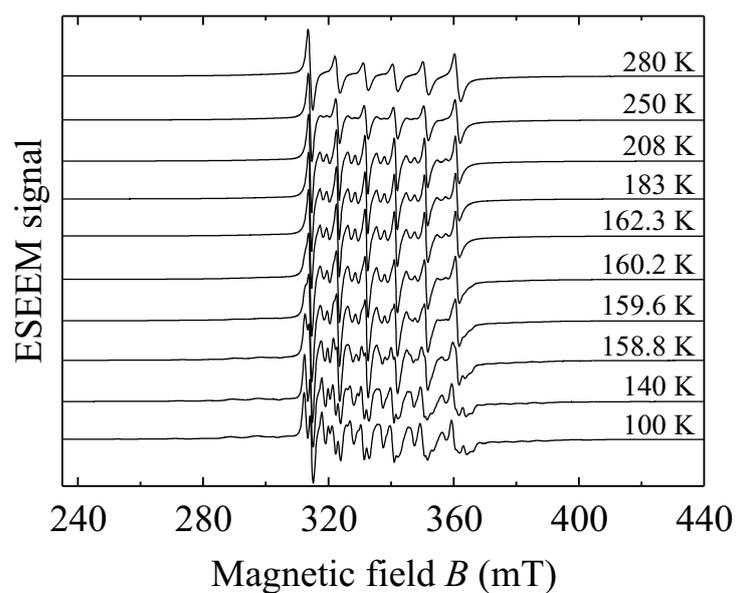
Appendix C

Additional EPR Data

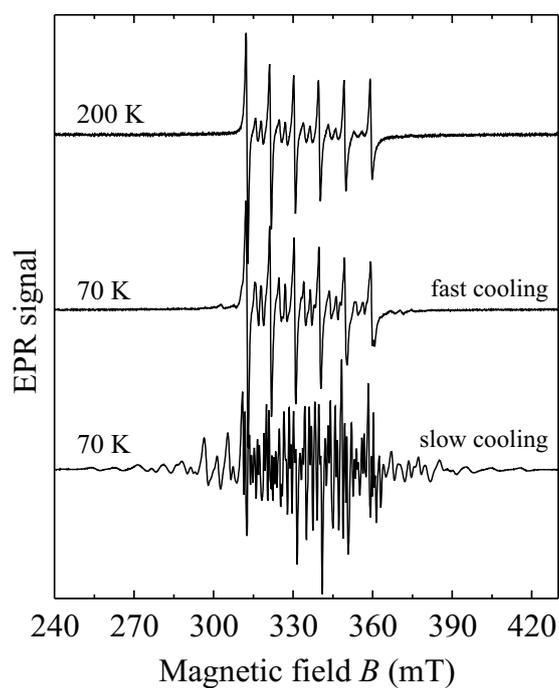Figure C.1: Normalized temperature dependent X-band CW EPR spectra of **DMAZn-15:Mn**.

Figure C.2: Single crystal X-band CW EPR spectra of **DMAZn:Mn** measured at arbitrary orientation after a rapid and slow cooling of the sample to 70 K. The spectrum recorded at 200 K at the same orientation is presented for comparison.
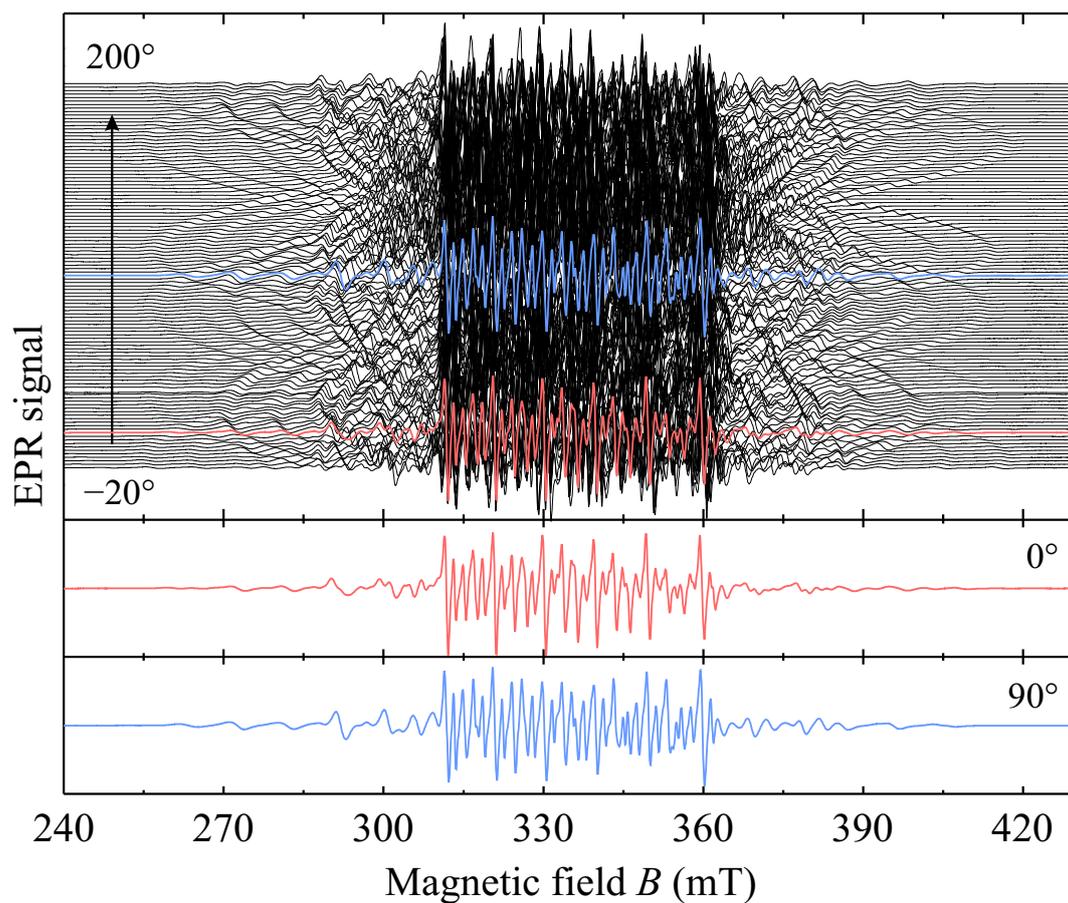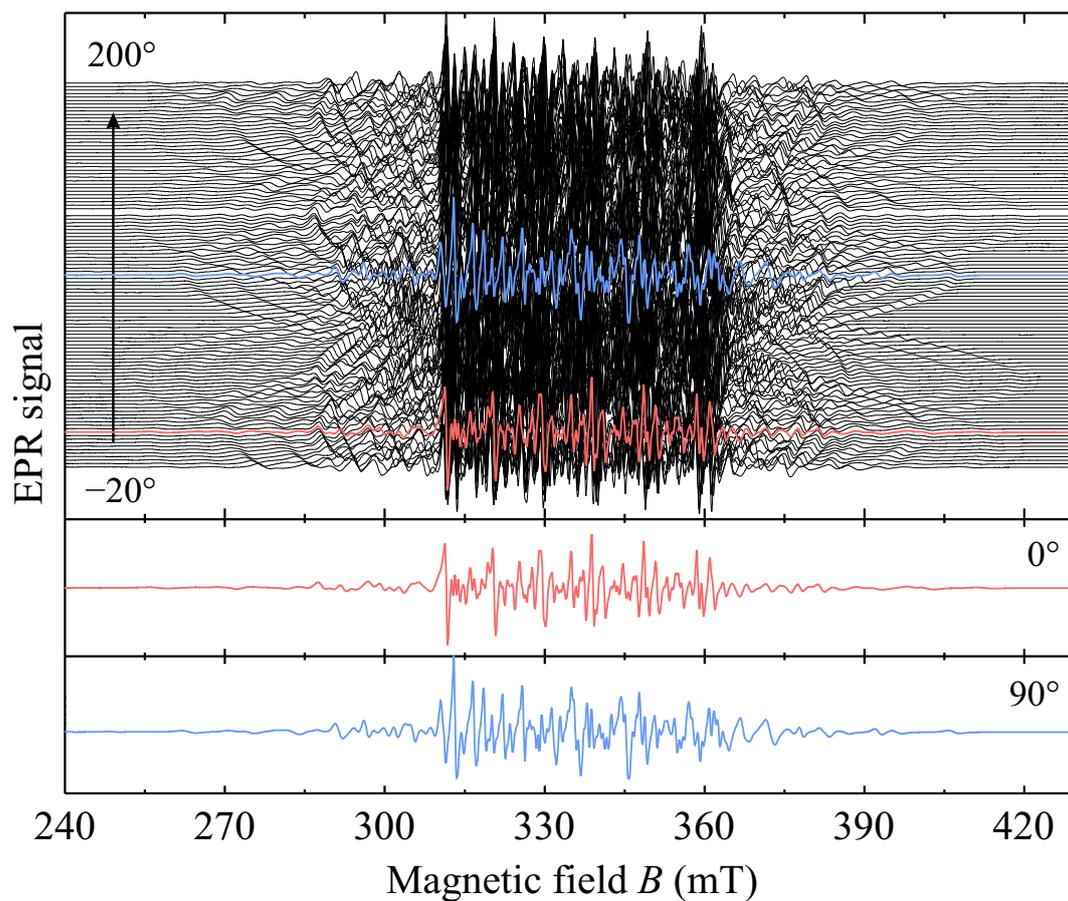
Figure C.3: Angular dependent CW EPR spectra of **DMAZn:Mn** single crystal obtained at 70 K by rotating the magnetic field vector in the $(\bar{1}02)$ plane. Spectra recorded at $0°$ and $90°$ are explicitly presented. The zero angle corresponds to the magnetic field vector in the (012) plane. Measurements performed by Anastasia Kultaeva at Leipzig University.
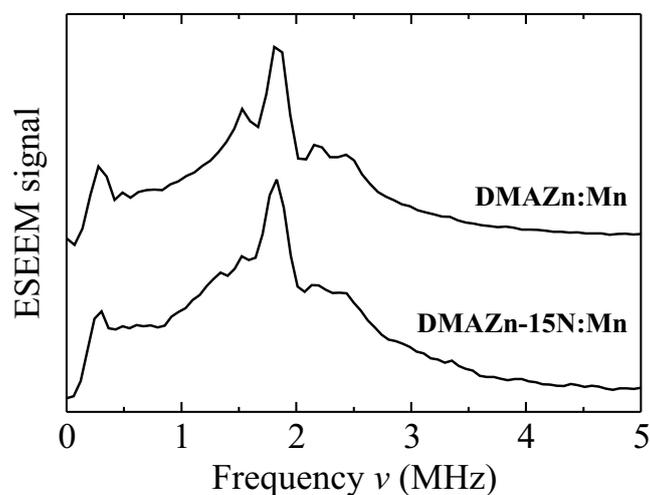
Figure C.4: Angular dependent CW EPR spectra of **DMAZn:Mn** single crystal obtained at 70 K by rotating the magnetic field vector in the (012) plane. Spectra recorded at 0° and 90° are explicitly presented. The zero angle corresponds to the magnetic field vector in the ($\bar{1}$02) plane. Measurements performed by Anastasia Kultaeva at Leipzig University.

Figure C.5: Comparison of the low-frequency 3p ESEEM signal of **DMAZn:Mn** and **DMAZn-15N:Mn**. Measurements performed at 325 mT, $\tau = 144$ ns and 10 K.
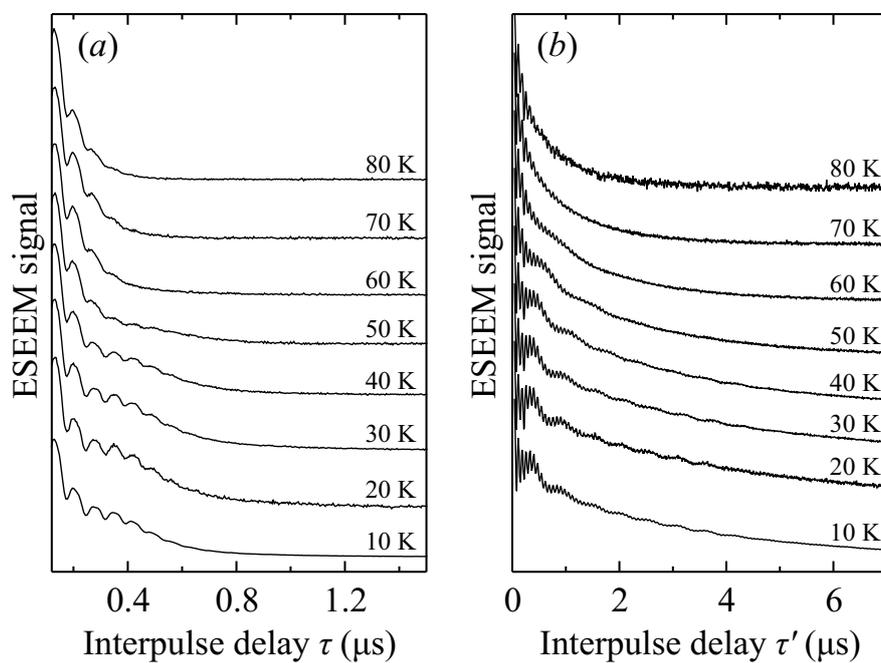

Figure C.6: X-band time-domain traces of (a) 2p and (b) 3p ESEEM experiments of **DMAZn:Mn** recorded at 325 mT and different temperatures. 3p ESEEM measurements were performed at $\tau = 108$ ns.
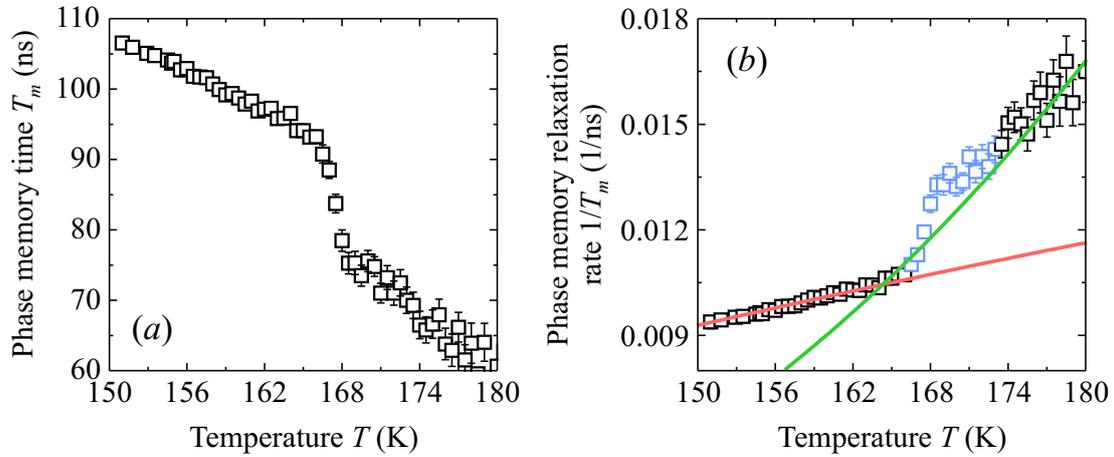
Figure C.7: Temperature dependence of the phase memory relaxation (a) time and (b) rate of the Mn^{2+} centers in **DMAZn:Mn** in the vicinity of the phase transition. The curves in (b) mark the Arrhenius processes with activation energies of 17(1) meV (red) and 78(5) meV (green), while the blue data points correspond to the phase transition region.
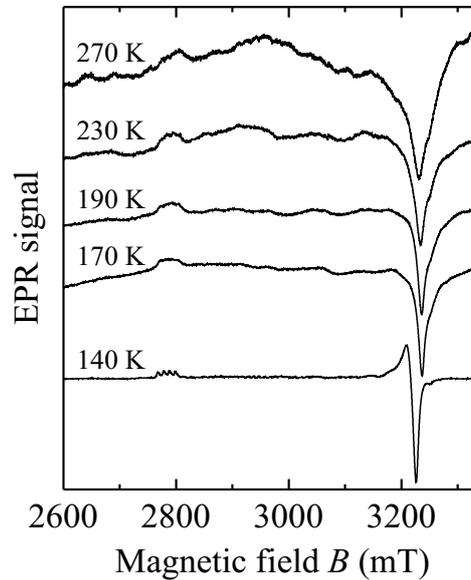

Figure C.8: Normalized temperature dependent W-band CW EPR spectra of Cu^{2+} ions in **DMAZn:Cu**.
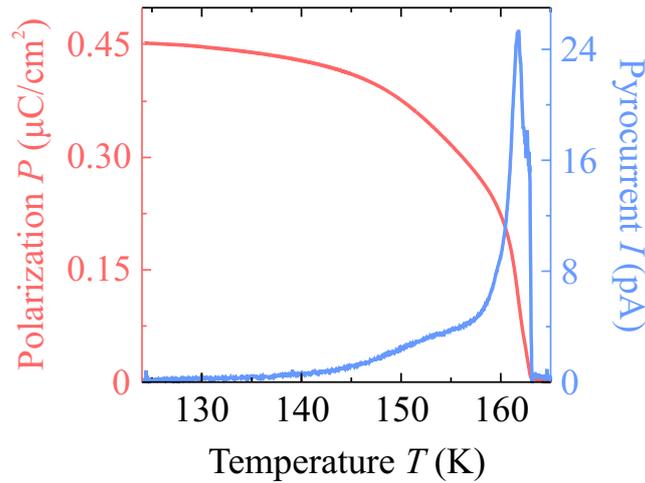
Appendix D

Additional Experimental Data

Figure D.1: Temperature dependence of the pyroelectric current and the corresponding electric polarization of **DMAZn** single crystal. Measurement performed along the [012] direction with poling field of $4.3\,\mathrm{kV/cm}$. The opposite poling field reverses the pyrocurrent.

The temperature dependence of the complex dielectric permittivity $\varepsilon^* = \varepsilon' - i\varepsilon''$ of **DMAZn** single crystal is presented in Figure D.2. An anomalous behavior is observed at T_0, as a significant decrease of ε' and ε''. This anomaly becomes weaker at higher frequencies, since the maxima of ε' and ε'' are shifted to higher temperatures. The permittivity ε^* is only slightly affected by the phase transition for frequencies above approximately 10 MHz.
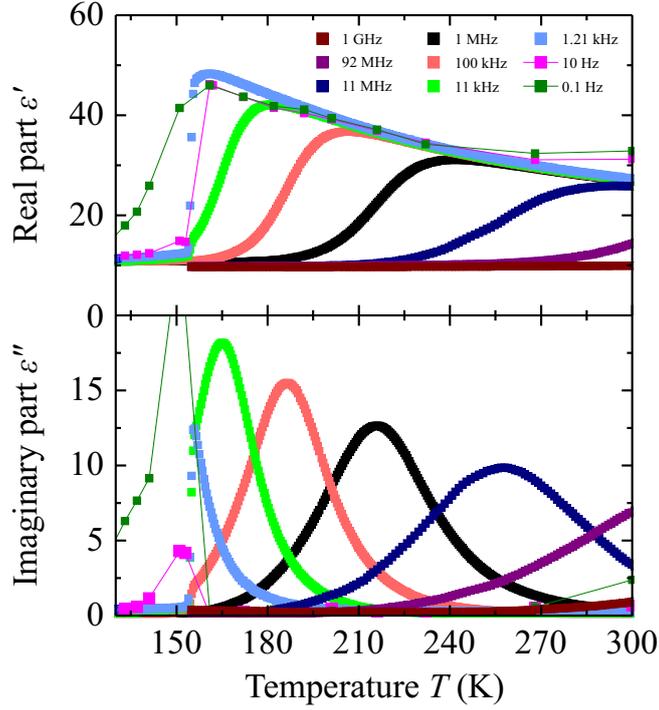
Figure D.2: Broadband temperature dependent complex dielectric permittivity of **DMAZn** single crystal. Measurement performed along the [012] direction.

The spectra of the dielectric permittivity are presented in Figure D.3a for several selected temperatures. The spectra recorded at $T > T_0$ reveal a typical relaxation process of the electric dipoles that can be well approximated using the Cole-Cole equation [145]:

$$\varepsilon^*(\omega) = \varepsilon(\infty) + \frac{\Delta\varepsilon}{1 + (i\omega\tau)^{1-\alpha}}. \tag{D.1}$$

Here $\varepsilon(\infty)$ is the dielectric permittivity in the infinite-frequency limit and $\Delta\varepsilon$ is the dielectric strength of the relaxation. Parameter τ is the mean relaxation time, and $\omega = 2\pi\nu$ denotes the angular measurement frequency. The parameter α determines the relaxation width. For $\alpha = 0$, Eq. D.1 reduces to the Debye relaxation.

The determined temperature dependence of τ is presented in Figure D.3b revealing the Arrhenius process with the activation energy of $E_a = 0.27(1)$ eV in a close agreement with the CW EPR results.
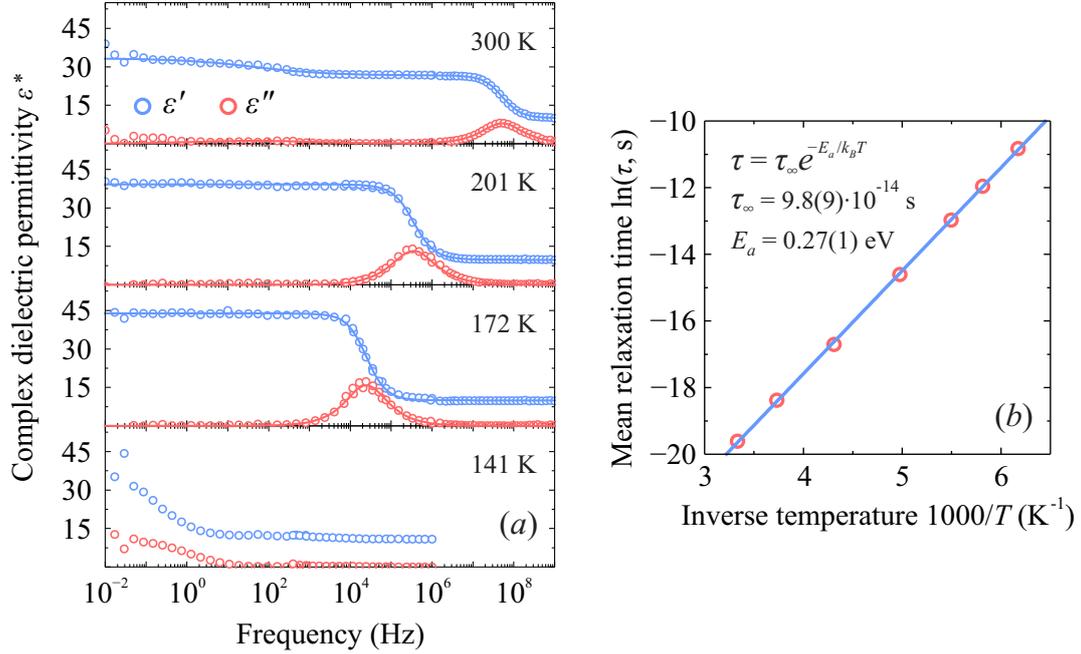
Figure D.3: (a) Frequency dependence of the complex dielectric permittivity of **DMAZn** for several selected temperatures. The solid curves are the best fits to the Cole-Cole relaxation model. (b) Inverse temperature dependence of the mean relaxation time.

The observed temperature dependence of the spin-lattice relaxation time of ^{15}N in **DMAZn-15N:Mn** is presented in Figure D.4. It was analyzed using the following equation [114]:

$$T_1^{-1} = \frac{C\tau}{1 + \omega_N^2 \tau^2},$$ (D.2)

where C is a constant, ω_N is the Larmor frequency of ^{15}N, and τ denotes the correlation time of motion. It is assumed that τ follows the Arrhenius law as

$$\tau = \tau_\infty e^{E_a/k_B T}.$$ (D.3)

Here τ_∞ is the correlation time at infinite temperature. The best fit of the minimum using Eq. D.2 is also presented in Figure D.4. The fit parameters are: $C = 1.8(3) \times 10^9$ s^{-2}, $\tau_\infty = 1.5(3) \times 10^{-12}$ s and $E_a = 0.20(1)$ eV. The obtained values of C and τ_∞ are similar to the values reported in other NMR studies of DMAZn [48, 54, 55]. The value of parameter C provides the N−H distance of 1.06(3) Å, which is in a very good agreement with previous ^{1}H NMR and XRD

studies [41, 55].

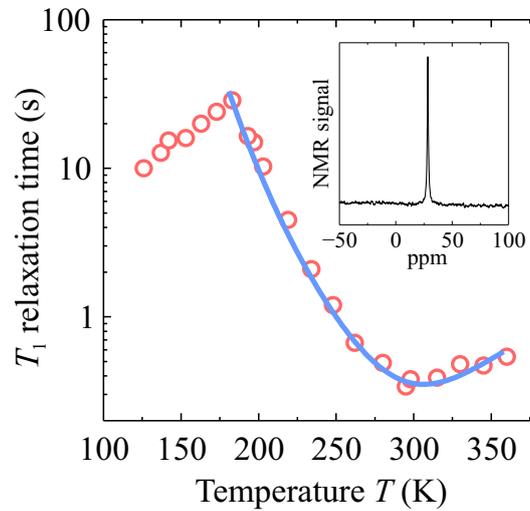Figure D.4: Temperature dependence of the spin-lattice relaxation time of ^{15}N in **DMAZn-15N:Mn**. The spectrum obtained using MAS at 300 K is presented in the inset. The blue curve marks the best fit to Eq. D.2.

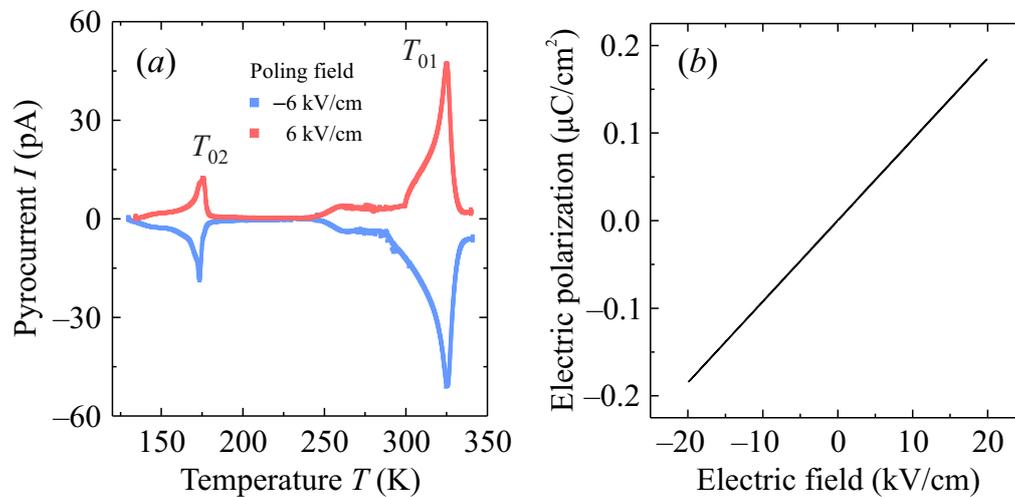Figure D.5: (a) Temperature dependence of the pyroelectric current of **MHyZn**. (b) Electric field dependence of the electric polarization of **MHyZn** obtained at 168 K. Measurements performed along the axis perpendicular to the (035) plane.

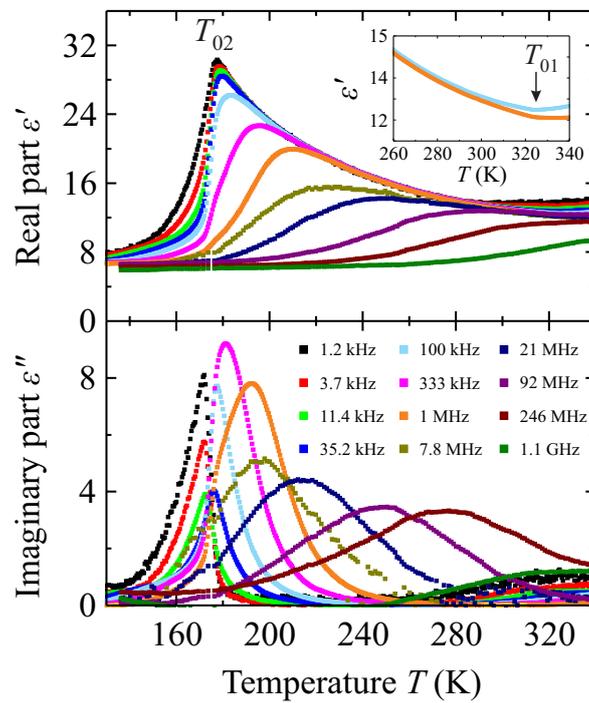Figure D.6: Broadband temperature dependent complex dielectric permittivity of **MHyZn** single crystal. Measurement performed along the axis perpendicular to the (035) plane.
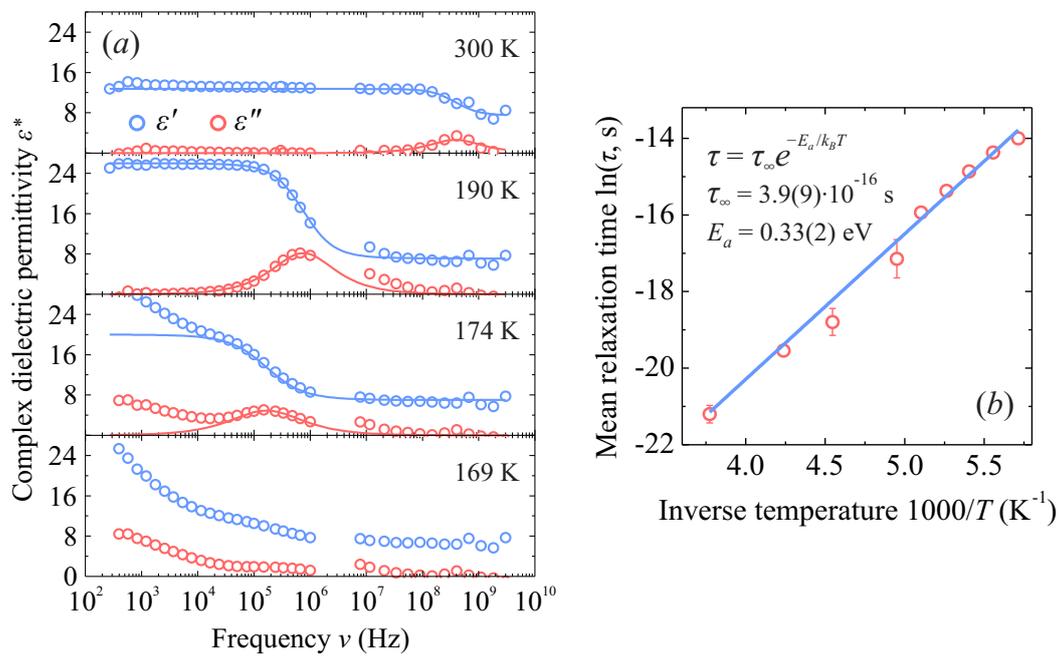
Figure D.7: (a) Frequency dependence of the complex dielectric permittivity of **MHyZn** for several selected temperatures. The solid curves are the best fits to the Cole-Cole relaxation model. (b) Inverse temperature dependence of the mean relaxation time.
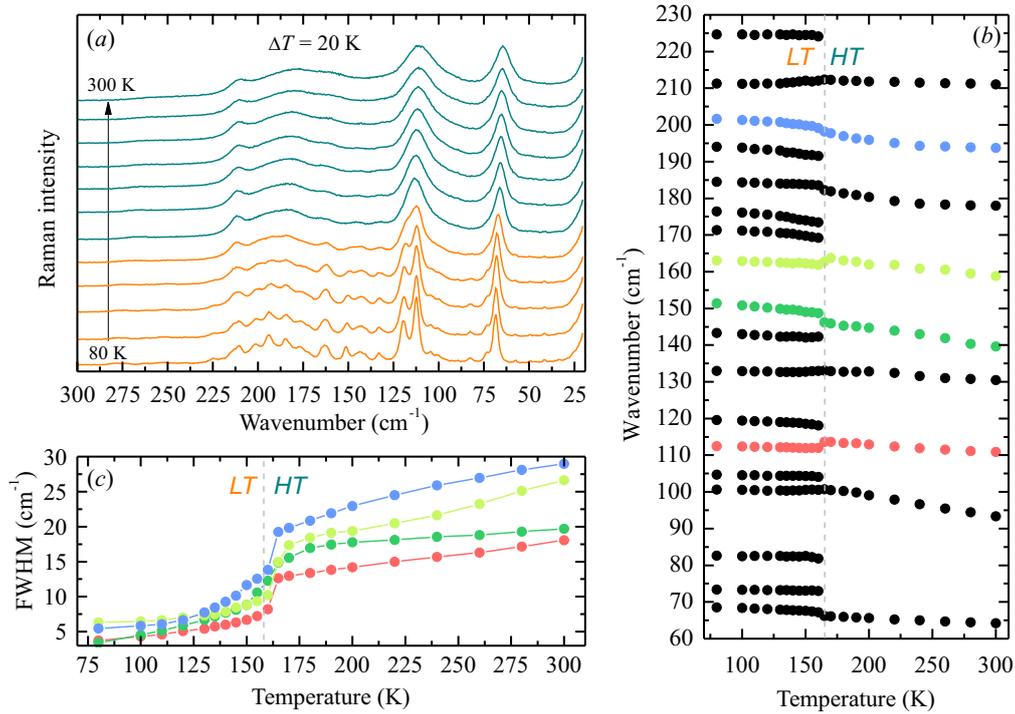
Figure D.8: (a) Temperature-dependent Raman spectra of **MHyZn:Mn**, (b) temperature dependence of the selected Raman wavenumbers and (c) temperature dependence of the FWHM for the 194 cm^{-1} (blue), 159 cm^{-1} (magenta), 140 cm^{-1} (green) and 111 cm^{-1} (red) Raman bands. Measurements performed in Prof. Dr. Mirosław Mączka group at Institute of Low Temperature and Structure Research.

Figure D.9: (a) Temperature dependence of the pyroelectric current of **BnZn**. (b) Electric field dependence of the electric polarization of **BnZn** measured above and below the phase transition temperature. Measurements performed along the c-axis.

Appendix E

Additional Theoretical Data

E.1 Monte Carlo simulations of phase transitions in hybrid perovskites

A proper microscopic description of the observed phase transition in DMAM family requires a detailed examination of the experimentally determined 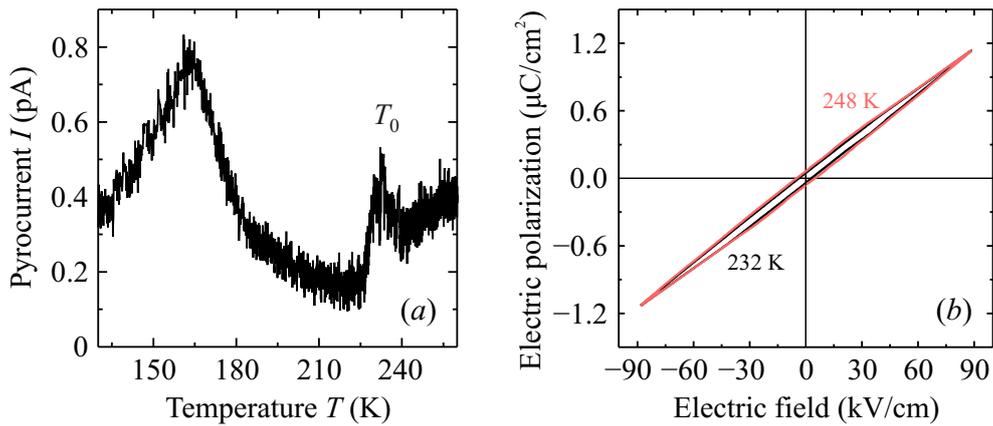framework structures. As a representative of this family DMAMn compound was chosen, since its structure is known in both phases [41]. It is believed that the other members except for DMACu are isostructural to DMAMn [8].

The structures of the disordered and ordered phases of DMAMn compound are presented in Fig. E.1. The $Mn(HCOO)_3^-$ cages in this framework can be divided into two types: A and B. In each cage, the DMA^+ cation can be in one of the three states. However, the states in A and B are different and thus in total there are six cation states which are denoted $s = \{1, 2, 3, 4, 5, 6\}$. All six states are depicted in Fig. E.2. In the A cage the cation can be in one of the first three states (1, 2 or 3), while the remaining states (4, 5 or 6) can be realized only in the B cages. In the ordered phase, the cation, depending on the cage type, is either in the $s = 1$ or $s = 4$ state. We denote such a ground state as GS_{14}. The symmetry dictates that there exist two other possible ground states: GS_{25} and GS_{36}.

For simplicity of the model, the structure of DMAMn is mapped onto the simple cubic lattice with lattice constant a (see Fig. E.2c). Then two cage types are
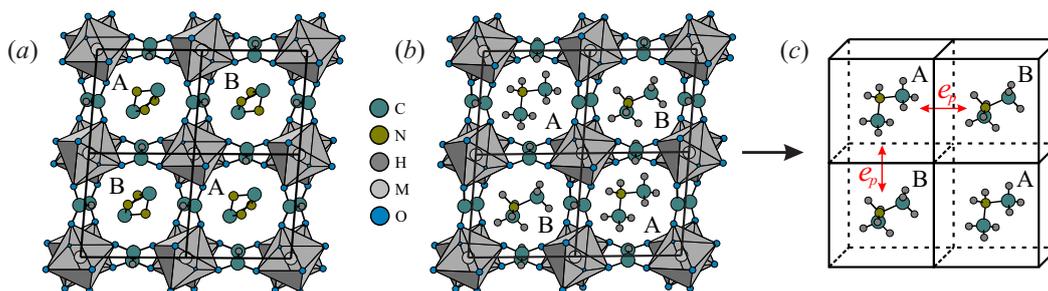
Figure E.1: Structure of DMAMn in the (a) high- and (b) low-temperature (GS$_{14}$) phases. In (c) the mapping to the simple cubic lattice is presented. In (a) the hydrogen atoms of the DMA$^+$ cation are not indicated, while the cation itself is shown as a superposition of three possible states. A and B denote two types of cages/sublattices. Red arrows in (c) indicate the nearest neighbor Potts type interactions.

transformed into two sublattices which again are denoted as A and B.
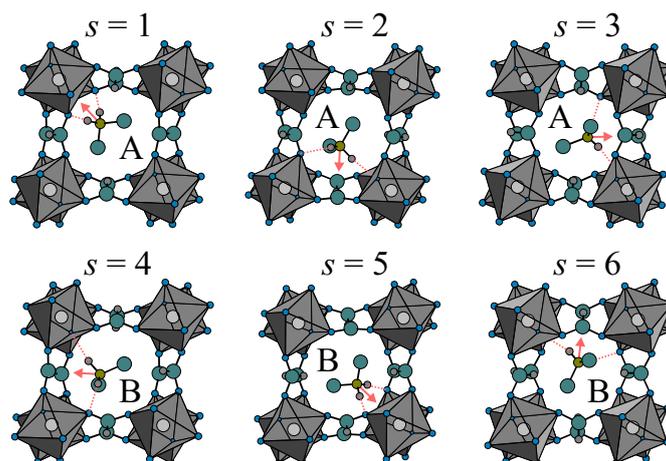
Figure E.2: Model states of the DMA$^+$ cation. Dashed red segments indicate N-H$\cdots$O H-bonds between the molecular cations and cages. Red arrows mark directions of the electric dipole moment vectors obtained using DFT calculations. For clarity, the methyl group hydrogen atoms are not shown.

It is expected that the phase transition in DMAM frameworks is mainly driven by the formation of the H-bonds between the oxygen atoms from the MO$_6$ octahedra and hydrogens from the DMA$^+$ cations [8]. The established bonds significantly deform the octahedra, as demonstrated by the CW EPR study. This in turn influences the whole Mn(HCOO)$_3^-$ cage causing a certain state of the neighboring cation. In the proposed model, the inter-cation influence mediated

via the metal-formate cages is mimicked by the effective Potts type interaction. Such interaction acts directly between the cation states leaving the cages aside.

The simplest case of the Potts type interaction between the cations can be realized on the first nearest neighbors (1NN). The corresponding Hamiltonian is expressed using the Kronecker delta δ representation as

$$\mathcal{H}_p = -e_p \sum_{<ij>} [\delta(s_i, 1)\delta(s_j, 4) + \delta(s_i, 2)\delta(s_j, 5) + \delta(s_i, 3)\delta(s_j, 6)]. \tag{E.1}$$

Here, for example, $\delta(s_i, 1)$ is equal to one whenever $s_i = 1$ and zero otherwise. The indices i and j enumerate the lattice (cation) sites. Such a representation ensures that the 1NN interaction is between either 1 and 4, 2 and 5 or 3 and 6 states only. Interaction between other states (e.g. 1 and 5) is neglected. The parameter e_p denotes the interaction strength and the sum is performed over the 1NN sites only.

Additionally, a symmetry of the DMA$^+$ cation indicates that it should possess a substantial electric dipole moment $\vec{p}$. Therefore, the dipole-dipole interactions between the cation states are also considered in the model. Note, previous DFT studies of [CH$_3$CH$_2$NH$_3$][Mn(HCOO)$_3$] [146] and [C(NH$_2$)$_3$][M(HCOO)$_3$] frameworks [147] revealed that the main contribution to the total polarization arises from the A$^+$ cations. The Hamiltonian describing the dipole-dipole interaction is

$$\mathcal{H}_{dd} = e_{dd} \sum_{i,j} \frac{\hat{p}_i \cdot \hat{p}_j - 3(\hat{p}_i \cdot \hat{r}_{ij})(\hat{p}_j \cdot \hat{r}_{ij})}{r_{ij}^3}. \tag{E.2}$$

Here $\hat{p}_i$ is the unit vector of the corresponding electric dipole moment at the lattice site i: $\vec{p}_i = p_0\hat{p}_i$. The r_{ij} and $\hat{r}_{ij}$ are the absolute value and the unit vector of $\vec{r}_{ij}$ which is a vector joining dipoles $\vec{p}_i$ and $\vec{p}_j$ situated at the lattice sites i and j, respectively. The parameter e_{dd} describes the characteristic dipole-dipole interaction energy and can be expressed as

$$e_{dd} = \frac{p_0^2}{4\pi\epsilon\epsilon_0 a^3} \tag{E.3}$$

where ϵ is the dielectric constant of the framework.

To determine a reasonable range of e_{dd} values, DFT calculations were performed

to estimate the dipole moment p_0 of a single isolated DMA$^+$ cation. The XRD determined structure [41] of the cation was used and the calculations were performed using B3LYP functional and 6-31G(2d,2p) basis set implemented in Orca 3.0.2 package [148]. The obtained magnitude is $p_0 = 1.28$ D. According to Eq. (E.3), the obtained p_0 results in e_{dd} of approximately 50 K. This value is certainly lower compared with the observed ordering temperature of about 160 K confirming that the dipole-dipole interaction, though being important, is not the main cause of the phase transition. In the model, the Potts type interaction (effectively related to the H-bond formation) is considered as the driving factor of the ordering. Consequently one obtains the ratio of interaction parameters to be $e_{dd}/e_p \sim 0.3$. Note that in DFT calculations, the influence of the charged $M(HCOO)_3^-$ cages was ignored, tough they may alter the electron distribution in the molecular cation resulting in a different value of p_0. Thus, in the most of the MC calculations, the parameter e_{dd}/e_p was varied from 0 up to 0.9.

The final Hamiltonian of the model is the sum of the Potts type (Eq. E.1) and dipolar (Eq. E.2) terms:

$$\mathcal{H} = \mathcal{H}_p + \mathcal{H}_{dd}. \tag{E.4}$$

It was numerically studied using MC simulations based on the typical single-flip Metropolis algorithm. All simulations were performed on a simple cubic lattice of sizes $L = 10, 14, 20$ and 30 (in units of lattice constant a) with implemented periodic boundary conditions. Temperature and e_{dd} parameter were normalized by e_p.

First, the proposed phase transition model was studied by neglecting the dipolar interactions ($e_{dd} = 0$). The calculated temperature dependence of the normalized z-component of the polarization P_z for $L = 20$ is presented in Fig. E.3a. A discontinuous increase of P_z is observed suggesting a first-order phase transition from the disordered phase to GS$_{14}$, GS$_{25}$ or GS$_{36}$ ground state. The obtained normalized phase transition temperature $T_0 = 1.81$ is the same as found for the well-known ferromagnetic 3-state Potts model in 3D [149]. It is known that the 3-state 3D Potts model exhibits a weak first-order phase transition demonstrating that the chosen model correctly accounts for the type of the phase transition observed in DMAM frameworks. However, CW EPR experiments of **DMAZn:Mn** revealed that the phase transition in DMAZn is of strong first-order
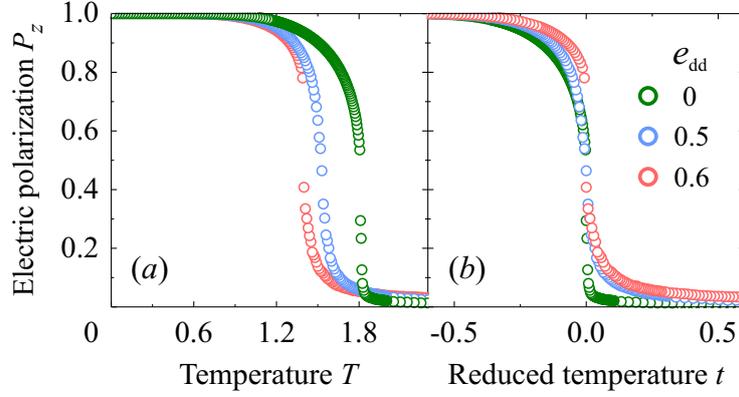
character (see Figure 3.4).

Figure E.3: (a) Temperature and (b) reduced temperature ($t = (T - T_0)/T_0$) dependence of P_z of DMAM calculated at different values of e_{dd} and $L = 20$.

This discrepancy was investigated by including the dipole-dipole interactions in our simulations. Calculated temperature dependences of the normalized polarization for $e_{dd} = 0.5$ and 0.6 are presented in Fig. E.3a. Besides the shift of the phase transition temperature T_0, the shape of the P_z curves is also modified by the dipolar interactions. The differences are better noticeable in Fig. E.3b. The obtained dependences demonstrate that the jump of P_z is slightly sharper for $e_{dd} = 0.6$ compared to 0 and 0.5. Additionally, below the phase transition temperature, the polarization saturates faster for higher values of e_{dd} indicating that dipolar interactions are necessary to obtain a better agreement with the experimental data.

The positive dipolar energy of the GS_{14}, GS_{25} and GS_{36} structures suggests that for sufficiently high e_{dd} these orderings may become unstable resulting in different ground states. It was found that the ground state remains uniform (i.e. either GS_{14}, GS_{25} or GS_{36}) up to $e_{dd} \approx 0.55$ (see Fig. E.4a). However, stronger dipolar interactions cause ordering into structures composed of interpenetrating layers of GS_{14}, GS_{25} and GS_{36}. A typical layered configuration formed of GS_{14} and GS_{25} at $e_{dd} = 0.6$ is presented in Fig. E.4b. For very strong dipolar interaction ($e_{dd} \gtrsim 0.9$), a ground state consisting of the interpenetrating GS_{14} and GS_{25} monolayers was obtained (Fig. E.4c).

A very similar phase transition model was also used to describe the ordering and charge screening in related methylammonium (MA) lead halide (MAPbX$_3$,
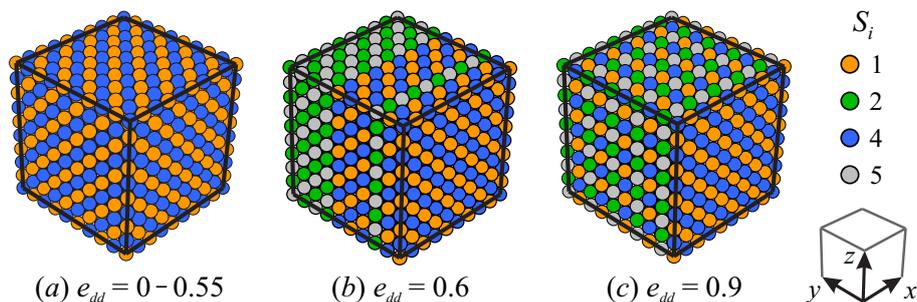
Figure E.4: Orderings at low temperature obtained for (a) $e_{dd} = 0$-0.55 (GS$_{14}$), (b) $e_{dd} = 0.6$ (a typical layered structure) and (c) $e_{dd} = 0.9$ (ground state formed by the interpenetrating monolayers). Color coding is used to differentiate between different cation states.

where X = I, Br or Cl) frameworks [150, 151]. These compounds attract exceptional attention of the scientific community due to their potential application as effective and affordable solar cells [28].

The temperature dependence of the heat capacity C_V of the phase transition model is presented in Figure E.5a revealing two anomalies at 315 and 155 K. They correspond to the two structural transitions from the cubic to tetragonal and from tetragonal to orthorhombic phases. The phase transition at 315 K is caused by the short-range interactions (similar to the Potts-type interactions used for DMAM family). The anomaly at 155 K is absent for $e_{dd} = 0$ indicating that the dipolar interactions between the cations are responsible for the low-temperature phase transition. In contrast, the peak of C_V at 315 K is weakly affected by these interactions. Figure E.5b presents the temperature dependent electric polarization of MA$^+$ cations.

The arrangement of the MA$^+$ cations in different phases are presented in E.6. There is no long-range order in the cubic phase, since the cations are constantly hopping between the six states. In the tetragonal phase, the cations are partially ordered into two sublattices in the ab-planes. The complete long-range order is established in the orthorhombic phase.
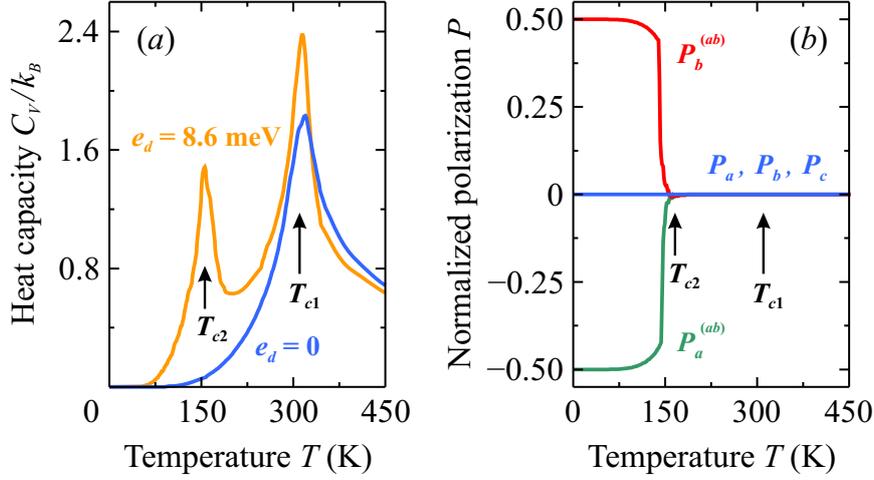
Figure E.5: Temperature dependence of (a) heat capacity and (b) electric polarization of a model describing the ordering in MAPbX$_3$ framework. The C_V curves were calculated for $e_{dd} = 0$ and 8.6 meV. The polarization was obtained for $e_{dd} = 8.6$ meV.
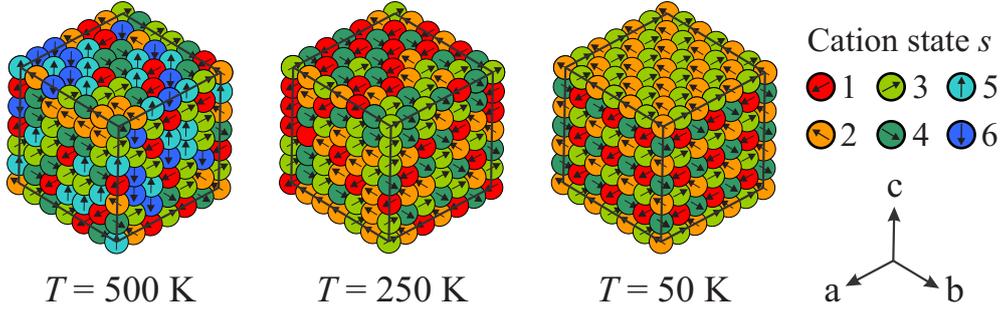
Figure E.6: Snapshots of the MC simulations at different temperatures corresponding to the cubic (left), tetragonal (middle) and orthorhombic (right) phases of MAPbX$_3$ frameworks. The MA$^+$ cation states are color-coded, and the dipole moments are indicated by the arrows.

E.2 DFT calculations of EPR parameters

DMAZn:Mn

All computations of the proton hf coupling tensors were carried out using the unrestricted DFT framework as implemented in Orca 3.0.3 program [148]. The experimental low-temperature crystal structure of DMAMn [41] was used for

calculations. Figure E.7 depicts the used geometry which includes a single Mn^{2+} ion coordinated by six formate linkers and surrounded by eight nearest DMA$^+$ cations. The total charge of this system is +4.
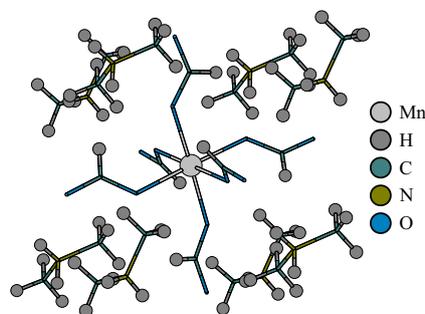
Figure E.7: Fragment of the low-temperature crystal structure used for DFT calculations of **DMAZn:Mn** EPR parameters.

The PBE0 exchange-correlation functional [152] along with the EPR-II double-zeta basis set [153] was selected for the organic moieties, whereas the aug-cc-pVDZ basis set [154] was adopted for the metal atom. The resolution of the identity approach, the so-called RIJCOSX method [155] as implemented in Orca, was utilized using the auxiliary aug-cc-pVDZ basis set in order to speed up the hybrid DFT calculations. The Lebedev 770 points grid was selected for the computation of the two-electron integrals. The tight criterion for the SCF procedure was chosen. The Fermi contact and spin dipolar contributions to the hf coupling tensors were computed, so that the spin-orbit contribution was ignored. The most significant calculated proton hf tensors are listed in Table E.1.

DMAZn:Cu

To model the local structure around the Cu^{2+} ion, the experimental low-temperature structure of DMAMn framework [41] was considered as a starting point. The molecular system was constructed in such a way that the Cu^{2+} ion is coordinated by six adjacent formate anionic linkers, each of which is in turn coordinated by the Zn^{2+} ions. Eight DMA$^+$ cations closest to the copper atom were also retained, making the entire molecular cluster to possess the total charge of +16. A partial geometry optimization of this system was performed where the positions of all Zn^{2+} ions as well as of carbon and nitrogen atoms in the DMA$^+$ moieties

Origin of ^{1}H	$\boldsymbol{A}^{\text{H}} = [A_{xx}, A_{yy}, A_{zz}]$ (MHz)
HCOO$^-$ linkers	[-2.39, -2.54, 4.76]
	[-2.36, -2.49, 4.84]
	[-2.50, -2.65, 5.13]
	[-2.57, -2.70, 5.23]
	[-2.53, -2.69, 5.22]
	[-2.41, -2.58, 5.01]
NH$_2$ groups	[-1.55, -1.63, 3.23]
	[-1.42, -1.49, 2.89]
CH$_3$ groups	[-1.27, -1.29, 2.55]
	[-1.07, -1.10, 2.17]
	[-1.19, -1.22, 2.42]
	[-1.58, -1.61, 3.19]*
	[-1.28, -1.33, 2.61]
	[-1.12, -1.14, 2.26]

Table E.1: The most significant ^{1}H hf tensors of **DMAZn:Mn** obtained by DFT calculations. The tensor indicated by the asterisk was adjusted to [-1.7, -1.7, 3.4] MHz to fit the experimental data.

were fixed to their experimental positions. The rest of the geometry was optimized using the unrestricted DFT approach. The B3LYP exchange-correlation functional [156] and the 6-31G* basis set [157] were utilized along with the pruned grid having 99 radial shells and 590 angular points for the computation of the two-electron integrals. Gaussian 09 program was used for the geometry optimization.

The EPR parameters were calculated for the optimized geometry which was modified by removing all Zn^{2+} ions (see Figure E.8). The unrestricted DFT framework as implemented in Orca 4.0.1 program [148] was employed. The *g*-tensor was calculated using the PBE0 exchange-correlation functional [152] and Dunning type cc-pVDZ basis set [158]. The spin-orbit coupling contribution to the *g*-tensor was accounted for by using a mean-field approach [159]. The Cu^{2+} hf coupling tensor was computed using the TPSS functional [160] along with the CP(PPP) basis set [161] for copper and EPR-II basis set for rest of the atoms. The hf coupling tensor for hydrogen atoms was computed using the same methods except for the basis set for Cu^{2+} ions which was now described using the smaller cc-pVDZ basis set. In addition, the spin-orbit coupling was not accounted for in the latter calculation. The resolution of the identity approach

Origin of ^{1}H	Cu$-^1$H distance (Å)	$\boldsymbol{A}^{\mathrm{H}} = [A_{xx}, A_{yy}, A_{zz}]$ (MHz)
HCOO$^-$ linkers	3.35	$[-0.79, -2.47, 4.05]$
	3.38	$[-1.05, -2.34, 3.65]$
	3.40	$[-1.50, -2.94, 2.99]$
	3.58	$[-1.33, -2.41, 2.64]$
	3.61	$[-1.14, -1.26, 2.51]$
NH$_2$ groups	3.53	$[-1.27, -1.44, 2.67]$
	3.58	$[-1.10, -1.71, 2.77]$
CH$_3$ groups	3.53	$[-1.11, -1.63, 2.77]$

Table E.2: The most significant ^{1}H hf tensors and the corresponding Cu$-^1$H distances for **DMAZn:Cu** calculated by DFT.

was used in all DFT calculations of EPR parameters [155].
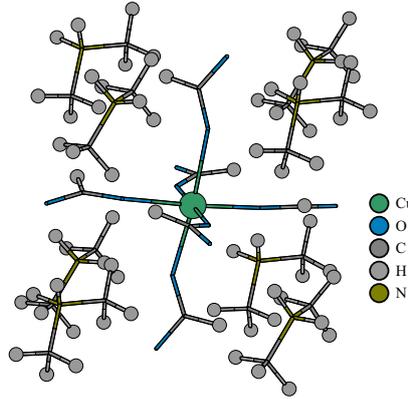
Figure E.8: Fragment of the low-temperature crystal structure used for DFT calculations of **DMAZn:Cu** EPR parameters.

The calculated Cu^{2+} $\boldsymbol{g}$- and $\boldsymbol{A}$ tensor components are: $g_{xx} = 2.084$, $g_{yy} = 2.173$, $g_{zz} = 2.346$, $A_{xx} = 31.9$, $A_{yy} = 191.7$, and $A_{zz} = -390.5$ MHz. The obtained orthorhombic tensors do not agree with the experimentally observed axially symmetric Cu^{2+} site in **DMAZn:Cu**. This likely indicates that the geometry used for DFT calculations is too small, as the defect site is expected to affect a much wider surrounding region. Unfortunately, it was not possible to optimize a bigger geometry due to too many atoms in the unit cell of DMAZn. In addition, the well known problems in calculating the Cu^{2+} EPR parameters may also contribute to the obtained discrepancy [159]. The calculated ^{1}H hf coupling tensors for protons closest to the Cu^{2+} center are presented in Table E.2.

Bibliography

[1] R. Blinc and B. Žekš. *Soft Modes in Ferroelectrics and Antiferroelectrics*. North-Holland Publishing Company (1974).

[2] M. E. Lines and A. M. Glass. *Principles and Applications of Ferroelectrics and Related Materials*. Oxford University Press (2001).

[3] S. Kitagawa, R. Kitaura and S. Noro. Functional Porous Coordination Polymers. *Angew. Chem. Int. Ed.* **43**, 2334 (2004).

[4] M. Guo, H.-L. Cai and R.-G. Xiong. Ferroelectric Metal Organic Framework (MOF). *Inorg. Chem. Commun.* **13**, 1590 (2010).

[5] W. Zhang and R.-G. Xiong. Ferroelectric Metal-Organic Frameworks. *Chem. Rev.* **112**, 1163 (2012).

[6] K. Asadi and M. A. van der Veen. Ferroelectricity in Metal-Organic Frameworks: Characterization and Mechanisms. *Eur. J. Inorg. Chem.* pages 4332–4344 (2016).

[7] P. Jain, N. S. Dalal, B. H. Toby, H. W. Kroto and A. K. Cheetham. Order-Disorder Antiferroelectric Phase Transition in a Hybrid Inorganic-Organic Framework with the Perovskite Architecture. *J. Am. Chem. Soc.* **130**, 10450 (2008).

[8] P. Jain, V. Ramachandran, R. J. Clark, H. D. Zhou, B. H. Toby, N. S. Dalal, H. W. Kroto and A. K. Cheetham. Multiferroic Behavior Associated with an Order-Disorder Hydrogen Bonding Transition in Metal-Organic Frameworks (MOFs) with the Perovskite ABX_3 Architecture. *J. Am. Chem. Soc.* **131**, 13625 (2009).

[9] R. Shang, S. Chen, K.-L. Hu, B.-W. Wang, Z.-M. Wang and S. Gao. A Variety of Phase-Transition Behaviors in a Niccolite Series of $[NH_3(CH_2)_4NH_3][M(HCOO)_3]_2$. *Chem. - Eur. J.* **22**, 6199 (2016).

[10] X.-Y. Wang, L. Gan, S.-W. Zhang and S. Gao. Perovskite-like Metal Formates with Weak Ferromagnetism and as Precursors to Amorphous Materi-

als. *Inorg. Chem.* **43**, 4615 (2004).

[11] M. Mączka, A. Gągor, B. Macalik, A. Pikul, M. Ptak and J. Hanuza. Order-Disorder Transition and Weak Ferromagnetism in the Perovskite Metal Formate Frameworks of $[(CH_3)_2NH_2][M(HCOO)_3]$ and $[(CH_3)_2ND_2][M(HCOO)_3]$ (M = Ni, Mn). *Inorg. Chem.* **53**, 457 (2014).

[12] W. Eerenstein, N. D. Mathur and J. F. Scott. Multiferroic and Magnetoelectric Materials. *Nature* **442**, 759 (2006).

[13] M. Gajek, M. Bibes, S. Fusil, K. Bouzehouane, J. Fontcuberta, A. Barthélémy and A. Fert. Tunnel Junctions with Multiferroic Barriers. *Nat. Mater.* **6**, 296 (2007).

[14] V. K. Jain and G. Lehmann. Electron Paramagnetic Resonance of Mn^{2+} in Orthorhombic and Higher Symmetry Crystals. *Phys. Status Solidi B* **159**, 495 (1990).

[15] F. J. Owens, C. P. Poole and H. A. Farach. *Magnetic Resonance of Phase Transitions*. Academic Press (1979).

[16] B. A. Strukov and A. P. Levanyuk. *Ferroelectric Phenomena in Crystals: Physical Foundations*. Springer-Verlag Berlin Heidelberg (1998).

[17] L. D. Landau and E. M. Lifshitz. *Statistical physics*, volume Volume 5, Part 1. Pergamon, 3 edition (1969).

[18] B. Naranjo, J. K. Gimzewski and S. Putterman. Observation of Nuclear Fusion Driven by a Pyroelectric Crystal. *Nature* **434**, 1115 (2005).

[19] A. K. Tagantsev, K. Vaideeswaran, S. B. Vakhrushev, A. V. Filimonov, R. G. Burkovsky, A. Shaganov, D. Andronikova, A. I. Rudskoy, A. Q. R. Baron, H. Uchiyama, D. Chernyshov, A. Bosak, Z. Ujma, K. Roleder, A. Majchrowski, J.-H. Ko and N. Setter. The Origin of Antiferroelectricity in $PbZrO_3$. *Nat. Commun.* **4**, 2229 (2013).

[20] B. Zalar, V. V. Laguta and R. Blinc. NMR Evidence for the Coexistence of Order-Disorder and Displacive Components in Barium Titanate. *Phys. Rev. Lett.* **90**, 037601 (2003).

[21] G. Völkel and K. A. Müller. Order-Disorder Phenomena in the Low-Temperature Phase of $BaTiO_3$. *Phys. Rev. B* **76**, 094105 (2007).

[22] A. P. Levanyuk and D. G. Sannikov. Improper Ferroelectrics. *Soviet Physics Uspekhi* **17**, 199 (1974).

[23] B. A. Strukov, M. Amin and V. A. Kopchik. Comparative Investigation of the Specific Heat of KH_2PO_4 (KDP) and KD_2PO_4 (DKDP) Single Crystals.

Phys. Status Solidi B **27**, 741 (1968).

[24] P. Opletal, J. Prokleska, J. Valenta, P. Proschek, V. Tkác, R. Tarasenko, M. Behounková, S. Matousková, M. M. Abd-Elmeguid and V. Sechovský. Quantum Ferromagnet in the Proximity of the Tricritical Point. *Npj Quantum Materials* **2**, 29 (2017).

[25] J. Hove, S. Mo and A. Sudbø. Vortex Interactions and Thermally Induced Crossover from Type-I to Type-II Superconductivity. *Phys. Rev. B* **66**, 064524 (2002).

[26] S. T. Meek, J. A. Greathouse and M. D. Allendorf. Metal-Organic Frameworks: A Rapidly Growing Class of Versatile Nanoporous Materials. *Adv. Mater.* **23**, 249 (2011).

[27] W. Li, Z. Wang, F. Deschler, S. Gao, R. H. Friend and A. K. Cheetham. Chemically Diverse and Multifunctional Hybrid Organic-Inorganic Perovskites. *Nat. Rev. Mater.* **2**, 16099 (2017).

[28] H. J. Snaith. Perovskites: The Emergence of a New Era for Low-Cost, High-Efficiency Solar Cells. *J. Phys. Chem. Lett.* **4**, 3623 (2013).

[29] L. J. Murray, M. Dinca and J. R. Long. Hydrogen Storage in Metal-Organic Frameworks. *Chem. Soc. Rev.* **38**, 1294 (2009).

[30] Y. He, W. Zhou, G. Qian and B. Chen. Methane Storage in Metal-Organic Frameworks. *Chem. Soc. Rev.* **43**, 5657 (2014).

[31] R. J. Kuppler, D. J. Timmons, Q.-R. Fang, J.-R. Li, T. A. Makal, M. D. Young, D. Yuan, D. Zhao, W. Zhuang and H.-C. Zhou. Potential Applications of Metal-Organic Frameworks. *Coord. Chem. Rev.* **253**, 3042 (2009).

[32] B. Abrahams, B. Hoskins, D. Michail and R. Robson. Assembly of Porphyrin Building Blocks into Network Structures with Large Channels. *Nature* **369**, 727 (1994).

[33] M. Rosseinsky. Recent Developments in Metal-Organic Framework Chemistry: Design, Discovery, Permanent Porosity and Flexibility. *Microporous Mesoporous Mater.* **73**, 15 (2004).

[34] M. O'Keeffe and O. M. Yaghi. Deconstructing the Crystal Structures of Metal-Organic Frameworks and Related Materials into Their Underlying Nets. *Chem. Rev.* **112**, 675 (2012).

[35] M. D. Allendorf, C. A. Bauer, R. K. Bhakta and R. J. T. Houk. Luminescent Metal-Organic Frameworks. *Chem. Soc. Rev.* **38**, 1330 (2009).

[36] P. Ramaswamy, N. E. Wong and G. K. H. Shimizu. MOFs as Proton

Conductors - Challenges and Opportunities. *Chem. Soc. Rev.* **43**, 5913 (2014).

[37] M. Kurmoo. Magnetic Metal-Organic Frameworks. *Chem. Soc. Rev.* **38**, 1353 (2009).

[38] J. Lee, O. K. Farha, J. Roberts, K. A. Scheidt, S. T. Nguyen and J. T. Hupp. Metal-Organic Framework Materials as Catalysts. *Chem. Soc. Rev.* **38**, 1450 (2009).

[39] H. Wu, Q. Gong, D. H. Olson and J. Li. Commensurate Adsorption of Hydrocarbons and Alcohols in Microporous Metal Organic Frameworks. *Chem. Rev.* **112**, 836 (2012).

[40] B. Pato-Doldan, M. Sanchez-Andujar, L. C. Gomez-Aguirre, S. Yanez-Vilar, J. Lopez-Beceiro, C. Gracia-Fernandez, A. A. Haghighirad, F. Ritter, S. Castro-Garcia and M. A. Senaris-Rodriguez. Near Room Temperature Dielectric Transition in the Perovskite Formate Framework $[(CH_3)_2NH_2][Mg(HCOO)_3]$. *Phys. Chem. Chem. Phys.* **14**, 8498 (2012).

[41] M. Sánchez-Andújar, S. Presedo, S. Yánez-Vilar, S. Castro-García, J. Shamir and M. A. Senarís-Rodríguez. Characterization of the Order-Disorder Dielectric Transition in the Hybrid Organic-Inorganic Perovskite-Like Formate $Mn(HCOO)_3[(CH_3)_2NH_2]$. *Inorg. Chem.* **49**, 1510 (2010).

[42] M. Sánchez-Andújar, L. C. Gomez-Aguirre, B. Pato Doldan, S. Yanez-Vilar, R. Artiaga, A. L. Llamas-Saiz, R. S. Manna, F. Schnelle, M. Lang, F. Ritter, A. A. Haghighirad and M. A. Senarís-Rodríguez. First-Order Structural Transition in the Multiferroic Perovskite-Like Formate $[(CH_3)_2NH_2][Mn(HCOO)_3]$. *CrystEngComm* **16**, 3558 (2014).

[43] P. Jain, A. Stroppa, D. Nabok, A. Marino, A. Rubano, D. Paparo, M. Matsubara, H. Nakotte, M. Fiebig, S. Picozzi, E. S. Choi, A. K. Cheetham, C. Draxl, N. S. Dalal and V. S. Zapf. Switchable Electric Polarization and Ferroelectric Domains in a Metal-Organic-Framework. *Npj Quantum Materials* **1**, 16012 (2016).

[44] D.-W. Fu, W. Zhang, H.-L. Cai, Y. Zhang, J.-Z. Ge, R.-G. Xiong, S. D. Huang and T. Nakamura. A Multiferroic Perdeutero Metal-Organic Framework. *Angew. Chem., Int. Ed.* **50**, 11947 (2011).

[45] H. D. Duncan, M. T. Dove, D. A. Keen and A. E. Phillips. Local Structure of the Metal-Organic Perovskite Dimethylammonium Manganese(II) Formate. *Dalton Trans.* **45**, 4380 (2016).

[46] M. Mączka, A. Sieradzki, B. Bondzior, P. Deren, J. Hanuza and K. Hermanowicz. Effect of Aliovalent Doping on the Properties of Perovskite-Like Multiferroic Formates. *J. Mater. Chem. C* **3**, 9337 (2015).

[47] J. Lopez-Beceiro, C. Gracia-Fernandez, S. Gomez-Barreiro, S. Castro-Garcia, M. Sanchez-Andujar and R. Artiaga. Kinetic Study of the Low Temperature Transformation of $Co(HCOO)_3[(CH_3)_2NH_2]$. *J. Phys. Chem. C* **116**, 1219 (2012).

[48] T. Asaji, S. Yoshitake, Y. Ito and H. Fujimori. Phase Transition and Cationic Motion in the Perovskite Formate Framework $[(CH_3)_2NH_2][Mg(HCOO)_3]$. *J. Mol. Struct.* **1076**, 719 (2014).

[49] W. Wang, L.-Q. Yan, J.-Z. Cong, Y.-L. Zhao, F. Wang, S.-P. Shen, T. Zou, D. Zhang, S.-G. Wang, X.-F. Han and Y. Sun. Magnetoelectric Coupling in the Paramagnetic State of a Metal-Organic Framework. *Sci. Rep.* **3**, 2024 (2013).

[50] Y. Tian, A. Stroppa, Y. Chai, L. Yan, S. Wang, P. Barone, S. Picozzi and Y. Sun. Cross Coupling between Electric and Magnetic Orders in a Multiferroic Metal-Organic Framework. *Sci. Rep.* **4**, 6062 (2014).

[51] M. Mączka, M. Ptak and L. Macalik. Infrared and Raman Studies of Phase Transitions in Metal-Organic Frameworks of $[(CH_3)_2NH_2][M(HCOO)_3]$ with M=Zn, Fe. *Vib. Spectrosc.* **71**, 98 (2014).

[52] R. Yadav, D. Swain, H. L. Bhat and S. Elizabeth. Order-Disorder Phase Transition and Multiferroic Behaviour in a Metal Organic Framework Compound $(CH_3)_2NH_2Co(HCOO)_3$. *J. Appl. Phys.* **119**, 064103 (2016).

[53] N. Abhyankar, J. J. Kweon, M. Orio, S. Bertaina, M. Lee, E. S. Choi, R. Fu and N. S. Dalal. Understanding Ferroelectricity in the Pb-Free Perovskite-Like Metal-Organic Framework $[(CH_3)_2NH_2]Zn(HCOO)_3$: Dielectric, 2D NMR, and Theoretical Studies. *J. Phys. Chem. C* **121**, 6314 (2017).

[54] T. Besara, P. Jain, N. S. Dalal, P. L. Kuhns, A. P. Reyes, H. W. Kroto and A. K. Cheetham. Mechanism of the Order-Disorder Phase Transition, and Glassy Behavior in the Metal-Organic Framework $[(CH_3)_2NH_2]Zn(HCOO)_3$. *Proc. Natl. Acad. Sci.* **108**, 6828 (2011).

[55] T. Asaji and K. Ashitomi. Phase Transition and Cationic Motion in a Metal-Organic Perovskite, Dimethylammonium Zinc Formate $[(CH_3)_2NH_2][Zn(HCOO)_3]$. *J. Phys. Chem. C* **117**, 10185 (2013).

[56] K. L. Svane, A. C. Forse, C. P. Grey, G. Kieslich, A. K. Cheetham, A. Walsh

and K. T. Butler. How Strong Is the Hydrogen Bond in Hybrid Perovskites? *J. Phys. Chem. Lett.* **8**, 6154 (2017).

[57] N. Abhyankar, S. Bertaina and N. S. Dalal. On Mn^{2+} EPR Probing of the Ferroelectric Transition and Absence of Magnetoelectric Coupling in Dimethylammonium Manganese Formate $(CH_3)_2NH_2Mn(HCOO)_3$, a Metal-Organic Complex with the Pb-Free Perovskite Framework. *J. Phys. Chem. C* **119**, 28143 (2015).

[58] A. J. Clune, K. D. Hughey, C. Lee, N. Abhyankar, X. Ding, N. S. Dalal, M.-H. Whangbo, J. Singleton and J. L. Musfeldt. Magnetic Field-Temperature Phase Diagram of Multiferroic $[(CH_3)_2NH_2][Mn(HCOO)_3]$. *Phys. Rev. B* **96**, 104424 (2017).

[59] K. D. Hughey, A. J. Clune, M. O. Yokosuk, A. al Wahish, K. R. O'Neal, S. Fan, N. Abhyankar, H. Xiang, Z. Li, J. Singleton, N. S. Dalal and J. L. Musfeldt. Phonon Mode Links Ferroicities in Multiferroic $[(CH_3)_2NH_2]Mn(HCOO)_3$. *Phys. Rev. B* **96**, 180305 (2017).

[60] M. Mączka, A. Gagor, M. Ptak, W. Paraguassu, T. A. da Silva, A. Sieradzki and A. Pikul. Phase Transitions and Coexistence of Magnetic and Electric Orders in the Methylhydrazinium Metal Formate Frameworks. *Chem. Mater.* **29**, 2264 (2017).

[61] Y. Imai, B. Zhou, Y. Ito, H. Fijimori, A. Kobayashi, Z.-M. Wang and H. Kobayashi. Freezing of Ring-Puckering Molecular Motion and Giant Dielectric Anomalies in Metal-Organic Perovskites. *Chemistry - An Asian Journal* **7**, 2786 (2012).

[62] G.-C. Xu, X.-M. Ma, L. Zhang, Z.-M. Wang and S. Gao. Disorder-Order Ferroelectric Transition in the Metal Formate Framework of $[NH_4][Zn(HCOO)_3]$. *J. Am. Chem. Soc.* **132**, 9588 (2010).

[63] Z. Wang, B. Zhang, K. Inoue, H. Fujiwara, T. Otsuka, H. Kobayashi and M. Kurmoo. Occurrence of a Rare $4^9 \cdot 6^6$ Structural Topology, Chirality, and Weak Ferromagnetism in the $[NH_4][M^{II}(HCOO)_3]$ (M = Mn, Co, Ni) Frameworks. *Inorg. Chem.* **46**, 437 (2007).

[64] G.-C. Xu, W. Zhang, X.-M. Ma, Y.-H. Chen, L. Zhang, H.-L. Cai, Z.-M. Wang, R.-G. Xiong and S. Gao. Coexistence of Magnetic and Electric Orderings in the Metal-Formate Frameworks of $[NH_4][M(HCOO)_3]$. *J. Am. Chem. Soc.* **133**, 14948 (2011).

[65] M. Mączka, A. Pietraszko, B. Macalik and K. Hermanowicz. Structure,

Phonon Properties, and Order-Disorder Transition in the Metal Formate Framework of [NH$_4$][Mg(HCOO)$_3$]. *Inorganic Chemistry* **53**, 787 (2014).

[66] M. Mączka, P. Kadlubanski, P. T. C. Freire, B. Macalik, W. Paraguassu, K. Hermanowicz and J. Hanuza. Temperature- and Pressure-Induced Phase Transitions in the Metal Formate Framework of [ND$_4$][Zn(DCOO)$_3$] and [NH$_4$][Zn(HCOO)$_3$]. *Inorganic Chemistry* **53**, 9615 (2014).

[67] M. Mączka, M. Ptak and S. Kojima. Brillouin scattering study of ferroelectric transition mechanism in multiferroic metal-organic frameworks of [NH4][Mn(HCOO)3] and [NH4][Zn(HCOO)3]. *Applied Physics Letters* **104**, 222903 (2014).

[68] R. Shang, S. Chen, K.-L. Hu, Z.-C. Jiang, B.-W. Wang, M. Kurmoo, Z.-M. Wang and S. Gao. Hierarchical Cobalt-Formate Framework Series with $(4^{12} \cdot 6^3)(4^9 \cdot 6^6)_n$ (n = 1-3) Topologies Exhibiting Slow Dielectric Relaxation and Weak Ferromagnetism. *APL Mater.* **2**, 124104 (2014).

[69] R. Shang, G.-C. Xu, Z.-M. Wang and S. Gao. Phase Transitions, Prominent Dielectric Anomalies, and Negative Thermal Expansion in Three High Thermally Stable Ammonium Magnesium-Formate Frameworks. *Chem. - Eur. J.* **20**, 1146 (2014).

[70] M. Mączka, A. Gagor, N. L. M. Costa, W. Paraguassu, A. Sieradzki and A. Pikul. Temperature- and Pressure-Induced Phase Transitions in the Niccolite-Type Formate Framework of [H$_3$N(CH$_3$)$_4$NH$_3$][Mn$_2$(HCOO)$_6$]. *J. Mater. Chem. C* **4**, 3185 (2016).

[71] R. Shang, Z.-M. Wang and S. Gao. A 36-Fold Multiple Unit Cell and Switchable Anisotropic Dielectric Responses in an Ammonium Magnesium Formate Framework. *Angew. Chem., Int. Ed.* **54**, 2534 (2015).

[72] M. Mendt, M. Šimėnas and A. Pöppl. *Electron Paramagnetic Resonance in "The Chemistry of Metal-Organic Frameworks, Synthesis, Characterization, and Applications"*, chapter 21, pages 629–656. Wiley-Blackwell (2016).

[73] M. H. L. Pryce. A Modified Perturbation Procedure for a Problem in Paramagnetism. *Proc. Phys. Soc., London, Sect. A* **63**, 25 (1950).

[74] J. E. Wertz and J. R. Bolton. *Electron Spin Resonance*. Chapman and Hall (1986).

[75] A. Schweiger and G. Jeschke. *Principles of Pulse Electron Paramagnetic Resonance*. Oxford University Press (2001).

[76] D. J. Griffiths. *Introduction to Quantum Mechanics, 2nd Edition*. Pearson

Education. Inc (2005).

[77] G. Gabrielse, D. Hanneke, T. Kinoshita, M. Nio and B. Odom. New Determination of the Fine Structure Constant from the Electron g Value and QED. *Phys. Rev. Lett.* **97**, 030802 (2006).

[78] J. D. Jackson. *Classical Electrodynamics, 3rd Edition*. New York: Wiley (1998).

[79] A. Abragam and B. Bleaney. *Electron Paramagnetic Resonance of Transition Ions*. Clarendon Press, Oxford (1970).

[80] N. M. Atherton. *Principles of Electron Spin Resonance*. Ellis Horwood Limited (1993).

[81] B. R. McGarvey. The Isotropic Hyperfine Interaction. *J. Phys. Chem.* **71**, 51 (1967).

[82] A. Pöppl and L. Kevan. A Practical Strategy for Determination of Proton Hyperfine Interaction Parameters in Paramagnetic Transition Metal Ion Complexes by Two-Dimensional HYSCORE Electron Spin Resonance Spectroscopy in Disordered Systems. *J. Phys. Chem.* **100**, 3387 (1996).

[83] I. Ryabov. On the Generation of Operator Equivalents and the Calculation of Their Matrix Elements. *J. Magn. Reson.* **140**, 141 (1999).

[84] J. Solyom. *Fundamentals of the Physics of Solids, Vol. I*. Springer (2002).

[85] A. Bencini and D. Gatteschi. *EPR of Exchange Coupled Systems*. Springer-Verlag (1990).

[86] G. R. Eaton, S. S. Eaton, D. P. Barr and R. T. Weber. *Quantitative EPR*. SpringerWienNewYork (2010).

[87] P. Neugebauer and A.-L. Barra. New Cavity Design for Broad-Band Quasi-Optical HF-EPR Spectroscopy. *Appl. Magn. Reson.* **37**, 833 (2009).

[88] A. Schweiger. Pulsed Electron Spin Resonance Spectroscopy: Basic Principles, Techniques, and Examples of Applications. *Angew. Chem., Int. Ed.* **30**, 265 (1991).

[89] W. B. Mims, K. Nassau and J. D. McGee. Spectral Diffusion in Electron Resonance Lines. *Phys. Rev.* **123**, 2059 (1961).

[90] L. G. Rowan, E. L. Hahn and W. B. Mims. Electron-Spin-Echo Envelope Modulation. *Phys. Rev.* **137**, A61 (1965).

[91] W. B. Mims. Envelope Modulation in Spin-Echo Experiments. *Phys. Rev. B* **5**, 2409 (1972).

[92] W. B. Mims. Pulsed ENDOR Experiments. *Proc. R. Soc. London, Ser. A* **283**,

452 (1965).

[93] E. Davies. A New Pulse ENDOR Technique. *Physics Letters A* **47**, 1 (1974).

[94] C. P. Slichter. *Principles of Magnetic Resonance*. Springer (1996).

[95] E. L. Hahn. Spin Echoes. *Phys. Rev.* **80**, 580 (1950).

[96] S. Stoll and A. Schweiger. EasySpin, a Comprehensive Software Package for Spectral Simulation and Analysis in EPR. *J. Magn. Reson.* **178**, 42 (2006).

[97] P. Hofer. Distortion-Free Electron-Spin-Echo Envelope-Modulation Spectra of Disordered Solids Obtained from Two-Dimensional and Three-Dimensional HYSCORE Experiments. *J. Magn. Reson., Ser. A* **111**, 77 (1994).

[98] H. Cho, S. Pfenninger, C. Gemperle, A. Schweiger and R. Ernst. Zero Deadtime Pulsed ESR by Remote Echo Detection. *Chem. Phys. Lett.* **160**, 391 (1989).

[99] M. Šimėnas, A. Ciupa, M. Mączka, A. Pöppl and J. Banys. EPR Study of Structural Phase Transition in Manganese-Doped [(CH$_3$)$_2$NH$_2$][Zn(HCOO)$_3$] Metal-Organic Framework. *J. Phys. Chem. C* **119**, 24522 (2015).

[100] M. Šimėnas, A. Kultaeva, S. Balčiūnas, M. Trzebiatowska, D. Klose, G. Jeschke, M. Mączka, J. Banys and A. Pöppl. Single Crystal Electron Paramagnetic Resonance of Dimethylammonium and Ammonium Hybrid Formate Frameworks: Influence of External Electric Field. *J. Phys. Chem. C* **121**, 16533 (2017).

[101] M. Šimėnas, L. Macalik, K. Aidas, V. Kalendra, D. Klose, G. Jeschke, M. Mączka, G. Völkel, J. Banys and A. Pöppl. Pulse EPR and ENDOR Study of Manganese Doped [(CH$_3$)$_2$NH$_2$][Zn(HCOO)$_3$] Hybrid Perovskite Framework. *J. Phys. Chem. C* **121**, 27225 (2017).

[102] M. Šimėnas, A. Ciupa, G. Usevičius, K. Aidas, D. Klose, G. Jeschke, M. Mączka, G. Völkel, A. Pöppl and J. Banys. Electron Paramagnetic Resonance of a Copper Doped [(CH$_3$)$_2$NH$_2$][Zn(HCOO)$_3$] Hybrid Perovskite Framework. *Phys. Chem. Chem. Phys.* **20**, 12097 (2018).

[103] M. Šimėnas, M. Ptak, A. H. Khan, L. Dagys, V. Balevičius, M. Bertmer, G. Völkel, M. Mączka, A. Pöppl and J. Banys. Spectroscopic Study of [(CH$_3$)$_2$NH$_2$][Zn(HCOO)$_3$] Hybrid Perovskite Containing Different Nitrogen Isotopes. *J. Phys. Chem. C* (2018).

[104] M. Šimėnas, S. Balčiūnas, M. Mączka, J. Banys and E. E. Tornau. Structural

Phase Transition in Perovskite Metal-Formate Frameworks: a Potts-Type Model with Dipolar Interactions. *Phys. Chem. Chem. Phys.* **18**, 18528 (2016).

[105] S. K. Misra. Estimation of the Mn^{2+} Zero-Field Splitting Parameter from a Polycrystalline EPR Spectrum. *Physica B: Condensed Matter* **203**, 193 (1994).

[106] E. Šimánek and K. Müller. Covalency and Hyperfine Structure Constant A of Iron Group Impurities in Crystals. *Journal of Physics and Chemistry of Solids* **31**, 1027 (1970).

[107] K. Nishimura and T. Hashimoto. ESR Investigation of TGS Doped with Cr^{3+} Ions. *J. Phys. Soc. Jpn.* **35**, 1699 (1973).

[108] G. Völkel, W. Brunner and W. Windsch. Critical Fluctuations in Trissarcosine Calcium Chloride (TSCC) Observed by the Electron Spin Echo (ESE) Method. *Solid State Commun.* **17**, 345 (1975).

[109] W. Windsch. Paramagnetic Resonance Studies in Ferroelectric Tris-Sarcosine Calcium Chloride. *Ferroelectrics* **12**, 63 (1976).

[110] T. von Waldkirch, K. A. Müller and W. Berlinger. Fluctuations in $SrTiO_3$ near the 105-K Phase Transition. *Phys. Rev. B* **7**, 1052 (1973).

[111] T. Hidaka and K. Oka. Isotope Effect on $BaTiO_3$ Ferroelectric Phase Transitions. *Phys. Rev. B* **35**, 8502 (1987).

[112] T. Hidaka and K. Oka. Nonhydrogen Isotope Effects on Structural Phase Transitions in Dielectric Crystals. *Phys. Rev. B* **42**, 8295 (1990).

[113] T. Hidaka. Isotope Effects on Structural Phase Transitions in Several Sulfates. *Phys. Rev. B* **45**, 440 (1992).

[114] M. H. Levitt. *Spin Dynamics: Basics of Nuclear Magnetic Resonance.* Wiley, 2 edition (2008).

[115] J. F. Scott. Ferroelectrics Go Bananas. *J. Phys. Condens. Matter* **20**, 021001 (2008).

[116] R. Blinc and P. Cevc. Electron Paramagnetic Resonance Study of Proton Dynamics in KH_2PO_4 - KH_2AsO_4 Mixed Crystals. *Solid State Commun.* **6**, 635 (1968).

[117] N. S. Dalal, C. A. McDowell and R. Srinivasan. Electron Paramagnetic-Resonance and Electron-Nuclear Double-Resonance Observations of Domains in the Irradiated Ferroelectrics KH_2AsO_4 and KD_2AsO_4. *Phys. Rev. Lett.* **25**, 823 (1970).

[118] K. Hukuda, H. Hanafusa and T. Kawano. Electron Spin Resonance of SeO_4^{3-} and SeO_3^{-} Radicals in KDP Single Crystal. *J. Phys. Soc. Jpn.* **36**, 1043

(1974).

[119] R. D. Truesdale, H. A. Farach and C. P. Poole. Hysteresis Effects in X-irradiated KH_2PO_4, KD_2PO_4, and RbH_2PO_4 Ferroelectric Single Crystals Observed with Electron-Spin Resonance. *Phys. Rev. B* **22**, 365 (1980).

[120] R. D. Truesdale, C. P. Poole and H. A. Farach. Low-Temperature Ferroelectric Polarization Reversal Monitored by Electron Spin Resonance of As_4^{4-} in X-irradiated KD_2PO_4-KH_2AsO_4 Mixed Crystals. *Phys. Rev. B* **25**, 474 (1982).

[121] N. S. Dalal. Electron Paramagnetic Resonance Detection of Electric Field Effect on the Nucleation of the Ferroelectric Phase of KD_2PO_4. *J. Am. Chem. Soc.* **104**, 5511 (1982).

[122] A. Raitsimring, A. Dalaloyan, A. Collauto, A. Feintuch, T. Meade and D. Goldfarb. Zero Field Splitting Fluctuations Induced Phase Relaxation of Gd^{3+} in Frozen Solutions at Cryogenic Temperatures. *J. Magn. Reson.* **248**, 71 (2014).

[123] H.-E. Müller, G. Völkel, W. Brunner, P. Cevc and I. N. Kurkin. Electron Spin Relaxation in Ferroelastic $KH_3(SeO_3)_2$. *Phys. Status Solidi B* **141**, 343 (1987).

[124] H. Langen, A. S. Montjoie, W. Muller-Warmuth and H. Stiller. NMR T_1-analysis of Methyl Tunnelling in Molecular Crystals at Intermediate Barriers. *Z. Naturforsch.* **42a**, 1266 (1987).

[125] G. Völkel, H.-E. Müller and W. Flohrer. Critical Anomaly of the Electron Spin-Lattice Relaxation in X-Irradiated Rochelle Salt. *Phys. Status Solidi B* **108**, 501 (1981).

[126] K. L. Svane and A. Walsh. Quantifying Thermal Disorder in Metal-Organic Frameworks: Lattice Dynamics and Molecular Dynamics Simulations of Hybrid Formate Perovskites. *J. Phys. Chem. C* **121**, 421 (2017).

[127] A. Pöppl, G. Völkel, J. Hoentsch, S. Orlinski and A. Klopperpieper. Electron Spin Relaxation of the PO_3^{2-} Radical in Ferroelectric Betaine Phosphite and in the Proton Glass Betaine Phosphate/Betaine Phosphite. *Chem. Phys. Lett.* **224**, 233 (1994).

[128] W. Brunner, G. Völkel, W. Windsch, I. Kurkin and V. Shlenkin. Electron Spin-Lattice Relaxation in Mn^{2+}-Doped Ferroelectric TSCC. *Solid State Commun.* **26**, 853 (1978).

[129] G. Völkel, W. Brunner, W. Windsch and D. Steudel. Electron Spin-Echo

(ESE) Investigations of Critical Paramagnetic Relaxation Anomalies in X-Irradiated Triglycine Sulphate (TGS:X). *Phys. Status Solidi B* **95**, 99 (1979).

[130] R. Böttcher, W. Brunner, B. Milsch, G. Völkel, W. Windsch and S. Kirillov. EPR, ENDOR and ESE Investigations on Chromium Modified $PbTiO_3$ Ceramics. *Chem. Phys. Lett.* **129**, 546 (1986).

[131] A. Pöppl, P. Baglioni and L. Kevan. Electron Spin Resonance and Electron Spin Echo Modulation Studies of the Incorporation of Macrocyclic-Complexed Cupric Ions into Siliceous MCM-41. *J. Phys. Chem.* **99**, 14156 (1995).

[132] S. Hoffmann, J. Goslar, S. Lijewski, K. Tadyszak, A. Zalewska, A. Jankowska, P. Florczak and S. Kowalak. EPR and UV-vis Study on Solutions of Cu(II) dmit Complexes and the Complexes Entrapped in Zeolite A and ZIF-Cu(IM)$_2$. *Microporous Mesoporous Mater.* **186**, 57 (2014).

[133] E. Sletten and L. H. Jensen. The Crystal Structure of Dimethylammonium Copper(II) Formate, $NH_2(CH_2)_2[Cu(OOCH)_3]$. *Acta Crystallogr. B* **29**, 1752 (1973).

[134] P. J. Baker, T. Lancaster, I. Franke, W. Hayes, S. J. Blundell, F. L. Pratt, P. Jain, Z.-M. Wang and M. Kurmoo. Muon Spin Relaxation Investigation of Magnetic Ordering in the Hybrid Organic-Inorganic Perovskites $[(CH_3)_2NH_2]M(HCOO)_3$ (M=Ni,Co,Mn,Cu). *Phys. Rev. B* **82**, 012407 (2010).

[135] B. Hathaway, M. Duggan, A. Murphy, J. Mullane, C. Power, A. Walsh and B. Walsh. The Stereochemistry and Electronic Properties of Fluxional Six-Coordinate Copper(II) Complexes. *Coord. Chem. Rev.* **36**, 267 (1981).

[136] Z. Wang, P. Jain, K.-Y. Choi, J. van Tol, A. K. Cheetham, H. W. Kroto, H.-J. Koo, H. Zhou, J. Hwang, E. S. Choi, M.-H. Whangbo and N. S. Dalal. Dimethylammonium Copper Formate $[(CH_3)_2NH_2]Cu(HCOO)_3$: A metal-Organic Framework with Quasi-One-Dimensional Antiferromagnetism and Magnetostriction. *Phys. Rev. B* **87**, 224406 (2013).

[137] R. S. Rubins and J. E. Drumheller. The Temperature Dependence of the EPR Spectrum of Cu^{2+} in $ZnTiF_6 \cdot 6\,H_2O$ between 4 and 160 K. *J. Chem. Phys.* **86**, 6660 (1987).

[138] M. Šimėnas, S. Balčiūnas, M. Trzebiatowska, M. Ptak, M. Mączka, G. Völkel, A. Pöppl and J. Banys. Electron Paramagnetic Resonance and Electric Characterization of a $[CH_3NH_2NH_2][Zn(HCOO)_3]$ Perovskite

Metal Formate Framework. *J. Mater. Chem. C* **5**, 4526 (2017).

[139] M. Mączka, K. Pasinska, M. Ptak, W. Paraguassu, T. A. da Silva, A. Sieradzki and A. Pikul. Effect of Solvent, Temperature and Pressure on the Stability of Chiral and Perovskite Metal Formate Frameworks of $[NH_2NH_3][M(HCOO)_3]$ (M = Mn, Fe, Zn). *Phys. Chem. Chem. Phys.* **18**, 31653 (2016).

[140] J. Kliava and J. Purans. Simulation of EPR Spectra of Mn^{2+} in Glasses. *J. Magn. Reson.* **40**, 33 (1980).

[141] K. Tsuchida and R. Abe. Anomaly of ESR Line Width in γ-Irradiated KH_2PO_4 and KD_2PO_4. *J. Phys. Soc. Jpn.* **38**, 1687 (1975).

[142] A. Maryanowska and J. Pietrzak. Critical-Point Anomalies in the EPR Linewidth of $Pb(Fe_{0.5}Nb_{0.5})O_3$. *Phys. Status Solidi A* **68**, 185 (1981).

[143] M. Šimėnas, A. Ciupa, M. Mączka, G. Völkel, A. Pöppl and J. Banys. EPR of Structural Phase Transition in Manganese- and Copper-Doped Formate Framework of $[NH_3(CH_2)_4NH_3][Zn(HCOO)_3]_2$. *J. Phys. Chem. C* **120**, 19751 (2016).

[144] M. Mączka, M. Ptak, S. Pawlus, W. Paraguassu, A. Sieradzki, S. Balčiūnas, M. Šimėnas and J. Banys. Temperature- and Pressure-Dependent Studies of Niccolite-Type Formate Frameworks of $[NH_3(CH_2)_4NH_3][M_2(HCOO)_6]$ (M = Zn, Co, Fe). *Phys. Chem. Chem. Phys.* **18**, 27613 (2016).

[145] A. Schonhals and F. Kremer. *Broadband Dielectric Spectroscopy*. Springer-Verlag Berlin Heidelberg, 1 edition (2003).

[146] S. Ghosh, D. D. Sante and A. Stroppa. Strain Tuning of Ferroelectric Polarization in Hybrid Organic Inorganic Perovskite Compounds. *J. Phys. Chem. Lett.* **6**, 4553 (2015).

[147] A. Stroppa, P. Jain, P. Barone, M. Marsman, J. M. Perez-Mato, A. K. Cheetham, H. W. Kroto and S. Picozzi. Electric Control of Magnetization and Interplay between Orbital Ordering and Ferroelectricity in a Multiferroic Metal-Organic Framework. *Angew. Chem. Int. Ed.* **50**, 5847 (2011).

[148] F. Neese. The ORCA Program System. *Wiley Interdiscip. Rev. Comput. Mol. Sci.* **2**, 73 (2012).

[149] W. Janke and R. Villanova. Three-Dimensional 3-State Potts Model Revisited with New Techniques. *Nucl. Phys. B* **489**, 679 (1997).

[150] M. Šimėnas, S. Balčiūnas, M. Mączka, J. Banys and E. E. Tornau. Exploring

the Antipolar Nature of Methylammonium Lead Halides: A Monte Carlo and Pyrocurrent Study. *J. Phys. Chem. Lett.* **8**, 4906 (2017).

[151] M. Šimėnas, J. Banys and E. E. Tornau. Screening of Point Defects in Methylammonium Lead Halides: a Monte Carlo Study. *J. Mater. Chem. C* **6**, 1487 (2018).

[152] C. Adamo and V. Barone. Toward Reliable Density Functional Methods Without Adjustable Parameters: The PBE0 Model. *J. Chem. Phys.* **110** (1999).

[153] D. Chong. *Recent Advances in Computational Chemistry-Vol. 1.* World Scientific Publishing (1995).

[154] R. A. Kendall, T. H. Dunning and R. J. Harrison. Electron Affinities of the First-Row Atoms Revisited. Systematic Basis Sets and Wave Functions. *J. Chem. Phys.* **96**, 6796 (1992).

[155] F. Neese, F. Wennmohs, A. Hansen and U. Becker. Efficient, Approximate and Parallel Hartree-Fock and Hybrid DFT Calculations. A 'Chain-of-Spheres' Algorithm for the Hartree-Fock Exchange. *Chem. Phys.* **356**, 98 (2009).

[156] A. D. Becke. Density Functional Thermochemistry. III. The Role of Exact Exchange. *J. Chem. Phys.* **98**, 5648 (1993).

[157] V. A. Rassolov, J. A. Pople, M. A. Ratner and T. L. Windus. 6-31G* Basis Set for Atoms K through Zn. *J. Chem. Phys.* **109**, 1223 (1998).

[158] N. B. Balabanov and K. A. Peterson. Systematically Convergent Basis Sets for Transition Metals. I. All-Electron Correlation Consistent Basis Sets for the 3d Elements Sc-Zn. *J. Chem. Phys.* **123**, 064107 (2005).

[159] F. Neese. Efficient and Accurate Approximations to the Molecular Spin-Orbit Coupling Operator and their use in Molecular g-tensor Calculations. *J. Chem. Phys.* **122**, 034107 (2005).

[160] J. Tao, J. P. Perdew, V. N. Staroverov and G. E. Scuseria. Climbing the Density Functional Ladder: Nonempirical Meta-Generalized Gradient Approximation Designed for Molecules and Solids. *Phys. Rev. Lett.* **91**, 146401 (2003).

[161] F. Neese. Prediction and Interpretation of the ^{57}Fe Isomer Shift in Mossbauer Spectra by Density Functional Theory. *Inorganica Chim. Acta* **337**, 181 (2002).

Curriculum Vitae

Personal Information

First/Last name	Mantas Šimėnas
Date of birth	1988 September 4
Place of birth	Rokiškis, Lithuania
Nationality	Lithuanian
Postal address	Kazio Ulvydo 11, LT-08247 Vilnius

Education

Rokiškis Juozas Tūbelis gymnasium 1996-2007	Secondary education
Vilnius University 2008-2012	Bachelor degree in Applied Physics (Cum Laude)
Leipzig University 2012-2014	Master of Science
Vilnius University 2014-2018	PhD in Physics

Professional Career

Vilnius University 2014-2018	Junior research fellow, lecturer

Scholarships, Grants and Awards

Research Council of Lithuania 2011-2012	Student scholarships

Deutscher Akademischer Austauschdienst (DAAD) 2012-2014	Scholarships
Research Council of Lithuania 2014-2018	Scholarships
Research Council of Lithuania 2014-2018	Travel grants
COST Action TO-BE 2015, 2016	STSM travel grants
Lithuanian academy of Sciences 2018	Best Young Researcher Award

Number of ISI Publications   28

Presentations at Conferences   33